FY05 Engineering Research and Technology Report

Laboratory Directed Research and Development

Technology Base

Acknowledgments

Cover:

Graphics representing projects from Engineering's technology areas.

FY05 Engineering Research and Technology Report

Laboratory Directed Research and Development

Technology Base

April
2006

Lawrence Livermore
National Laboratory

Steven R. Patterson
Associate Director for Engineering

This report summarizes the core research and technology accomplishments in Lawrence Livermore National Laboratory's Engineering Directorate for FY2005. These efforts exemplify Engineering's more than 50-year history of developing and applying the technologies needed to support the Laboratory's missions. A partner in every major program and project at the Laboratory throughout its existence, Engineering has prepared for this role with a skilled workforce and technical resources developed through both internal and external venues. These accomplishments embody Engineering's mission: "Enable program success today and ensure the Laboratory's vitality tomorrow."

Engineering's investment in technologies is carried out primarily through two internal programs: the Laboratory Directed Research and Development (LDRD) program and the technology base, or "Tech Base," program. LDRD is the vehicle for creating technologies and competencies that are cutting-edge, or require fundamental discovery to be fully understood. Tech Base is used to prepare those technologies to be more broadly applicable to a variety of Laboratory needs. The term commonly used for Tech Base projects is "reduction to practice." Thus, LDRD reports have a strong research emphasis, while Tech Base reports document discipline-oriented, core competency activities.

This year, we combine the LDRD and Tech Base reports in one volume, organized into eight thematic technical areas: Engineering Modeling and Simulation; Micro-Meso-Nanoscale Engineering; Sensors to Knowledge; Energy Manipulation; Ultrafast Technologies; Nondestructive Characterization; Precision Engineering; and Materials Engineering.

Engineering Modeling and Simulation efforts focus on the research, development, and deployment of software technologies to aid in most facets of Engineering's mission. Current activities range from fundamental advances to enable accurate modeling of full-scale DOE and DoD systems performing at their limits, to advances for treating photonic and microfluidic systems.

FY2005 LDRD projects encompassed advances in adaptive mesh refinement for finite-element analysis (FEA), coupling standard FEA methods with "meshless" methods to address systems at and beyond failure; integration of electromagnetic forces with structural mechanics solutions; and nonlinear materials treatments for photonic systems. Tech Base projects included enhancements, verification, and validation of engineering simulation tools and capabilities; progress in visualization and data management tools; and extensions of our competence in structural damage analysis.

Micro-Meso-Nanoscale Engineering and technology efforts fuel the commercial growth of microelectronics and sensors, while simultaneously customizing these technologies for unique, noncommercial applications that are mission-specific to LLNL and DOE. LLNL's R&D talent and unique fabrication facilities have enabled highly innovative and custom solutions to technology needs in Stockpile Monitoring and Stewardship, Homeland Security, and Intelligence.

FY2005 LDRD projects included the development of a novel solution-based assay using Nanobarcodes, ™ and novel capabilities to perform automated front-end processing of complex biological samples. Tech Base projects included the demonstration of an automated and general-purpose microfluidic workstation to test and evaluate microfluidic modules; integration and testing of a contact stress-sensing array and a modular optical assembly for the weapons programs; and demonstration of inkjet technology to dispense ultra-precise quantities (nanoliter to picoliter volumes) of complex liquids at specific locations.

Sensors to Knowledge, an emerging focus area for Engineering as well as for the country at large, encompasses a wide variety of technologies. The area embodies development and deployment of sensors and the integration (or fusing) of their resulting data streams. The goal is to generate new understanding or knowledge of situations, thereby allowing anticipation or prediction of possible outcomes. With this knowledge, a more comprehensive solution may be possible for

problems as complex as the prediction of disease outbreaks or an advance warning of terrorist threats.

FY2005 LDRD research included a project to determine the location and contents of atmospheric releases based on sensors in the field. Tech Base efforts included geo-location methods for harsh environments; a cooperative discrimination sensor system for detecting and tracking humans; and new miniature echelle gratings for spectrometry.

Energy Manipulation, a re-emergent focus area, encompasses the fundamental understanding and technology deployment for many modern pulsed power applications. This area has broad applications for magnetic flux compression generators and components for modern accelerators.

FY2005 LDRD research included thermal batteries to enable persistent monitoring platforms. Tech Base efforts involved implementation of new multipoint initiation concepts for safer ignition of high explosives.

Ultrafast Technologies comprise activities to enable high-bandwidth sampling of signals with unprecedented resolution in both time and space. The advances in this area are essential for the future experimental needs in both the Inertial Confinement Fusion and the High-Energy-Density Physics programs.

FY2005 LDRD research featured transient recording extensions for streak cameras and investigations into terahertz systems for explosion detection. Tech Base projects included a new infrastructure for the fabrication of photonic integrated circuits and the implementation of a new transient sampling data recorder.

Nondestructive Characterization advances and applies measurement technologies to improve the Laboratory's nonintrusive inspection, design, and refurbishment of systems and components. This area plays a vital role in scientific and engineering characterization technologies, such as electromagnetic waves (e.g., infrared, microwave, visible, and x rays), acoustics, and particles (e.g., neutrons). In conjunction with signal and image processing, advances in characterization measurement technologies enable Engineering to address the needs of a broad spectrum of Laboratory and DOE programs.

FY2005 LDRD projects included acoustic characterization of mesoscale objects; phase effects on mesoscale object x-ray absorption images; and research on the structure and properties of nanoporous materials. Tech Base projects included an as-built modeling translational tool; super-resolution algorithms for ultrasonics imaging; application of seismic Unix for nondestructive imaging; upgrade of neutron digital radiography and computed tomography at the McClellan Nuclear Radiation Center at the University of California, Davis; and comparison of registration methods for MRI brain images.

Precision Engineering core technologies are the building blocks for the machines, systems, and processes that will be required for future Laboratory and DOE programs. These technologies help advance the Laboratory's high-precision capabilities in manufacturing, dimensional metrology, and assembly. Precision engineering is a multidisciplinary systems approach to achieve an order of magnitude greater accuracy than currently achievable.

FY2005 Tech Base projects included advances in interferometer filter systems; a digital tachometer for precision machine tools; a hydraulic power unit for hydrostatic bearings; and a continuation of fabrication projects with other technology areas.

Materials Engineering technology encompasses the foundations for understanding the response of material at its limits, and the experimental grounding required for accurate computational simulations.

FY2005 LDRD activities included the development of new data for large strains in bcc crystals; new IR diagnostics for the dynamic failure of materials; and basic research into the possibilities for *in-situ* nanobarometers. Tech Base activities included new temperature capabilities for a transmission electron microscope nanostage and the implementation of a dynamic impact test capability.

Contents

Micro-Meso-Nanoscale Engineering

Sensors to Knowledge

CONTENTS

Precision Engineering

Materials Engineering

Author Index

Engineering Modeling and Simulation

Adaptive Mesh Refinement Algorithms for Parallel Unstructured Finite-Element Codes

At LLNL, the state-of-the-art solvers used for solid mechanics and electromagnetic simulations have sufficient architectural and functional maturity to benefit from the introduction of appropriate adaptive mesh refinement (AMR) strategies. These new tools will enable analysts to conduct more reliable simulations at reduced cost, in terms of both analyst and computer time. Previous academic research in AMR has produced a voluminous literature focused on error estimators and demonstration problems. Relatively little progress has been made on producing efficient implementations suitable for large-scale problem solving on state-of-the-art computer systems. Research issues that we will consider include: effective error estimators for nonlinear structural mechanics and electromagnetics problems, local meshing at irregular geometric boundaries, and constructing efficient software for parallel computing environments.

Project Goals

The objective of this research is to implement AMR algorithms in unstructured finite-element codes used for solving nonlinear structural and electromagnetics problems on ASC-class, multiprocessor parallel (MPP) computers.

Relevance to LLNL Mission

Many programmatic problems will be solved with greater precision and accuracy using the new AMR technology. Successful completion of this project will position LLNL as a leader in parallel finite-element technology, providing capabilities not present in other analysis systems.

FY2005 Accomplishments and Results

A parallel AMR capability has been added to Diablo, a structural analysis code. This includes the data structures and algorithms required to refine a user-defined mesh and error estimators based on patch recovery techniques and residual computations.

Various test problems have been constructed to confirm the correctness of the implementations. The AMR implementation is able to perform both isotropic and anisotropic refinement as well as derefinement of a mesh (Fig. 1). Anisotropic refinement

Anistropic
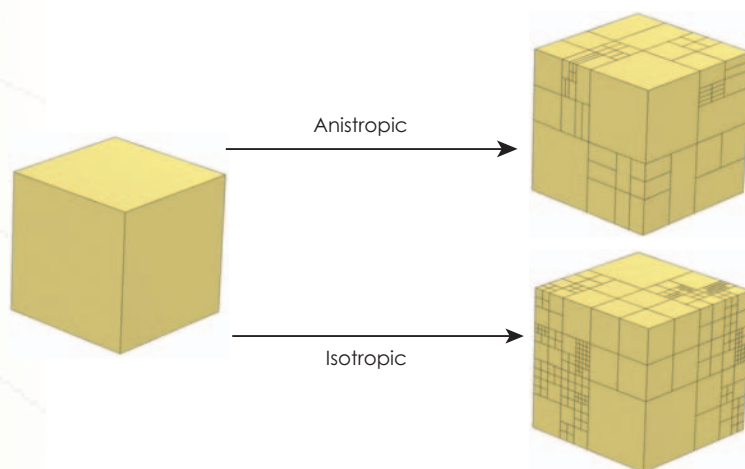
Isotropic

Figure 1. Meshes generated using isotropic and anisotropic h-refinement.

For more information contact
Dennis Parsons
(925) 422-5208
parsons14@llnl.gov

(refinement based on a directional error estimator) and derefinement are crucial for solving highly transient problems and implicit analysis, where the cost of solving equations can increase considerably with problem size. Savings of the order of 40% in both numbers of elements used and total CPU time required have been observed for some representative test problems.

Gregory patches are used to track evolving nonplanar boundaries. This allows the refined mesh to accurately capture the large geometric changes that are often encountered in structural analysis (Fig. 2).

Figure 3 shows mesh refinement for two bodies in contact. Algorithm and software documentation are being produced using the Unified Modeling Language that will form the basis of the abstraction of the AMR schemes. Coupled thermomechanics simulations have been conducted to demonstrate the capabilities of the current AMR implementation in Diablo.

For electromagnetics, both local and residual-based patch recovery have been developed and implemented within the EMSolve production code. Figure 4 shows results obtained from an eddy current pipe demonstration problem. In this example, an alternating current flows up and down the inner surface of a metal pipe. The current diffuses outward into this pipe. The exact solution is a magnetic field that wraps around the core of the pipe with an amplitude that oscillates while decaying radially as a cylindrical Bessel function. Good agreement between actual and estimated errors has been observed for this and several other relevant test problems.
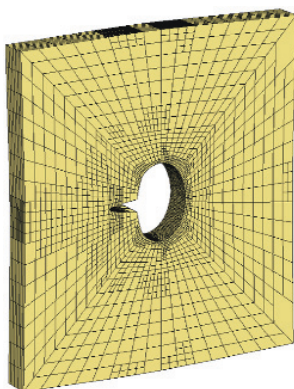
Figure 2. Refined mesh created using Gregory patches to track nonplanar boundaries.
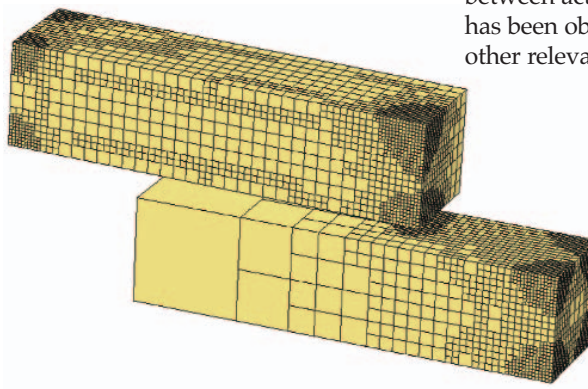
Figure 3. Refined meshes created for two bodies in contact.

(a)

(b)
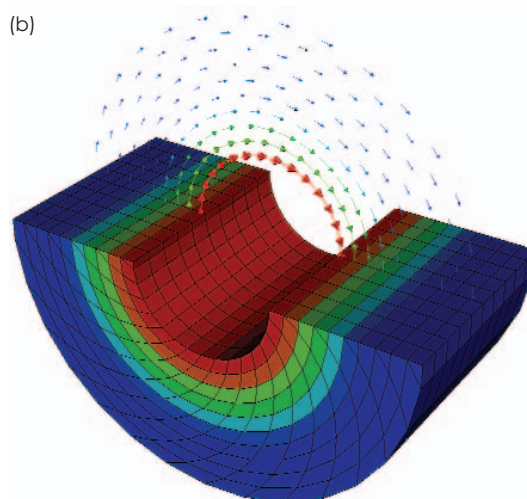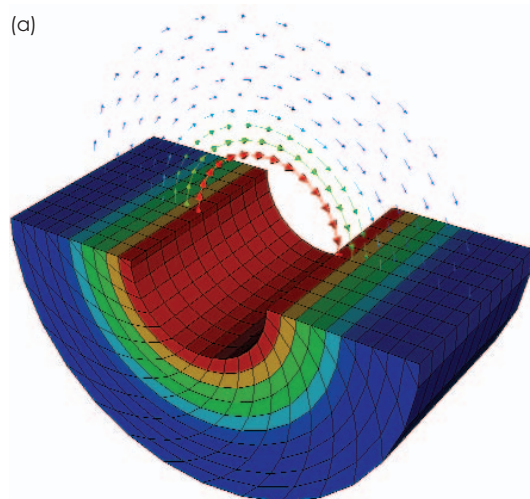
Figure 4. Results for the eddy current pipe: (a) actual error, and (b) error estimated using a patch recovery scheme, showing the effectiveness of the error estimator.

New "Natural Neighbor" Meshless Method for Modeling Extreme Deformations and Failure

The objective of this work is to develop a fully Lagrangian approach based on a "natural neighbor" discretization technique to model extreme deformation and failure for analyses such as earth penetration and dam failure. In these problems, our standard Lagrangian finite-element approach fails, due to mesh tangling, and our Eulerian codes do not allow us to track particles and free surfaces to the degree necessary. Meshless particle methods, such as smooth particle hydrodynamics (SPH) and element-free Galerkin (EFG), have been used for modeling such large deformations but have a variety of numerical problems that the new natural neighbor method can potentially solve. To use the new approach successfully, issues such as numerical integration, time-step calculation, and adaptive point insertion are researched.

Project Goals

The goal of this work is to develop a more stable, more accurate meshless particle approach by overcoming the numerous problems inherent in these methods. The new approach will provide an improved method for modeling extreme events such as earth penetration and dam failure. Furthermore, because it is meshless, the approach can be used for applications where nondestructive characterizations are available, such as as-built weapons analysis and biomechanics. Overall, we will be able to solve a much larger class of problems.

Relevance to LLNL Mission

High-rate penetration dynamics has been identified as a challenge area in engineering and our new particle methods apply directly to applications in that field. Along with earth- and armor-penetration problems, vulnerability evaluation of infrastructures such as dams can be analyzed. As-built x-ray tomography of NIF targets and *in-vivo* MRI imaging for biomechanics create "point clouds" and are other good examples of where a meshless method could be exploited to expedite stress analyses.
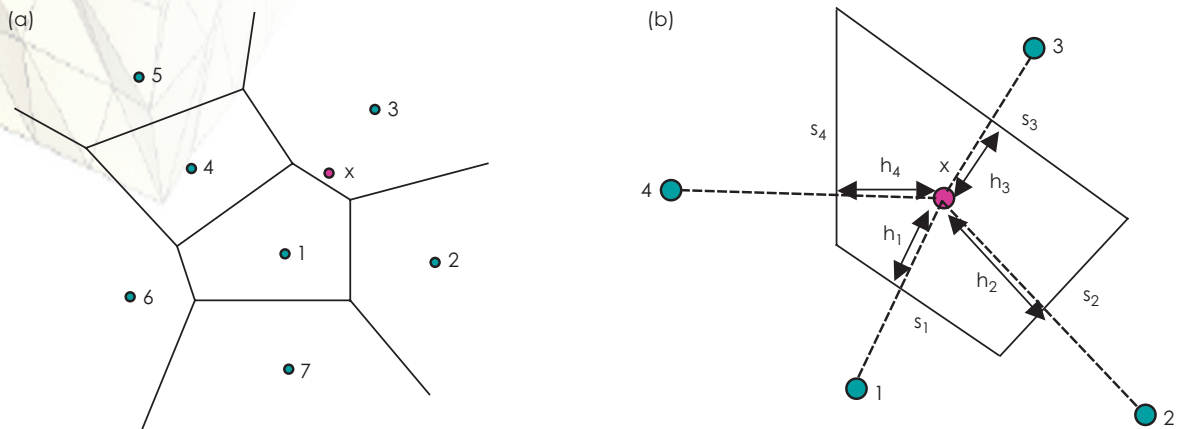
Figure 1. (a) Cloud of seven points and associated Voronoi diagram. (b) Considering the arbitrary location, **x**, in (a), a secondary local Voronoi cell is formed about this location **x** using its "nearest neighbors," points 1 to 4.

For more information contact
Michael A. Puso
(925) 422-8198
puso1@llnl.gov

FY2005 Accomplishments and Results

We implemented the natural neighbor interpolation method during FY2004. The Laplace shape function is defined from a Voronoi diagram of the cloud of points. Consider the 2-D cloud of points and the associated Voronoi diagram in Fig. 1(a). The shape function, N_i, for node $i = 1,4$ evaluated at the location, x, is computed from the local Voronoi cell in Fig. 1(b), about the point, x, using the lengths, s_i (the length of the edge), and h_i (the distance between x and p_i), in the equation,

$$N_i(x) = \frac{s_i/h_i}{\sum_{j=1}^{5} s_j/h_j}$$

We used a nodal integration scheme of the weak Galerkin form, where the strain at a node, i, is volume-averaged over the associated Voronoi cell using Green's theorem.

In 2005, we found that the method is, in fact, rank stable but is not stable in the H_1 norm. The problem was fixed using a perturbation stabilization technique that subdivides the Voronoi cell into subelements. This eliminated the weak mode present in the original implementation (Fig. 2). This technique was also successfully applied in FY2005 to the piecewise linear interpolation.

The Voronoi diagram provides integration domains for the new meshless method. Voronoi diagrams are simple to produce on convex domains but not so on nonconvex domains. Furthermore, Voronoi cells need to be capped at perceived boundaries. FY2005 work continued this effort. Figure 3 shows the resulting trimmed Voronoi diagram from a cloud of points using the "alpha approach." Finally, a technique for computing a stable explicit time step was developed by computing an upper bound on the maximum frequency of the discrete system. Until now, no method has been available for doing this for arbitrary meshless discretizations.

FY2006 Proposed Work

FY2006 will be dedicated to finishing NIKE3D/DYNA3D small deformation implementations, and extending the work to handle large deformations and damage. Tasks also include exploring different damage models and implementing adaptive point insertion.
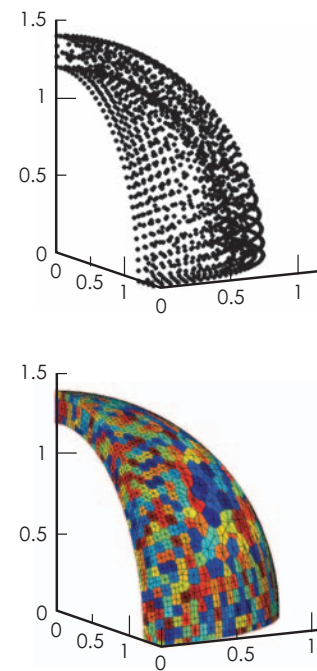
Figure 3. Cloud of points and trimmed Voronoi cells.

(a)

(b)

(c)

Figure 2. First eigenmode from (a) FEM 0.258 Hz; (b) NN (stabilized) 0.253 Hz; (c) NN (unstabilized) 0.161 Hz, illustrating the poor behavior of an unstabilized natural neighbor discretization.

Electro-Thermal-Mechanical Simulation Capability

LLNL has long been a world leader in computational solid mechanics. Recently several solid mechanics codes have become "multiphysics" codes, with the addition of fluid dynamics, heat transfer, and chemistry. However, these multiphysics codes do not incorporate the electromagnetics required for a coupled electro-thermal-mechanical (ETM) simulation. The purpose of this project is to research and develop numerical algorithms for 3-D ETM simulations. There are numerous applications for this capability, such as explosively-driven magnetic flux compressors, electromagnetic launchers, inductive heating and mixing of metals, and MEMS. A robust ETM simulation capability will enable physicists and engineers to better support current DOE programs, and will prepare LLNL for long-term DoD applications.

Project Goals

We define a coupled ETM simulation as a simulation that solves, in a self-consistent manner, the equations of electromagnetics (primarily statics and diffusion), heat transfer (primarily conduction), and nonlinear mechanics (elastic-plastic deformation, and contact with friction). The goal is to add electromagnetics to two existing mechanics codes, ALE3D and Diablo. ALE3D is a heavily used arbitrary-Lagrangian-Eulerian hydrodynamics code; Diablo, currently under development, is an implicit Lagrangian thermal-mechanics code. A finite-element discretization will be used for the electromagnetics. The coupling of the electromagnetic equations, thermal equations, and mechanics equations will be initially done in an operator-split manner. The coupling mechanisms are illustrated in Fig. 1.

Figure 1. Illustration of the ETM coupling mechanism assumed for this project. The EM module computes the fields E, B and J; the thermal module computes the temperature, T; the mechanics module computes the position, U, and work, W, of the materials.

The EM equation shown:
$$\frac{\partial B}{\partial t} = -\nabla\times\frac{1}{\sigma}\nabla\times\frac{1}{\mu}B + g + \nabla\times\upsilon\times B$$

Thermal equation:
$$c\frac{\partial T}{\partial t} = \nabla\bullet k\nabla T + J\bullet E$$

Mechanics equation:
$$\rho\frac{\partial^2 U}{\partial t^2} = \nabla\bullet S + J\times B$$
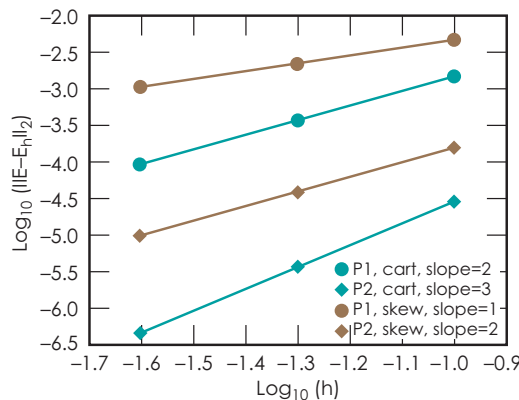
Figure 2. Example convergence result for the higher-order $H(curl)$ discretization of the time-dependent eddy current equations. The blue lines are for a Cartesian mesh and show superconvergence; the red lines are for a distorted mesh and illustrate standard $O(h^p)$ convergence.

For more information contact
Daniel A. White
(925) 422-9870
white37@llnl.gov

Relevance to LLNL Mission

We are developing a novel simulation capability. With this capability, LLNL will have an unprecedented ability to simulate, design, and optimize ETM systems. This project is aligned with LLNL's core competency in simulation science and engineering. It contributes to the mission to enhance and extend simulation capabilities, and specifically addresses this need in the area of energy manipulation. This project complements ongoing Advanced Simulation and Computing (ASC) work and will use ASC computers and software, such as linear solver packages and visualization tools.

FY2005 Accomplishments and Results

We investigated several different formulations for the electromagnetics, namely the *E*-field formulation, the *H*-field formulation, and the *A-Phi* formulations. We applied the Galerkin procedure to each formulation using *H(curl)*-conforming finite elements,

yielding a discrete system of equations that is integrated in time implicitly. The key differences between the three formulations are the *natural* and *essential* boundary conditions. We developed a consistent $O(h^p)$ method for computing the magnetic flux density, *B*, and the induced eddy current density, *J*, for each of the three formulations, and verified the convergence, as shown in Fig. 2.

We have begun to incorporate the electromagnetics into the ALE3D and Diablo codes. In each code the electromagnetics is updated in an operator-split manner, the *JxB* force is added to the momentum equation, and the J*E heating is added to the heat equation. Figure 3 shows the results of a simulation in which a 10-kV capacitor bank is discharged into an aluminum can structure with 1-mm walls. The sequence of images shows the deformation of the can due to the *JxB* force. We will verify this computation with experiments in early FY2006.

FY2006 Proposed Work

The following are some of the key research issues that will be investigated during FY2006:
1. Advection of Electromagnetic Quantities. In the ALE3D case, we need the ability to advect electromagnetic fields while still maintaining the divergence-free character of the fields. If the conductivity of the materials is wildly varying, an accurate subzonal interface treatment may be necessary to avoid artificial diffusion of parameters such as current and magnetic flux.
2. Contact/Slide Surfaces. The continuity conditions of electromagnetic fields and currents across material interfaces are somewhat different than for mechanical stress; hence, new algorithms will be developed for contact and slide surfaces.
3. Zero Conductivity Regions. It is not possible to simply set $\sigma = 0$ in the electromagnetic diffusion equation: this would lead to an ill-posed problem. Instead, it is necessary to model air or vacuum regions by some other means. A simple solution is to use small, but nonzero, values of conductivity in air or vacuum regions, and this may be acceptable for many applications. An alternative approach is to solve a magnetostatic problem in the $\sigma = 0$ region, either by finite elements or boundary elements, and this solution must be fully coupled (*i.e.*, solved simultaneously) with the electromagnetic diffusion equation.

T = 30 μs

T = 70 μs

T = 50 μs

T = 90 μs

Figure 3. Sequence of snapshots of a preliminary fully-coupled ETM simulation using our EM-enhanced Diablo code. In this experiment a 10-kV capacitor bank is discharged into a can-shaped structure. The color indicates the y-component of the stress caused by the magnetic pressure in the can. The deformation has been exaggerated for clarity.

Three-Dimensional Vectorial Time-Domain Computational Photonics

Customers with requirements for secure data transmission, computer networking, and high-bandwidth instrumentation are accentuating the need for photonic integrated circuit (PIC) technology. PICs will be the high-speed processing chips of the future and will impact both commercial and LLNL programmatic needs. Compact (LSI to VLSI), low-latency (sub-ps), wide-bandwidth (THz), ultrafast (100 Gb/s) miniaturized digital-logic, transmission, and sensor systems are potentially feasible. The design of novel integrated structures poses a considerable challenge, requiring models incorporating both microscopic and macroscopic physics.

Despite the strong photonic modeling capability at LLNL, new numerical methods are necessary as more complex photonic devices, materials, and configurations are devised. We are doing the research necessary to create these new numerical methods.

Project Goals

We are filling the gap between existing modeling tools and those needed for LLNL programs by extending the state of the art in simulation for the design of 3-D PICs. We have defined challenges that must be addressed in our codes, such as models for optical gain and nonlinearities, as well as microscopic, nonuniform, inhomogeneous structures. Our tools leverage LLNL's expertise in computational electromagnetics and photonics.

We are developing models and algorithms for incorporation into a new generation of 3-D simulation tools. These tools will be general enough to be adapted to problems in many areas, and flexible enough to embrace the design of future mixed-signal systems as well as stand-alone systems in disparate regions of the EM spectrum.

Relevance to LLNL Mission

The ability to model complex 3-D photonic devices in the time domain is essential to LLNL for a broad range of applications. These include: high-bandwidth instrumentation for NIF diagnostics; microsensors for weapon miniaturization within the DNT programs; encryption devices and circuits for secure communications for NAI surveillance applications; high-

Figure 1. (a) Electron wave functions for a 70-Å wide quantum well. (b) Absorption due to the quantum well as a function of photon energy and carrier density. The absorption can be converted to an index of refraction through the Kramers-Kronig relations.

(a)

Electron energy states of an $Al_{0.2}Ga_{0.8}As$/GaAs quantum well

E (meV)

- 208.0
- 154.1
- 71.1
- 18.0
- 0.0

AlGaAs GaAs AlGaAs

(b)

Aborption vs. N and NE for an Al0.2Ga0.8As quantum well
well width = 7 nm, barrier width = 40 nm,
diffusion length = 2 nm

Absorption (cm^{-1}) (10^5)

Legend:
- 1×10^{16}
- 3×10^{16}
- 1×10^{17}
- 2×10^{17}
- 3×10^{17}
- 5×10^{17}
- 7×10^{17}

Energy E(eV)
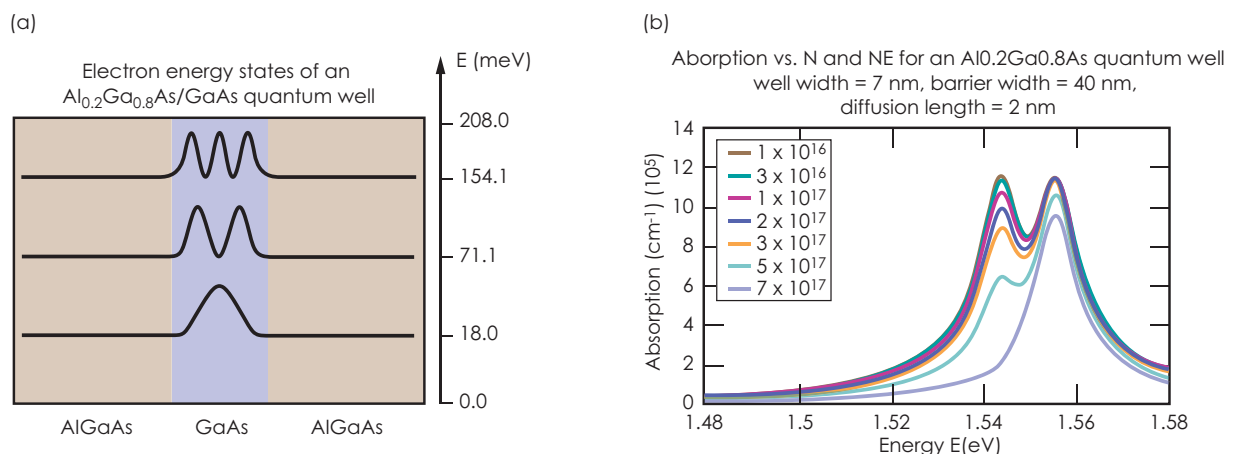
For more information contact
Jeffrey S. Kallman
(925) 423-2447
kallman1@llnl.gov

density optical interconnects for high-performance computing; and detection devices for homeland security.

FY2005 Accomplishments and Results

Most of our work has been focused on extending our two research codes: Quench3D and EMSolve. Quench3D is a narrow-bandwidth scalar beam-propagation-method code built for modeling large devices in which light propagates in a preferred direction. EMSolve is a vector time-domain code used for modeling small devices with either complicated geometries and/or no preferred direction for propagation.

In the past year we have:
1. written a vector finite-element beam-propagation solver for incorporation into the Quench3D suite;
2. written a significantly faster matrixless solver for EMSolve (which will speed simulation of materials with time-varying constitutive parameters);
3. incorporated new finite-element operators (wedge products) into EMSolve;
4. incorporated a drift diffusion model for carriers (electron-hole pairs) into EMSolve; and
5. written software to extract constitutive parameters for quantum well materials as a function of carrier density (Fig. 1).

We have been using the results of this work to examine designs for Auston-Switch Terahertz (THz) sources (Fig. 2), examine the effects of operating phased arrays of Auston Switches, and simulate the time course of electron-hole carrier diffusion in bulk semiconductor material.

Related References
1. Bond, T. C., and J. S. Kallman, "Time-Domain Tools for the Investigation of Gain-Quenched Laser Logic," *International Semiconductor Device Research Symposium,* Washington, DC, December 10-12, 2003.
2. Koning, J. M., D. A. White, R. N. Rieben, and M. L. Stowell, "EMSolve: A Three-Dimensional Time Domain Electromagnetic Solver," *Fifth Biennial Tri-Lab Engineering Conference,* Albuquerque, New Mexico, October 21-23, 2003.

FY2006 Proposed Work
Next year's work will consist of developing and incorporating gain and spontaneous emission algorithms into the EMSolve code, and replacing Quench3D's scalar beam-propagation solver with a wide angle vector finite-element beam-propagation solver. The upgrade to EMSolve will allow us to model optically-driven THz sources and Vertical Cavity Surface Emitting Lasers (VCSELs). The upgrade to Quench3D will allow us to examine the polarization dependence of the light emitted from semiconductor lasers, as well as that of gain-quenched laser logic. We will continue modeling devices for a variety of program-related projects.

(a)

(b)

(c)
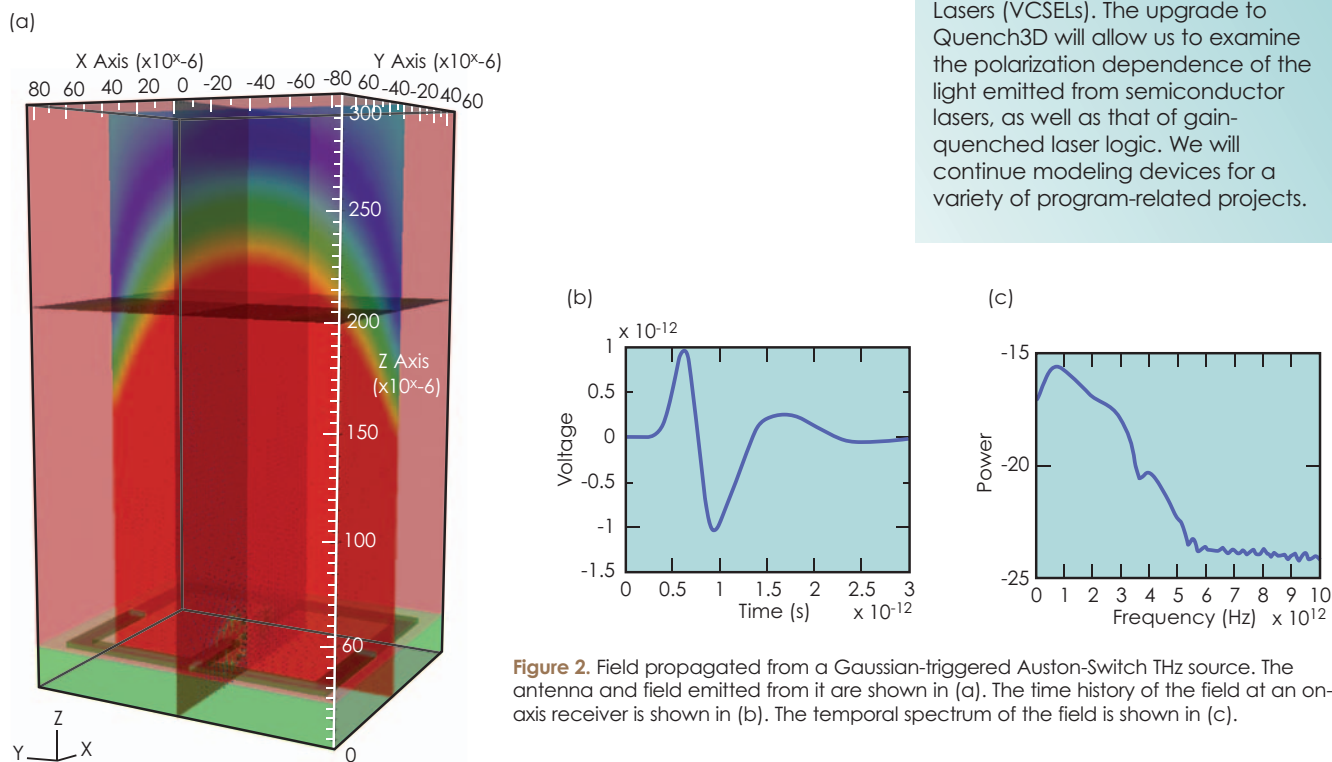
Figure 2. Field propagated from a Gaussian-triggered Auston-Switch THz source. The antenna and field emitted from it are shown in (a). The time history of the field at an on-axis receiver is shown in (b). The temporal spectrum of the field is shown in (c).

Broadband Radiation and Scattering

Electromagnetic phenomena are a central thread through much of modern engineering. There are two fundamental classes of applications: open region problems (where the energy propagates in unbounded space) and closed region problems (where the energy is guided by a waveguide structure or cavity).

This effort strives to enhance our computational electromagnetics (CEM) capability in broadband radiation and scattering in open regions. Broadband fields consist of energy with a robust spectrum, and include applications such as electromagnetic interference and electromagnetic compatibility noise analysis, broadband radar, and accelerator wakefield calculations.

LLNL analysis codes are limited by the accuracy of radiation boundary conditions (RBCs), which truncate space. We will develop improved RBCs by extending the perfectly

Figure 1. Full hybrid solution for a dipole radiating from the interior of a cube, including surface contours of the magnitude of the electric field together with vectors of the interior field.

matched layer (PML) approach to non-Cartesian meshes, and by developing discrete-time-domain, boundary-integral techniques, which are compatible with high-accuracy, finite-element methods and capable of arbitrary accuracy. We will compare the two approaches for accuracy and efficiency for a variety of radiation and scattering problems.

Project Goals

The ultimate deliverable is an enhanced CEM capability that can provide accurate and efficient computational solutions to broadband radiation and scattering problems. The algorithms for improved RBCs will be incorporated into LLNL's existing EMSolve code. The result will be a 10- to 1000-fold improvement in the accuracy of simulations. Improved algorithms and our existing high-performance computer hardware will place LLNL's CEM activity among the top capabilities in the world. This research and the resulting capability will be documented in appropriate peer-reviewed publications.

Relevance to LLNL Mission

Electromagnetics is a truly ubiquitous discipline that touches virtually every major LLNL program. Our work supports the national security mission by reducing the time and money spent in building and testing existing programs. It will enable computer simulations for new devices and systems, performance analysis of systems critical to nonproliferation efforts, and the design of micropower impulse radar and other microwave systems.

For more information contact
Robert M. Sharpe
(925) 422-0581
sharpe1@llnl.gov

FY2005 Accomplishments and Results

Figures 1 to 4 are sample results for our FY2005 CEM work. We have completed the initial development for the full parallel hybrid finite-element boundary element code. We have validated the basic parallel algorithms and made comparisons with less accurate ABC boundary conditions. We have collaborated with a professor at the University of Washington, an expert on time-domain integral equations. Several stability issues have been addressed and better quadrature techniques have been developed and implemented. Several research papers have been submitted for publication and results have been presented at national conferences.

Related References

1. Fasenfest, B., D. White, M. Stowell, R. Rieben, R. Sharpe, N. Madsen, J. Rockway, N. Champagne, V. Jandhyala, and J. Pingenot, "Differential Forms Basis Functions for Better Conditioned Integral Equations," *Antennas and Propagation Society International Symposium, IEEE,* **4 A**, pp. 292- 295, July 8, 2005.
2. Pingenot, J., C. Yang, V. Jandhyala, N. Champagne, D. White, M. Stowell, R. Rieben, R. Sharpe, N. Madsen, B. Fasenfest, and J. Rockway, "Surface Based Differential Forms," *IEEE/ACES International Conference on Wireless Communications and Applied Computational Electromagnetics,* April 3-7, 2005.

FY2006 Proposed Work

The main effort in FY2006 will be to improve the computational efficiency of the hybrid code by developing and implementing fast algorithms for the boundary element solutions. We will continue collaboration with the University of Washington. Filtered Green's functions, FFTs and QR fast solvers are under consideration. We will also compare the new hybrid code results with results from our previously developed high-order PML boundary conditions.
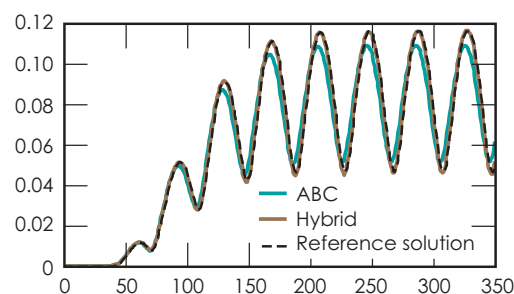
Figure 2. Hybrid solution and ABC boundary condition solution compared with the reference solution, for a plane wave scattering from an interior cubical box. Note that the hybrid solution is significantly better.
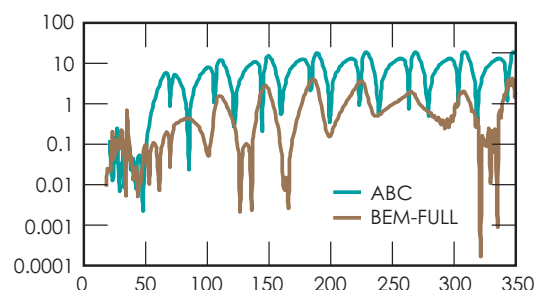
Figure 3. Relative percent error of the full hybrid solution compared to the solution obtained using hybrid and ABC boundary condition solutions. Again, the hybrid solution is better.
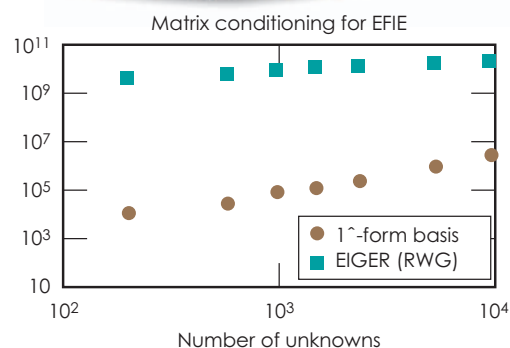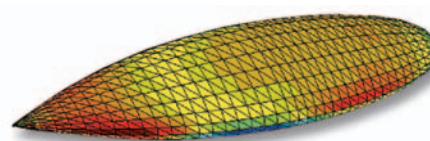
Figure 4. Unexpected results: We have found dramatic improvement in the matrix conditioning for the NASA almond problem when our differential forms bases and nonuniform spectral basis functions.

Dynamic Simulation Tools for the Analysis and Optimization of Novel Collection, Filtration and Sample Preparation Systems

We have developed novel multiphysics simulation capabilities to address design and optimization needs in the general class of problems that involve the transport of air- and water- borne species and fluid (liquid and gas phases) through sieving media. This new capability is designed to characterize subsystem efficiencies, such as filter efficiency, based on the details of the microstructure, surface interactions, and environmental effects.

To accomplish this we developed new lattice-Boltzmann (LB) simulation tools that include detailed microstructure descriptions, relevant surface interactions, and temperature effects, and that will be able to handle both liquid and gas phase systems. Additionally, the new capability has been used to help design particle-focusing apparati, predict shear forces on adhered species, and evaluate the permeability of porous materials, all in support of LLNL programs.

Project Goals

The goal of this project was to equip scientists and engineers with the computational tools to analyze and optimize novel collection, filtration, and sample preparation systems. Specifically, our goal was to develop tools that describe macroscopic transport phenomena in filtration, sample preparation, and filtration (porous media) systems, based on the details of the micro- and nanostructure.

Relevance to LLNL Mission

This work directly impacts continuing and future LLNL efforts that involve filtration, collection, and sample preparation. This capability is directly applicable to characterization of transport in porous media and multi-component sample preparation for detection systems relevant to LLNL programs such as Weapons, Energy and Environment, Medical Technology, Chemical and Biological Counter-Proliferation, Genomes to Life, and Homeland Security. The capability has been demonstrated and used to meet customer needs in the areas of aerosol transport, adhesion and re-suspension, and fluid and chemical transport in porous media.

FY2005 Accomplishments and Results

In FY2005, our effort was focused on fluid and suspension transport for a useful spectrum of Knudsen numbers (Kn). To accomplish this, the particle dynamics capability was augmented to account for particle Reynolds-number effects in aerosol transport phenomena
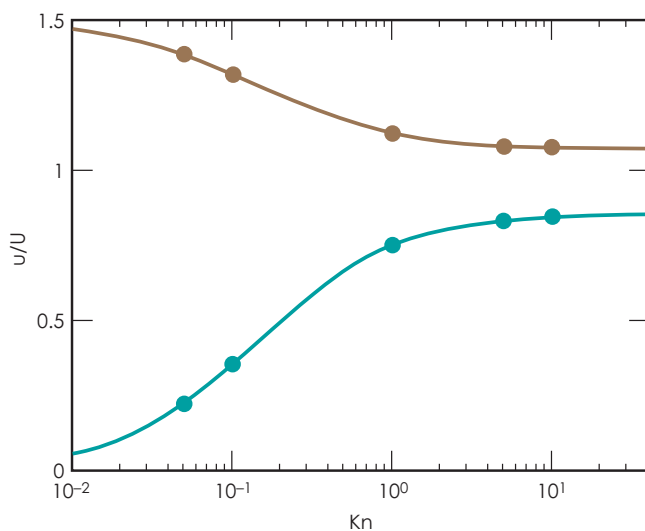
Figure 1. Dimensionless fluid slip velocity in channel flow, predicted using the new LB boundary condition (circles), compared with predictions from theory (lines), as a function of Kn.

For more information contact
David S. Clague
(925) 424-9770
clague1@llnl.gov

in the gas phase. This advancement enabled the study of bulk phase gas and particle dynamics. However, in such flow conditions, the fluid experiences increasing slip as Kn increases; therefore, to ensure accurate prediction of fluid and particle transport properties, the boundary condition at solid surfaces must account for a Kn-dependent slip condition. A major accomplishment was the development of a novel, Kn-dependent, boundary condition that enables accurate prediction of fluid slip velocities for a wide range of conditions (Fig. 1).

As shown in Fig. 1, our results exhibit nearly exact agreement with theory. Prior to this breakthrough, LB boundary conditions were accurate to $Kn < 1$. This result constitutes a significant improvement over the state of the art.

Our particle dynamics/tracking capability was further advanced to handle complex geometries. To demonstrate this new advancement, the capability was used to explore and optimize particle focusing (sample preparation/conditioning) for mass spectrometry, *i.e.*, particle transport and focusing in rarified gas conditions. Figure 2 shows the results from actual design simulations that were later used to support related DARPA research efforts.

In addition to developing new gas phase fluid and particle dynamics capabilities, the force prediction in external field(s) modules was augmented in the viscous suspension capability. This was accomplished through advancing the accuracy of the dielectrophoretic (DEP) force prediction by including higher order moments such as the quadrupole

contribution to the DEP force. This new advancement was incorporated into the viscous fluid/suspension capability.

Related References

1. Clague, D. S., B. D. Kandhai, R. Zhang, and P. M. A. Sloot, "Hydraulic Permeability of (Un)Bounded Fibrous Media Using the Lattice Boltzmann Method," *Phys. Rev. E*, **61**, 1, pp. R1-985, 2000.
2. Baron, P. A., and K. Willeke, Eds., <u>Aerosol Measurement: Principles, Techniques, and Applications</u>, John Wiley and Sons, New York, New York, 2001.
3. Karniadakis, G. E., and A. Beskok, <u>Micro Flows: Fundamentals and Simulation</u>, Springer-Verlag, New York, New York, 2002.
4. Liang, E., R. L. Smith, and D. S. Clague, "Dielectrophoretic Manipulation of Finite Sized Species and the Importance of the Quadrupolar Contribution," *Phys. Rev E.*, January 2005.
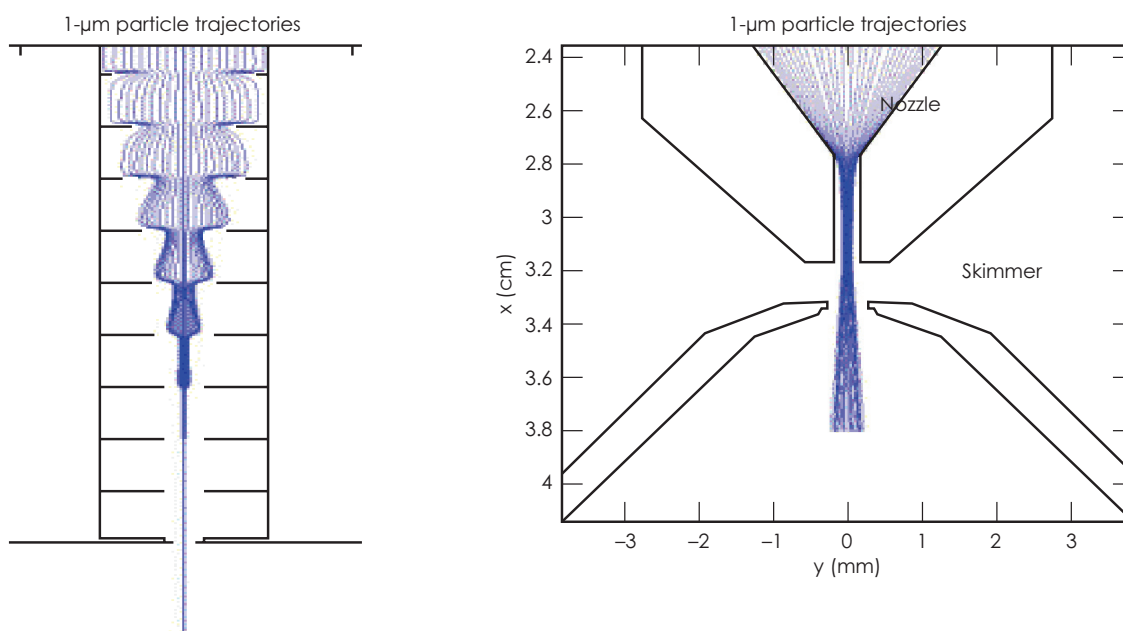
Figure 2. Particle trajectories in "inlet" design for mass spectrometry.

Virtual Polymerase Chain Reaction

The polymerase chain reaction (PCR) stands among the keystone technologies for analysis of biological sequence data. PCR is used to amplify DNA, to generate many copies from as little as a single template. This is essential, for example, in processing forensic DNA samples, pathogen detection in clinical or biothreat surveillance applications, and medical genotyping for diagnosis and treatment of disease. It is used in virtually every laboratory doing molecular, cellular, genetic, ecologic, forensic, or medical research. Despite its ubiquity, we lack the precise predictive capability that would enable detailed optimization of PCR reaction dynamics. We are developing Virtual PCR (vPCR) software, an *in silico* method to model the kinetic, thermodynamic, and biological processes of PCR reactions.

Project Goals

The challenges that we plan to address using vPCR include:

1. computational optimization of signatures for pathogen detection, for a significant savings in cost and time over purely empirical assay optimization; and
2. assessment of signatures for forensic discrimination of closely related sequences.

The result of this project, a suite of programs that predict PCR products as a function of reaction conditions and sequences, will be used to address outstanding questions in pathogen detection and forensics at LLNL. vPCR should enable scientists to optimize PCR protocols in terms of time, temperature, ion concentration, and primer sequences and concentrations, and to estimate products and error rates in advance of performing experiments. Our proposed capabilities are well ahead of all currently available technologies, which do not model nonequilibrium kinetics, polymerase extension, or predict multiple or undesired PCR products. Licensing opportunities will be explored, and a publication is being prepared. A provisional and a full patent application have been filed.

Figure 1. The diagram of a single thermocycle. We model four types of reactions: annealing, dissociation, polymerase extension, and melting. Although each of these predominantly occurs in a specific temperature regime, they are in constant competition throughout the thermocycle.
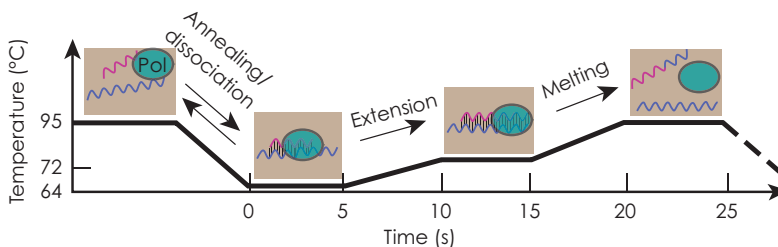
Figure 2. Simplified code overview.
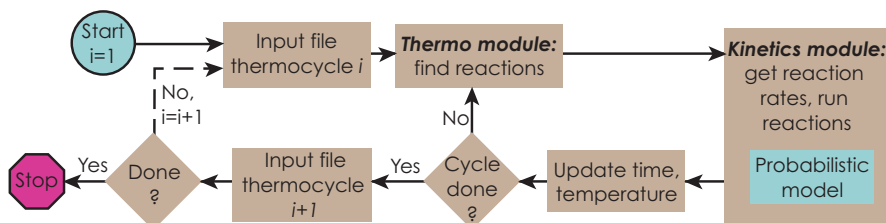
For more information contact
Shea N. Gardner
(925) 422-4317
gardner26@llnl.gov

Relevance to LLNL Mission

vPCR supports LLNL missions in homeland security, Genomes to Life (GTL), and human health. Any field that uses PCR, including bioforensics, biodetection, basic research in GTL, and disease research will benefit.

FY2005 Accomplishments and Results

We have written prototype code for much of the vPCR software, and we have drafted a manuscript. The code incorporates simulation during the temperature ramps as well as the constant-temperature soaks; competition between multiple (dozens to hundreds) of potential reaction pathways, including both hybridization and denaturation; and several alternative formulations of stochastic kinetic simulation algorithms that we have compared and optimized to balance speed and accuracy to handle the complexity of our library of test cases.

In addition, we model temperature-dependent extension of DNA and decay of the Taq polymerase enzyme, and track all reaction particles and their concentrations through time. We have incorporated more efficient data structures, a speedier simulation algorithm, and reasonable approximations to improve the capacity to handle more complex reactions than could the prototype version of the code. Combined, these improvements in speed give running times that are two orders of magnitude faster. We are in the process of including hairpin kinetics of DNA secondary structure in the simulations. Experiments have been performed, and the data are now being analyzed.

Figures 1 through 4 show overviews of our modeling activities and sample results. The code is documented on the web at https://kpath.llnl.gov/vpcr/docs/vPCR_API/.

Related References

1. Allawi, H. T., and J. Santalucia, Jr., "Thermodynamics and NMR of Internal GT Mismatches in DNA," *Biochem.*, **36**, pp. 10581-10594, 1997.
2. Gillespie, D., and L. R. Petzold, "Improved Leap-Size Selection for Accelerated Stochastic Simulation," *J. Chem. Phys.*, **119**, pp. 8229-8234, 2003.
3. Cao, Y., D. T. Gillespie, and L. R. Petzold, "The Slow-Scale Stochastic Simulation Algorithm," *J. Chem. Phys.* **122**, 2005.
4. Maheshri, N., and D. V. Schaffer, "Computational and Experimental Analysis of DNA Shuffling," *Proc. Natl. Acad. Sci. USA,* **100**, pp. 3071-3076, 2003.
5. Wetmur, J. G., "DNA Probes: Applications of the Principles of Nucleic Acid Hybridization," *Crit. Rev. Biochem. Mol. Biol.*, **26**, pp. 227-59, 1991.
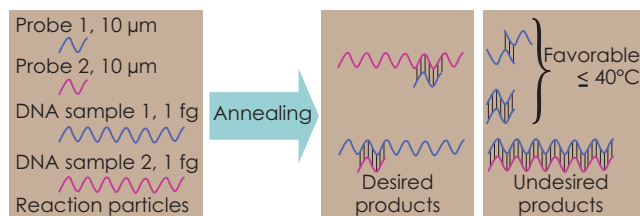
Figure 3. Example competing annealing reactions. At lower soak temperatures, annealing reactions are generally more favorable, opening pathways to undesired products.

FY2006 Proposed Work

In FY2006, we plan to parallelize various portions of the code for running on the LC machines; complete experimental data analysis and compare it to predictions from the software; submit our first manuscript and prepare a second that includes the results of our work; continue the process of debugging and optimization, generating additional test cases; and complete the incorporation of hairpin kinetics.

Figure 4. The system diagrammed in Fig. 3 is simulated through 40 thermocycles, at soak temperatures of 40°C and 64 °C. Note that higher concentrations of desired amplicons are output at 40 °C, where pathways to undesired products also exist. Lowering the soak temperature increases the rates of all annealing reactions, which in this case outweighs the addition of undesired reactions. Optimizing the annealing temperature requires finding a balance between generating detectable yield and amplification of undesired products.

New Features and Improvements in DYNA3D

DYNA3D is a simulation code for nonlinear structural dynamics. Its ability to model high-speed, large-deformation impacts of complex assemblies makes it a fundamental tool for national-security-related programs at LLNL. This project funds the implementation of user-requested features, general technical support, document updates, and Software Quality Assurance (SQA) compliance for DYNA3D. This project also supports Collaborator Program activities. The Collaborator Program grants access to selected licensed users to LLNL's computational mechanics/thermal codes in exchange for the collaborators' information and results. These collaborative parties include our sister laboratories, U.S. government agencies, and other institutions.

Project Goals

For FY2005, the planned tasks included the implementation of functionalities for various programmatic users' needs, the addition of new result display capabilities, and continued improvement of contact algorithms for modeling the interaction of material surfaces.

Relevance to LLNL Mission

Technical support and new functionalities are essential to ongoing uses for nuclear weapons engineering and projects involving LLNL's collaboration with other institutions and federal agencies, such as the Los Alamos National Laboratory, the Department of Homeland Security, the Bureau of Reclamation, and the Boeing Company.

FY2005 Accomplishments and Results

In FY2005, two new material models were implemented in DYNA3D. Several display capabilities were added through use of the Mili I/O Library and the postprocessor Griz. We also completed the first-phase implementation and assessment of an alternative segment-to-segment contact methodology. The preliminary results show promise for dealing with extreme contact situations.

A new concrete material was adopted in DYNA3D. This model is an improvement over the older material type, including a capability for self-generation of material model parameters. Given the user-provided key concrete strengths determined by
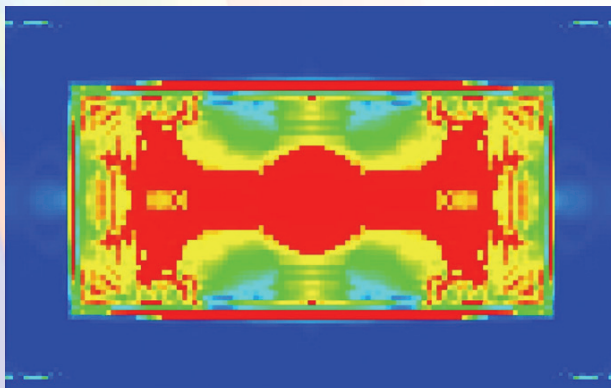

Figure 1. Stress distribution of a blast-loaded RC wall computed using the homogenized RC material model.
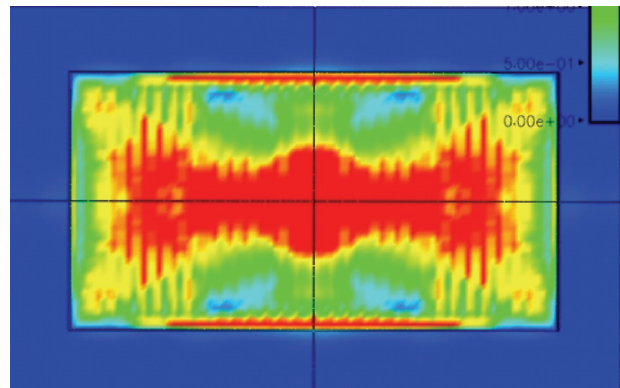
Figure 2. Stress distribution of a blast-loaded RC wall computed using individual concrete and rebar materials elements and material models.

For more information contact
Jerry I. Lin
(925) 423-0907
lin5@llnl.gov

experiment, this model is coded to automatically generate the remainder of the necessary material properties.

Another new concrete-related material is a homogenized rebar-reinforced concrete model. This model was developed by another LLNL analyst, with this project providing collaboration and integration to the main DYNA3D source. This model integrates the presence of rebar into concrete material, hence alleviates the need for analysts to mesh reinforced concrete as an explicit combination of small concrete continuum and rebar beam elements.

A precision test of a blast-loaded reinforced-concrete (RC) wall was used to demonstrate the effectiveness of the homogenized concrete-rebar model. Two RC walls, one modeled via the new homogenized material and the other using small continuum and beam elements, were simulated

under the same blast loads. The close agreement shown in Figs. 1 and 2 attests to the value of the new material model.

In impact/penetration analyses, engineers often want to see the movement of the fragmented debris and monitor how the penetrator momentum changes over time. For this purpose, capabilities for displaying the released particles after material failure and the momentum time history of materials were implemented into DYNA3D and Griz.

A contact algorithm based on checking the interference between quadrilateral patches was studied as a possible complement to the existing contact algorithms in DYNA3D. The preliminary results are promising. One of the examples tested is the simulation of two colliding strips. This problem creates an edge-to-edge contact scenario, which the existing

contact algorithms do not handle well. Comparison between Figs. 3 and 4 demonstrates that the prototyped method captures the right phenomena.

FY2006 Proposed Work

In addition to the general technical support for DYNA3D users and SQA-compliance work, we also plan to start or continue the following projects:
1. A new surface class entity is nearing release in the Mili data management library. Upon its availability, it will be implemented into the DYNA3D output database. This new class will enable many additional result variables and parameters, including applied boundary condition specifications, to be included in the results database. This will enhance our users' ability to verify their problem specification and interrogate the results.
2. More implementation and assessment effort will be devoted to the prototyped contact algorithm. The planned tasks include coding optimization, efficiency studies and further application.
3. We will continue to modernize DYNA3D. All new features will be implemented under a uniform FORTRAN 95-compliant programming structure, and the existing code will be gradually migrated toward that standard as well.
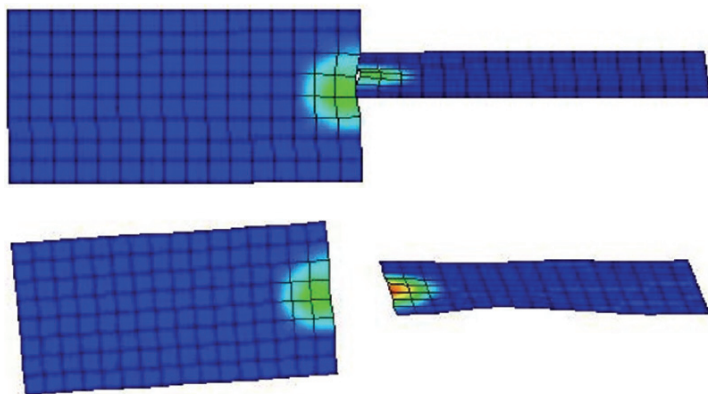
Figure 3. Colliding strips simulated using the new contact algorithm.

Figure 4. Colliding strips simulated using the existing contact algorithm.

NIKE3D Code Support and Enhancement

Engineering Modeling and Simulation

The objective of this work is to support, maintain, and enhance the implicit structural mechanics finite-element code NIKE3D. The code is used by engineering analysts to evaluate static and low-frequency dynamic response. User support includes assisting analysts in model debugging and general analysis recommendations. Maintenance includes bug fixes and code porting to the various platforms available. New features are added to accommodate engineering analysis needs.

Project Goals

Our goals included implementing the following enhancements:

1. An advanced contact algorithm, known as a mortar method. This involved modifications to existing prototype code, eliminated any fixed-memory constraints, and extended data structures to accommodate multiple surface definitions. In addition, an improved algorithm was implemented for computing and integrating the overlapping segments.

2. User-requested thermal expansion capabilities were added to NIKE3D material models 1 (hypoelastic), 15 (hyperelastic), and 27 (hyperelastic-plastic material).

3. Interface to parallel (threaded) symmetric and unsymmetric linear equation solvers for the Linux and AIX platforms. We also ported NIKE3D to the Red Hat Linux and AIX operating systems.

Relevance to LLNL Mission

Structural analysis is one of the most important functions of LLNL's mechanical engineering efforts, supporting assessment activities. The in-house codes are crucial for meeting these needs. NIKE3D, in particular, is a premier code for handling difficult nonlinear static structural analysis problems.

FY2005 Accomplishments and Results

A new mortar contact method has demonstrated vastly superior nonlinear convergence behavior and has led to a number of papers. This approach effectively smoothes the numerical behavior near the interface and eliminates instabilities ("locking") long observed with standard contact methods. Consequently, contact analyses that failed in the past can now be successfully analyzed using implicit finite elements (Fig. 1).
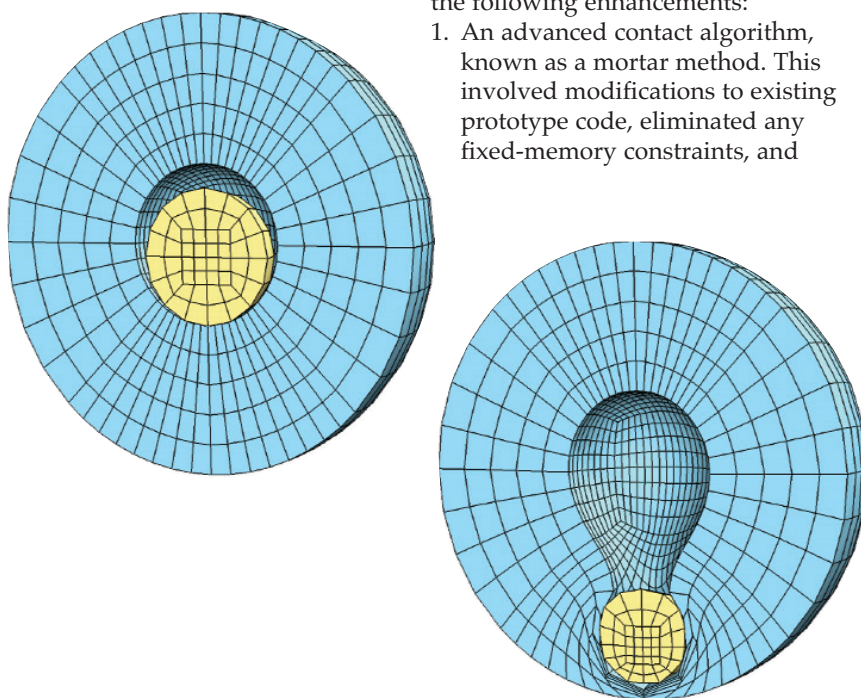
Figure 1. Elastic sphere forced into thick elastic shell. Analysis was performed with implicit finite-element method using mortar contact. Standard contact methods cannot nearly approach this significant amount of deformation with implicit finite elements.

For more information contact
Michael A. Puso
(925) 422-8198
puso1@llnl.gov

On the other hand, the programmed data structures involved with mortar contact proved much more complicated than the standard, widely-used node-on-segment algorithms in most codes. Consequently, while the prototype code established the feasibility of the method, many simplifying assumptions limited its applicability to large-scale simulation. In the present work, upgraded data structures were implemented that provide the ability for multiple contact surface definitions. Figure 2 demonstrates the compression of four blocks where three individual contact surface definitions were used. The results in Fig. 3 show the applied force vs. time from analyses using the mortar contact and the default node-on-segment algorithm. For a variety of reasons, the standard contact algorithm fails when the soft blocks experience strains around 8%, whereas the mortar contact algorithm can go past 50% strains. This capability is now being used for production work by engineering analysts, showing better numerical behavior and simplifying their model generation efforts.

Related References

1. Puso, M. A., and T. A. Laursen, "A Mortar Segment-to-Segment Contact Method for Large Deformation Solid Mechanics," *Computer Methods in Applied Mechanics and Engineering*, **193**, pp. 601-629, 2004.

2. Puso, M. A., and T. A. Laursen, "A Mortar Segment-To-Segment Frictional Contact Method for Large Deformations," *Computer Methods in Applied Mechanics and Engineering*, **193**, pp. 4891-4913, 2004.

FY2006 Proposed Work

In addition to the ongoing general technical support for NIKE3D users, the following enhancements are currently planned:
1. Node relocation during initialization for curved, unmatched mortar contact surfaces that have unintentional interpenetrations defined by the original mesh geometry.
2. Improved quasi-Newton nonlinear equation solvers to handle the evolving active contact constraints. Algorithms that perform secant updates such as BFGS but better account for active constraints will be targeted.

Figure 3. Applied force vs. time for vertically loaded blocks from analyses using mortar and node-on-segment contact algorithms. The plot displays the enhanced robustness of the mortar method.

(a) (b) (c)

Figure 2. (a) Undeformed soft and hard blocks separated by three individually defined contact surfaces. A vertical load is applied to the top block. (b) Effective stress at the maximum deformation attainable using the standard contact in NIKE3D. The soft blocks experience about 8% strain. (c) NIKE3D mortar contact results after 50% strain to soft blocks.

Simulation Visualization and Data Management

A key component of our effort is support for postprocessing and visualization tools, which include the Griz finite-element postprocessor, the Mili Data Input/Output Library, and an associated data tool XmiliCS. These tools are heavily used by LLNL analysts to interpret data from a variety of simulation codes such as DYNA3D, ParaDyn and NIKE3D.

Griz is our primary tool for visualizing finite-element analysis results computed on 3-D unstructured meshes. Griz also calculates and displays auxiliary result quantities for a variety of codes. Griz provides modern 3-D visualization techniques such as isocontours and isosurfaces, cutting planes, vector field display, and particle traces. Griz also incorporates the ability to animate all representations over time. Mili provides the primary data path between analysis codes and Griz. Xmilics is a utility that consolidates results from large parallel simulations into a single data stream suitable for Griz.

Project Goals

The primary goal of this project is to provide ongoing support for postprocessing tools and add new capabilities to support unique programmatic requirements. The "free-node" capability that was implemented this year is an example of a capability that was added to support one project team, yet is subsequently available to support all programs.

Relevance to LLNL Mission

Postprocessing tools such as Griz and Mili provide important user interfaces for our simulation capabilities and are critical elements in
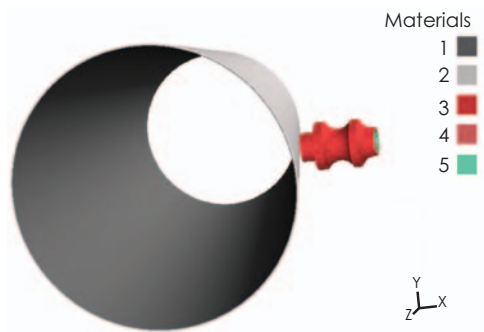
Figure 1. Projectile penetrating a tube (initial state).

Figure 2. Tube penetration and deformed penetrator.

Global maximum: 4.35×10^{-2}. nodal 222286
Global minimum: 0.00. nodal 2023
Displacement scale: 1.0/1.0/1.0

Figure 3. Projection simulation with free node visualization.

For more information contact
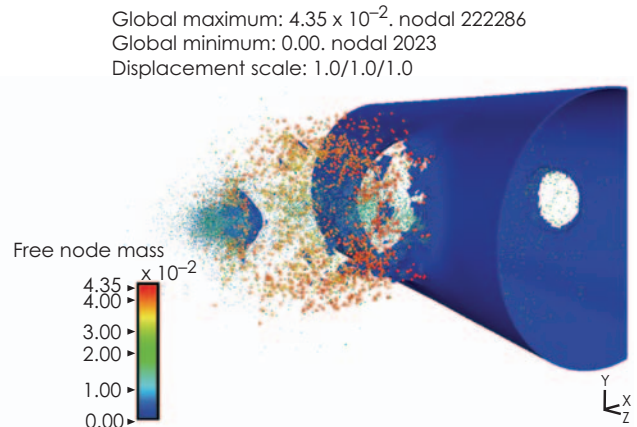**Ivan R. Corey**
(925) 423-3271
corey3@llnl.gov

our simulation tool suite. Ultimately, the analyst synthesizes analytical conclusions through visual interrogation of the simulation output.

FY2005 Accomplishments and Results

We made significant progress in adding capabilities to Griz and Mili to manage and display surface objects. This is an essential step for facilitating the writing of boundary conditions and data onto surfaces from the analysis programs. The entire GUI implementation and database work has been completed. We are in the process of performing integration tests.

We made a variety of enhancements to support visualization for a project team modeling fragmentation and debris from hypervelocity impacts. Griz can display the nodes of elements having material that failed, and thus

constitute a debris field. These nodes are called "free nodes," and are rendered as spheres. The size of the sphere is based on the mass of the node and a user-defined scaling factor. We can also plot by element volume.

Figures 1 to 3 are snapshots taken from the initial and end states of a simulation, showing the fragmentation and the added representational power of the free node visualization.

We implemented a new capability in Griz to display the extreme minimum or maximum values per element for a selected result quantity. When activated, the values for all states are evaluated and the requested extreme displayed on the deformed mesh at a user-selected time state. We also completed a project to support validation efforts at LANL by providing a plotting capability in Griz for strain data from time-history databases. We were able to speed the

calculations by reducing the required amount of data-file reading by a factor of eight.

We continued to make improvements in the software engineering practices of the Griz tool suite. We added several enhancements to the configuration scripts. We also added a feature to allow users to select a specific version of the software at runtime. The code user can query the code for configuration parameters such as build time, data, platform, configuration options, and run-time options.

We made significant progress in converting the Griz window management software from the old Motif library to the modern Qt toolkit. Qt is a comprehensive open source C++ framework for building GUIs. It includes a class library and tools for cross-platform deployment. Figure 4 is a sample screen shot of Griz/Qt.

Figure 4. Griz GUI implemented with the Qt toolkit.
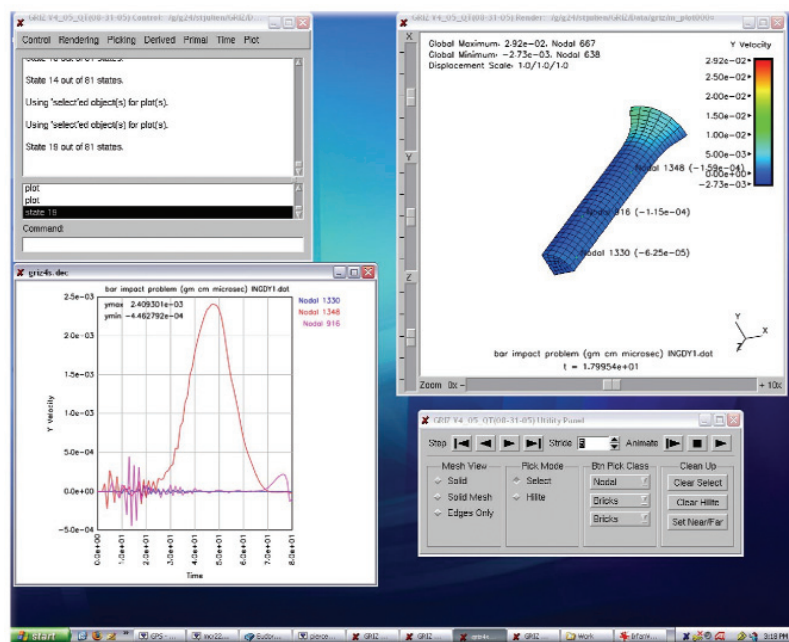
FY2006 Proposed Work

We will continue to provide support and enhancements for our user-base at LLNL, LANL, and at several other sites. A major revision of the Mili I/O library is being evaluated for its potential to facilitate more flexible output from our simulation codes and broader data interrogation and fusion by our analysts. These revisions will also be weighed with an eye toward leveraging the state of the art, parallel visualization capabilities created by LLNL's VisIt tool, to enable our analysts to productively use larger models for our most demanding simulation tasks.

Technologies for Structural Damage Analysis

Accurately simulating the effects of reinforced concrete structures subjected to extreme events, such as blast or aircraft impact, in an efficient and timely manner continues to be extremely challenging. Many large concrete structures contain an extensive amount of rebar, which can be very time consuming for the analyst to model explicitly, using either brick or beam elements. Brick elements provide dimensionality and also allow the use of arbitrary Lagrangian-Eulerian (ALE) schemes where rebar is modeled. However, this requires a very finely resolved mesh. It is also currently difficult to model a fully-coupled blast simulation of large buildings with substantial beam and column detail. Beam element implementation in ALE3D would allow efficient detailed calculations of large buildings.

Finally, we need improved metrics of concrete damage or postprocessing techniques. In essence, when the analyst hands over a display of "damage" to the customer, there should be no guessing as to the health of the structure in question.

Project Goals

Our main objective is to enhance our ability to simulate the response of reinforced concrete structures exposed to extreme loading environments. We are also implementing codes that can handle all aspects of a blast simulation, for example, in one seamless calculation.

Figure 1. Comparisons among rebar brick elements, homogenized rebar, and homogenized rebar preprocessed with FiberGrid for a blast experiment.

- Primary test wall reinforcing is No 3 rebar spaced at 3 in. on center.

- Secondary test wall reinforcing is size D-3 deformed wire spaced at 3 in. on center.

- Stirrups in the test wall are size D-2.5 deformed wire spaced at 3 in. on center in both directions.

- Primary and secondary reinforcing in the flanges are No. 5 rebar spaced at 4 in. on center.

- Stirrups in the flanges are No. 3 rebar spaced at 4 in. on center in both directions.

- All steel rebar reinforcing is Grade 60 and conforms to ASTM specifications A615.

- All deformed wire conforms to ASTM specification A496.

Test wall and stubs, 6% rebar by mass (side view).

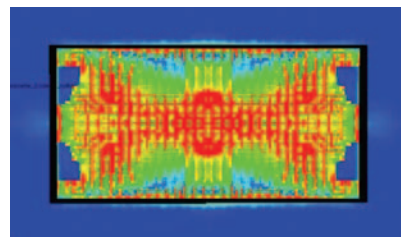Precision test wall study: modeling a U.S. Army-ERDC test of blast loaded RC. Time comparison for mesh generation: brick rebar models ~7 days; homogenized rebar model ~ 1/2 day.

ALE3D – Rebar brick elements

ALE3D – Homogenized rebar
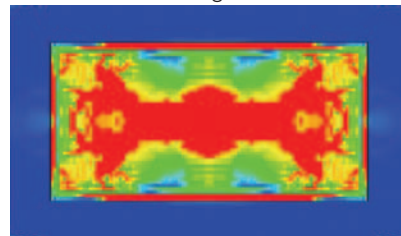
ALE3D – Homogenized rebar w/ FiberGrid

Damaged concrete

For more information contact
Charles R. Noble
(925) 422-3057
noble9@llnl.gov

Relevance to LLNL Mission

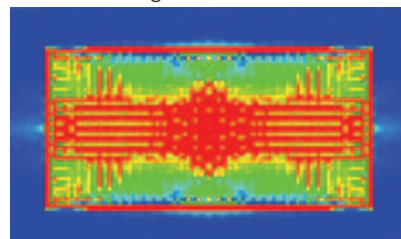The computational tools implemented for this project will decrease the mesh generation time and the computation time. These tools will significantly enhance our ability to analyze the response of reinforced concrete structures for the Department of Homeland Security, the Homeland Operations and Defense Planning Systems, and Underground Analysis and Planning Systems. This project will also help LLNL programs expand their expertise in advanced computational analysis.

FY2005 Accomplishments and Results

The following are the accomplishments for FY2005:
1. Implementation of DYNA3D's beam elements into ALE3D;
2. Implementation and validation of homogenized rebar model into DYNA3D;
3. Validation of homogenized rebar model for ALE3D;
4. Implementation of FiberGrid into ALE3D's generator for use with the homogenized rebar model;
5. Validation of FiberGrid;
6. Implementation of nonlinear concrete model into NIKE3D;
7. Validation of the new damage metric using VisIt.

Validation of the new homogenized rebar/concrete material model and its preprocessor, FiberGrid, has been completed using the Precision Test Wall experiments conducted by the U.S. Army Engineer Research and Development Center. In the original implementation of the homogenized rebar/concrete model, the rebar was specified as a volume fraction in an approximate region where rebar is located. FiberGrid will implement the volume fractions of rebar in the individual concrete elements (and not a whole concrete region) where rebar is located in reality. Using FiberGrid, the rebar will look and behave in a manner very similar to truss elements overlaid inside the concrete. A quick validation of FiberGrid was performed on the Precision Test Wall and the results are shown in Fig. 1. As is seen in the comparison of results, the homogenized rebar with FiberGrid simulation begins to converge very nicely towards the rebar brick element simulation. The time comparison for generating a model using brick

elements for the rebar is approximately seven days, while the generation of a homogenized rebar/concrete model is only half a day.

In addition to validating that the homogenized rebar model is working properly, a new spall or damage criterion was validated against a blast experiment conducted by the U.S. Army Corps of Engineers Waterways Experiment Station (WES).

The spall or damage criterion is a very simple idea: concrete spallation might be able to be predicted in these complicated concrete plasticity models if a certain portion of a concrete structure (subjected to very large blast pressures or impact) has both tensile or compressive damage and a significant velocity. For this simulation, the concrete damage threshold was 0.85 (from a scale of 0 to 1, where 1 is complete tensile or compressive damage of concrete) and the velocity threshold was chosen to be 20 in./s. Figure 2 shows the fringe plot of this spall/damage criterion. As a result of using these two threshold values, the predicted spall was approximately 30 cm, which matches experiment reasonably well.
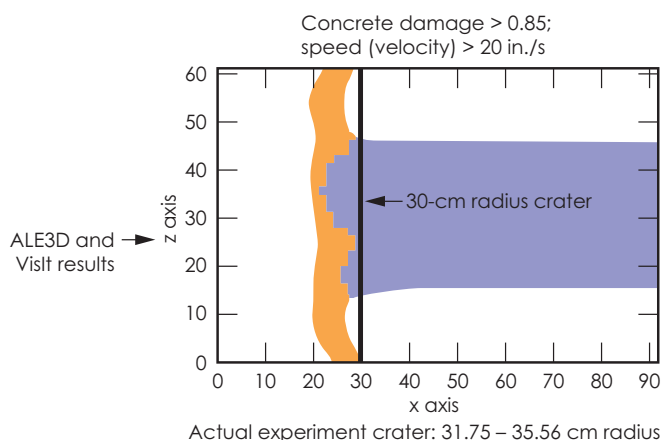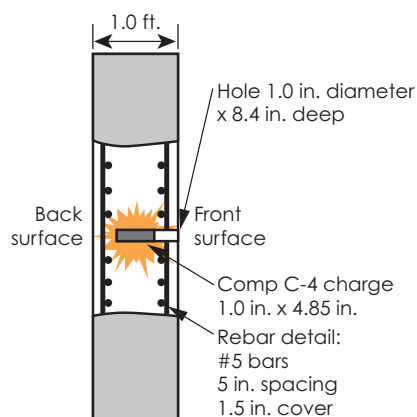
Figure 2. Validation of new concrete damage metric using the VisIt postprocessor.

Modeling Production Plant Forming Processes

The ability to model and optimize material manufacturing processes and predict resulting material properties is important where product performance, costs and/or waste reduction are concerns. Predictions of material response during processing and in final parts can be achieved by combining robust finite-element simulations with advanced material models. This project couples state-of-the-art capabilities to predict material property evolution through forming processes of metal alloys, including uranium. This is an important step in demonstrating a predictive capability. The material model, provided by LANL, accounts for twinning, plasticity, and phase transformations. This is particularly important because the phase change during processing affects formability and subsequent properties in final parts.

Project Goals

The goal of this project is to make advanced material models available for process modeling and to work with DOE's Y-12 (Tennessee) in validating the model for rolling simulations. The intention is to continue interaction with Y-12 for a longer-term relationship to address multiple production optimization. The demonstrated capability will be made available to LLNL, government laboratories and production facilities, and U. S. industries meeting export control requirements. The capability will be beneficial in the optimization of forming processes for steel, aluminum, and specialty metals to achieve desired properties and microstructures.

Relevance to LLNL Mission

This effort will contribute to LLNL's role and core competency in numerical modeling and material response. The capability demonstrated in this project is supportive of other forming processes where geometric fidelity and control of material properties are critical.

FY2005 Accomplishments and Results

A material model for uranium alloys, including twinning and phase change, has been implemented into the
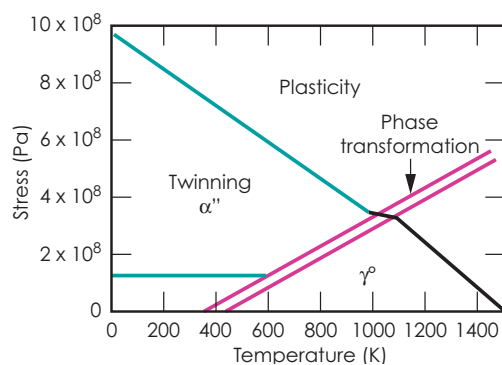
Figure 1. Phase diagram of U6%Nb.
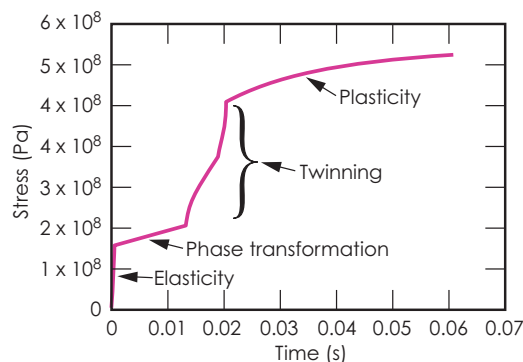
Figure 2. Stress response under constant strain rate. The material is initially in the bcc γ^0 phase. When the stress reaches approximately 160 MPa, the material begins to deform by phase transformation (to a monoclinic α'' phase). Once the transformation is complete, twinning occurs until the stress reaches approximately 500 MPa, where plasticity due to dislocation motion begins.
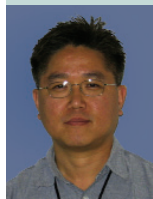
For more information contact
Moon Rhee
(925) 424-4990
rhee1@llnl.gov

ALE3D code. A phase diagram is shown in Fig. 1, where regions for elasticity, phase transformation, twinning, and plasticity are separated by solid boundary lines. Results (Fig. 2) of a simulated uniaxial tension test at 720 K and with a constant rate illustrate that the material deforms by several mechanisms.

Rolling simulations of U6%Nb have been carried out for verification. A snapshot of the phase change fraction contour is given in Fig. 3. The temperature-pressure history of a surface element has been plotted in the phase diagram, Fig. 4.

Related Reference

Addessio, F., Q. Zui, T. Mason, and L. Brinson, "Model for High-Strain-Rate Deformation of Uranium-Niobium Alloys," *Journal of Applied Physics*, **93**, 12, pp. 9644-9654, 2003.

FY2006 Proposed Work

We will continue to collaborate with Y-12 to determine other forming processes, including hydroforming and drawing, which can be used for validation. We are proposing to implement existing models for recrystallization and constitutive response for the materials of interest. We will then perform validation simulations against the available data.

In FY2006, we will:

1. accumulate relevant forming data for uranium and uranium alloys;
2. evaluate grain-size evolution models for implementation and validation;
3. implement a material model for recrystallization into ALE3D; and
4. perform code validation calculations where appropriate.

DB: ur3d_016_072525
Cycle: 72525   Time: 1.940
Mech
Var: mech_3d
Pseudocolor
Var: Hot/ur_3/zeta

— 1.000
— 0.7500
— 0.5000
— 0.2500
— 0.0000

Max: 1.000
Min: 0.0000
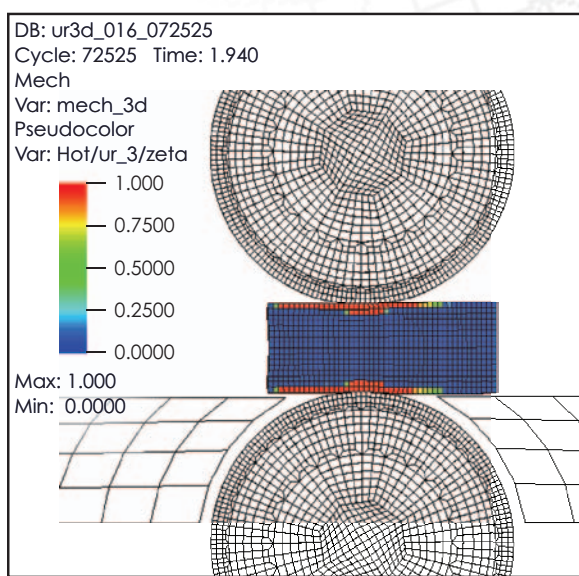
Figure 3. Plot of phase fraction contour of center plane.
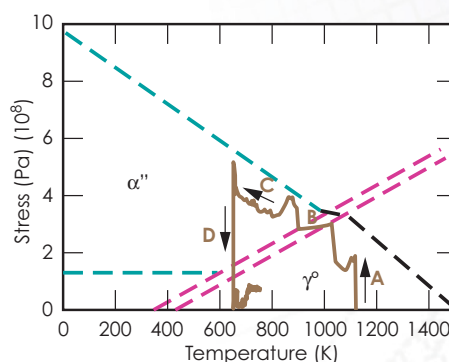
Figure 4. Temperature-pressure history of a surface element in slab. The element is initially in the elastic region (A) and progresses to the phase change region (B). Simultaneously, the temperature of the slab decreases due to the contact with the cold rolls. When the phase transformation is complete, the material phase has changed completely from γ^o to α'' phase (C). Once the material exits the roll bite, the stress is relieved (D) and conduction from the slab interior raises the temperature.

Crystal Models to Simulate Seeding of Rayleigh-Taylor Instabilities in Beryllium

Engineering Modeling and Simulation

We have implemented initial crystal-level modeling capabilities for beryllium in an existing framework. Capabilities include elastic, plastic, and thermal anisotropies related to the hexagonal crystal structure. These capabilities enable assessment of beryllium components under complex loading conditions such as those anticipated in NIF capsule implosions.

Project Goals

In this project, the primary sources of anisotropic response in beryllium are incorporated into existing crystal plasticity models available in the ALE3D finite-element program. We have also implemented enhancements for the incorporation of x-ray preheat data. We have tested capabilities, and built expertise in working with the models and interpreting results in light of interacting deformation mechanisms.

Relevance to LLNL Mission

Improved model descriptions for beryllium contribute to the capability to represent the general class of low-symmetry crystalline materials. A variety of programmatically important materials have low crystal symmetry. Capabilities for beryllium immediately benefit efforts for beryllium inertial confinement fusion capsules. For these beryllium capsules, x-ray preheat effects may have detrimental effects on surface roughness at the inner capsule surface and on perturbations within the bulk of the material. Anisotropic material response relates directly to the effects of interest. Perturbations that are exacerbated by material anisotropy play a role in the seeding of Rayleigh-Taylor instabilities, which are of concern in experimental physics studies of inertial confinement fusion.
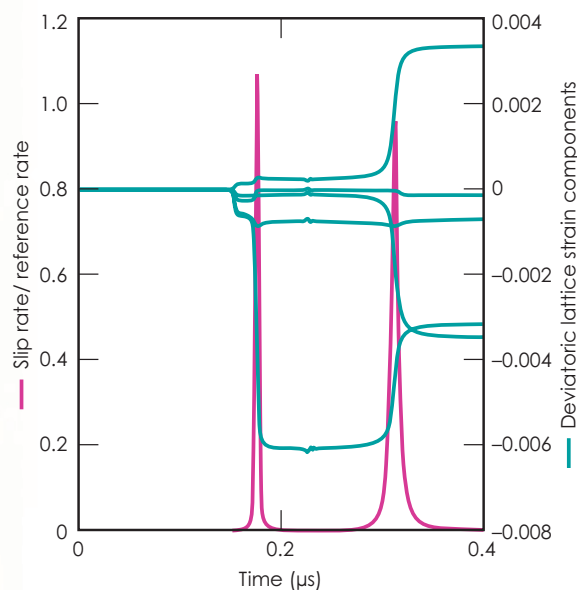
Figure 1. Time histories at a material location in a single crystal impact, showing plastic slip rate and lattice strain evolution. The elastic precursor is followed by two plastic waves. During the second plastic wave, there is a substantial shift in lattice strain, an effect related to plastic anisotropy.

For more information contact
Nathan R. Barton
(925) 422-9426
barton22@llnl.gov

FY2005 Accomplishments and Results

ALE3D now includes a material model for beryllium that includes elastic, plastic, and thermal anisotropies. A capability has also been added for depositing x-ray preheat energy as a function of Lagrangian position. Model parameters have been calibrated using data from existing experimental work, and limited validation work has been performed using gas gun data.

The model reproduces the multiple plastic shocks observed experimentally at relatively low impact velocities, as shown in the 1-D single crystal impact results in Fig. 1.

Complex material response is predicted for more general loading scenarios and microstructures. Results for a bicrystal are shown in Fig. 2, with considerable differences in break-out velocity for the two crystals.

Anisotropic thermal expansion alone can produce considerable nonuniform grain-level internal strains in a polycrystal, as shown in Fig. 3. These strains can lead to plastic deformation and the new capabilities allow for a first order assessment of this effect.

These new modeling capabilities have been tested in scenarios involving both spatially and temporally varying x-ray preheat and

shocks induced by boundary loading. We have built expertise in interpreting material response under these combined loading conditions.

Related References

1. Migliori, A., H. Ledbetter, D. J. Thoma, and T. W. Darling, "Beryllium's Monocrystal and Polycrystal Elastic Constants," *Journal of Applied Physics,* **95**, 5, pp. 2436-2440, 2004.
2. Pope, L. E., and J. N. Johnson, "Shock-Wave Compression of Single-Crystal Beryllium," *Journal of Applied Physics,* **46**, 2, pp. 720-729, 1975.
3. Touloukian, Y. S., R. K. Kirby, R. E. Taylor, and P. D. Desai, "Thermal Expansion: Metallic Elements and Alloys," *Thermophysical Properties of Matter,* **12**, 1975.

Figure 3. Lattice strain in a polycrystal due to temperature changes and anisotropic thermal expansion. Lattice strains are largest at grain boundaries where anisotropic expansion is accommodated.
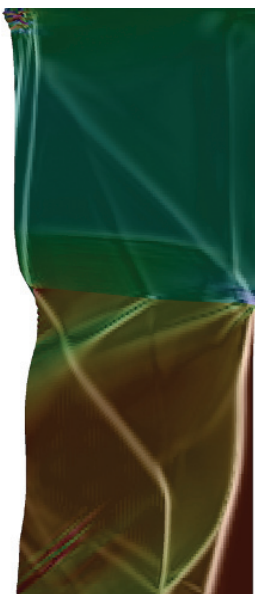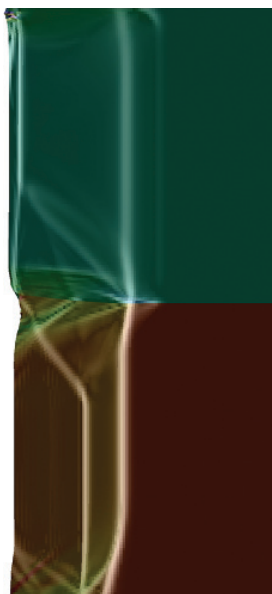
Figure 2. Results for a bicrystal at two time instances. Higher plastic strain rates are indicated by brightness; crystal lattice orientation is indicated by color. Loading is by an applied pressure on the left boundary; the right boundary is a free surface. Each of the two crystals initially has a uniform lattice orientation.

Modeling Initiation in Exploding Bridgewire Detonators

There is great interest in the dynamics of exploding bridgewire (EBW) performance and its role in the process of initiation in EBW detonators. We need to better understand the mechanism by which electrical energy stored in a fireset transforms into initiating energy within a high explosive, and how this mechanism is disrupted by changing materials and geometry.

This project uses LLNL's magnetohydrodynamic (MHD) code CALE to model the explosion of an EBW when placed in a circuit with a fireset. The models began as 1-D and have been generalized to 2-D, with the capability of including details due to aging, such as the growth of intermetallic compounds.

Project Goals

The project is complete at this time, having reduced to practice a first-principles-based approach to computational simulation of EBW performance. The goals of this project included: implementation of sufficiently accurate 2-D models for pure metal EBWs surrounded by high explosive; implementation of models that predict performance of aged systems; and preliminary validation of the MHD models in CALE at the energies of interest.

Relevance to LLNL Mission

This project has enhanced Engineering's toolset by producing techniques for evaluating performance margins in detonators, a capability critical to LLNL Stockpile Stewardship.

Figure 1. (a) Initial configuration of a 2-D axial model of a new gold EBW, showing mesh density and location of header (blue region). (b) As wire explodes, it sends a shock into the surrounding medium. Relative pressures predicted by the model from high (magenta) to low (blue) and zero (white) are shown at the instant the shock reaches the header. (c) By the time the shocked region doubles in width, the wire vapor has expanded and cooled, and the confinement and reflection provided by the header on the shock increases pressure in the magenta "pinch" zones.
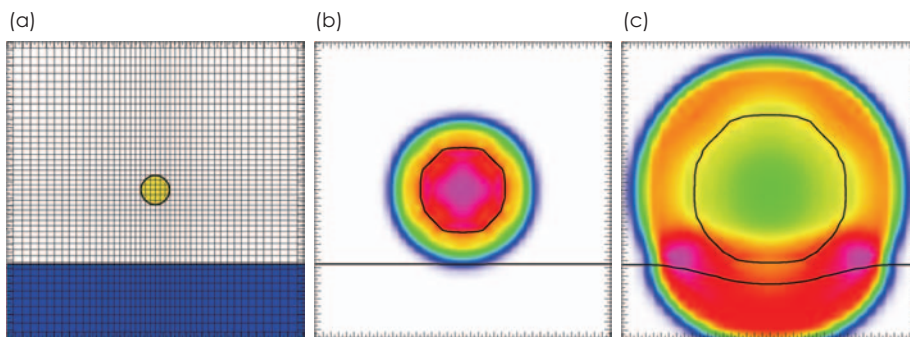
Figure 2. (a) Initial configuration of a 2-D axial model of an aged soldered gold EBW close to the solder mound. (b) The $AuIn_2$ layer heats and explodes first, followed shortly by the pure gold core. In this example, it takes 20% more time for the shock to reach the header, and at this instant, the highest pressure in the powder is reduced by 25% compared to normal (Fig. 1). (c) By the time the shocked region doubles in width, peak pressures in the powder above the wire and in the pinch zone near the header are both 20% less than normal.

TechBase
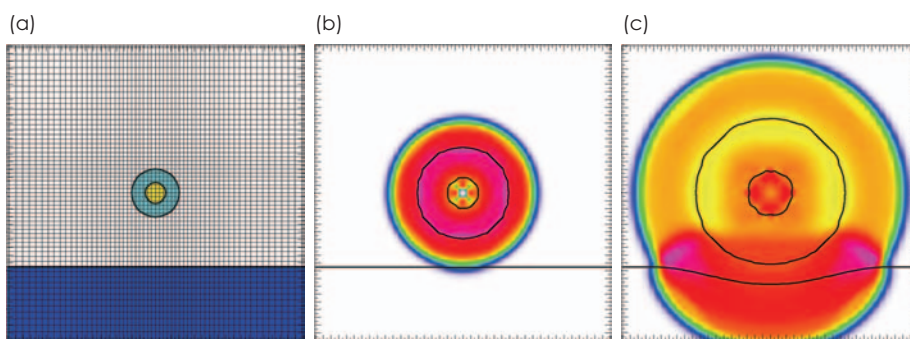
For more information contact
Constantine A. Hrousis
(925) 423-4744
hrousis1@llnl.gov

FY2005 Accomplishments and Results

In FY2005, 2-D models were created to better understand both longitudinal and axial aspects of EBW performance. A material model for gold-indide (AuIn$_2$) was introduced, based on our experimental studies to find this material's coefficient of thermal expansion (see reference 1). The explosive most commonly used with gold EBWs, pentaerythritol tetranitrate (PETN), has also been incorporated into our models.

Figure 1 shows an axial model of normal gold EBW burst, including header effects. The header provides confinement to the high explosive powder and reflects energy back toward the EBW, creating something like a Mach stem effect. Figure 2 shows a model of an aged soldered gold EBW, at similar stages, for comparison.

Figure 3 shows the effect of a large air gap, filling the space between the EBW and the header. Because of the expansion of the gold vapor into the gap space and an effective loss of confinement due to the gap, pressure intensities in the powder are reduced relative to normal. These are examples of the type of sensitivity and impact studies that this new modeling tool can provide.

The 2-D models are now also capable of evaluating square geometries, as in slapper-initiated detonators and exploding bridgefoil (EBF) (Fig. 4).

Due to problems experienced while fabricating specimens for model validation, the EBW and EBF models demonstrated are only partially validated at this time. The anticipated Engineering Cluster Tool will be able to create appropriate specimens for more complete model validation.

Related References

1. Saw, C. K., and W. J. Siekhaus, "Thermal Expansion of AuIn$_2$," *Scripta Materialia,* August 2005.
2. Chace, W. G., and H. K. Moore, Exploding Wires, Plenum Press, Inc., New York, 1959.
3. Maninger, R. C., "Predicting Time-of-Burst of Exploding Bridgewires from Thermodynamic and Electrical Properties," *Fourth Symposium on Engineering Aspects of Magnetohydrodynamics*, April 1963.
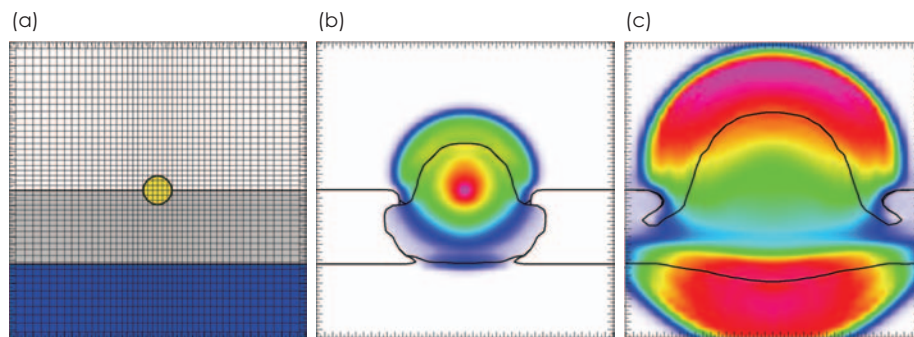
Figure 3. (a) Initial configuration of a 2-D axial model of a gold EBW with a significant gap between the powder and the header (grey region). (b) As the wire explodes, its vapor expands into the gap space, reducing its effect on the powder. It takes 5% more time to reach the header, and at this time peak pressures above the EBW are reduced by 25% relative to normal (Fig. 1). (c) By the time the shocked region doubles in width, peak pressures in the powder above the wire are 25% less than normal and the pinch zone near the header is nonexistent, due to the loss in confinement from the gap.
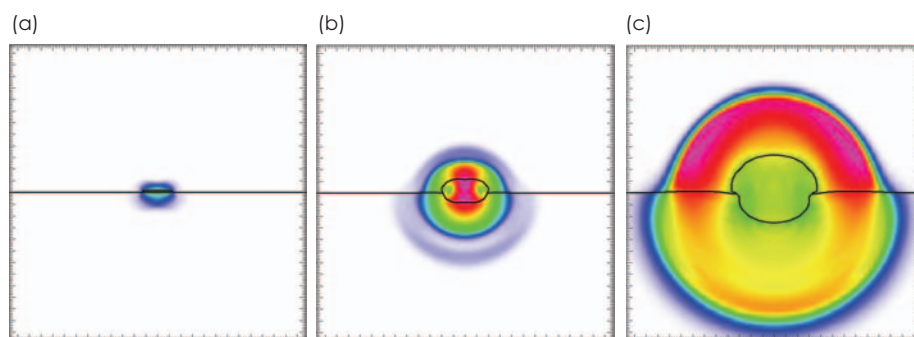
Figure 4. Very early in a 2-D axial model of an EBF. The very thin bridge is just beginning to vaporize. (b) Early in the explosion of the foil, the shock is planar near the centerline of the foil, transitioning to a more cylindrical geometry as the edge effects propagate inward from the sides. (c) Later in time, the shock in the powder is almost purely cylindrical in shape, again enhanced near the header.

Adaptive Coupling Techniques for CFD and Porous Flow

Modern computational fluid dynamics (CFD) capabilities can reliably predict the long time behavior of complex systems, provided that the time and length scales governing the various processes involved are comparable. This condition is not satisfied when simulating multiphase gas and moisture fluid flow in an open volume (a tunnel or drift) surrounded by a porous solid medium (a rock mass with embedded moisture). This problem presents unique practical challenges because it cannot be simulated through direct coupling of the physics; the time scales for the gas/moisture flow (seconds) are many orders of magnitude smaller than those for porous media flow (years). Coupling must be achieved efficiently through implementation of periodically applied "hand-off" boundary conditions between two sophisticated computational models.

Figure 1. Benchmark problem geometry.

To implement this coupling, we have established a computational methodology to integrate a commercial finite volume CFD package (STAR-CD) and an LLNL hydrological code for porous media (NUFT). The two codes run independently while hydro-dynamic, thermal, and moisture information is periodically exchanged at the gas/rock interface boundary. The immediate application is to characterize the thermal and humidity environment in the drifts of an underground waste repository where the nuclear materials in the waste packages provide high-temperature thermal sources, driving convection and transport in the drift. Successful coupling will result in the ability to predict heat and moisture evolution inside both the drifts and the surrounding rock over thousands of years.

Project Goals

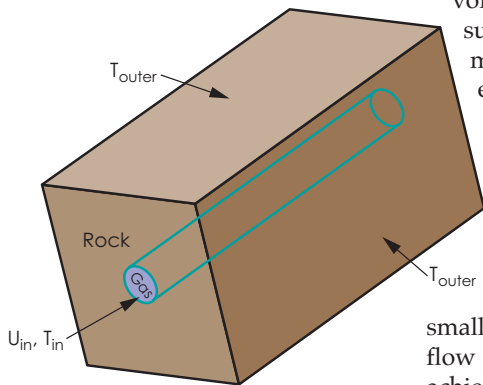To establish this capability and lay the groundwork for future simulations of complex large-scale
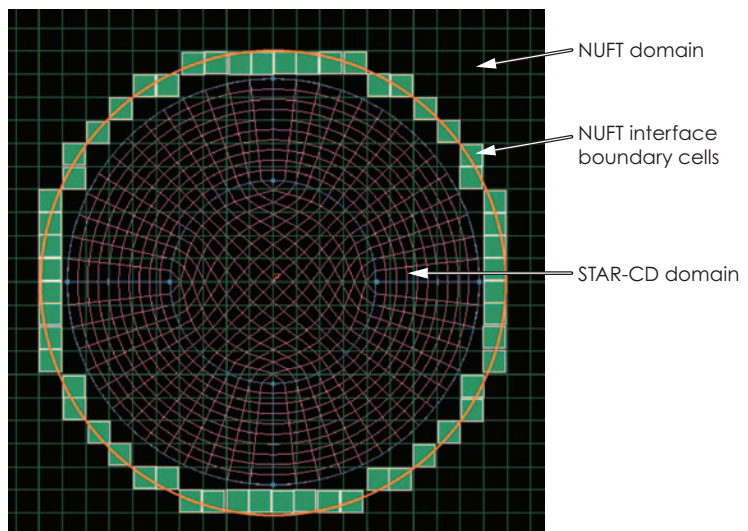

Figure 2. Cross-section of STAR-CD (purple) and NUFT (green) grids. The extended layer resides between the tube wall and the orange boundary. NUFT interpolation cells are shaded green.

For more information contact
Kambiz Salari
(925) 424-4625
salari1@llnl.gov

problems, we first needed to select a basic problem representative of the drift tube application to benchmark our methodology. We then determined the most optimum method to link the CFD and NUFT computational grids and transfer information. Our last goal was to demonstrate the convergence of the solution using the coupling methodology.

Relevance to LLNL Mission

This effort provides a flow-modeling capability that can simulate coupled porous flow and CFD. Many LLNL programs, such as the Yucca Mountain Project, DNT, and NAI can benefit from this flow modeling capability.

FY2005 Accomplishments and Results

Our benchmark study consisted of the steady-state conjugate heat-transfer problem of flow through a circular pipe surrounded by a layer of earth (Fig. 1). STAR-CD calculated the flow field within the pipe, and NUFT determined the heat transfer through the porous rock. The difference between the inlet and outer wall temperature boundary condition produces a heat flux between the fluid and the solid medium. We first determined how to transfer information between the two codes by examining various methodologies to overlay the two domains. Since NUFT is limited to structured orthogonal grids, extending the STAR mesh into the surrounding rock and interpolating flow variables onto the NUFT grid was the most effective coupling method. Errors in the interpolation scaled with the size of the NUFT cells.

Figure 2 shows a cross-section of the pipe mesh and surrounding porous domain. Boundary information from the tube walls is transferred into the extended region (bounded by the orange circle) and interpolated onto the NUFT boundary, shown as filled cells. Likewise information from NUFT was projected back onto the extended region of the STAR-CD domain. We

wrote scripts to facilitate the data translation and transferred the boundary information through shared files.

With the methodology in place to exchange data between the two solvers we began the iteration process. An initial thermal flux was prescribed on the boundary of the tube along with the inflow conditions, and STAR-CD computed the steady-state solution for the temperature in the drift shown in Fig. 3. We alternately ran STAR-CD and NUFT to steady state and exchanged temperature and thermal flux data at the interface using the coupling methodology. The temperature data along the interface plotted in Fig. 4 indicates the solution is converging, and successfully demonstrates the effectiveness of the coupling algorithm.

Related References

1. Bird, R. B., W. E. Stewart, and E. N. Lightfoot, Transport Phenomena, John Wiley, New York, 2002.
2. Buscheck, T. A., L. G. Glascoe, and K. H. Lee, "Validation of the Multiscale Thermohydrologic Model Used for Analysis of a Proposed Repository at Yucca Mountain," *J. Containment Hydro.*, **62-3**, pp. 421-440, 2003.
3. Danko, G., and D. Bahrami, "Heat and Moisture Flow Simulation with Multiflux," *ASME Heat Transfer/Fluids Summer Conference*, Charlotte, North Carolina, 2004.

2RT

Temperature
absolue
Kelvin
Iter = 300
Local MX = 320.0
Local MN = 317.6
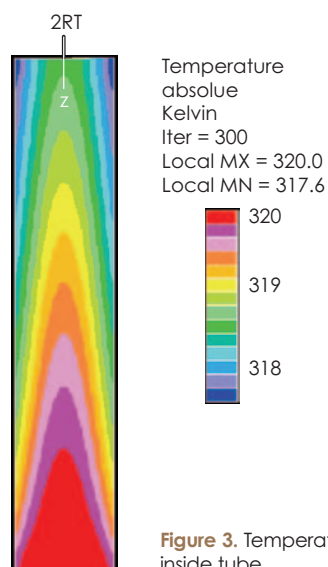
Figure 3. Temperature field inside tube.
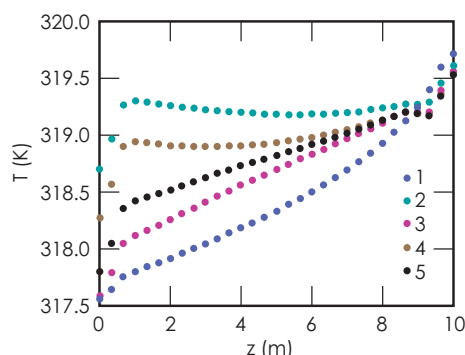
Figure 4. Interface temperature profiles at each iteration.

µLatte3D: Tool for Lattice-Boltzmann Phase Analysis

In this effort, user-interface capabilities were added to existing lattice-Boltzmann (LB) capabilities, which include analysis for filtration, collection, separation, and sample preparation processes. They also enable analysis of both viscous and gaseous fluid phases, particulates, and sieving media. The packaged capability integrates interfaces, analysis tools, and physics modules into a single software package that facilitates ease of use and hybrid analysis with other computational capabilities.

Project Goals

The package framework incorporates all of the scripts for problem set-up, job control, data analysis and visualization, and a user-friendly interface to enable pedestrian use of this capability. Now known as µLatte3D, the tool handles both gaseous and viscous fluids. It is a 3-D and parallel analysis tool that currently runs on Linux, AIX, and DEC/Compaq platforms.

Relevance to LLNL Mission

The LLNL programs that will benefit directly are Homeland Security, Medical Technologies (Bioengineering), programs related to Earth and Environmental Sciences, and bio-computations (Genomes To Life and fundamental biology). µLatte3D enables predictive analysis of complex fluids in complex micro- and nano- environments.

FY2005 Accomplishments and Results

In FY2005, the existing LB capabilities, both viscous and gaseous phase, were packaged into a single capability, now known as µLatte3D. To facilitate ease of use, a user interface,
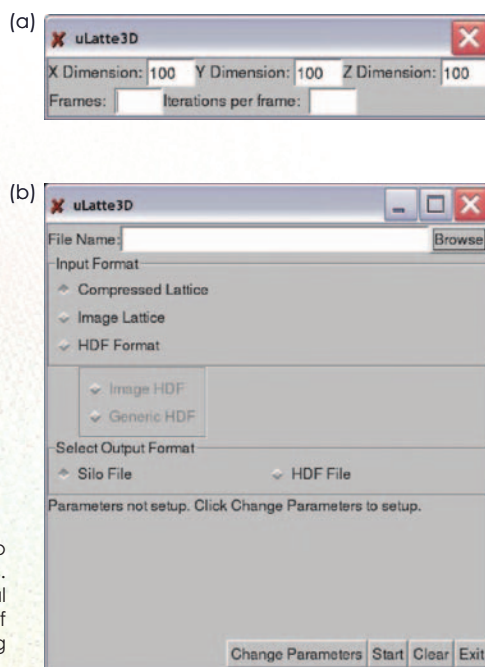
Figure 1. User interface to set up and launch µLatte3D simulations. (a) Set-up of the computational domain and duration of simulation "time;" (b) importing the lattice structure.

For more information contact
David S. Clague
(925) 424-9770
clague1@llnl.gov

for both input and output/visualization, was also integrated with the overall μLatte3D package. The input facilities were enabled by leveraging the geometry infrastructure from CASC's Overture framework (www.llnl.gov/CASC/Overture/). The framework was modified to include a new lattice generation module. This tool can be used to interactively create new problem definitions (geometry) or to import geometry from CAD via the industry standard IGES file format. Overture's fast geometry query tools are then used to generate the computational domain and boundary information required by μLatte3D.

To facilitate easy problem set-up, all flags, physics, and lattice parameters are now integrated into a single input file. This single input file can be accessed and modified directly or through an easy-to-use interface, as shown in Fig. 1.

All input, run time, and output data structures are stored in Silo and/or HDF5 formats, and the output data structures are directly accessible to visualization tools. Figure 2 shows an example: VisIt visualization output for the velocity field around a suspension of spherical particles.

A variety of data will be written to the graphics files and viewable with VisIt, including materials (walls and channels); and particle data, to include position, velocity, and bulk suspension behavior. Additionally, fluid velocity, shear, and temperature fields can be displayed. The capability enables characterization of particle and fluid transport in complex micro- and nano-environments, both gas and liquid phases, with parallel restarts.
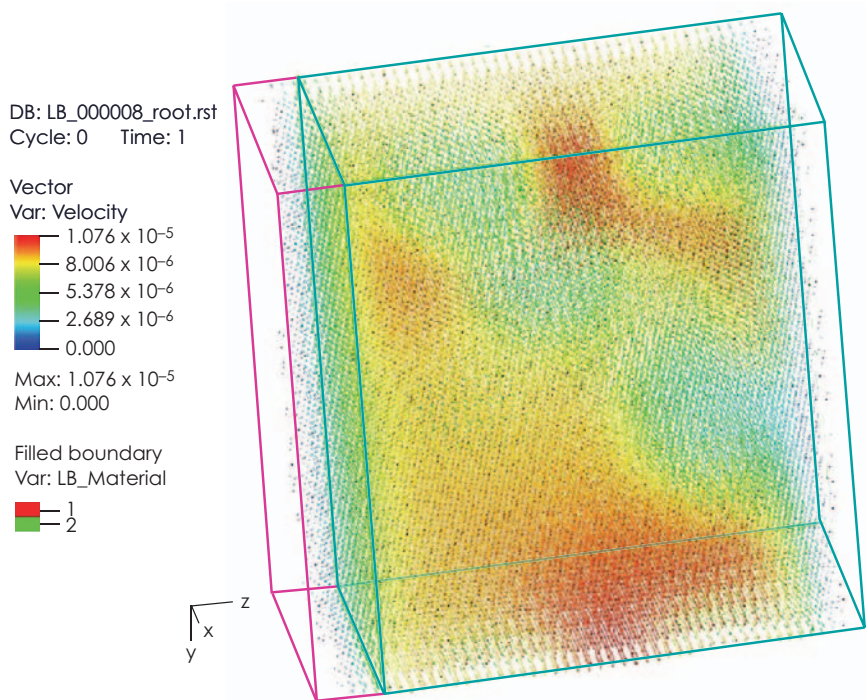
Figure 2. Frame from a movie of particles in channel flow. Velocity field is produced by μLatte3D viewed using VisIt.

Enhanced Fluid Dynamics Modeling Capability for Anatomically-Correct Endovascular Flows

Over the past several years, computational fluid dynamics (CFD) has been increasingly used as a tool for simulating hemodynamic flows within the human body. CFD simulations have the advantage of providing 3-D, time-dependent velocity and pressure fields that are not easily measured with *in vivo* diagnostics or *in vitro* experimental techniques. Combined with advances in medical imaging technology, such as magnetic resonance imaging (MRI) and computed tomography (CT), CFD can offer patient-specific data of hemodynamic flows within endovascular geometries acquired through these imaging methods. Doctors can then use this image-based data to make more informed medical diagnoses and to predict the outcomes of various treatment alternatives.

Project Goals

The purpose of this project is to demonstrate a modeling and simulation capability for the hemodynamic flow through an endovascular geometry obtained from CT scan data. To successfully achieve this goal, we identified the steps and software tools required to extract an arterial surface from raw CT scan data, to generate a volumetric mesh within this surface, and to simulate the hemodynamic flow throughout the mesh.

Relevance to LLNL Mission

The technical capability to extract surface geometry information from CT scan data, produce a 3-D
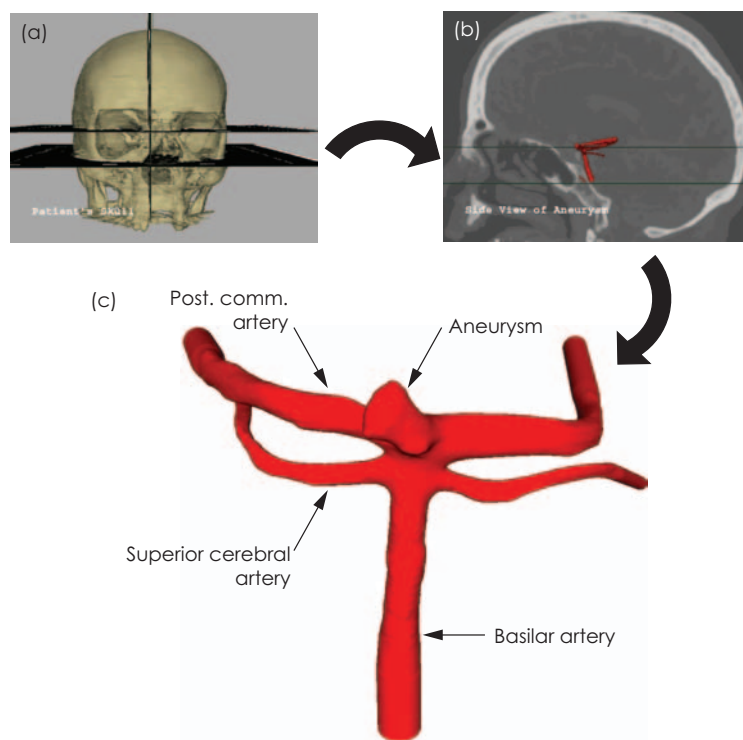
Figure 1. (a) CT scan data of the skull of a 51-year-old female patient with a basilar brain aneurysm. (b) Position of the endovascular geometry within the patient's brain. (c) Arteries and aneurysm included in the CFD simulation.
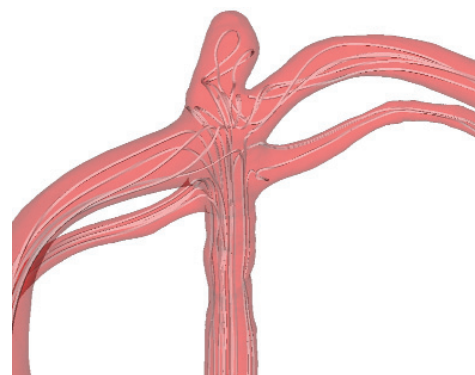
Figure 2. Streamlines of the steady-state velocity field through the bifurcation and aneurysm.

For more information contact
Jason Ortega
(925) 423-3824
ortega17@llnl.gov

computational mesh based upon this geometry, and conduct CFD simulations using this mesh has numerous applications to LLNL's mission. For example, this capability could be used to examine the flow field through an autonomous pathogen detection system (APDS) returning from the field, and to quantitatively assess the impact of bio-fouling or particulate contamination on the flow through the collector system.

FY2005 Accomplishments and Results

Numerical simulations were performed with a commercial code, STAR-CD, on an endovascular geometry extracted from CT scan data of a 51-year-old female patient with a brain aneurysm (Fig. 1). The complexity of the flow field within this geometry is highlighted by the 3-D streamlines shown in Fig. 2.

A streamline plot at one cross-section of the computational domain

(Fig. 3) shows that the flow at the bifurcation is comprised of a jet from the basilar artery that impinges upon the aneurysm neck at multiple locations to form a swirling, vortical structure. Figure 4 shows a plot of the shear stress over the entire arterial geometry. It can be seen that there is significant variation of the wall shear stress at the aneurysm neck due to the underlying flow patterns. Such behavior in the wall shear stress and wall shear stress gradient has often been identified as one of the prime mechanisms for arterial wall degradation.

Related References

1. Berger, S. A., and L.-D. Jou, "Flows in Stenotic Vessels," *Ann. Rev. Fluid Mech.*, **32**, pp. 347-382, 2000.
2. Cebral, J. R., M. A. Castro, O. Soto, R. Lohner, and N. Alperin, "Blood-Flow Models of the Circle of Willis from Magnetic Resonance Data," *J. Eng. Math.*, **47**, pp. 369-386, 2003.
3. Chatziprodromou, I., V. D. Butty, D. Poulikakos, and Y. Ventikos, "Pulsatile Blood

Flow in Anatomically Accurate Vessels With Multiple Aneurysms: A Medical Intervention Planning Application of Computational Hemodynamics," *Flow, Turbulence, and Combustion*, **71**, pp. 333-346, 2003.
4. Stuhne, G. R., and D. A. Steinman, "Mesh Resolution Requirements for the Numerical Analysis of Flow Through Stented Aneurysms," *Summer Bioengineering Conference*, Sonesta Beach Resort, Key Biscayne, Florida, 2003.

FY2006 Proposed Work

To enhance the capability for simulating endovascular flows, we will implement and demonstrate non-Newtonian and temperature-dependent blood viscosity models with STAR-CD. The models will be validated using experimental data from the literature and demonstration simulations will be performed with an endovascular geometry obtained from CT/MRI scan data.
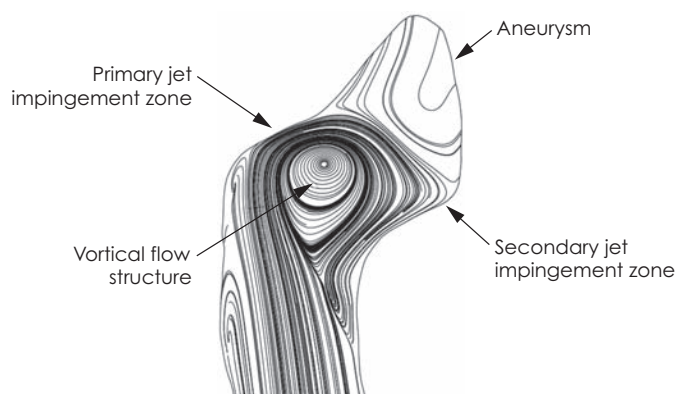
Figure 3. Velocity streamlines at a cross-section of the bifurcation and aneurysm.
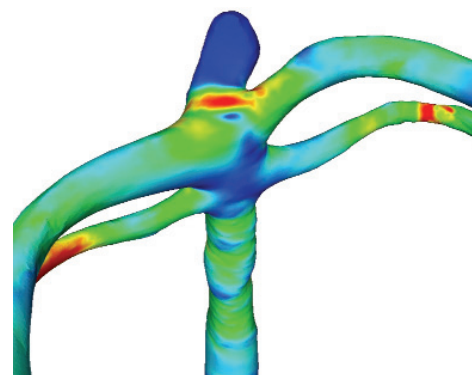
Figure 4. Shear stress distribution over the arterial walls.

Engineering Visualization Theater

The Engineering Visualization Theater (EVT) was established in 2001 as a venue in which to highlight important work being performed by LLNL's electronics and mechanical engineering personnel. It provides the infrastructure, tools, and visualization expertise necessary to help communicate engineering concepts through the production and presentation of high-quality audio/visual media.

As a presentation theater, the facility integrates a large projection video screen and surround audio system with a number of media sources including computer display output, digital disk recorder, VCR, DVD, and a video network feed from LLTN. Presenters can easily

patch a laptop computer into the system or use the resident hardware to display their material. The room provides seating for 10 to 15 people and provides an unclassified environment suitable for small-group collaborations, software demonstrations, or video presentations.

As a media production workshop, the facility also enables the creation of high-quality visualizations to help engineers better communicate their ideas. The intent is to enhance good engineering with the best possible media tools and presentation techniques. High-end animation, compositing, and image processing software staffed by knowledgeable operators, provide the tools and expertise necessary to achieve this goal.

The hardware for this project includes two computers, a large screen display, a digital disk recorder, an S-VHS video recorder, a video monitor, a DVD player, surround sound speakers, and an AV receiver.

Software includes 3-D animation, compositing, image processing, video editing, and DVD authoring.

Project Goals

The primary goal of the EVT is to assist engineers in communicating their ideas. Specifically, the EVT aims to provide the ability to fuse engineering analysis and data with professional animation to clearly articulate complex concepts.

Relevance to LLNL Mission

The need for good communication is ubiquitous and ongoing. LLNL's Engineering Directorate needs to be able to articulate its ideas and results in a modern venue commensurate
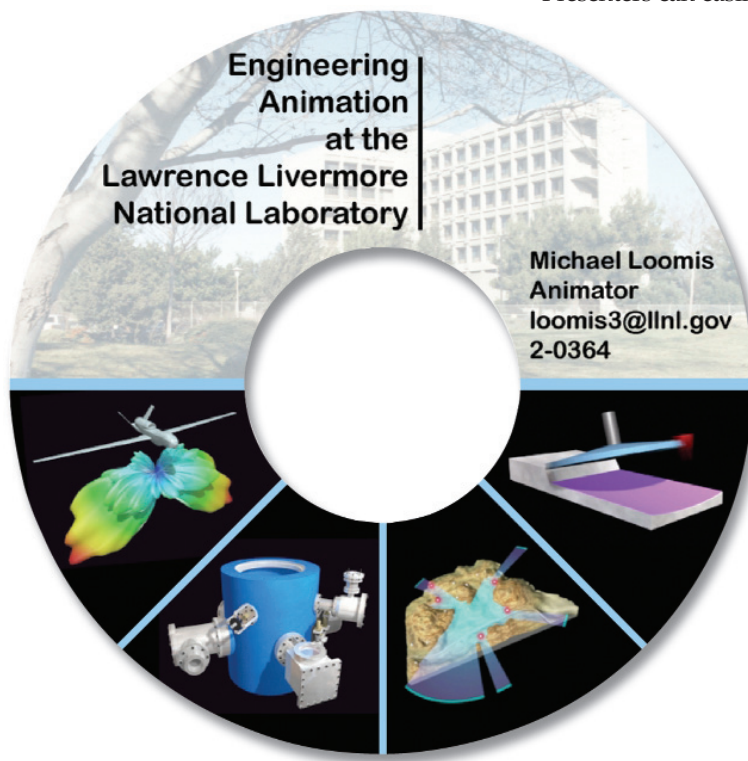

Figure 1. Sample of EVT graphics capability.

For more information contact
Michael D. Loomis
(925) 422-0364
loomis3@llnl.gov

with its abilities and those of its customers.

FY2005 Accomplishments and Results

EVT activities this year fall under three main categories: upgrades, marketing, and animation production.

Due to rising maintenance costs and creeping obsolescence, the aging SGI Onyx 2 system that once served as our primary animation production machine has been replaced with a more capable Apple G5. On the software side, improvements include upgrading to the latest version of Alias MAYA (V6.5) for animation/rendering. We also switched from Alias Composer to the Apple Shake system for compositing. These upgrades bring greater efficiency and new capability to the EVT.

Marketing efforts were increased this year in an attempt to expand the client base for the facility. As in previous years, we conducted in-house demonstrations for key Engineering personnel. A DVD entitled, "Engineering Animation at the Lawrence Livermore National Laboratory," was presented as a marketing tool to highlight animation projects created at the EVT.

Animation production activity this year included work for a number of clients in LLNL programs, on topics such as finite-element methods, adaptive urban dispersion modeling, hazardous materials bunker simulation, and tunnel failure simulations.

Like past EVT productions, we created movies that would:
1. fill a programmatic need;
2. demonstrate a path for visualizing computational results by incorporating actual data;
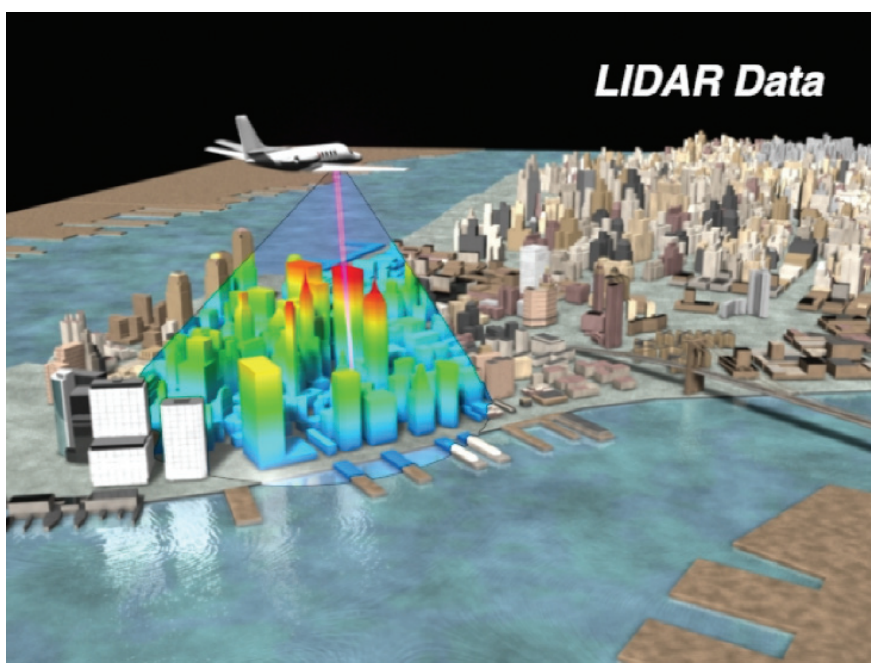
Figure 2. Sample of programmatic use of EVT's capabilities.

3. showcase various types of animation to illustrate the creative possibilities and techniques that are available for engineers to use in future animation productions; and
4. generally demonstrate the EVT's capability.

In each case, the result was a movie that brought engineering ideas to life in a form that was both instructive and visually compelling. By combining creative media production with the display capabilities inherent in the assembled hardware, we believe that these presentations demonstrate the potential for using the EVT as a tool to effectively communicate engineering concepts.

Figures 1 and 2 show samples of EVT's graphics capability.

FY2006 Proposed Work

The EVT intends to provide its services on an ongoing basis.

Micro-Meso-Nanoscale Engineering
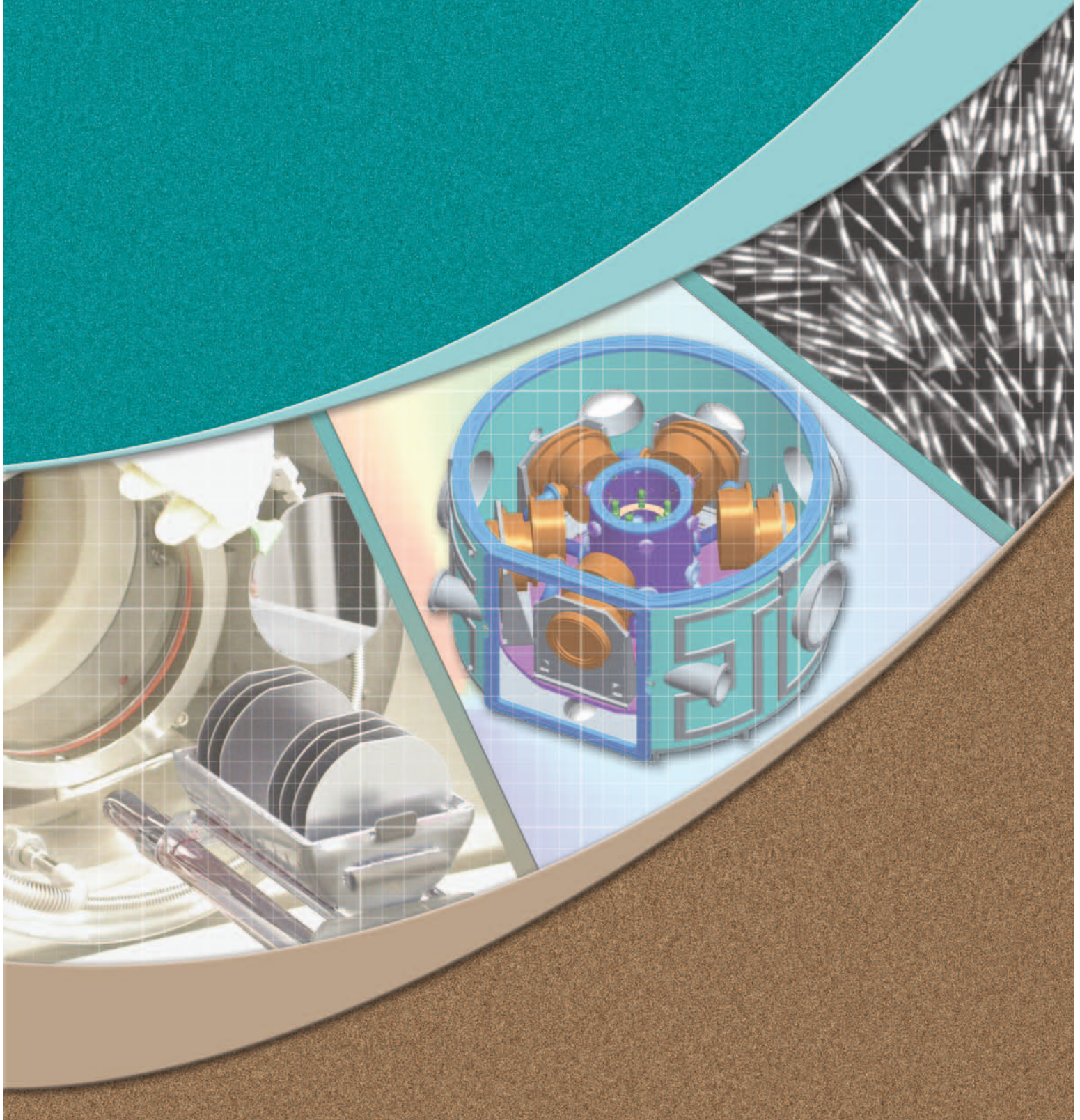
Rapid Defense Against the Next-Generation Biothreat

Bioengineered and emerging pathogens represent a significant threat to human health. The best defense against a rapidly expanding pandemic is to isolate the pathogen quickly from biological samples for analysis. The one persistent technology gap in the process of identifying and quantifying the presence of pathogenic agents has been sample handling and preparation that must precede any assay.

Project Goals

The objective of this project is to replace cumbersome, manual techniques with new automated technologies for sample handling and preparation. Specifically, we will use microfluidics with ultrasonic, electrophoretic, and dielelctrophoretic techniques to separate and purify viruses, the most transmissible and infectious agents, from biological and environmental samples.

Relevance to LLNL Mission

By making it possible to rapidly isolate and detect engineered and naturally emerging biothreats, this project contributes to the nation's defense against bioterrorism, which is central to LLNL's homeland security mission. In addition, this project supports LLNL's mission in bioscience to improve human health.
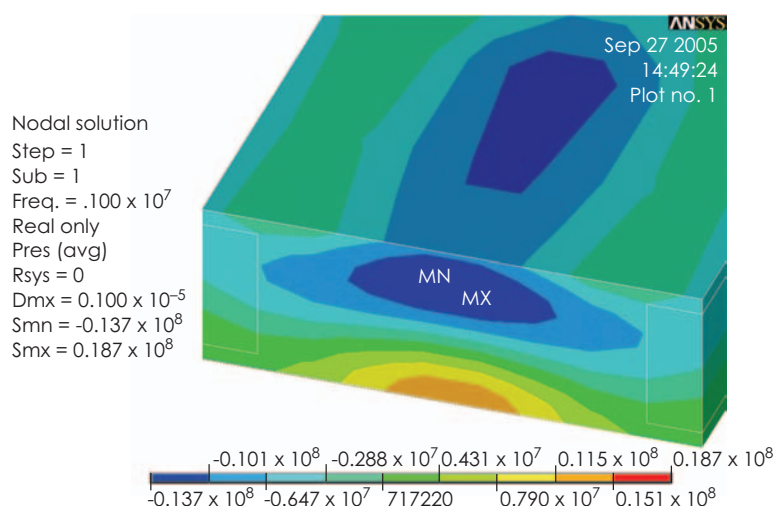
Figure 1. Oblique cross-sectional view of 3-D acoustic model results, showing the predicted shape of an ultrasonic standing wave in a fluid channel. At the chosen frequency, a single stationary node (green region) exists within the channel, as desired, so that particles in the flow will collect at this region for subsequent separation.
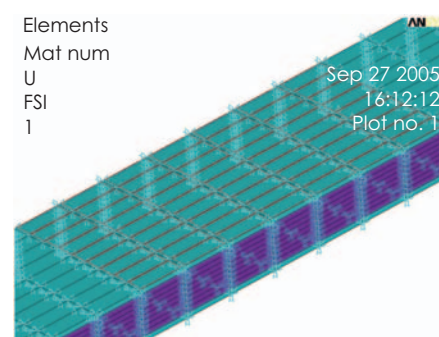
Figure 2. Portion of finite-element acoustic model of a fluid channel, before solving. The top and bottom of the channel are modeled as glass, the sidewalls as plastic (polystyrene).

For more information contact
Raymond P. Mariella, Jr.
(925) 422-8905
mariella1@llnl.gov

FY2005 Accomplishments and Results

In FY2005, we ordered and received the electronics and control instrumentation to set up microfluidic test stations, as well as a selection of fluorescent beads ranging from 30 nm to 5 μm in diameter. These will be used to calibrate our flow system and align the microscope-based test station. Using existing microfluidics models and published data on the physical properties of human cells, bacteria, and viruses, we calculated the scales of systems (channel lengths and cross-sections, electrode size, distributions, and voltages for dielectrophoresis and electrophoresis), to manipulate and separate bacteria and smaller particles from the larger particles.

Figures 1 to 4 show representative results for acoustic/ultrasonic forces.

We expect the new capabilities developed in this project to reduce the time required to identify a new pathogen, such as SARS, by up to an order of magnitude, in part, by better matching methods for sample preparation with the needs of emerging assay technology. These capabilities will also be critical to developing ubiquitous, high-performance autonomous pathogen-sensing systems envisioned as sentinels that monitor for aerosol-transmitted pathogens by screening, for example, air filters or handrails at international airports.

FY2006 Proposed Work

In FY2006, we will instantiate a capability to propagate, characterize, and purify Risk-Group-1 viruses, which will be selected based on the availability of virus and detection reagents. Using simulations that will be continuously validated and improved, we will begin design and fabrication of single-function microfluidic devices to perform manipulations using ultrasonics, electrophoresis, and dielectrophoresis. We will use ultrasonics to disrupt aggregates and divert the unwanted larger particles into the waste stream. Once we have a stream that consists primarily of bacteria and viruses, electrokinetic transport will be used to trap the bacteria and to pass a stream of purified viruses for analysis.
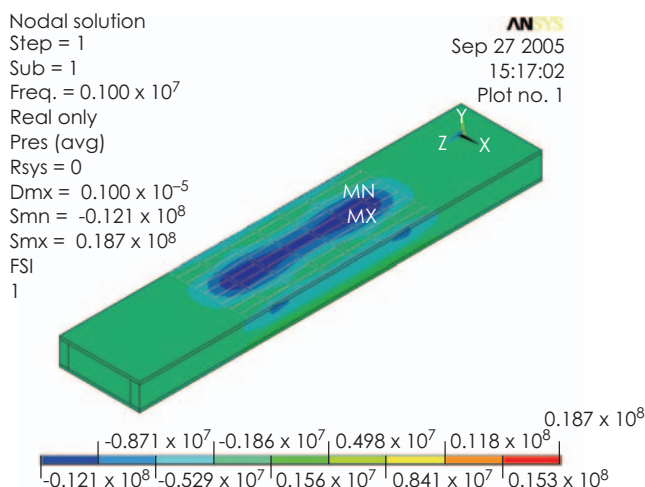
Figure 3. Solved model, showing that the region of the ultrasonic wave stays confined to the area very near the transducers (white outlines), as desired.
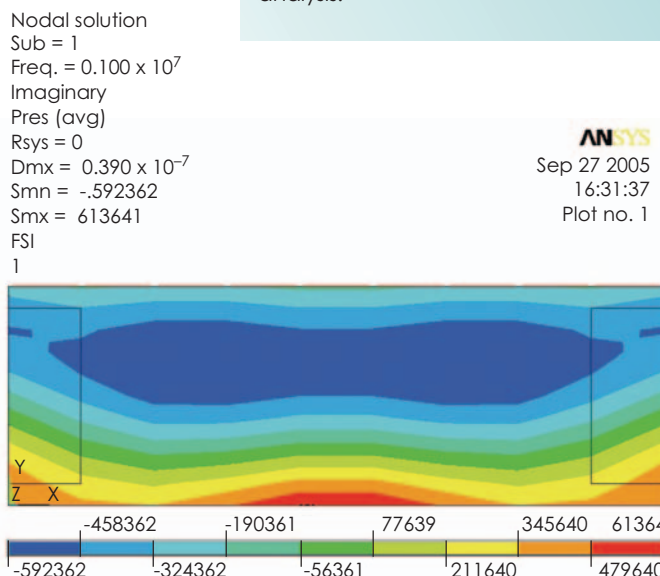
Figure 4. Cross-section of results of a different 3-D acoustic model, showing the detailed shape of an ultrasonic standing wave inside a fluid channel. Waviness in the standing wave is due to the presence of the sidewalls. Finite-element analysis allows for more detailed predictions than those from 1-D theory.

Microfluidic System for Solution-Array-Based Bioassays
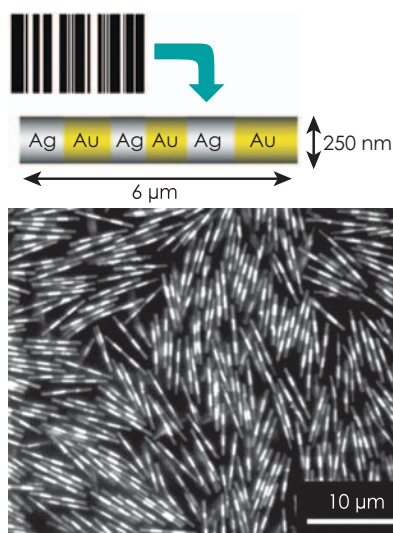
Figure 1. Optical microscope image of Nanobarcodes™ particles.

Ag Au Ag Au Ag Au — 250 nm — 6 µm — 10 µm

We are developing an integrated, reconfigurable microfluidic system for performing user-specified multiplexed biomarker assays for the early detection of disease-causing agents, using solution array technology. Solution arrays are similar to gene and protein chips, but use surface-functionalized particles in solution, rather than the binding of biomolecules to a fixed surface. Instead of correlating fluorescence with location, as in a chip format, the particles are encoded for identification. Results are read by examining particles for their encoded type and for the presence or absence of the fluorescence indicative of a positive binding event. The flexibility of solution arrays means that different types of functionalized particles can be added as desired by an end user, and particles for DNA, RNA, and protein detection can be used simultaneously in a single low-cost format.

The particles used in this project are Nanobarcodes™ particles (Fig. 1), short metallic nanowires that bear patterns of light and dark stripes analogous to the stripes in a supermarket barcode. These particles offer unique advantages in their ability to be identified using standard light microscopy, avoiding the need for complicated spectroscopic or flow cytometry methods. Surface functionalization of metal particles is understood, and the Nanobarcodes™ can be made with magnetic materials, opening new possibilities for manipulating, transporting, and trapping the particles using magnetic and electric fields.

Project Goals

The goal of the project is to demonstrate a prototype bioassay system based on Nanobarcodes™ particles. This system will be capable of performing simultaneous assays for several biowarfare-agent simulants. Along the way, we expect to achieve a number of important scientific goals, advancing the state of the art in particle-based biochemical assays and in the manipulation and control of metallic nanoparticles within aqueous solutions.

Relevance to LLNL Mission

Biodefense is a major research focus at LLNL, in support of technology needs for homeland security and national defense. The technology developed in this project will also benefit medical diagnosis and treatment of disease.

FY2005 Accomplishments and Results

In this final year of the project, many of the lines of research we pursued in earlier stages were completed and brought together.

The development of the multiplex immunoassay was advanced to the point that we could obtain full dose-response curves of the entire multiplex assay to different concentrations of biowarfare-agent simulants, such as *Bacillus globigii* bacterial spores (Fig. 2). These results showed that the assay itself is mature, with very low background and cross-talk.

The studies of the physical properties of the particles were completed, yielding a great deal of new information. This included measurements of the relative physical effects of several different self-assembled monolayer (SAM) coatings,

For more information contact
George M. Dougherty
(925) 423-3088
dougherty9@llnl.gov

plus the addition of coatings of antibodies and other proteins used in the immunoassay process. The Nanobarcode™ particle synthesis process was successfully modified to include ferromagnetic nickel stripes, 25 to 75 nm in length, allowing the particles to be captured and collected using magnetic fields. This important advantage of Nanobarcodes™ was further developed through studies of the rate of travel under magnetic field attraction and the evaluation of techniques for performing magnetic capture within microchannels.

This knowledge has been leveraged to develop an integrated microfluidic system for carrying out automated Nanobarcode™-based multiplexed assays, using a low-cost microfluidic card (Fig. 3).

Related References

1. Nicewarner-Pena, S. R., R. G. Freeman, B. D. Reiss, L. He, D. J. Pena, I. D. Walton, R. Cromer, C. D. Keating, and M. J. Natan, "Submicrometer Metallic Barcodes," *Science*, **294**, pp. 137-141, 2001.

2. Keating, K. D., and M. J. Natan, "Striped Metal Nanowires as Building Blocks and Optical Tags," *Adv. Mater.*, **15**, pp. 451-454, 2003.

3. Dougherty, G. M., F. Chuang, K. Rose, S. Pannu, S. Penn, and M. Natan, "Multiplex Biodetection Using Solution Arrays Based on Encoded Nanowire Particles," *Materials Research Society Spring Meeting*, San Francisco, California, April 12-16, 2004.

4. Dougherty G. M., J. B.-H. Tok, S. Pannu, K. A. Rose, G. Chakarova, and S. Penn, "Zeta Potential Behavior of Functionalized Metallic Nanorod Particles in Aqueous Solution," *Particles 2005*, San Francisco, California, August 13-16, 2005.

Figure 2. Nanobarcodes™-based multiplex bioassay results for a four-plex biodetection panel.
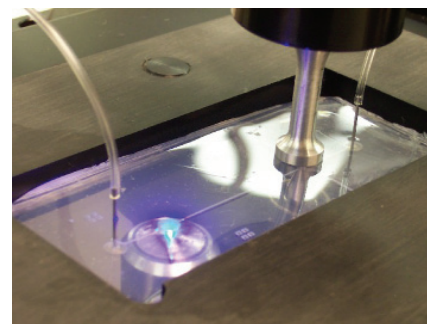
Figure 3. Microfluidic card in use. The card interfaces with the microscope, automated fluidics, an ultrasonic transducer for mixing, and a capture electromagnet with focusing cone (located beneath the card).

Colocation of Electronics with Microfabricated Actuators

This project will bridge the gap between micro-electro-mechanical systems (MEMS) sensors and the electronics necessary to control and extract data from them. Since the advent of MEMS, macroscopic wires have connected MEMS devices to electronics for control and sensing. The parasitic capacitance of these wires, the sheer number of wires sometimes necessary, and the additional volume required by wires and a second chip, makes macroscopic wires an unacceptable solution for many projects.

Several groups have produced MEMS devices on the same chips as electronics by putting the electronics next to the MEMS, or by using exotic materials that can be deposited without exceeding the thermal budget of the electronics. However, one often needs to fabricate MEMS devices that are incompatible with the exotic materials, and dense arrays of devices cannot tolerate the space used by placing MEMS next to electronics. The advent of the ability to bond chips together with microfabricated metal bumps will allow MEMS structures to be fabricated in conventional processes and then bonded to their controlling electronics.

Project Goals

This project demonstrates a technology to colocate MEMS with electronics. To do this we need to produce a test MEMS device and electronics, and colocate the two. We use the spatial light modulator (SLM) as a test system. The SLM has the advantage that it benefits from both the scalability and the increased sensitivity of colocation. Our goal was to produce a 19-pixel array of actuators attached to electronics.

Figure 1 is a schematic of the bonding process.

Relevance to LLNL Mission

This project has relevance to a variety of LLNL areas of interest. The work will enable sensors that require large arrays, are sensitive to parasitics, or require very small packages. This project will also extend mesoscale fabrication capabilities.
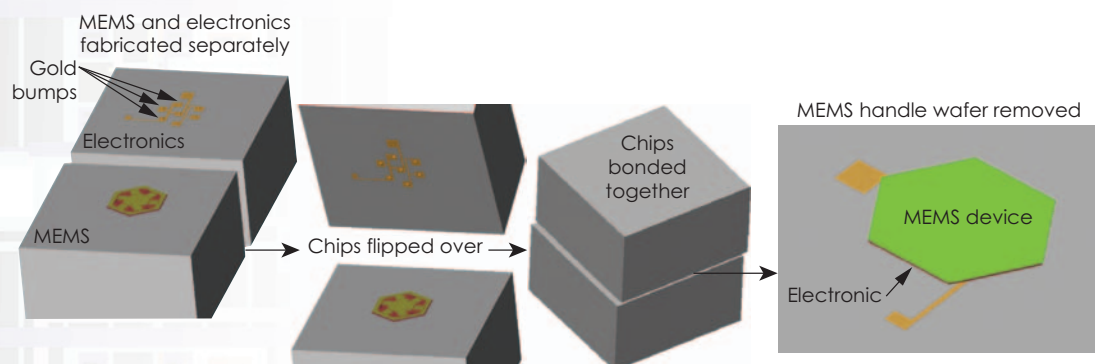
Figure 1. Schematic of bonding process.

For more information contact
Alex Papavasiliou
(925) 423-1952
papavasiliou1@llnl.gov

FY2005 Accomplishments and Results

This year the project moved toward the goal of bonding MEMS actuators to complementary metal oxide silicon (CMOS) circuitry. The high-voltage configuration was completed. We prepared application-specific integrated circuits (ASIC). Files with the parameters of the technology to be used were created. Following the production of the technology files, the circuit was simulated using SPICE software, the chip was laid out (Fig. 2), and the layout was simulated to determine that it would produce the expected results.

The MEMS actuators were reconfigured such that they would be compatible with the wafer release process as well as the electronics. The reconfiguration (Fig. 3) is complete and ready for fabrication.

Related References

1. Singh, A., D. A. Horsley, M. B. Cohn, A. P. Pisano, and R. T. Howe, "Batch Transfer of Microstructures Using Flip-Chip Solder Bonding," *Journal of Microelectromechanical Systems*, **8**, 1, pp. 27-33, March 1999.
2. Humpston, G., and S. J. Baker, "Diffusion Bonding of Gold," *Gold Bulletin*, **31**, 4, 1998.

FY2006 Proposed Work

For FY2006, we will fabricate the MEMS actuators in parallel with plans for a second-generation of electronics with a digital multiplexer. When the MEMS has been completed and the first ASIC returns from the foundry, they will be bonded together. Finally, a third-generation ASIC with capacitive position sensing will be fabricated and bonded to the MEMS actuators. This generation of ASIC will be capable of driving the MEMS actuators with a voltage based on the sensed position, providing closed-loop control.
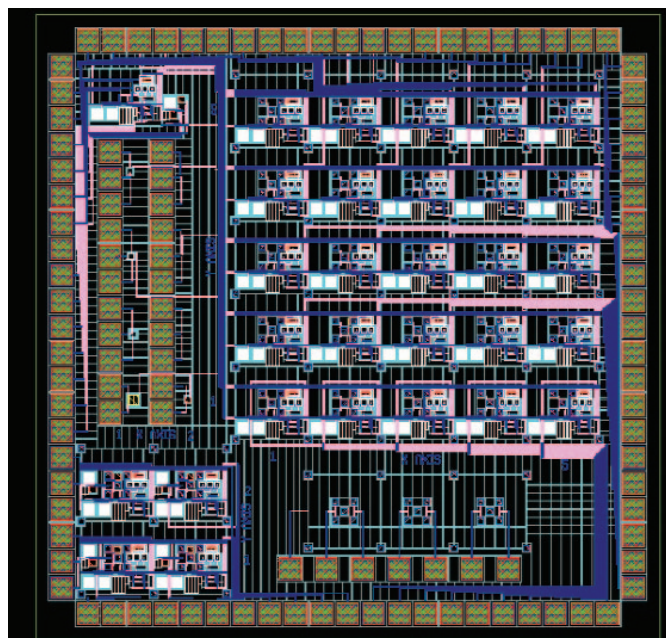
Figure 2. Layout for ASIC currently in fabrication. Upper right: 5-x-5 voltage-driver array; bottom left: 2-x-2 voltage-driver array; bottom middle: 1-x-3 direct-voltage array; top left: test circuits.
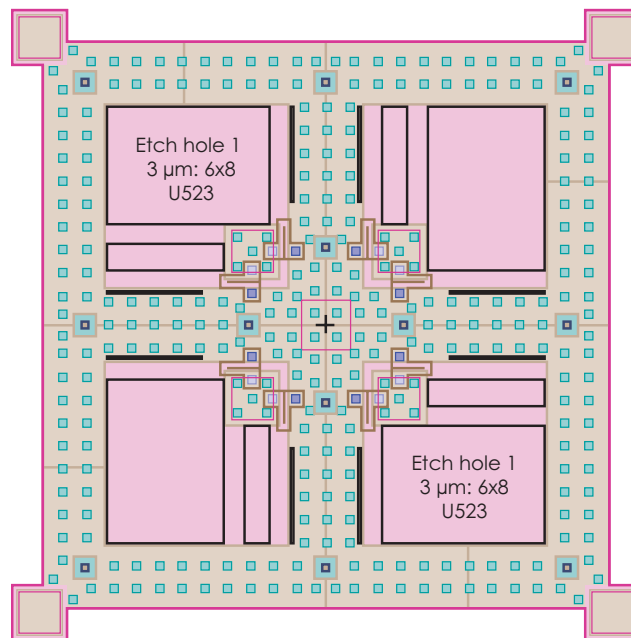
Figure 3. Layout for a MEMS actuator.

Custom Microinstrumentation for Sensing Systems

Various technology programs at LLNL demand new sensors that measure physical phenomena like contact stress, force, displacement, strain, acceleration and temperature. LLNL engineers provide custom instruments that are required to meet a myriad of constraints. This effort builds capabilities and tools that may find use in a variety of applications, including stockpile diagnostics and surveillance.
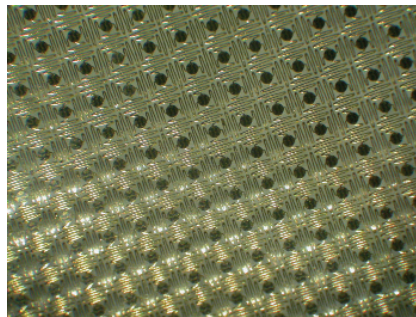
Figure 1. Contact-Stress Sensing Array with 900 independent silicon sensor islands on flexible and extensible interconnects.
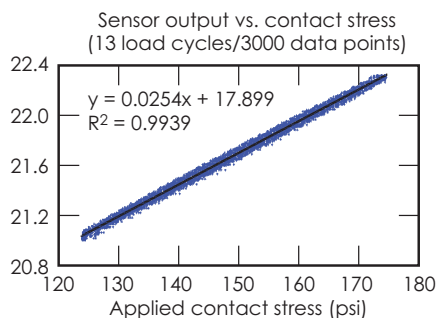
Figure 2. Contact-stress sensor data.

Project Goals

This project consists of three major parts. The first goal was to prove, integrate, and test all the components necessary to form a contact-stress-sensing array (CSSA) and to test the completed system. The second was to produce and implement all components of an Optical Force Probe (OFP) to be used for measurements with an optical readout system. The third was to characterize and implement a Modular Optical Assembly (MOA) to be used in the OFP and other optical instruments. The MOA addresses alignment and protection of the sensitive optical chamber necessary for the optical instruments' functions.

Relevance to LLNL Mission

Custom microinstrumentation for stockpile stewardship and other LLNL applications is in great demand. LLNL's Microsensors Program leverages capabilities in meso-, micro-, and nanotechnology to field microscale sensors for high-fidelity
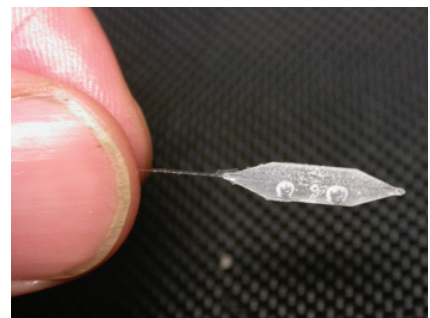
Figure 3. Photograph of Optical Force Probe.

For more information contact
Jack Kotovsky
(925) 424-3298
kotovsky1@llnl.gov

measurements. These instruments provide new diagnostic capabilities to measure the state of health of complex systems.

FY2005 Accomplishments and Results

The components of the CSSA system have been built and tested and are currently being integrated (Figs. 1 and 2). MEMS process refinement has been completed and will now facilitate the production of large, 2-D arrays of contact-stress sensors interconnected by flexible and extensible wiring that can conform to surfaces of complex curvature. These arrays readily conform to complex curvatures of less than 12 mm radius.

New individual sensing mechanisms offer contact-stress sensing with an accuracy of +/- 6% with a 50-μm-thick silicon device. These devices show a hysteresis of less than 2% of full scale, 0.03 mV/V/psi sensitivity and +/- 0.46%/°C thermal

dependence, with a load range of 0 to 3.5 MPa. Alternate load ranges can be accommodated with silicon geometry scaling.

Modeling shows the multiplexed control and readout system offers array communication with a minimal wire set and less than 1% error. The minimal wire set facilitates array fabrication, performance, and system integration. Based on the models, the electronics and acquisition software have been completed. They have been characterized and proven with a mock array and have been connected to a 64-sensor MEMS array to show full-system integration. New capabilities have been established to package, load-test, and thermally characterize the devices.

For the OFP (Fig. 3), new plasma- and wet-etching processes have been defined to form high-performance silicon devices. These processes provide superior mechanical deformation through surface

polishing, allowing the devices to far exceed expectations and criteria. A packaging methodology has been defined and executed that permits fielding of the completed system in a variety of systems. The package protects delicate features of the device and can be tuned to adapt the sensor to a variety of load ranges and system geometries.

The MOA has been characterized with commercial and LLNL-built components. This system has been successfully deployed as part of the OFP. Additionally, the system has been demonstrated in a custom Optical Gap Gauge (Figs. 4 and 5) with programmatic applications. A typical device shows 0.23 μm/mm displacement-measurement sensitivity for a system capable of resolving 0.001 μm to 20 μm range. This device can measure displacements of several millimeters and can be readily scaled to accommodate other displacement ranges.
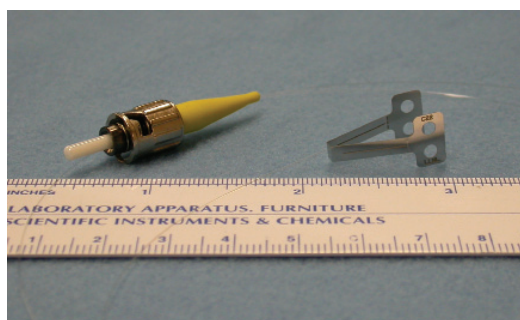
Figure 4. Optical Gap Gauge.

Optical gap gauge output vs. displacement

$y = 229.68x + 9798.7$
$R^2 = 0.9984$
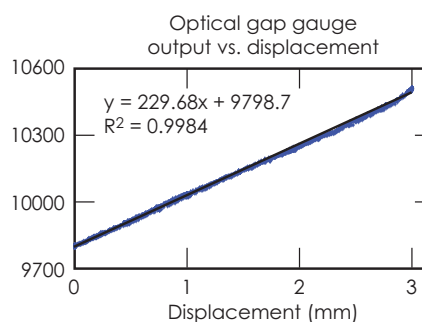
Figure 5. Optical Gap Gauge data.

Evaluation of Electrets for MEMS/NEMS

The term *electret* was conceived as a counterpart of *magnet* about one hundred years ago. A dielectric material that has been electricized (polarized) is called an electret.

The thermoelectret effect was discovered in 1925, when a Japanese scientist solidified a mixture of carnauba wax, resin, and beeswax in the presence of a high DC electric field. The energy absorbed during the charging process resulted in space-charge polarization by the trapping of positive and negative charges at the interstitial sites. Although electrets are formed by a variety of processes and in a variety of dielectrics, they are all basically a dielectric with charge trapped near the surface. Typical modern-day electrets are materials such as Teflon or silicon dioxide that have been charged. The beauty of the electret is that the charge stays in place over time and can be used in applications that require a charge source.

Typical commercial devices that use electrets are microphones, radiation detectors, and furnace filters.

Project Goals

Our interest in electrets is their eventual use for actuators and release mechanisms. Also we have an interest in scavenged energy generators. As a precursor to device fabrication, we have looked at making measurements of the various properties of electrets, such as charge density, surface voltage, and electrostatic force. Our goal has been to start with whatever commercial electrets we could obtain and make these measurements.
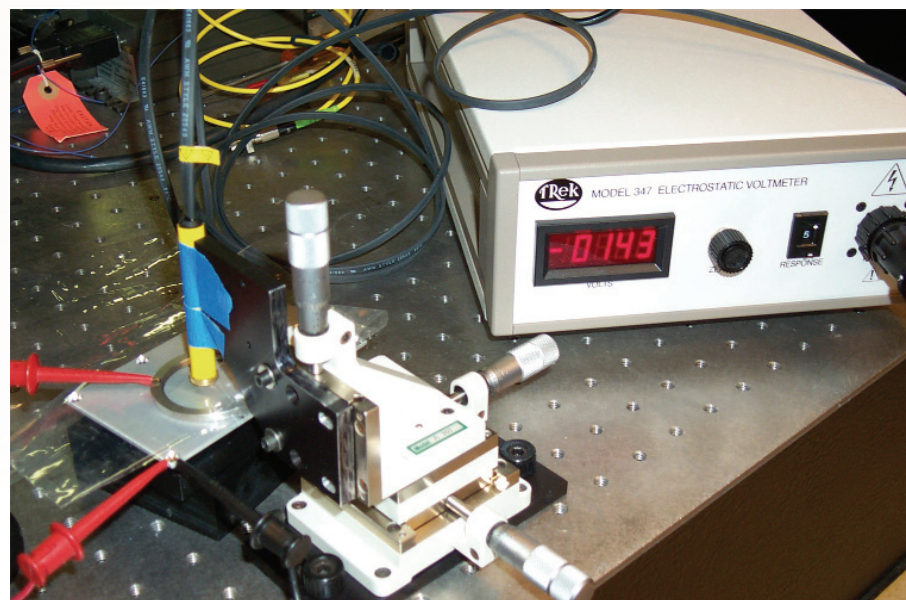
Figure 1. Electrostatic voltmeter and readout head (yellow) measuring surface voltage on a 3M electret (under metallic ground ring).

For more information contact
Michael D. Pocha
(925) 422-8664
pocha1@llnl.gov

Relevance to LLNL Mission

Incorporating electrets with MEMS technology may be useful for scavenged energy production by movement of conductors in an electric field. This energy could be used to power microsensors for various covert surveillance applications. In addition new types of microactuators and release mechanisms by countering induced charge are useful for micro-robotics applications.

FY2005 Accomplishments and Results

Commercial electrets were procured from RadElec Inc., and 3M. RadElec uses electrets in radon detectors. These electrets are approximately 5-mil-thick sheets of Teflon that are on a conductive back plate. The 3M electrets are free-standing films of poly-carbonate, about 0.04 mm thick, with charge embedded on both sides.

Our first goal was to measure the surface voltage, which can be mathematically transformed to calculate charge density. We were able to make accurate measurements of the surface potential with mm to cm spacing from the charged surface (Fig. 1).

The RadElec electret was measured to have a positive surface voltage around 800 V. This is consistent with the surface voltage quoted by RadElec for these electrets (~740 V). The 3M electret material was measured to have a negative surface potential of greater than -2000 V. This material did not have the conductive back plate, resulting in an increased effective surface voltage. A measurement without a back plate does not have an accurate reference to ground and therefore does not correlate directly to charge density. A second measurement with a conductive back plate yielded approximately -150 V.

Related References

1. Eguchi, M., *Philos. Mag.*, **49**, pp. 178–181, 1925.
2. Hsieh, W. H., T. Y. Hsu, and Y. C. Tai, "A Micromachined Thin Film Teflon Electret Microphone," *International Conference on Solid-State Sensors and Actuators*, pp. 425-428, June 16-19, 1997.
3. Huang, A., P.-J. Chen, J. Boland, D. Alberer, T.-S. Wong, H. Q. Yang, Y.-C. Tai, and C.-M. Ho, "Liquid-Rotor Electret Power Generator Energized by a MEMS-Based Pulsed Combustor," *Digest Tech. Paper, Power MEMS'04 Conference*, Kyoto, Japan, November 28-30, 2004.

FY2006 Proposed Work

With knowledge of the charge density we can calculate the force between electrets and other objects. We will perform this calculation, and attempt to verify the force by use of a force probe. A preliminary test has verified that both electrets exert sufficient force to support the weight of our miniature silicon platforms (~ 2.3 mg) (Fig. 2).

Future work will focus more on the actual fabrication and tailoring of electrets for specific MEMS devices such as power generators or release mechanisms.
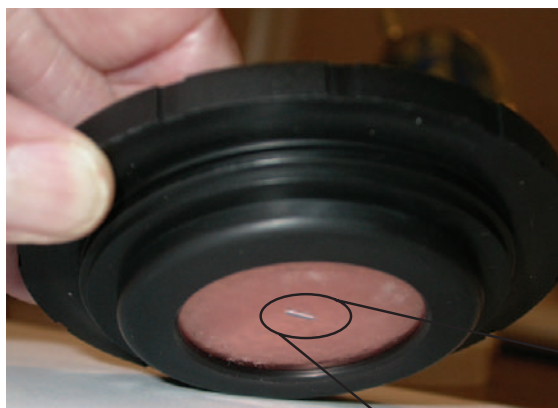
Figure 2. Miniature sensor platform (arrow-like) being held by electrostatic force to a RadElec electret with copper backing.

Advanced Microelectrodes for Chemical and Biological Detection

We are evaluating robust, highly sensitive microelectrode materials for detection of chemical or biological threats. Boron doped diamond (BDD), in the form of chemical vapor deposited (CVD) films, has been extensively studied as an electrode material in electrochemical environments. At high boron-doping levels, BDD has been shown to exhibit metal-like conductivity. BDD further exhibits a wide electrochemical window in water and other solvents, enabling a broader range of voltage sweep, with low background current. Furthermore, BDD is phenomenally durable under harsh electrochemical conditions. Such properties make BDD an attractive candidate as a microelectrode sensor material. We use reactive ion etch (RIE) of BDD films to make electrode structures that can be tested and integrated within microfluidic configurations compatible with existing systems for collection and separation of potential threats.

This realm is not without its drawbacks, however. As electrode size decreases, any lack of electrode durability exacerbates problems with device service life, and places limits on size and operating conditions. Graphite microelectrodes are prone to fouling and corrosion, and noble metals experience dissolution over time in environments, such as biological systems, that contain chloride. Integrated BDD microelectrode sensors may offer a compact, ultrasensitive alternative to detection of chemical and biological threats.

Project Goals

The goal of this work is to demonstrate the fabrication and performance of diamond microelectrode arrays for the detection of chemical and biological samples. We will further determine the limits of detection for the BDD electrode configurations we choose.

Relevance to LLNL Mission

Microelectrodes offer many possibilities for increased sensitivity and flexibility in electrochemical detection, an area of interest to LLNL.

FY2005 Accomplishments and Results

BDD microelectrodes have been fabricated and characterized. Comparison of BDD microelectrode performance to other metal electrodes
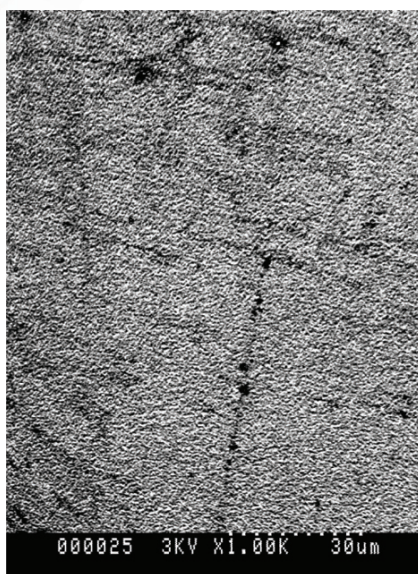
Figure 1. SEM image of BDD film before RIE etching.

For more information contact
Jeffrey D. Morse
(925) 423-4864
morse3@llnl.gov

demonstrates metal-like behavior under nominal testing conditions.

The as-deposited nanocrystalline CVD BDD film is illustrated in Fig. 1. The process is as follows: Microelectrode arrays are formed in the BDD film using RIE. The electrode patterns are formed using photolithography and electroplating to create a thick gold hardmask pattern. RIE is then used to remove the diamond everywhere except beneath the gold patterns. After etching, the gold masking layer is stripped off, leaving the BDD microelectrodes (Fig. 2). To determine the electrochemical behavior of the BDD microelectrodes, cyclic voltammetry (CV) is performed by sweeping the voltage on one of the diamond strip electrodes and measuring the resulting current.

Figure 3 compares voltammograms for BDD microelectrodes and gold electrode structures in a hydroquinone solution. BDD is a very inert electrode surface. In the case of hydroquinone, it is a two-electron reaction, and requires the intermediate, semiquinone, to stay stuck to the electrode long enough for the second electron to come off/get put on. The hydroquinone and semiquinone adhere well to the gold electrode and, hence, easily undergo the electrochemistry on gold electrodes. Their lack of adhesion to BDD greatly retards the kinetics of this process on BDD electrodes. The result is that a higher voltage is needed on either side of the reaction, to speed up the process. Thus, compared to the gold electrodes, the BDD electrode exhibited sluggish kinetics, resulting in an asymmetric voltammogram with a

peak separation of > 700 mV, while a gold electrode in the same solution displayed reversible behavior.

For the case of simple, one-electron, outer-sphere transfers we anticipate a fast reaction. Using a ruthenium hexamine solution, the BDD electrode was compared to a platinum electrode under similar conditions. In this case, the BDD electrode exhibited the typical fast, metallic-like kinetics expected of a highly-boron-doped-diamond electrode, comparable to that of a platinum electrode under the same conditions.

In summary, we've shown that BDD microelectrodes will prove to be a robust, low-noise detection technique for a variety of potential chemical- and biological-sensing applications.
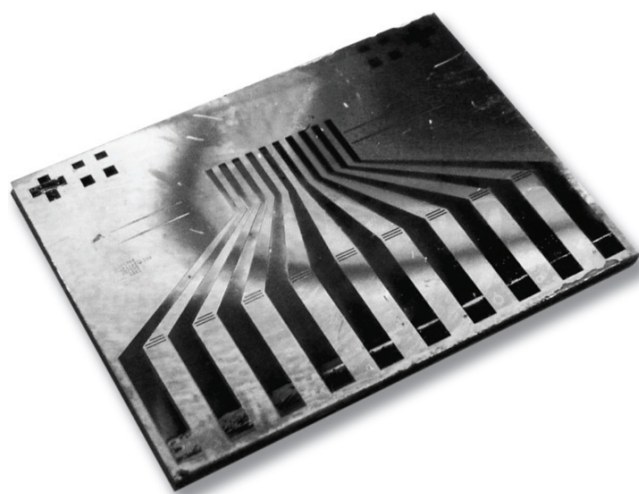
Figure 2. RIE-fabricated multi-electrode BDD array on SiO_2/Si wafer. The dark areas are the BDD electrodes.
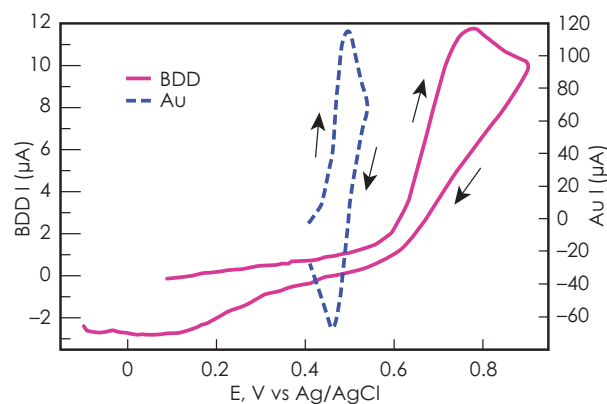
Figure 3. CV of 1mM hydroquinone in 1 M sulfuric acid, with RIE BDD electrode (~ 0.5 mm x 2 mm) and a 5-mm diameter Au electrode. Scan rate is 50 mV/s. Scan directions are as marked.

Modular Front-End Sample Preparation Microdevice for Integrated Hydrophobic Protein Separation System

Environmental and clinical sample preparation is one of the most critical steps in biological and chemical detection. Although biological and chemical assays are becoming increasingly more sensitive, absolute detection limitations are often a function of sample background contaminant concentrations. Purifying sample streams prior to detection will greatly improve the sensitivity and performance of the assays. Separating the various components present in the sample, such as molecules, lysed cell matter, and solutes, into hydrophilic and hydrophobic fractions will

provide a first order purification. A device capable of separating constituents based on hydrophobicity must be able to mix and separate immiscible fluids as well as interface with subsequent assay/detection devices. This project addresses these technical challenges.

Project Goals

The goal of this project is to improve microscale-mixing capabilities of immiscible fluids. To achieve this, a novel microelectromechanical system (MEMS) vertical mixer is fabricated and demonstrated. The system includes a multiplexed fluid inlet system, MEMS vertical vortex mixer, and fluidic I/O packaging.

Relevance to LLNL Mission

Work on this device advances several processing techniques and packaging to extend LLNL capabilities in areas such as silicon/glass anodic bonding, non-conventional glass etching, immiscible fluid mixing and integrated vertical microfluidic systems. The project will have a significant technological impact on the instrumentation community and will enhance the state of the art in biological and chemical detection, part of LLNL's national security mission.

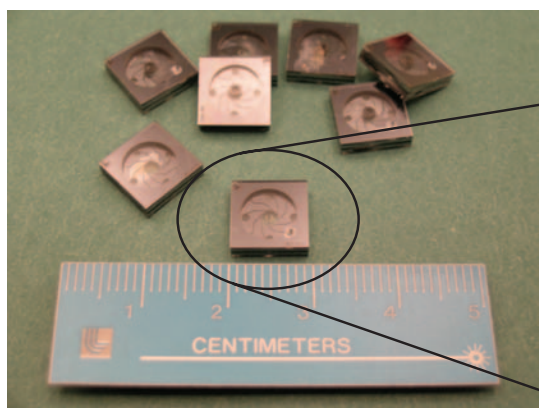**Figure 1.** Wafer-level photograph of completed devices.

Figure 2. Final five-layer device with close up of final out-of plane 5-layer mixer.

For more information contact
Erik V. Mukerjee
(925) 423-4841
mukerjee2@llnl.gov

FY2005 Accomplishments and Results

During FY2005, we reached milestones that include novel five-/seven-layer silicon/glass anodic bonding, specialized glass etching, and immiscible-fluid mixing. An overarching technical challenge was to construct a multilayer (> 4) glass/silicon structure.

Demonstration of novel processing approaches allowed for the bonding of multiple multilayered sets, such as bonding a three-layered bonded set (glass/silicon/glass) to a two-layered bonded set (Fig. 1). Fracture testing of the bond demonstrated that the glass/silicon interface was stronger than the Pyrex glass, confirming the reliability of the novel anodic bond process.

A five-layer prototype was built using acetate overlay masks for photolithography as an attempt to reduce fabrication costs and prototyping time. The devices suffered from inadequate photolithographic resolution due to

UV masking limitations, causing irregular silicon structures and fluid flow. Shifting to laser-cut polymer masking materials for glass etching and conventional glass/chrome masks for silicon etching eliminated these problems (see Figs. 2 and 3).

It is now possible to fabricate an out-of-plane modularized, multilayered, glass/silicon microdevice. Each layer performs a distinct function; therefore, simply adding additional layers can extend the functionality of the device. The packaging uses O-ring compression fitting to introduce and extract fluids to/from the device, eliminating the necessity for glue or epoxy to connect off-chip fluidic I/O (Fig. 4).

A key element of the micromixer is the ability for direct visual diagnostics during mixing. The glass/silicon structure provides a glass-viewing window of the emulsion chamber and linear-mixing channel, which affords visual confirmation of mixing (in conjunction with fluorescent/colored

dyes) prior to chemical analysis of solute concentrations.

A multilayer, modular, fluidic micromixer device was fabricated and tested as a first order sample preparation/purification bio-instrument. Preliminary results of the device demonstrate good mixing of aqueous solutions (aqueous color dye solution and plain DI water) for modest-pulsed inlet pressures (~30 psi).

Related References

1. Lingeman, H., *et al.*, "Sample Preparation for Peptides and Proteins in Biological Matrices Prior to Liquid Chromatography and Capillary Zone Electrophoresis," *Anal. Bioanal. Chem.* **382**, pp. 535-558, 2005.
2. Kirner, T., *et al.*, "Static Micromixers for Modular Chip Reactor Arrangements in Two-Step Reactions and Photochemical Activated Processes," *Chemical Engineering Journal* **101**, pp. 65-74, 2004.
3. Lemenand, T., *et al.*, "Droplets Formation in Turbulent Mixing of Two Immiscible Fluids in a New Type of Mixer," *International Journal of Multiphase Flow* **29**, pp. 813-840, 2003.

(a)   (b)

Glass 3 (outlet)

Silicon 2 (emulsion chamber)

Glass 2 (mixing channel)

Silicon 1 (fluidic channels)

Glass 1 (inlet)
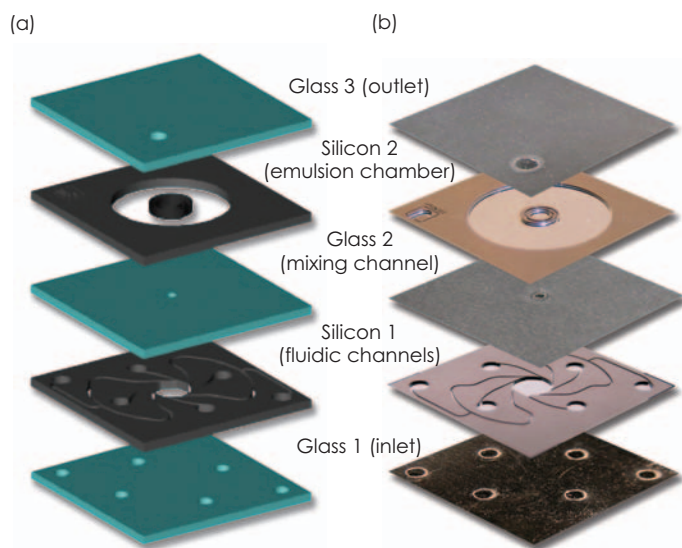
Figure 3. (a) Composite diagram and (b) photograph of five-layer mixer.
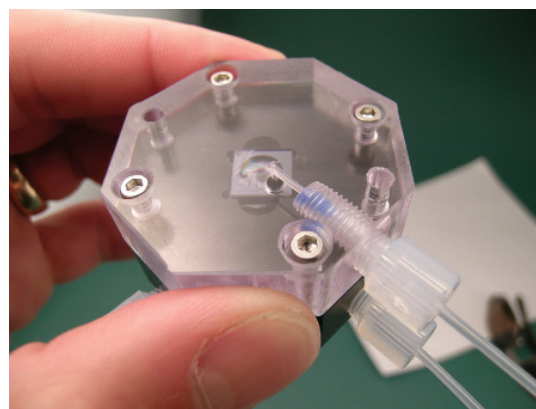
Figure 4. Photograph of custom fluidic I/O packaging with device at center.

Microfluidic Test Station

Front-end sample preparation is an often-neglected aspect in the implementation of chemical- and biological-warfare-detection instrumentation. Over the past ten years LLNL has created many microfluidic-based modules to aid in the separation, concentration, purification and/or fractionation of "trace" analytes from a complex noisy-background matrix. These modules have their own application space, yet all improve the overall system performance by starting the assay with a more concentrated and purified sample. For all the microfluidic technologies involved in the suite of front-end sample preparation projects, there is one common aspect: the need for an experimental data acquisition system.

This project aims to integrate existing experimental capabilities into one common platform to aid in the construction and the testing capabilities of microfluidic-based modules when applied to chemical- and biological-detection instrumentation.

Project Goals

The goal of this project is to deliver an automated microfluidic-based test station to control and sense temperatures, voltages, pressures, and fluid-flow rates while performing quantitative fluorescent image acquisition. This platform needs to manage all the necessary output data
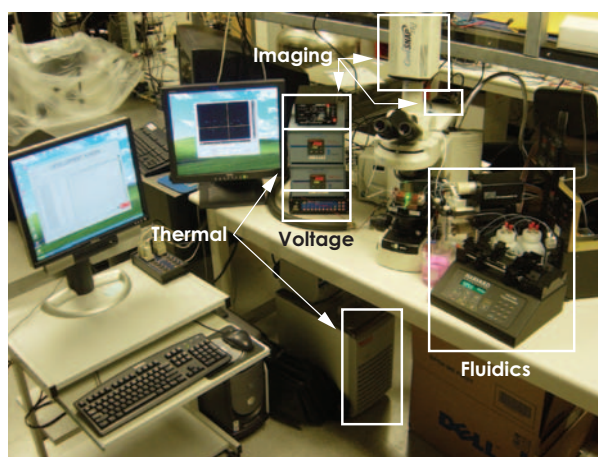
Figure 1. Adaptable, automated microfluidic test station.
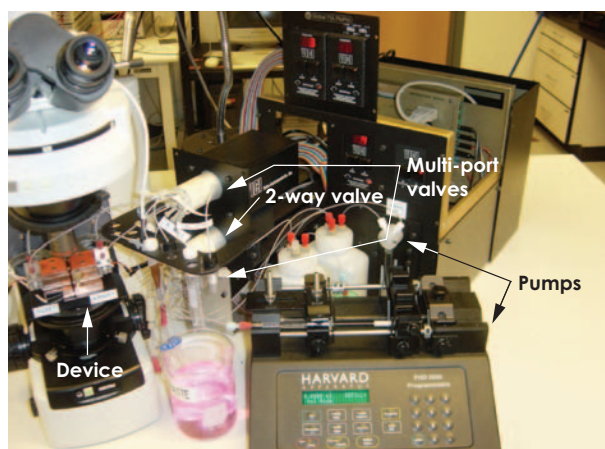
Figure 2. Fluidic control scheme.
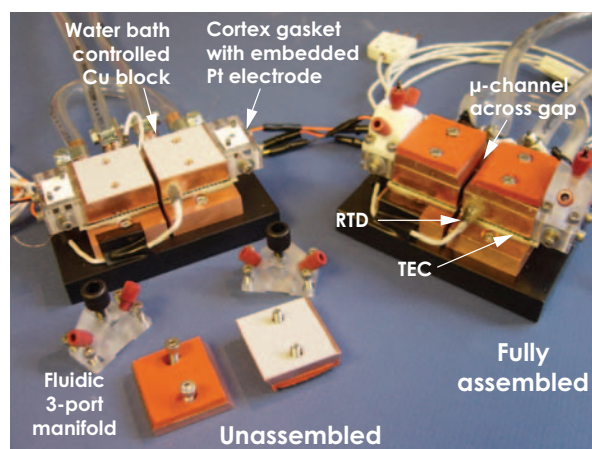
Figure 3. General package for loading microcapillaries.

For more information contact
Kevin D. Ness
(925) 423-1856
ness5@llnl.gov

with minimal user interaction for possible future integration into a deployable system. In addition, this project includes a standardized package for both high-aspect-ratio microcapillaries and microfluidic chips. The package must allow for ease of integration with future microfluidic projects and must have the ability to control temperatures, voltages, and fluid-flow rates in each of the microchannel geometries. Thus, a complete microfluidic workstation, minus the actual microfluidic module, is the delivered product.

Relevance to LLNL Mission

This microfluidic test station (software and hardware) will reduce the typical prototype implementation cycle by reducing and improving the experimental testing/validation phase for front-end sample preparation devices. A significant benefit will be the cross-pollination of available testing procedures from the many LLNL projects (standardized through the software).

FY2005 Accomplishments and Results

Two complete systems have been requested and are being built for LLNL programs. Our accomplishments are as follows.

Software. We have produced easy-to-use and adaptable software for large experimental studies, with an automatic data management system.

Hardware. We have achieved integration of and simultaneous synchronized control over multiple pieces of equipment (Figs. 1 and 2) common to the microfluidics community:
1. "n" TEC regulating units;
2. a chilled-water-bath recirculation system;
3. an eight-channel high-voltage power supply;
4. "n" liquid-flow monitors;
5. "n" multi-port valves;
6. "n" two-way switching valves;
7. eight negative/positive pressure lines for pneumatic valves;
8. six different pumps (spanning low- and high-flow rates);
9. an electronic shutter for a light source; and
10. a scientific CCD camera.

Packaging I. We have created a general package for loading microcapillaries with a six-port fluidic manifold containing internally integrated electrodes, two independent temperature control regions, and optical access to fluid (Fig. 3).

Packaging II. We have created a package for loading a standardized microfluidic chip with eight fluid ports, eight electrodes, two heating elements, eight temperature sensors, self-sealing fluidic interconnects, and an overall low-profile (< 5 mm) for optical access (Fig. 4).

Chip Layout. We have prepared guidelines for microfluidic chips with heaters, temperature sensors, and internal electrodes for fabrication from identified external foundries in glass or plastic (Fig. 5).
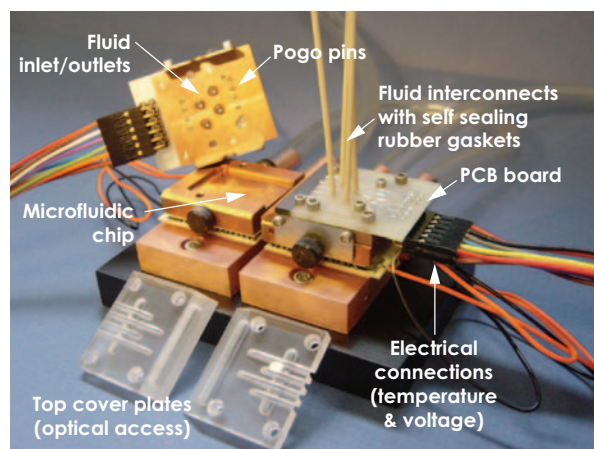

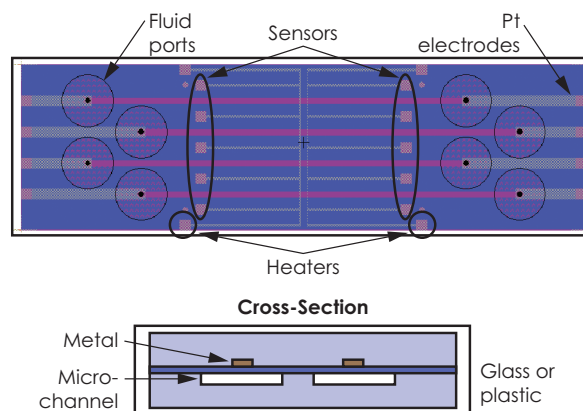**Figure 4.** Standard package for a multi-port microfluidic chip.

Figure 5. Drawing of a typical mask layout for a microfluidic chip.

High-Precision Multimode Ultrasonic Liquid Applicator

One of the core engineering competencies at LLNL is the precise fabrication of complex assemblies at the millimeter scale or smaller. The broader concept of mesoscale manufacturing—the fabrication of millimeter-scale assemblies using combinations of dissimilar materials, and having features on the micrometer or nanometer scale—has been identified as one of LLNL's key areas of enabling technology. To advance the state of the art in this area, we are reducing to practice novel approaches to the construction and assembly of increasingly more challenging objects.

Applications include the adhesive assembly of laser targets for the National Ignition Facility and other experiments (Fig. 1), and the application of biochemical solutions and other liquids to biosensors and microfluidic devices. These uses require the ultra-precise application of nanoliter or picoliter quantities of special liquids to specific locations.

Traditionally, the application of liquid adhesives to laser targets and other small objects is done manually, using single camel hairs as paintbrushes. We are using a new approach, a combination of commercially available specialty inkjet components, and custom-engineered hardware, to build new equipment that uses inkjet techniques to apply tiny droplets of different liquids to complex parts.

Project Goals

The project goals include the construction of two complete systems: one specialized for target fabrication, to be located in LLNL's target fabrication facilities, and a more general purpose system, to be located in LLNL's Microfabrication Laboratory.

Relevance to LLNL Mission

Mesoscale manufacturing is a core technology supporting LLNL missions in stockpile stewardship, high-energy-density physics, and national and homeland security. This project advances capabilities and tools for mesoscale manufacturing.

FY2005 Accomplishments and Results

The inkjet techniques used in this project are fundamentally the same as

Figure 1. Representation of an application of liquid adhesive: the adhesive joining of the hemispherical halves of laser targets for the National Ignition Facility.

Assembled hemispheres

Inkjet head
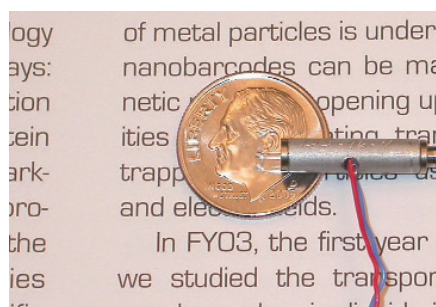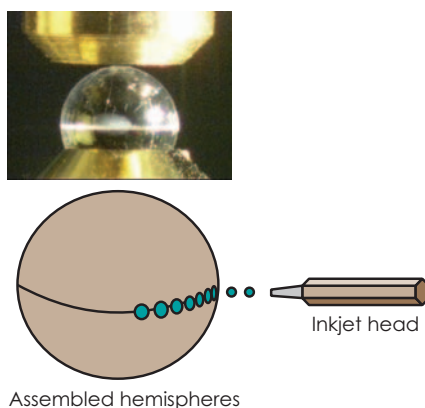
Figure 2. Typical inkjet device used in the project. The "business end" of the device is a tiny glass nozzle that generates droplets as small as 10 μm in diameter.

For more information contact
George M. Dougherty
(925) 423-3088
dougherty9@llnl.gov

those used to generate high-quality printed material. A typical inkjet device used in the project is shown in Fig. 2.

Tests were conducted to verify that the inkjet methods being considered are indeed capable of "printing" individual droplets of custom liquids such as low-viscosity adhesives. These tests involved deposition onto various substrate materials as well as bond lines between small plastic parts, and confirmed that the method would work. The droplets generated in this way are less than a quarter the width of a human hair. The results of one such test are shown in Fig. 3.

We then turned to two new systems at LLNL. For the target fabrication system, close cooperation with the target fabrication community was essential. Working with their engineers and technicians, a system was created that mates directly to the existing target assembly station, and can be attached and removed as required. The ultrasonic inkjet tip is located on a long probe that allows it to approach a small target being held within the vertical fixturing of the assembly station. A computerized motion controller manipulates the probe, and a special compact microscope mount allows the operator to view the deposition process.

The general-purpose system is similar in capability but very different in form. This system has an open geometry that allows excellent access to a wide range of substrates, and a 2-D computerized linear stage that enables either the precise placement of individual droplets or the large-area printing of complex patterns. The general-purpose system, installed in the Microfabrication Laboratory and available for use, is shown in Fig. 4.
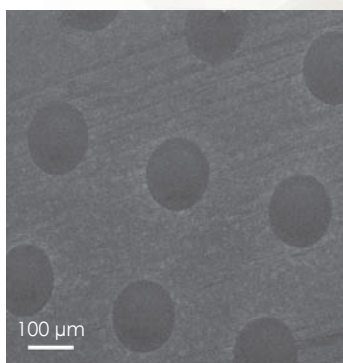
Figure 3. Scanning electron microscope image showing part of a large array of spots made by depositing individual droplets of low-viscosity adhesive onto a hydrophilic polished glass substrate.

Figure 4. General-purpose ultrasonic inkjet system in LLNL's Microfabrication Laboratory.

Scale-Up of the SLIP Process

A variety of applications require the use of nanoengineered surfaces for separation applications. The traditional approach of functionalization has two severe limitations: 1) the polymer used must be soluble; and 2) the solvent used must be removed from the final coating. The first limitation often eliminates many potential candidate polymers. The second limitation is influential on the transport and separation properties of the coating. These two issues can be overcome by the use of solventless vapor deposition followed by *in-situ* polymerization (SLIP).

Project Goals

Our goal was to create a roadmap for a scale-up of the SLIP process.

Relevance to LLNL Mission

A scaled-up SLIP process is critical to the growth of a membranes program within LLNL, providing vital resources to programs such as Energy and Environment, Defense and Nuclear Technologies, and NAI.

FY2005 Accomplishments and Results

The SLIP system is shown in Fig. 1. The SLIP process offers the capability to deposit and polymerize films of high-temperature polymers that are prepared using a condensation mechanism (as compared to a free radical type of polymerization). This includes high-temperature and high-performance polymers such as polyimides, nylons, polybenzimidazoles, and polybenzoxazoles.

Polyimide films that range in thickness from 50 to 400 nm were deposited onto a range of substrates. These substrates include polymers such as polycarbonate, Teflon AF, nylon, and silicone, as well as inorganics such as silicon wafers and glass. Excellent adhesion was observed in all cases.
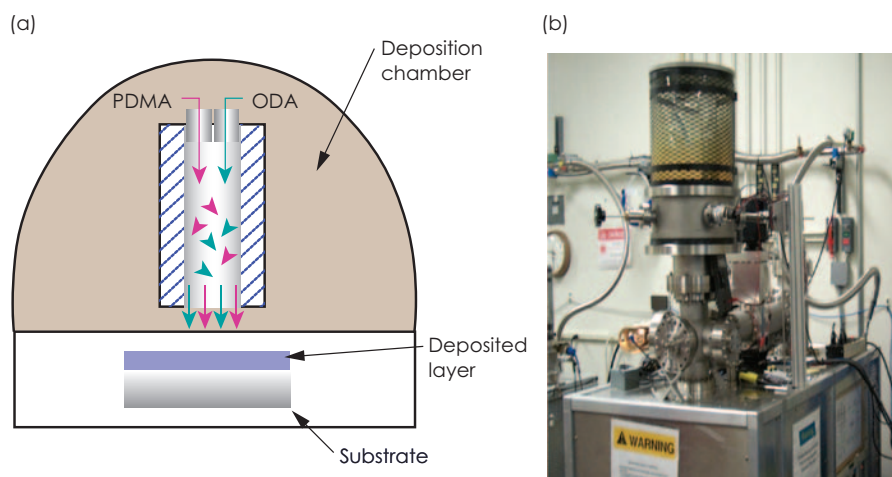
Figure 1. (a) Schematic of SLIP process; (b) photograph of benchtop SLIP deposition system.

For more information contact
Kevin C. O'Brien
(925) 422-7782
obrien14@llnl.gov

We also evaluated the economic viability of the SLIP process to determine whether the scaled-up process was economically attractive. Calculations were made using different values for parameters such as transit distance, width of web, and required thickness. Other factors that effect process economics are deposition pressure, and blocking, which refers to the ease of handling the coated web. Results show that the process is economically feasible at specified coating rates.

Based on our studies, we produced a preliminary configuration for a pilot-scaled SLIP coater (Fig. 2). An equipment vendor was identified and assisted in the production of a pilot-scale system that would be capable of coating fiber at a rate of approximately 200 km/day.

Risks can be reduced significantly by producing a prototype system that simulates the pilot scale system. We have created a prototype system that can be used to apply SLIP coatings to small-scale samples of fibers and films. This system was used to apply SLIP coatings to porous polypropylene substrates (see Fig. 3).

The SLIP process has been shown to be robust, and plans are in place to scale-up the process. This scale-up would enable the coating of flat sheets and fibers.

FY2006 Proposed Work

Future work involves additional tests using the prototype system. Once validated the pilot system will be constructed.

Take-up roll with coated fibers | Coating area | Feed roll with uncoated fibers
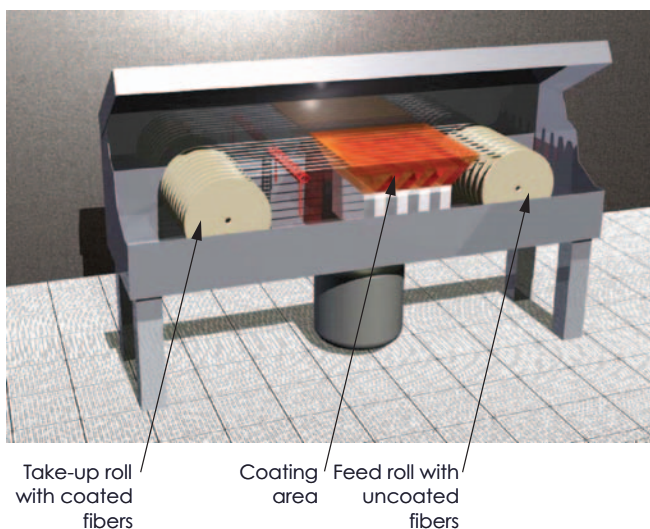
Figure 2. Preliminary configuration for pilot-scale SLIP coater. The system is shown with the top cover raised.
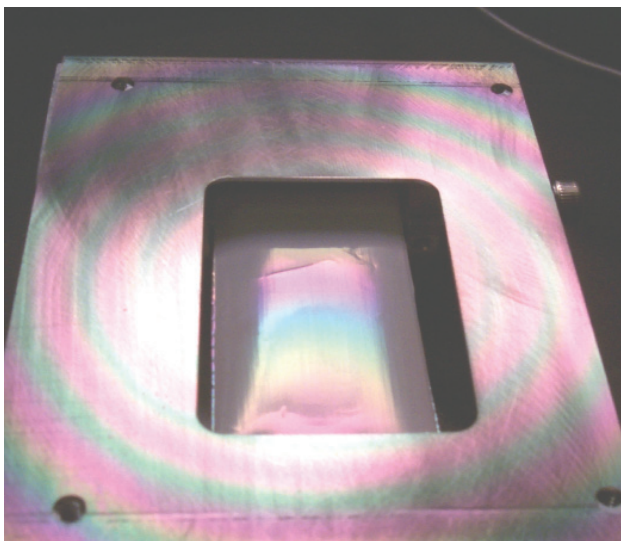
Figure 3. Close-up of coated substrate in prototype coater.

Silicon-Deposition Process Implementation

The deposition of silicon layers is one of the key steps in the fabrication of microelectronics, microsensor devices, and micro-electromechanical systems (MEMS). As the technology of microfabrication (and now nanofabrication) advances, silicon continues to be a key material, and more advanced systems for depositing silicon are needed to keep pace. In addition to the needs for ever-increasing layer quality and uniformity, modern equipment must be able to deposit such layers on wafers of ever larger size.

This project involved the installation and testing of a new high performance system for silicon layer deposition, as well as the engineering of the layer deposition process itself in order to tune the system to produce the high-quality films required by

current research. The system is a Thermco low-pressure chemical vapor deposition (LPCVD) system. LPCVD is the process used by large-scale, high-reliability production semiconductor fabrication facilities. Based on the thermally-induced decomposition of a reactive silicon-bearing source gas such as silane (SiH_4), this process yields very high quality films that are deposited conformally over the substrate wafers with minimal variation in thickness or microstructure.

The process development effort has resulted in process recipes for both undoped (electrically insulating) and phosphorus-doped (electrically conductive) layers. The process characterization involved the measurement and adjustment of such parameters as deposition rate,
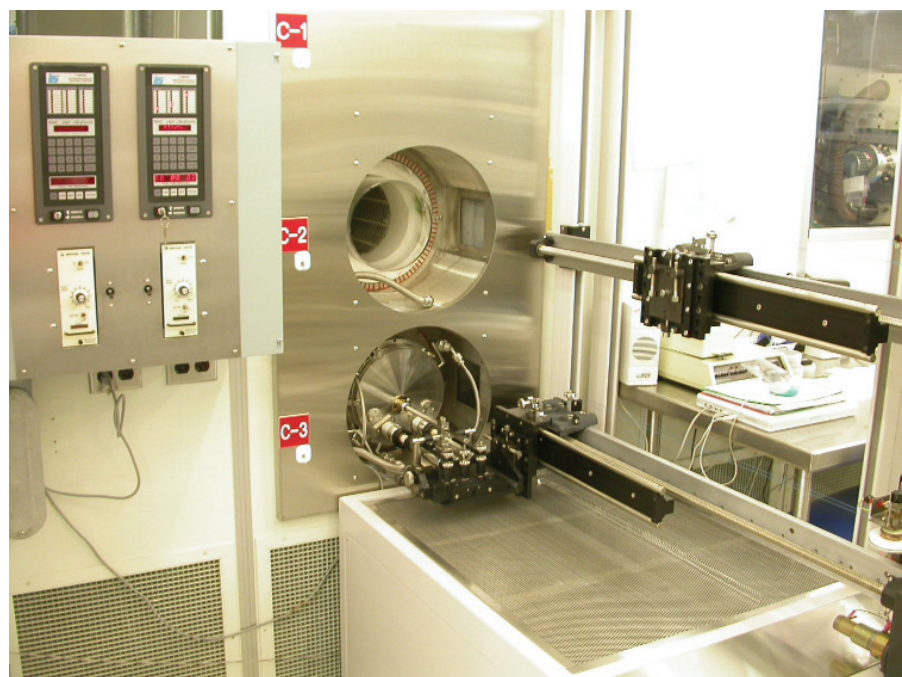
Figure 1. The new Thermco LPCVD silicon-deposition system installed in LLNL's Micro-fabrication Laboratory. The silicon system is located in the lower unit. The upper unit allows for a comparably upgraded silicon-nitride-deposition capability in the future.

For more information contact
George M. Dougherty
(925) 423-3088
dougherty9@llnl.gov

uniformity, film conductivity, and residual stress. Now ready for use, the system allows the deposition of high-quality silicon layers on all types of substrates up to 6 in. in diameter.

Project Goals

The goal of this project was to complete the installation and testing of the new LPCVD silicon-deposition system (Figs. 1 and 2). This includes the implementation and characterization of new process recipes that can be used to deposit the different types of films required for different types of microfabricated devices.

Relevance to LLNL Mission

The availability of a new, state-of-the-art silicon-deposition capability is a boost to the core microfabrication capabilities at LLNL, which serve both internal and external customers.

FY2005 Accomplishments and Results

The installation of the system was completed, including connections to electrical and mechanical utilities in the facility; the modification of gas-handling manifolds and other interface hardware; and the plumbing of specialty gas lines to provide the SiH_4 and phosphine (PH_3) source gases used for silicon deposition. Process recipes were written and tested, and characterization of the resulting films was used to fine-tune the recipes.

Characterization included film thickness and deposition rate, residual film stress, and electrical conductivity. The control of residual stresses in the deposited films is very important for MEMS and other mechanical devices, and the measurement of residual stress also provides information about the microscale structure of the deposited silicon layers. Electrical conductivity is important in the case of doped films, in which atoms from a secondary source (such as PH_3) are incorporated to allow electrons to flow through the silicon. Doped films are required for the fabrication of a great many types of silicon sensors and actuators, as well as microscale heaters and some types of microelectronic devices.

As a result of this project, the Microfabrication Laboratory and its customers now enjoy the capability to deposit both undoped (resistive) and phosphorous-doped (conductive) silicon films for a wide range of applications.
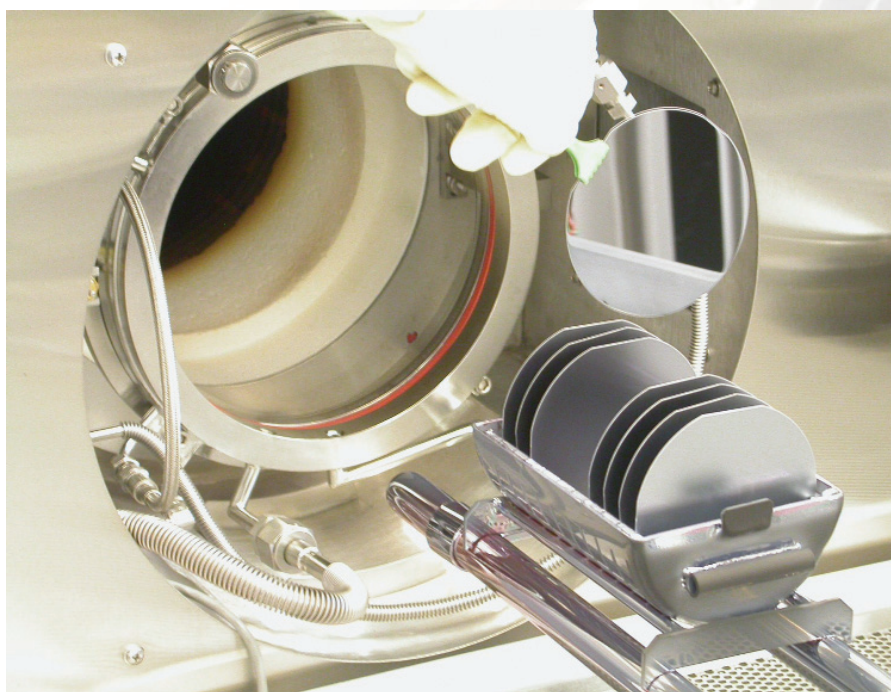
Figure 2. Close-up of the LPCVD silicon-deposition system. This modern system allows us to deposit high-quality doped and undoped silicon films on 4- or 6-in. wafers.

Characterization and Integration of New Patterned Nanostructure Deposition Cluster Tool

The purpose of this project is to provide support of a new capability being brought to LLNL in support of multiple programs. The new capability is a unique physical vapor deposition tool to address the generation and integration of advanced initiation system components and to fabricate membranes for gas and liquid separation applications for carbon management and water purification efforts, respectively.

Project Goals

This is the first year of a three-year project to support a state-of-the-art DC-pulsed magnetron cluster tool for the fabrication of low-volume, high-energy-density nanostructure components. Current component fabrication methods have limitations in mask alignment, source performance, film stoichiometry, and defect repeatability. These limitations affect component miniaturization and yield. Our goal is to overcome the limitations, and apply our multifaceted engineering expertise through designing, modeling, and characterizing critical process equipment for the fabrication and integration of nanostructure components with energy densities 10 to 100 x greater than what is currently available.

Relevance to LLNL Mission

The first deposition technology will be a cluster that has a reactive sputter process. In addition, this cluster will allow the deposition to occur through precisely placed shadow masks. This technology combination enables LLNL to build electrical components and circuitry without resorting to photolithographic processes. The cluster can then be used for advanced initiation system technologies with high-energy electrical components. These next-generation systems will have greater safety and reliability. Further miniaturization of components and development of high-energy circuitry with the cluster tool is crucial to meet volume constraints and cost goals. Since the tool can produce nano-layered oxides, materials research opportunities are also opened in the areas of superconductors, high-powered laser coatings, and catalysts.
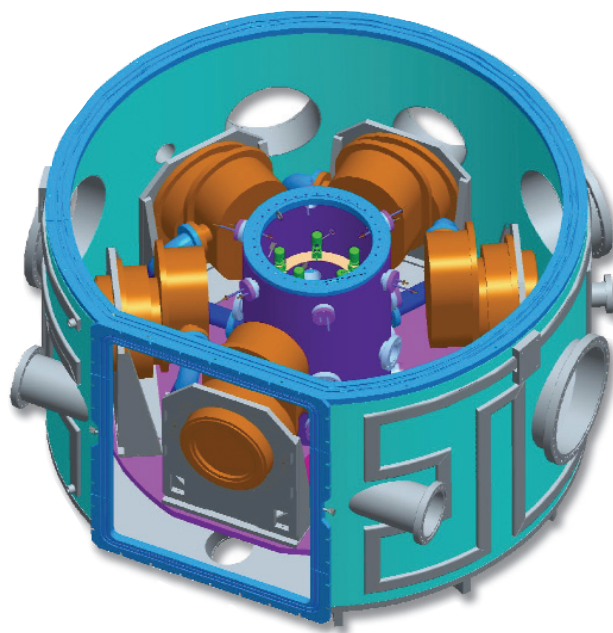

Figure 1. Isometric view of the main process chamber.

For more information contact
Mark A. Schmidt
(925) 422-9118
schmidt15@llnl.gov

FY2005 Accomplishments and Results

Accomplishments to date have included the design of the main chamber (Fig. 1); enhanced design of the robotic sampling transport system, as well as the shadow mask; contract award for a high-density plasma source tailored to our applications; and contract award of the substrate system required to make high-energy-density components.

As part of the design of a sputtering tool for physical vapor deposition, it is necessary to obtain uniform reactive gas concentrations across the deposition surface to maintain film stoichiometry. Using Star-CD, we created a computational fluid dynamics (CFD) model of the surface and reactive gas injection ring to gain an understanding of the flow mechanics.

One question facing us was whether the inlet flow would come in the form of a jet from the nozzles or a stream that quickly dispersed once it entered the chamber. Based on the assumption of a constant mass flow, Star showed that at higher pressures (between 0.25 and 1 ATM), the stream enters the chamber and maintains coherence. This can be seen by the velocity of the inlet gas in Fig. 2. In this case, the stream slowly entrains the gas around it until it collides with the other inlet streams at the middle of the chuck. At lower pressures (between 0.0010 and 0.0625 ATM), however, the stream cannot maintain its coherence, as seen in Figs. 3 and 4. Here, with such low pressures around it, the stream is quickly pulled apart and disperses throughout the chamber.

Chief amongst the questions left unresolved is that of the molecular concentration of oxygen at the deposition surface. With its continuum assumption, Star was not able to get to low enough pressures to discern the appreciable density differences that must occur within the deposition chamber.

Thus, future modeling of the physical vapor deposition apparatus needs to account for the transition regime between the continuum approximation and rarified gases. The most likely candidate for such modeling is a direct simulation Monte Carlo (DSMC) code.

FY2006 Proposed Work

The goal for FY2006 is to test and characterize a new high density plasma source for producing reactive films with higher packing densities at increased deposition rates than current sputtering methods. Efforts will also include managing the integration and installation of the tool into a new cleanroom.
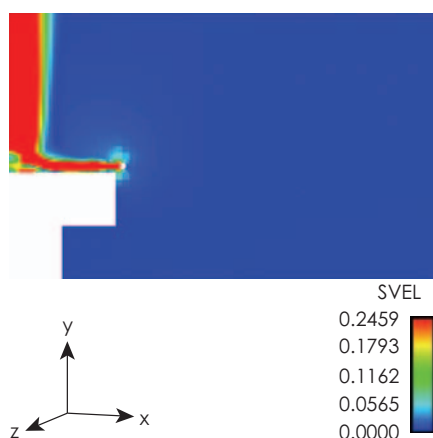
Figure 2. The stream at 1 ATM (760 Torr): the stream into the chamber maintains its coherence, as seen by the velocity profile of this radial slice of the model at the inlet.
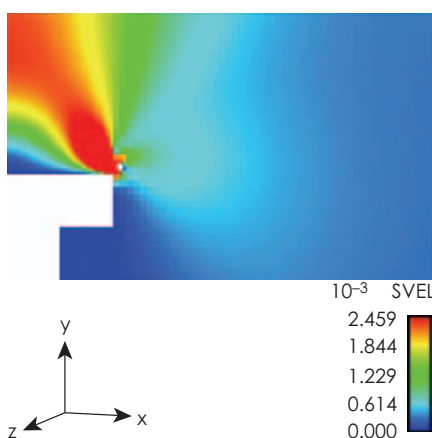
Figure 3. The stream at 0.001 ATM (0.760 Torr): the stream quickly begins to disperse throughout the chamber, as seen by the velocity profile of this radial slice of the model at the inlet.
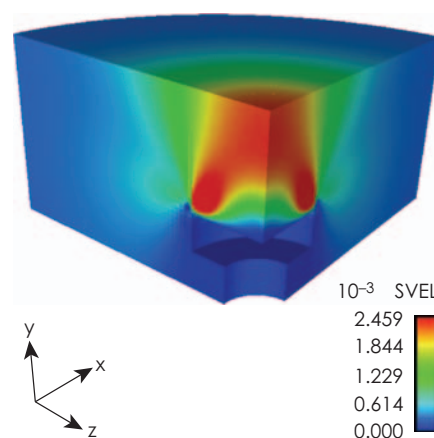
Figure 4. Three-dimensional map of the reactive gas velocities at 0.001 ATM (0.760 Torr).

Sensors to Knowledge
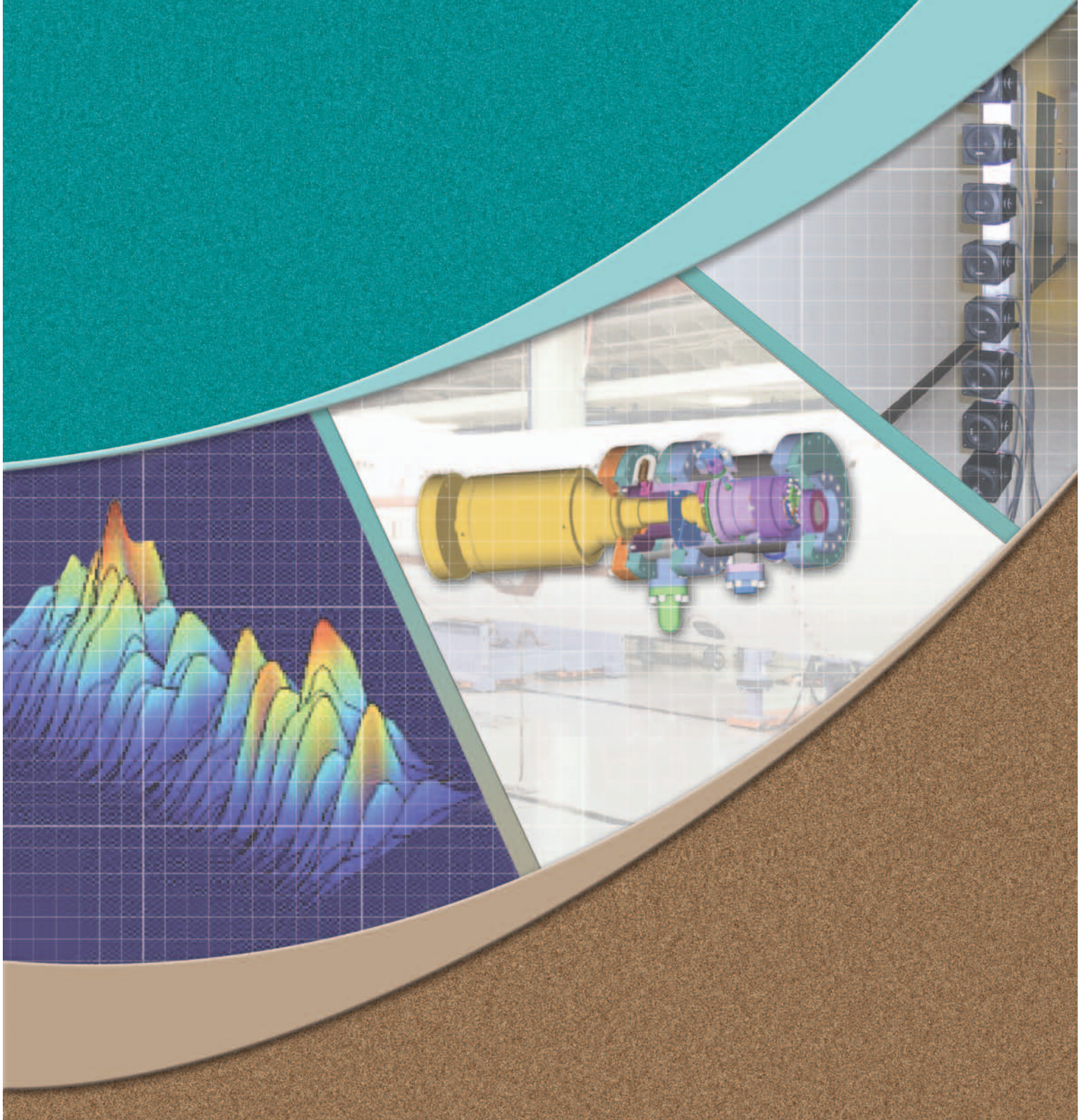
Dynamic Data-Driven Event Reconstruction for Atmospheric Releases

The role of an event-reconstruction capability in a case of an atmospheric release is to characterize the source by answering the critical questions: How much material was released? When? Where? What are the potential consequences? Accurate estimation of the source term is essential to accurately predict plume dispersion, effectively manage emergency response, and mitigate consequences. We are developing a capability that seamlessly integrates observational data streams with predictive models to provide probabilistic estimates of unknown source term parameters consistent with both data and model predictions. Our approach uses Bayesian inference with stochastic sampling with Markov Chain Monte Carlo (MCMC) and Sequential Monte Carlo (SMC) methodology.

Project Goals

We are developing a flexible and adaptable data-driven event-reconstruction capability that provides 1) quantitative probabilistic estimates of principal source-term parameters such as the time-varying release rate and location; 2) predictions of increasing fidelity as an event progresses and additional data become available; and 3) analysis tools for sensor network design and uncertainty studies. Our computational framework incorporates multiple stochastic algorithms, operates with a range and variety of atmospheric models, and runs on multiple computer platforms, from workstations to large-scale computing resources. Our final goal is a multi-resolution capability for both real-time operational response and high-fidelity multiscale applications.

Relevance to LLNL Mission

This project addresses a critical need for tools to support the rapidly growing number of operational detection, warning, and incident characterization systems being developed and deployed by the Department of Homeland Security (DHS) and DOE. Our event-reconstruction and sensor-siting tools are targeted for integration into the next-generation National Atmospheric Release Advisory Center (NARAC) and DHS's new Interagency Modeling and Atmospheric Analysis Center, based at LLNL.

FY2005 Accomplishments and Results

In FY2005, we accomplished the following:

1. demonstrated efficiency and robustness of MCMC capability with the NARAC 3-D Lagrangian particle dispersion model LODI, using concentration measurements from a ~10 km-scale tracer field experiment;
2. developed a hybrid MCMC-SMC methodology and demonstrated its effectiveness in characterizing releases from complex, multiple sources;
3. used optimization methods to develop a prototype sensor network design tool;
4. implemented a computational fluid dynamics model for the simulation

For more information contact
Branko Kosovic
(925) 424-4573
kosovic1@llnl.gov

of urban dispersion into the MCMC capability and tested it using data from the Oklahoma City Joint Urban 2003 experiment;

5. developed a computational framework including MCMC, SMC, and hybrid algorithms on massively-parallel platforms;

6. explored methods for incorporating alternative input data types; and

7. significantly enhanced performance on massively-parallel platforms for efficient event reconstruction of complex atmospheric releases.

The figure shows sample results.

Related References

1. Chow, T., B. Kosovic, and S. Chan, "Source Inversion for Contaminant Plume Dispersion in Urban Environments Using Building-Resolving Simulations," *Ninth Annual George Mason University Conference on Atmospheric Transport and Dispersion Modeling,* July 18-20, 2005.

2. Kosovic, B., G. Sugiyama, S. Chan, F. Chow, K. Dyer, R. Glaser, W. Hanley, G. Johannesson, S. Larsen, G. Loosmore, J. Lundquist, A. Mirin, J. Nitao, R. Serban, and C. Tong, "Stochastic Source Inversion Methodology and Optimal Sensor Network Design," *Ninth Annual George Mason University Conference on Atmospheric Transport and Dispersion Modeling,* July 18-20, 2005.

3. Kosovic, B., G. Sugiyama, K. Dyer, W. Hanley, G. Johannesson, S. Larsen, G. Loosmore, J. K. Lundquist, A. Mirin, J. Nitao, and R. Serban, "Dynamic Data-Driven Event Reconstruction for Atmospheric Releases," *Second Sandia Workshop on Large-Scale PDE-Constrained Optimization*, Santa Fe, New Mexico, May 19-21, 2004.

4. Kosovic, B., G. Sugiyama, K. Dyer, W. Hanley, G. Johannesson, S. Larsen, G. Loosmore, J. K. Lundquist, A. Mirin, J. Nitao, and R. Serban, "Dynamic Data-Driven Event Reconstruction for Atmospheric Releases," *Eighth Annual George Mason University Transport and Dispersion Modeling Conference*, Fairfax, Virginia, July 13-15, 2004.

5. Johannesson, G. and W. Hanley, "Sequential Monte Carlo Approach to Dynamic Data-Driven Event Reconstruction for Atmospheric Releases," *Joint Statistical Meetings*, Minneapolis, Minnesota, August 2005.

FY2006 Proposed Work

In FY2006 we will:

1. extend the event-reconstruction capability to handle complex continental-scale atmospheric releases;

2. implement quantification procedures for data, input parameters, and internal model error, into the computational framework;

3. implement a multi-resolution capability for more efficient source characterization;

4. continue developing and testing efficient stochastic sampling and convergence algorithms;

5. demonstrate methods for incorporating alternative input data types; and

6. continue performance enhancement of the computational framework on the range of platforms for efficient event reconstruction of complex atmospheric releases.
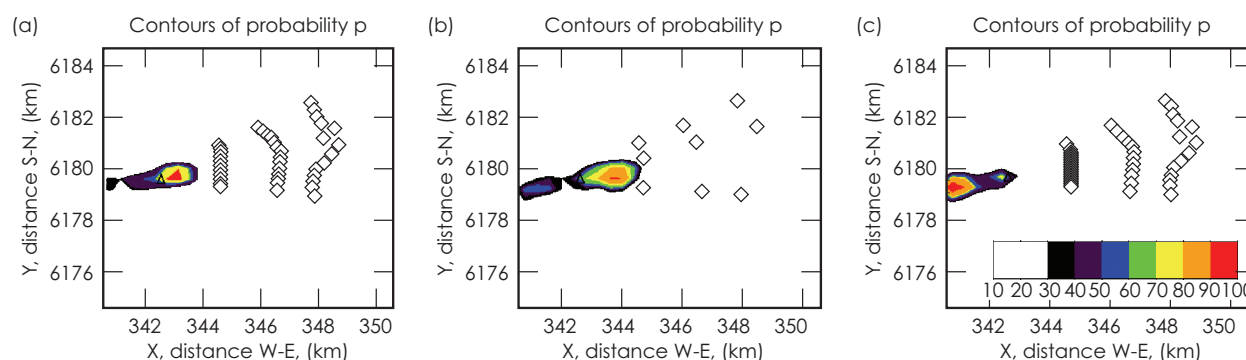
Sample results using data from Copenhagen tracer field experiment. Color contours represent probability distribution of source location. The actual source is denoted with a triangle; the sensors are denoted with diamonds. (a) Event reconstruction using data from all 51 sensors; (b) source characterization based on data from only nine sensors; (c) results obtained using all 51 sensors, of which 30% were broken in some way. The effect of inaccurate data is evident through the bias in the solution; however, the robustness of the methodology is demonstrated.

Space-Time Secure Communications for Hostile Environments

Communicating in a complex environment is a difficult problem in situations like a hostile urban setting populated with a multitude of buildings and vehicles, or a maze of tunnels and caves. This project uses multichannel time-reversal (T/R) processing techniques to communicate in a highly reverberative environment.

For our final year, we focused our attention on 1) wideband acoustic communications using a time reference modulation technique; and 2) multichannel communications in a tunnel (or cave or pipe) with many obstructions, multipath returns, severe background noise, disturbances, long (~180 ft) propagation paths with disruptions (bends). For this environment, we showed that multichannel T/R receivers can be extended to the wideband designs while demonstrating their performance in both the "canonical" stairwell of our previous work as well as a tunnel-like structure.

Acoustic information signals are transmitted with an eight-element host or base station array to two client receivers with a significant loss in signal levels due to the hostile environment. In this project, the results of the new wideband T/R processor and modulation scheme demonstrate the overall performance of both high (24-bit) and low (1-bit) bit level analog-to-digital (A/D) converter designs. We validated these results by performing proof-of-principle acoustic communications experiments in air, showing that T/R receivers are capable of extracting the transmitted coded sequence from noisy microphone array measurements with zero-bit error.

The multichannel communications problems we solve using wave propagation physics are shown in Fig. 1, where we see that the host or base array transmits its coded information along different and unique paths to each client receiver.

Project Goals

Successful implementation and demonstration of T/R receiver performance will lead to the next generation advance for military and defense applications, as well as potential commercialization. Ultimately, our success will provide improved communications in noisy, distorted environments, with a potential breakthrough technology for both military and civilian (commercial) applications. This proposal is aimed at developing a core competency in wireless
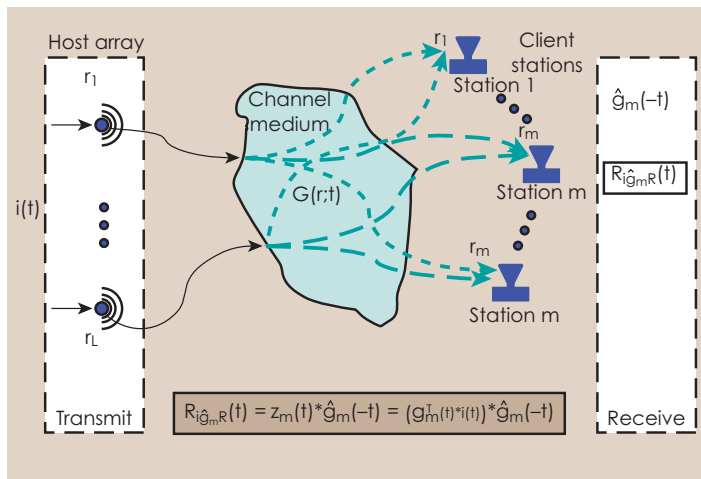
Figure 1. Basic communications environment, including the host T/R, hostile medium, the corresponding unique sets of Green's functions, and T/R pairs from host array to client receiver stations.

$$R_{i\hat{g}_m R}(t) = z_m(t) * \hat{g}_m(-t) = (g_m^T(t) * i(t)) * \hat{g}_m(-t)$$

For more information contact
James Candy
(925) 422-8675
candy1@llnl.gov

communication networks, and falls within the advanced sensor and instrumentation competency area.

Relevance to LLNL Mission

Both the maintenance of communications in a strong multipath environment, and the protection of the communication against intercept, are important to LLNL. Thus, there is a strong need for reliable channels in corrupting environments, with the additional feature that they be secure. Secure communications can be derived from T/R principles that will lead to novel applications, ranging from military applications (such as battlefield communications, urban warfare, tunnel complexes, and pipes) to the hostile urban environment. The T/R receiver technology also promotes protection of communication channels against intercept, and thus supports LLNL's national security mission as well as homeland defense applications.

FY2005 Accomplishments and Results

Our FY2005 accomplishments included:
1. development of multichannel theory for T/R communications;
2. implementation of new wideband T/R modulation scheme;
3. performance of controlled acoustic experiments in various environments;
4. demonstration of T/R performance;
5. investigation of experimental design for EM hardware; and
6. initiation of hardware design for FPGA technology.

The experimental set-up in the tunnel-like structure is shown in Fig. 2, with all of its bends, pipes, blind corners and multitude of reflectors, creating an extremely hostile acoustic communication environment for T/R receiver performance analysis.

We have obtained results for one-receiver performance in this environment, for both a 24-bit and a 1-bit receiver design. We have noted a degradation going from 24- to 1-bit A/D conversion.

Related References

1. Candy, J., A. Poggio, D. Chambers, B. Guidry, C. Robbins, and C. Kent, "Multichannel Time Reversal Processing for Acoustic Communications in a Highly Reverberant Environment," *Journal of the Acoustical Society of America,* **118**, 4, pp. 2339-2354, 2005.
2. Candy, J., A. Meyer, A. Poggio, and B. Guidry, "Time Reversal Processing for an Acoustics Communications Experiment in a Highly Reverberant Environment," *Journal of the Acoustical Society of America,* **115**, pp. 1621-1631, 2004.
3. Chambers, D. H., J. V. Candy, S. K. Lehman, J. S. Kallman, A. J. Poggio, and A. Meyer, "Time Reversal and the Spatial-Temporal Matched Filter," *Journal of the Acoustical Society of America,* **116**, pp. 1348-1350, 2004.
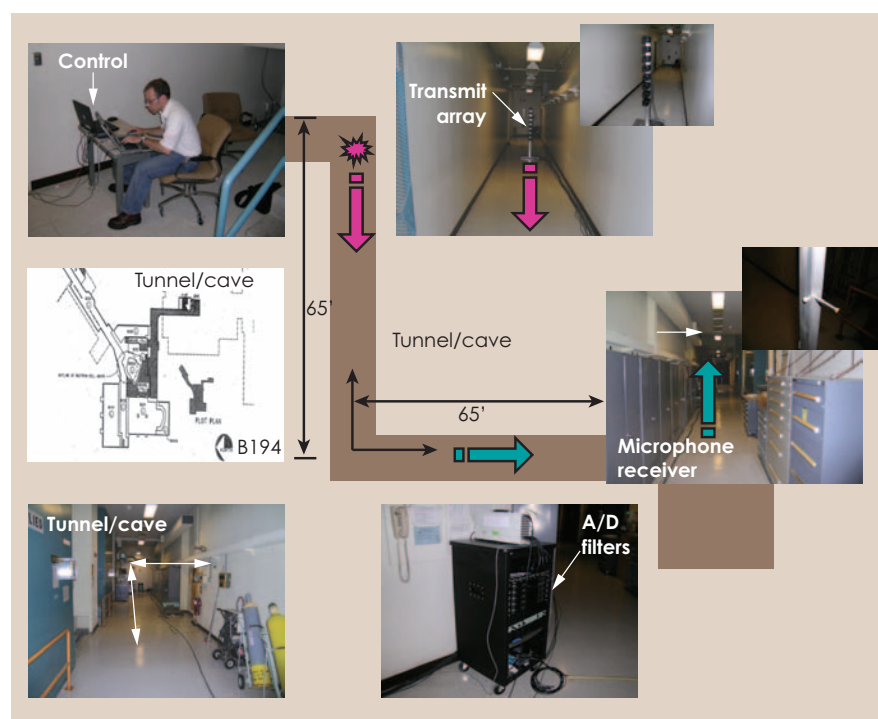
Figure 2. The experimental and environment set-up in a tunnel-like structure, with bends, pipes, blind corners and multitude of reflectors. Note that a schematic map demonstrates the tunnel communications path, with the client receiver approximately 180 ft away.

Experimental Verification of Correlation-Based Wavefront Sensing

This project has explored the use of a correlation-based algorithm for wavefront sensing in a wide range of scenarios. Wavefront sensing is a technique by which the phase aberration (or, more typically, its gradient) is measured in an optical system. These measurements can be used in real time in an adaptive optics (AO) system to reduce the residual error and improve performance. In the case of an imaging system, the wavefront sensor (WFS) measurements can also be used in a postprocessing scheme.

In our first year, we showed the benefits of correlation in AO systems that used a point source that was either noisy or suffered from distortion. We also did initial experimental tests of correlation-based wavefront sensing in the remote-imaging scenario. In that case, no point source (such as a laser) is available for the WFS and instead the target itself is used. We established baseline requirements for SNRs and scene content. Such remote imaging is done in difficult conditions; the

atmosphere along short horizontal or slant paths greatly reduces image quality. Scene-based wavefront sensing (so termed because of the use of the scene that is observed) could facilitate either real-time AO or improved image-processing techniques for surveillance applications.

Project Goals

In FY2005 our goal was to determine how a scene-based WFS can be used in a remote-imaging system to lead to improved imaging performance. We investigated the use of the scene-based WFS information in a range of established methods, including AO and the postprocessing techniques of speckle imaging and deconvolution.

Relevance to LLNL Mission

AO is an area of expertise at LLNL. This project will further extend LLNL capabilities in AO applications. Remote imaging is an important area for national security applications.

| 0 m | 40 m | 100 m | 150 m |
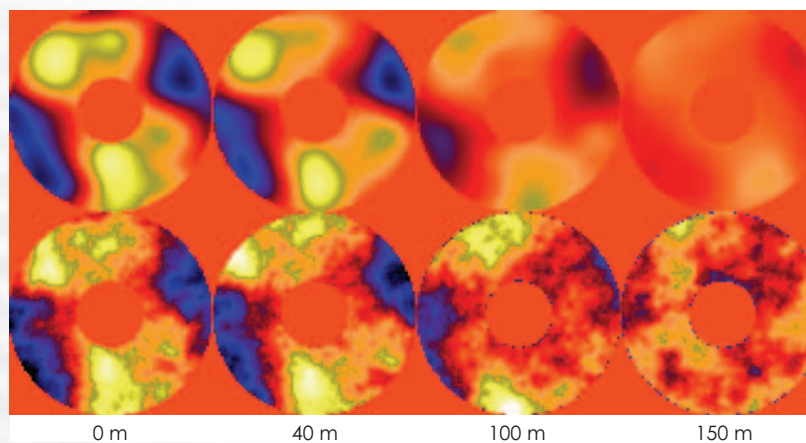
Figure 1. Reconstructed phases from scene-based WFS in wave-optics simulation along 200-m path. Top row: reconstruction. Bottom row: true phase. The turbulence is at the indicated distance from the telescope pupil.

For more information contact
Lisa A. Poyneer
(925) 423-3360
poyneer1@llnl.gov

FY2005 Accomplishments and Results

It is necessary to verify that under distributed turbulence, the WFS measures the correct phase. Our wave-optics simulations have allowed us to determine that as the turbulence moves farther from the pupil, the aniso-planatism in the scene itself reduces both the resolution and the gain of the WFS measurement of the phase. Figure 1 shows phase reconstructions as the turbulence moves back from the pupil on a 200-m path.

Even with correct phase information, AO is limited, due to its use of phase conjugation. A single-mirror AO system will produce a small region of correction on-axis or a larger field with a low level of correction. A multi-mirror system has the potential to provide a wider field, but at significant complexity and cost. Instead, postprocessing techniques that provide much wider fields should be used.

As a baseline for postprocessing techniques, we consider the speckle-imaging technique, established for the remote-imaging scenario. This technique uses a series of short-exposure images for the average phase aberration. We augment this technique by using more detailed atmospheric information as obtained from the scene-based wavefront sensing. This extra information allows speckle to not depend on a model, and allows operation with fewer frames and in non-typical conditions.

The second technique for post-processing is deconvolution with WFS data. This is an established image-processing technique that undoes the convolution of the object with the optical transfer function, which blurs the image. Simulations show that even low-order WFS measurements can lead to good deconvolutions. Deconvolution performance is comparable to speckle performance when accurate information about the PSF across the field is used.

We tested this approach in our experimental telescope set-up and verified that a scene can provide accurate phase information and significantly improve image quality. We observed on a 75-m horizontal path over asphalt and took twelve 1-ms exposures. Figure 2 shows a portion of a WFS CCD image with the shamrock used as the scene. Figure 3 shows the shift-and-add image of the nearby resolution target and the restored image, after deconvolution with the WFS information.

Related References

1. Poyneer, L. A., D. W. Palmer, K. N. LaFortune, and B. Bauman, "Experimental Results for Correlation-Based Wavefront Sensing," Invited Paper, *Proc. SPIE 5894, Advanced Wavefront Control: Methods, Devices, and Applications III*, M. T. Gruneisen, J. D. Gonglewski, and M. K. Giles, Eds., pp. 58940N 2005.
2. Poyneer, L. A., "Scene-Based Shack-Hartmann Wavefront Sensing: Analysis and Simulation," *Appl. Op.*, **42**, pp. 5807-5815, 2003.
3. Poyneer, L. A., K. LaFortune, and C. Chan, "Scene-Based Wavefront Sensing for Remote Imaging," *Proc. SPIE 5162, Advanced Wavefront Control: Methods, Devices, and Applications*, J. D. Gonglewski, M. A. Vorontsov, and M. T. Gruneisen, Eds., pp. 91-102, 2003.
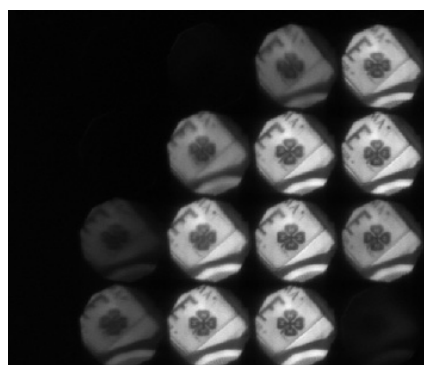
Figure 2. Portion of WFS CCD image from experiment. The shamrock is successfully used for scene-based wavefront sensing.

Figure 3. Left: shift-and-add image of resolution target near the shamrock. Right: image deconvolved with scene-based WFS data. This technique improves target contrast and resolution.

Geo-Location in Harsh Environments

Localization of radio devices operating in indoor channels is a daunting task due to the presence of severe multipath and low probability of a line-of-sight (LOS) signal between the transmitter and receiver. This harsh propagation environment for radio signals results from the shadowing and reflections from walls and objects in such channels.

We have built a set of high-accuracy indoor ranging devices using ultra-wideband (UWB) RF signals. UWB radios are particularly suited to ranging because of their short-duration (high-bandwidth) pulses. Our ranging and positioning techniques directly address some known challenges in UWB localization. A single distance measurement is gathered from repeated range measurements across a channel, and distance measurements from many locations surrounding the target are combined in a way that minimizes the range biases associated with indirect flight paths and through-wall propagation delays.

Project Goals

Our goals are to build UWB radios to collect range measurements suited for positioning; implement the signal processing necessary to recover pulses in highly reverberant environments; and execute an experimental plan to document the signal-to-noise ratio (SNR), resolution, and accuracy of the system.

Figures 1 and 2 show the hardware and the ranging routine of our system. The remote unit receives the request stream and responds with its own uniquely encoded reply pulse stream. The tracking unit receives and time-stamps the reply to find elapsed round-trip travel time, and thus distance.
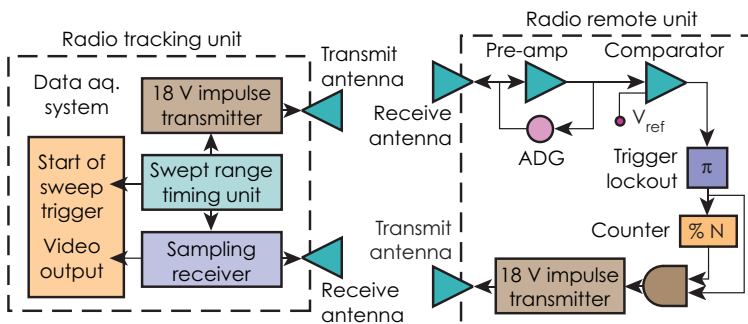
Figure 1. Block diagram of the round-trip TOF ranging pair, consisting of two units. The radio tracking unit sends a pulse to the remote unit, which replies with its own pulse. The main unit records the total round-trip TOF to extract the distance between the units.
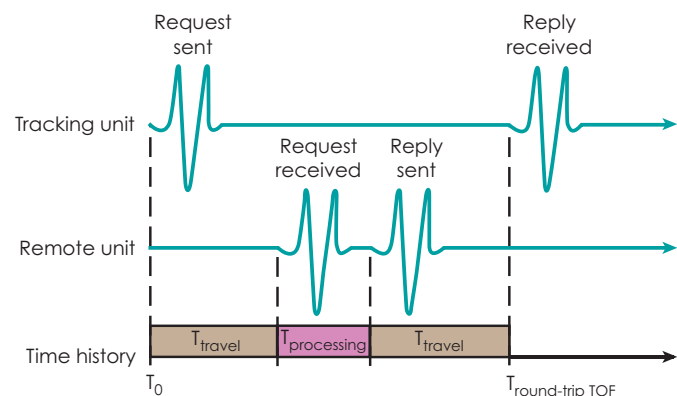
Figure 2. The round-trip TOF, consisting of travel time to and from the remote unit (approximately equal) and time spent in processing at the remote location (a known value we can subtract out). Distance between the tracking and remote units can then be calculated.

For more information contact
Claudia Kent Hertzog
(925) 424-3043
hertzog3@llnl.gov

Relevance to LLNL Mission

Several LLNL programs have an interest in the high strategic potential of urban tracking. Applications for a high-accuracy system for use in complex, urban environments is growing, and LLNL's established technology in MIR UWB radios allows us to be at the cutting edge of this technology.

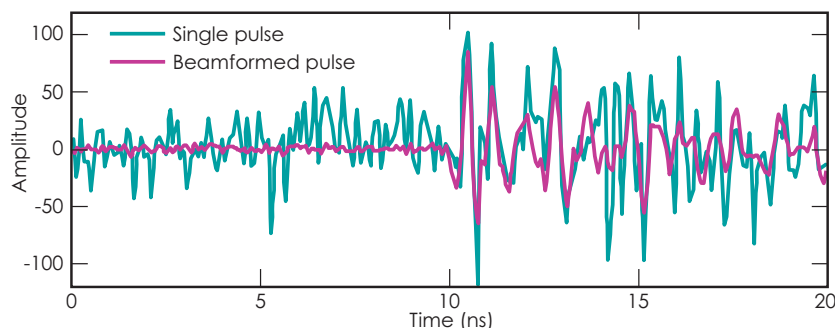## FY2005 Accomplishments and Results

We set up several scenarios to test the performance of the time-of-flight (TOF) ranging radios in three areas: SNR gain using beam-formed signals across a channel; resolution of the beam-formed measurement; and absolute accuracy of a measurement obstructed by several types of walls. To date, we have built, tested, and documented performance of the ranging radios meeting all of our expected goals. We tested the ranging performance in several harsh environments.

Ranging accuracy depends heavily on being able to resolve the exact arrival time of the incoming signals. In harsh ranging environments, signals are forced to travel though walls or around corners along a non-line-of-sight (NLOS) transmission channel. Our approach is to combine multiple repetitions of the transmission into a single beam-formed signal. Figure 3 compares a single NLOS range measurement in a volcanic rock cave with a beam-formed range collection under the same conditions. Combining 100 copies of the same range measurement gives back 17 dB of the lost SNR.

With the radios in LOS as well NLOS environments, repeated measurements fall within a standard deviation of less than 0.5 in. by thresholding a ratio of short- to long-term amplitude to find the peak arrival time.

UWB range measurement residual errors from several distances in a clear LOS show our ability to measure range distance within 1.5 in. of the actual value. Through a sheet-rock wall we can measure range distance within several inches of the actual value, and behind a concrete wall we can measure range distance within a foot.

Related References

1. Gezici, S., *et al.*, "Localization Via Ultra-Wideband Radios: A Look at Positioning Aspects for Future Sensor Networks," *IEEE Signal Processing Magazine,* **22**, 4, pp. 70-84, 2005.
2. Young, D., *et al.*, "Ultra-wideband (UWB) Transmitter Location Using Time Difference of Arrival (TDOA) Techniques," *Conference Record of the Thirty-Seventh Asilomar Conference on Signals, Systems and Computers,* 2003.
3. Jourdan, D., *et al.*, "Monte Carlo Localization in Dense Multipath Environments Using UWB Ranging," *Proceedings of the IEEE Conference on UWB,* Zurich, Switzerland, 2005.
4. Lee, J., and A. Scholtz, "Ranging in a Dense Multipath Environment Using an UWB Radio Link," *IEEE Journal on Selected Areas in Communications,* **20**, 9, pp. 1677-1683, 2002.
5. Smith, J., and J. Abel, "Closed-Form Least-Squares Source Location Estimation from Range-Difference Measurement," *IEEE Transactions of Acoustics, Speech, and Signal Processing,* **ASSP-35**, 12, 1987.

FY2006 Proposed Work

For FY2006 we have proposed The Urban Tracking and Positioning System to be a high-resolution (~1-ft accuracy) urban tracking demonstration system, similar to GPS but suitable for indoor use in urban combat scenarios: buildings, city streets, and caves. Together with proven technologies from past years, this system can provide a packaged, real-time, high-resolution, urban tracking demonstration system.

Figure 3. UWB pulse received inside a volcanic rock cave with NLOS between tracking and remote radios. Only a slightly discernable pulse is seen with a single signal, but by beam-forming 100 frames we decrease the noise to clearly identify the pulse.

Hyperspectral Processing Using FPGAs and DSPs

As focal-plane technology advances, it becomes increasingly practical to reduce the size and increase the portability of remote-sensing instruments. To achieve smaller and more portable instruments, supporting electronics hardware and computing elements must similarly decrease in scale and power consumption, while also increasing in computing ability to meet new real-time processing (RTP) needs. To meet the packaging, power, and processing (P3) requirements, RTP systems will need to be assembled using combinations of field-programmable gate arrays (FPGAs) and digital signal processing (DSP) processors rather than bulky, expensive, and less efficient general purpose computing devices.

Project Goals

Our FY2005 goals include the following:

1. evaluate processing requirements to perform covariance estimation, eigenfactorization, and matched filtering (L3 processing) hyperspectral data processing;
2. build a controller to archive data and operate the A/D and DSP components using a single board computer;
3. build a prototype to digitize at least four channels of analog information clocked off a hyperspectral focal-plane array, and process the data prior to L3 by performing bad-pixel correction and spectral calibration (L1 processing);
4. build a prototype that performs real-time hyperspectral data processing from a complete data cube through one or more algorithms selected from the L1 and L3 processing chains.

Relevance to LLNL Mission

This project will provide engineering experience in small scale, low-power, low-cost, RTP systems for hyperspectral imagery, which can be extended to any complex
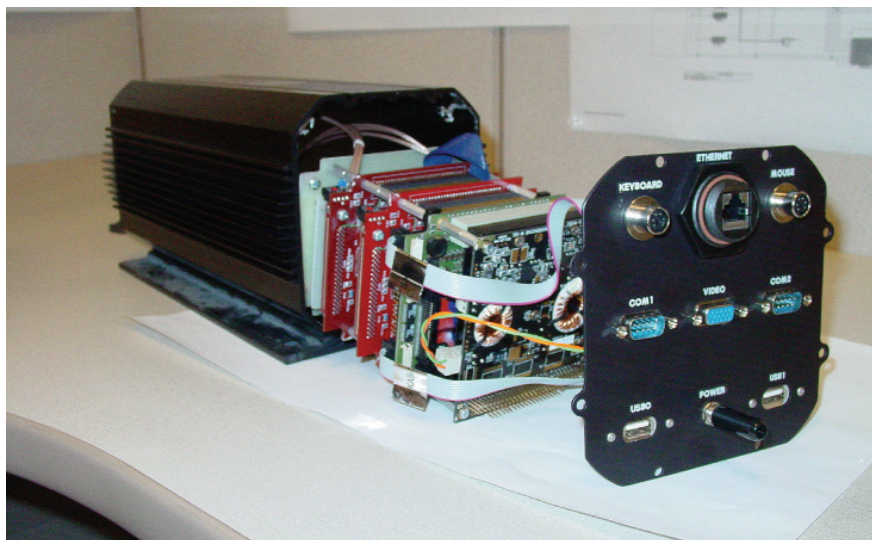
Figure 1. Hardware for hyperspectral embedded processing system.

For more information contact
Erik D. Jones
(925) 424-4757
jones157@llnl.gov

mathematical problem where P3 requirements are key. This project will also result in a package that can be used for any application that digitizes analog input and can benefit from processing the resulting data in real-time. An added benefit is that this technology will be used to increase the efficiency of automated, non-real-time ground data processing of hyperspectral data.

FY2005 Accomplishments and Results

Figures 1 and 2 show some of the hardware for the hyperspectral embedded processing system. We achieved four major milestones this year. First, using EDMA and compiler optimization techniques, we increased the performance of the covariance matrix calculation 300%. The speed and performance is comparable to a generalized CPU with I/O bandwidth still the limiting factor. Second, we refined a covariance matrix algorithm and segmented the calculation into two parts, to divide the workload between the two DSP processors. By exploiting the linearity of the calculation and distributing the

workload, performance was improved another 30%. Third, we achieved a reduction of FPGA fabric use by moving memory storage from flip-flops and combinatorial logic to on-board block RAM available on Xilinx Virtex II FPGAs. Fourth, we simplified the VHDL coding by using Mentor Graphics FPGA Advantage tools.

Covariance matrix generation is required for background estimation prior to performing matched filtering and identification in L3 processing of hyperspectral data. This computation requires a significant number of memory accesses and this has been the largest bottleneck in using conventional DSP chips. While performance improved some 330% over FY2004 performance, the DSP is still too slow to perform full-frame processing in real-time. A parallel project using graphics processors to perform L3 processing demonstrated performance that would meet RTP requirements.

The pervasiveness of high-definition television and streaming video has created a large demand for fixed-point processing. Until DSP manufacturers improve input/output

performance of floating-point chips, it appears the graphics processor market is more suitable for this type of RTP.

Related References

1. Hinnrichs, M., and B. Piatek, "Hand-Held Hyperspectral Imager for Chemical/Biological and Environmental Applications," *Proceedings of the SPIE*, **5270**, pp. 10-18, 2004.
2. Reza, H., and B. Sreedharan, "A Hybrid Number System and Its Application in FPGA-DSP Technology," *International Conference on Information Technology: Coding and Computing*, **2**, p. 342, 2004.
3. Guo, Z., W. Najjar, F. Vahid, and K. Vissers, "A Quantitative Analysis of the Speedup Factors of FPGAs Over Processors," *Proceedings of the 2004 ACM/SIGDA Twelfth International Symposium on Field Programmable Gate Arrays*, Monterey, California, pp. 162-170, February 22-24, 2004.
4. Choi, S., R. Scrofano, V. K. Prasanna, and J. Jang, "Energy-Efficient Signal Processing Using FPGAs," *Proceedings of the 2003 ACM/SIGDA Eleventh International Symposium on Field Programmable Gate Arrays*, Monterey, California, February 23-25, 2003.
5. Haijun, L., L. Dehua, X. Lei, and G. Jinghuo. "Aerial Image Parallel Processing System Based on FPGA + DSP," *Journal of Huazhong (Central China) University of Science & Technology*, **30**, 11, pp. 28-30, November 2002.
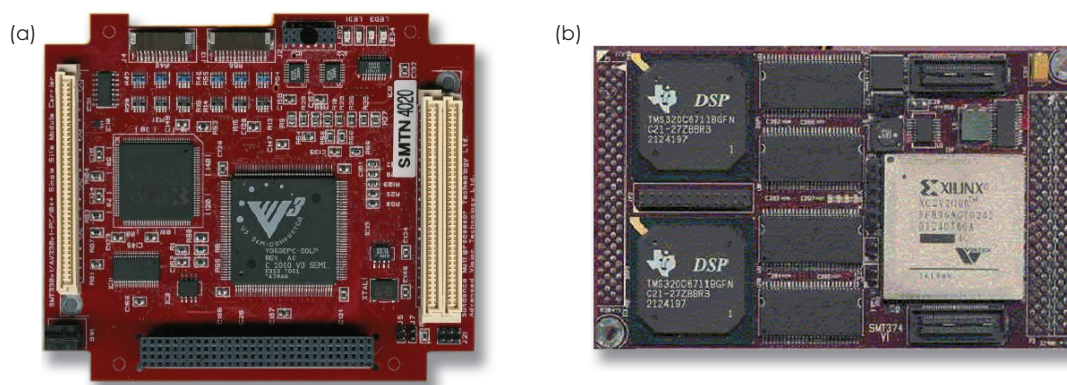
Figure 2. (a) Sundance PC-104+ carrier board, and (b) Sundance dual TI 6713 DSP module.

Flexible Testbed for Evaluation of Ultra-Wideband Radios

The proposed effort is to quantify and demonstrate the advantages of bandwidth, multiple pulse integration, and feedback loops through the use of a flexible narrowband (NB) and ultra-wideband (UWB) testbed.

Project Goals

This work is intended to assess and demonstrate the relative advantages of UWB compared to legacy NB links in terms of link robustness. Additionally, it will assess the impact of capacity (*e.g.*, bit rate) on vulnerability (*e.g.*, ease of detection) and the merits of different link configurations such as single-pulse modulation, feedback loops, and recursive demodulation.

Specific goals are to:
1. define techniques to improve the robustness of UWB communication;
2. provide a working flexible NB/UWB testbed;
3. establish validated and augmented analytic models characterizing benefits of spatial and temporal processing in UWB;

4. build preliminary models characterizing UWB propagation at longer non-line-of-sight ranges and demanding link situations; and
5. evaluate novel techniques such as single-pulse modulation and channel-matched signaling.

Relevance to LLNL Mission

The implementation of this software radio testbed will provide a better understanding of UWB and NB performance in realistic and stressed EM environments.

FY2005 Accomplishments and Results

For end-to-end testing and comparison of both UWB and NB, a software radio testbed was put together as shown in Figs. 1 through 3. This testbed system consists of two sections—the data generation/transmitter section and a data logging/receiver section—that are GPS synchronized. GPS synchronization permits time synchronization of the two for collection of high-speed RF data for analysis.
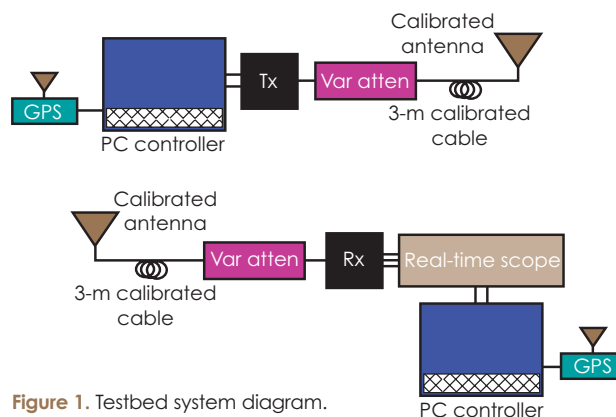

Figure 1. Testbed system diagram.

Figure 2. Testbed transmitter, antenna, and GPS.

For more information contact
Peter C. Haugen
(925) 422-0749
haugen2@llnl.gov

The merits of multiple-pulse integration and feedback loops were studied using the testbed system.

The multiple pulses/bit metric plots (Fig. 4) show the added benefit of sending multiple RF UWB bursts per each bit of data transmitted. The receiver accumulates the energy from all of these bursts to create one received data bit. In the plots, the blue lines represent the received SNR at various locations (path lengths) for a received "1" bit. The red lines provide a baseline for the noise at those locations or, the expected energy received for a "0" bit (no UWB transmission). As can be seen, by averaging a thousand RF pulses per data bit, the SNR can be greatly improved. Sending and averaging multiple RF pulses per data bit can reduce the ERP of the transmitter while still maintaining the same received SNR, which increases link covertness. However, the overall radiated power required to attain the same bit error rate (BER) can be shown to be greater than if a single, more powerful, burst had been sent.

Similarly, the feedback loop plots (Fig. 5) use the same criteria to represent the added benefit from a UWB feedback loop implemented on the receiver. These two plots show how the addition of a feedback loop can further improve the SNR by adding the correlated UWB "1" bit RF bursts (blue), while removing some of the uncorrelated "0" bit RF noise (red).

Through the use of this software radio testbed and special algorithms, numerous RF subsystems have been tested, to the benefit of RF communications projects at LLNL.
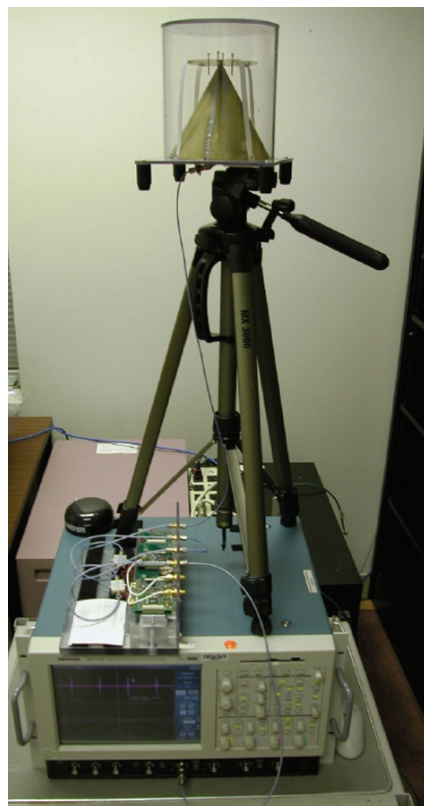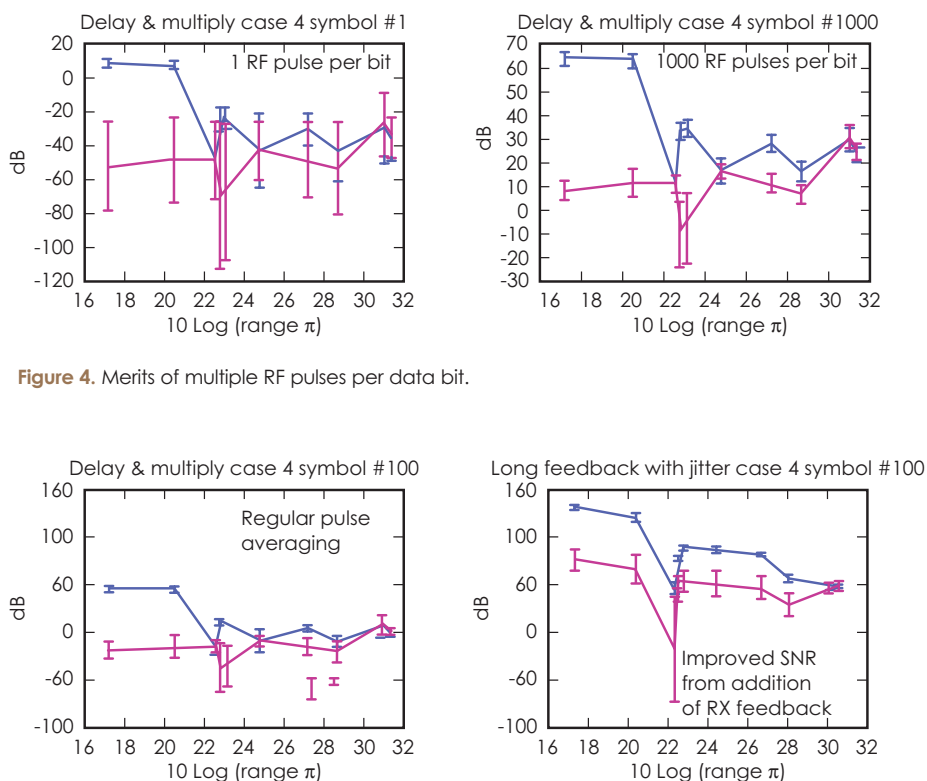

Figure 4. Merits of multiple RF pulses per data bit.

Figure 5. Merits of a receive feedback loop.

Figure 3. Testbed receiver system.

Cooperative Discrimination Sensor: Detecting and Tracking Human Activity

Current low-power intrusion-mitigation networks suffer from a variety of problems including short lifetimes, inadequate communication channel capacity, and weak on-board sensor processing. These networks have the ability to detect activity at each sensor, but often lack the ability to discriminate, due to complexities and inconsistencies in the sensors, environment, and potential targets. This can result in costly nuisance alarms and poor system reliability.

Our solution at LLNL is the reduction to practice of several existing micropower impulse radar technologies into a single cooperative discrimination sensor (CDS) system that can be networked to provide detection, tracking, and discrimination of human activity. A low-power network of these sensors is able to detect motion, track that motion through the monitoring region, and reliably determine if the dominant moving object was a human.

Project Goals

We leveraged results from current radar projects to identify possible sensors for a detection, tracking, and discrimination platform. After extensive evaluation of current technologies and the specification of data-processing algorithms, we selected the sensor combination best suited to perform the required tasks.

We combined the sensors profiled in our first year to build multiple CDS nodes and integrate them into a three-node network. Once constructed, we implemented the previously identified algorithms in the specified network to
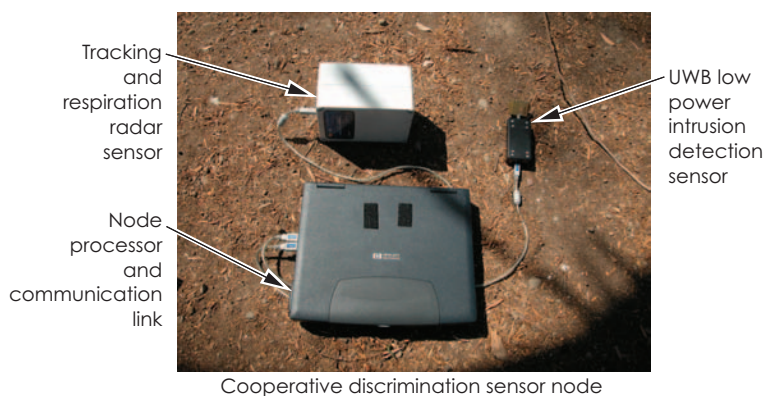

Tracking and respiration radar sensor

UWB low power intrusion detection sensor

Node processor and communication link

Cooperative discrimination sensor node

Figure 1. Basic CDS network node components.

Detection Perimeter

Region of tracking and discrimination

CDS node detection and tracking perimeters

Figure 2. Deployed CDS node in operation.

Node 1   Node 2   Node 3

PTZ camera fellows targets detected and tracked by the network

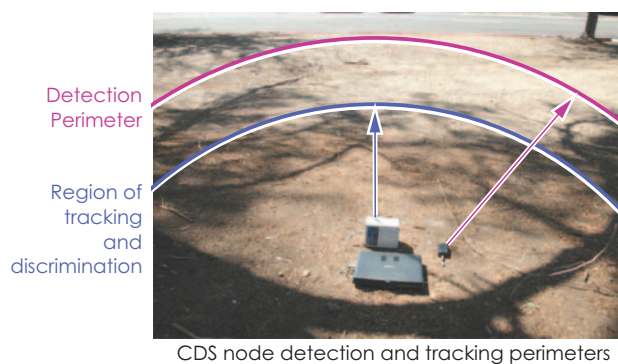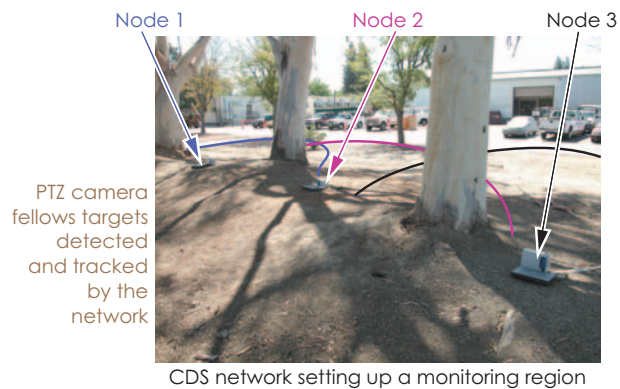CDS network setting up a monitoring region

Figure 3. Multiple CDS nodes forming a network.

For more information contact
Richard R. Leach, Jr.
(925) 423-3351
leach1@llnl.gov

produce a low-power intrusion-detection, tracking, and discrimination network. The network was then deployed in multiple scenarios for performance and capabilities evaluation.

Relevance to LLNL Mission

LLNL is gaining a multifunction, integrated radar sensor system that is capable of not only detection but also tracking and discrimination in a single package. This package can be used in a deployable perimeter security network, operating at power levels previously unattainable by conventional methods, thus opening up opportunities for large-sensor security networks for applications such as antiterrorism, border and battlefield monitoring, and facility monitoring.

FY2005 Accomplishments and Results

This year we combined the radars selected and evaluated in the earlier phase of the project into complete network nodes, as shown in Fig. 1. Each node consists of two ultra-wideband (UWB) radar units and a data processor/communications link. The first UWB radar is a low-power intrusion detection radar. It has a long sensing distance and operates with a very low power draw. This radar can monitor a bubble-shaped region around the CDS node and is used to sense when a potential target enters the area. It then turns on the other, more power-hungry radar and electronics as needed. The second radar is an UWB tracking radar capable of measuring the distance to potential targets within the detection region. When active, it constantly measures the distance from the node to the potential target as it moves through the detection region, in addition to monitoring the target's radar cross-section for discrimination information.

In a typical setup (Figs. 2 and 3), several nodes are deployed to monitor a large area or corridor. Once deployed, each node sets up and monitors its own detection and tracking perimeters. When a target is detected, each node sends its detection, tracking, and discrimination information to a central monitoring station. Then, that monitoring station intelligently combines the information from each node to perform discrimination and 2-D position mapping of the potential intruder.

The intruders are monitored as they pass through the detection region and, in the testbed system, a Pan, Tilt, Zoom (PTZ) camera was steered by the network's position estimates to follow the intruders for ground truth information.

The central monitoring station combines and displays all this information as shown in Fig. 4. A 2-D position plot shows the current location of the tracked intruder relative to the CDS nodes, and the PTZ camera video of the intruder is displayed next to the plot as they are tracked while moving through the network's coverage area. Testing and preliminary data analysis has shown this hardware/software system to be a robust intrusion-monitoring system that shows strong potential for numerous security applications.
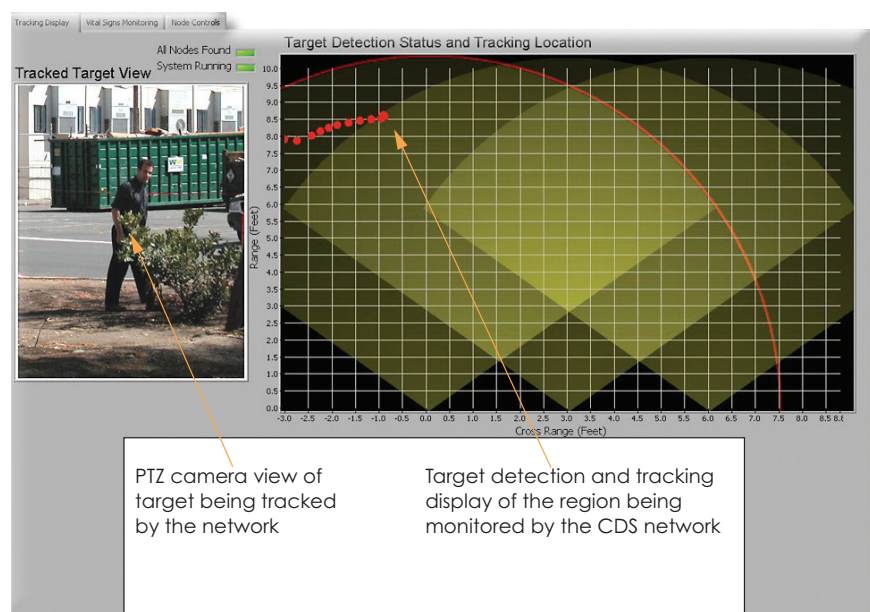

PTZ camera view of target being tracked by the network

Target detection and tracking display of the region being monitored by the CDS network

Figure 4. CDS monitoring station showing the tracking of a target.

Ultra-Wideband Dynamic Pulse Shaping for Communications and Remote Sensing

Improvements in covertness and security for communications links are a constant area of interest in modern industry. The advent of ultra-wideband (UWB) communications has allowed investigation into RF transmission systems using ultra-short time-domain pulses to produce widely spectrally-spread RF bursts. However, state-of-the-art UWB communications systems still rely on traditional pulse-spacing techniques and constant pulse shapes to send data across the channel. This leaves the systems vulnerable to detection and interception.

Recent semiconductor processing advancements have permitted the realization of new ultra-short-pulse-generation hardware using current-steering methods. These new pulse-generation techniques permit ultra-short bursts of pulses to be electronically shaped as they are generated, and their shapes to be altered at high speeds from pulse to pulse.

Project Goals

This capability has two unique applications to data transmission systems. First, by encoding data into the shape of ultra-short bursts, instead of using burst presence/absence or spacing to transfer data, a system's throughput can be greatly increased. Second, since each pulse transmitted has a different shape, it has a different spectral content, even in UWB systems. By combining pulse-to-pulse spectral alteration with transmission schemes pioneered at LLNL, that allow pulses to be sent at untimed, random intervals, the potential for highly covert and secure communications systems can be demonstrated.

This project will test and evaluate this advanced pulse-generation technology, which has the potential to be used in ultra-fast transient digitizers and real-time sampling applications. Such technology can be applied to numerous areas of communications, security, and precision engineering.

Relevance to LLNL Mission

This technology offers numerous advantages over traditional UWB pulse-generation techniques. The existing technologies have limitations, such as ~500-MHz maximum pulse-repetition rates, poor matching
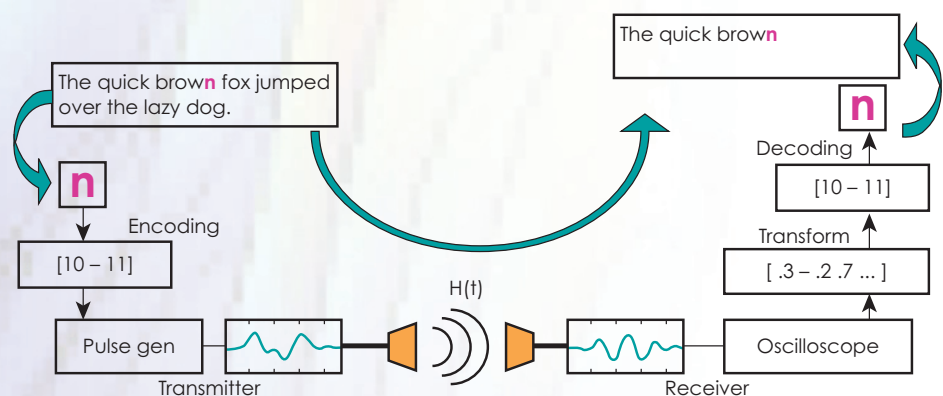

Figure 1. Data flow diagram for the pulse-shape transmission system.

For more information contact
Peter C. Haugen
(925) 422-0749
haugen2@llnl.gov

between multiple units, jitter, and poor temperature stability. This new technology has the potential to be an important addition to current pulse generation and UWB work at LLNL.

FY2005 Accomplishments and Results

The dynamic pulse-shape-generation technique was calibrated for performance against other UWB pulse-generation techniques currently used at LLNL, in terms of time jitter, power output, power consumption, maximum pulse-repetition rate, repeatability, and stability over a wide temperature range. It was then integrated into a demonstration data-coded pulse-shape transmission scheme.

This system was implemented and can be used to transfer data across a free-space link. A series of data bits are encoded into each RF burst using the pulse shaper linked to a PC, and the resulting pulse is amplified and transmitted across the link. On the receiver end, an oscilloscope (with appropriate preamps and filters) is used to capture the RF burst, which is then downloaded to the PC for decoding in an automated process. As expected, the antenna, filters, and amplifiers distort the generated pulse shapes to some extent, so a transfer function must be applied to the received data to recover the original data. This was implemented and the final data flow happens as shown in the data flow diagram (Fig. 1).

The data reconstruction plot (Fig. 2) shows the data flow as it is encoded into RF burst shapes, transmitted, received, and reconstructed. The frequency content plot (Fig. 3) shows how the RF energy spectrum changes as the burst shape changes with the

transmitted data. In our testing we have found that, while this pulse-shaping technique does have limitations, it can be readily used to enhance several areas, such as the potential for the creation of reliable, highly covert UWB communication links, and channel-matched transmitters for radar and remote sensing.
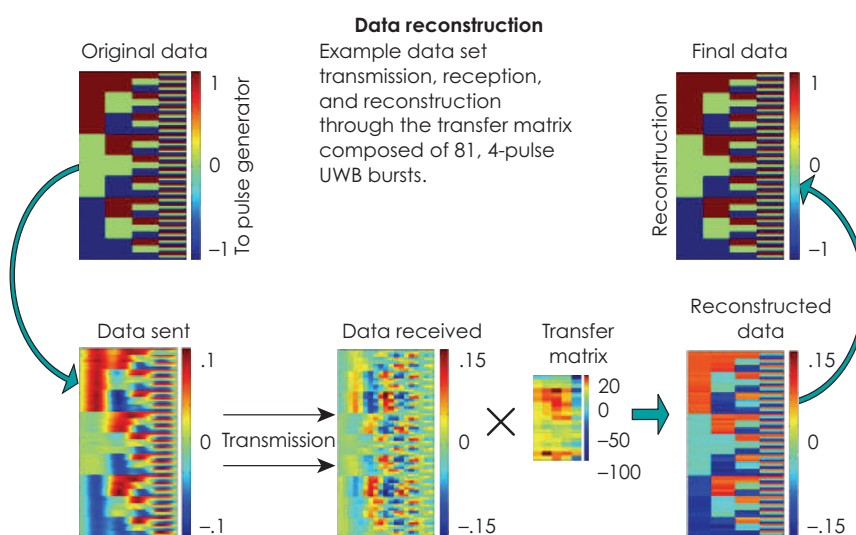

Data reconstruction
Example data set transmission, reception, and reconstruction through the transfer matrix composed of 81, 4-pulse UWB bursts.

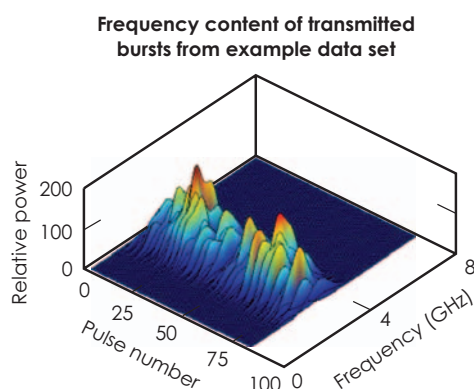**Figure 2.** Data reconstruction process of example data set.

Figure 3. RF spreading spectrum of example data set.

Fast Image Reconstruction

Over the last decade, LLNL has become a world leader in the application of microwave radar imaging techniques to NDE problems.

The challenge lies in the real-time processing of the raw data. Past systems have relied on collecting the data and conducting off-line postprocessing to achieve the desired effect. There is a need to be able to perform these evaluations at a faster, closer-to-real-time rate. The small form factor of the micropower-impulse radar (MIR) sensors, coupled with fast imaging techniques would provide a valuable tool in the nondestructive characterization of structures, materials, and personnel. The advent of FPGAs, CPLDs, fast programmable microcontrollers, DSP cores, and current innovations in parallel programming afford us the opportunity to work with a small platform capable of conducting image-reconstruction techniques at the rate of 4 fps.

Project Goals

This project will reduce to practice a small, flexible, computationally efficient platform to carry out image reconstruction of a radar-analyzed scene at the rate of 4 fps, based on real-time raw microwave radar input.

Relevance to LLNL Mission

This problem is of interest to LLNL because it affords a new modality with which to inspect and characterize structures, materials, and personnel. Additionally, such a platform could be used for image reconstruction of other modalities, such as ultrasound.
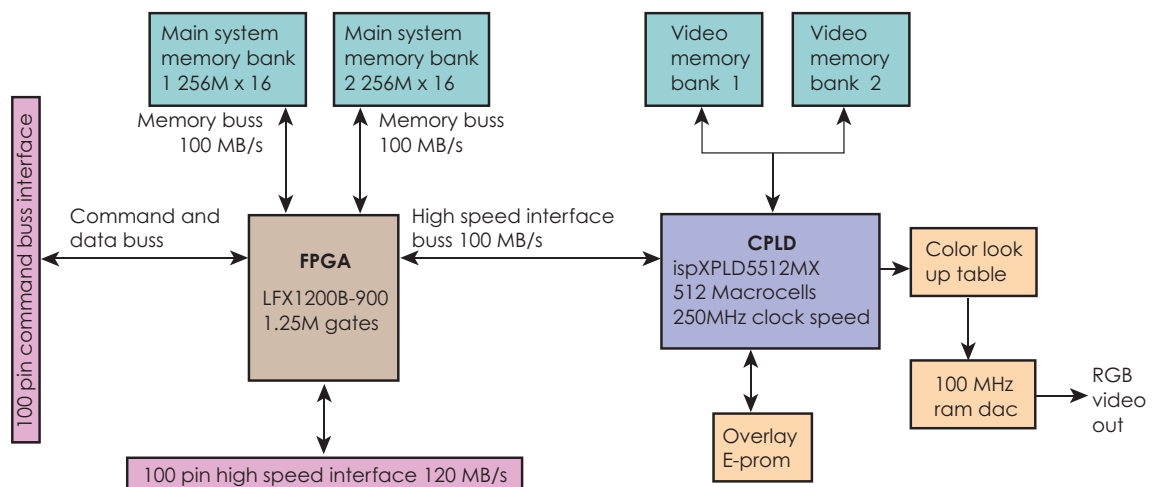
Figure 1. Block diagram of the imaging board. The system contains dual gate arrays: a 1.1-million gate FPGA capable of processing the 48-bit image channel, running at 80 MB/s, and a 512-macrocell CPLD used for image formatting and display. A proprietary video interface bus between the two gate arrays is capable of running at 100 MB/s. The system memory consists of 512 MB of main memory divided into two banks. For communication, there is a 100-pin high-speed video bus, a 100-pin general communication/control bus, a USB2 bus, a high-speed RS232 bus and a standard video display connector. Video imaging formats include 1024 x 768 at 70 fps and 640 x 480 at 60 fps, with 24-bit color.

For more information contact
Carlos E. Romero
(925) 423-2830
romero29@llnl.gov

This effort will enhance the technology base of engineering at LLNL in the areas of computational systems, radar/ultrasound imaging, and NDE.

FY2005 Accomplishments and Results

For FY2005, deliverables included a prototype image reconstruction board and identification of an algorithm for image reconstruction of microwave radar scenes. Both these goals were achieved and exceeded. A finalized PC board was constructed and loaded with the necessary algorithms to perform 4-fps image reconstructions.

A block diagram (Fig.1) outlines the functionality of the imaging board and specifies the components. The hardware, in conjunction with the identified and implemented reconstruction algorithms, permits real-time visualization of radar data in a format that is intuitive to an untrained observer. As an example, Figs. 2 and 3 contrast four frames of real-time raw data with reconstructed data at a rate of 4 fps.
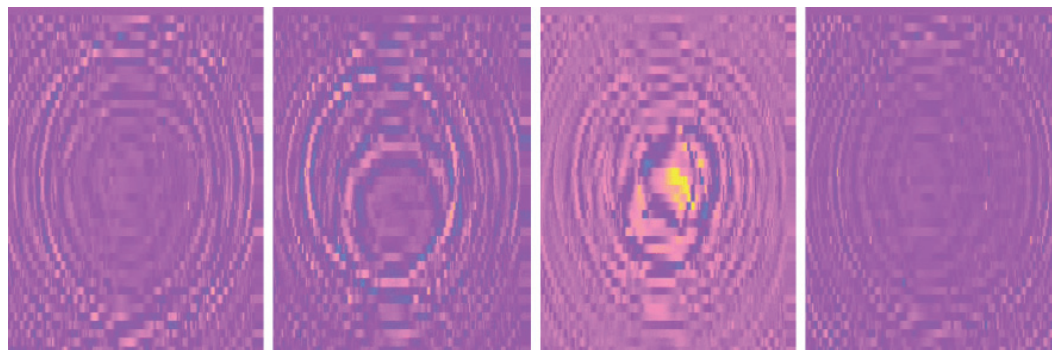

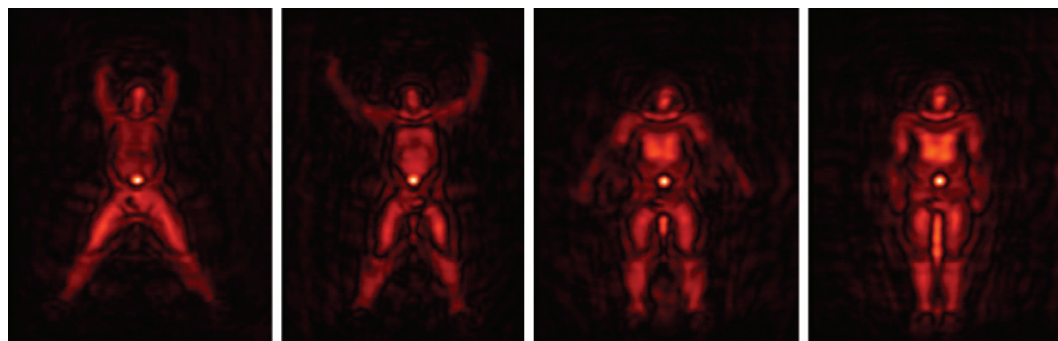**Figure 2.** Raw radar data.

Figure 3. Reconstructed radar data.

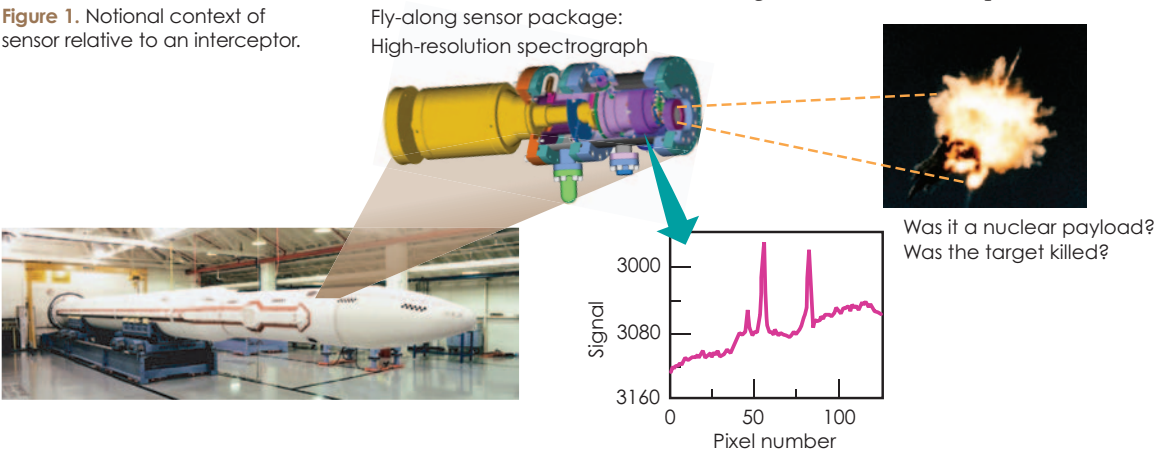# Miniature Echelle Grating Spectrometer Cartridge

Current missile defense systems do not identify the content of an intercepted warhead payload. Spectral sensors could be used remotely to "type" the intercepted warhead based on detection of key signatures of warhead components. A platform for such a sensor is the last stage of the booster that releases the kill vehicle. To be compatible with this platform, a ten-fold reduction in size, weight, and power as compared to existing technology would be required. We have verified the optical feasibility of a sensor miniaturization concept, based on proven cross-dispersive

spectrographic techniques used in larger systems. Figure 1 shows the context of a possible sensor concept relative to an interceptor.

Using an echelle grating spectrograph (EGS), which disperses light in two orthogonal directions to efficiently fill a 2-D focal plane, high spectral resolution is attained at the relatively high frame rates needed for short-lived events such as explosions. The dramatic reduction in size (Table 1) was due to the use of immersive gratings; a multipass architecture; folding the beam path; the physical combination of a grating and focusing element; and the availability of advanced diamond fly-cut ruling technology. Two records of invention were generated.

Project Goals

After performing initial scoping and exploration in FY2004 of a compact echelle spectrograph, we sought to demonstrate a configuration that has the high strategic potential of performing real-time, remote-target forensics on warheads as they are being destroyed. We focused on the mid-wave IR band with an approach that is extendable to other IR bands to collect potential nuclear warhead signatures of uranium, plutonium,

Table 1. Summary of improvements.

	EGS (existing)	MiniEGS (proposed)	Improvement factor
Optical path volume	6600 cm^2	100 cm^2	66x reduction
Cooler power	1000 W	200 W	5x reduction
Cool-down time	10 h	1 h	10x reduction
Optical transmission	Fiber fed	All-reflective optics	10x increase
Frame rate	10 Hz	100 Hz	10x increase
Dewar and cooler assembly weight	300 lb	20 lb	15x reduction
Total system weight	600 lb	60 lb	10x reduction

Figure 1. Notional context of sensor relative to an interceptor.

Fly-along sensor package: High-resolution spectrograph

Was it a nuclear payload? Was the target killed?

For more information contact
Joel Bowers
(925) 423-6877
bowers2@llnl.gov

tritium, their potential compounds, and high-explosives combustion by-products. This evidence would be critical to support decision processes that would likely follow an attack.

The down-selected optical systems were incorporated into precision mounts that maximized use of an existing cartridge-style mechanical infrastructure developed at LLNL for hyperspectral remote detection of WMD production signatures. This relatively modest investment of a new optical cartridge configuration created a completely new instrument concept (Table 2). The goal was to complete a feasible configuration for an echelle spectrograph optical cartridge, including optical prescriptions, performance predictions, an FPA technology assessment, and an optomechanical cartridge packaging concept.

Relevance to LLNL Mission

LLNL's national security mission requires special multidisciplinary capabilities that are also used to pursue programs in advanced defense technologies. The small form factor makes this sensor attractive for other applications requiring high spectral resolution and low volume, weight, and power.

FY2005 Accomplishments and Results

The optical configuration was refined and characterized with regard to diffraction efficiency, ghosting, and stray light analyses. The very high spectral resolution of one-quarter of a wavenumber over the mid-wave IR spectrum was verified. Out of necessity for optical formatting, we invented a microperiscopic beam-slicer (Fig. 2) that will rearrange an incoming 3-x-3 pixel array into a 9-x-1 array at the sensor entrance slit.

Commercial off-the-shelf focal plane array technologies were investigated and verified for feasibility at this form factor. The mechanical study was completed after modeling the cross-dispersive configuration and identifying components of the existing hyperspectral optical cartridge that could be used without modification in the new system. Estimates were generated based on this gap analysis to determine the complete scope of the effort needed for a prototype system.

Related References

1. Kuzmenko, P. J., D. R. Ciarlo, and C. G. Stevens, "Fabrication and Testing of a Silicon Immersion Grating for Infrared Spectroscopy," *Optics, Imaging, and Instrumentation*, SPIE, **2266**, pp. 566-577, 1994.

2. Stevens, C. G., P. Kuzmenko, T. W. Alger, and N. L. Thomas, "An Echelle Grating Spectrometer (EGS) for Mid-IR Remote Chemical Detection," *Optics, Imaging, and Instrumentation*, SPIE, **2266**, pp. 2-12, 1994.

3. Thomas, N. L., S. A. Johnson, and C. G. Stevens, "Design of an Immersion Echelle Grating Mid-IR Spectrograph for Chemical Remote Sensing," *Optics, Imaging and Instrumentation*, SPIE, **2266**, pp. 13-24, 1994.

4. Hulthen, E., and H. Neuhaus, "Diffraction Gratings in Immersion," *Arkivfur Fysik*, **8**, pp. 343-353, 1954.

5. Hinkle, K. H., S. T. Ridgway, and F. E. Stuart, "Optical Design for a High Resolution, 2-5 Micron Infrared Cryogenic Echelle Spectrometer," *Instrumentation in Astronomy*, SPIE, **1232**, 1990.

FY2006 Proposed Work

A key technology that was invented in this project is the microperiscopic image slicer, consisting of an internally reflecting mirror system that is a fraction of a millimeter in size. This enabling technology will require a mesoscale manufacturing demonstration to determine credibility of the concept.

Table 2. Optical parameters.

|	
Spatial image format	3 x 3
Reformat to spatial slit	9 pixels
Spectrometer f-number	4
Detector array	256 x 256 with 30-μm pixels
Wavelength range	3.1 to 4.8 μm
Wavelength resolution	0.25 wavenumber/ pixel equivalent to 0.4 nm at 4 μm)
Number of pixels along spectrum	4250
Orders to cover spectrum	~17 orders
Number spatial pixels assigned to each row	13 pixels
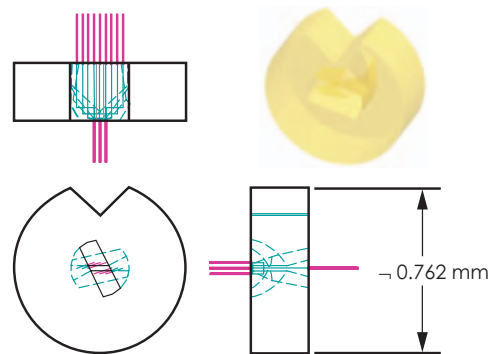
Figure 2. Microperiscopic image slicer.

Energy Manipulation
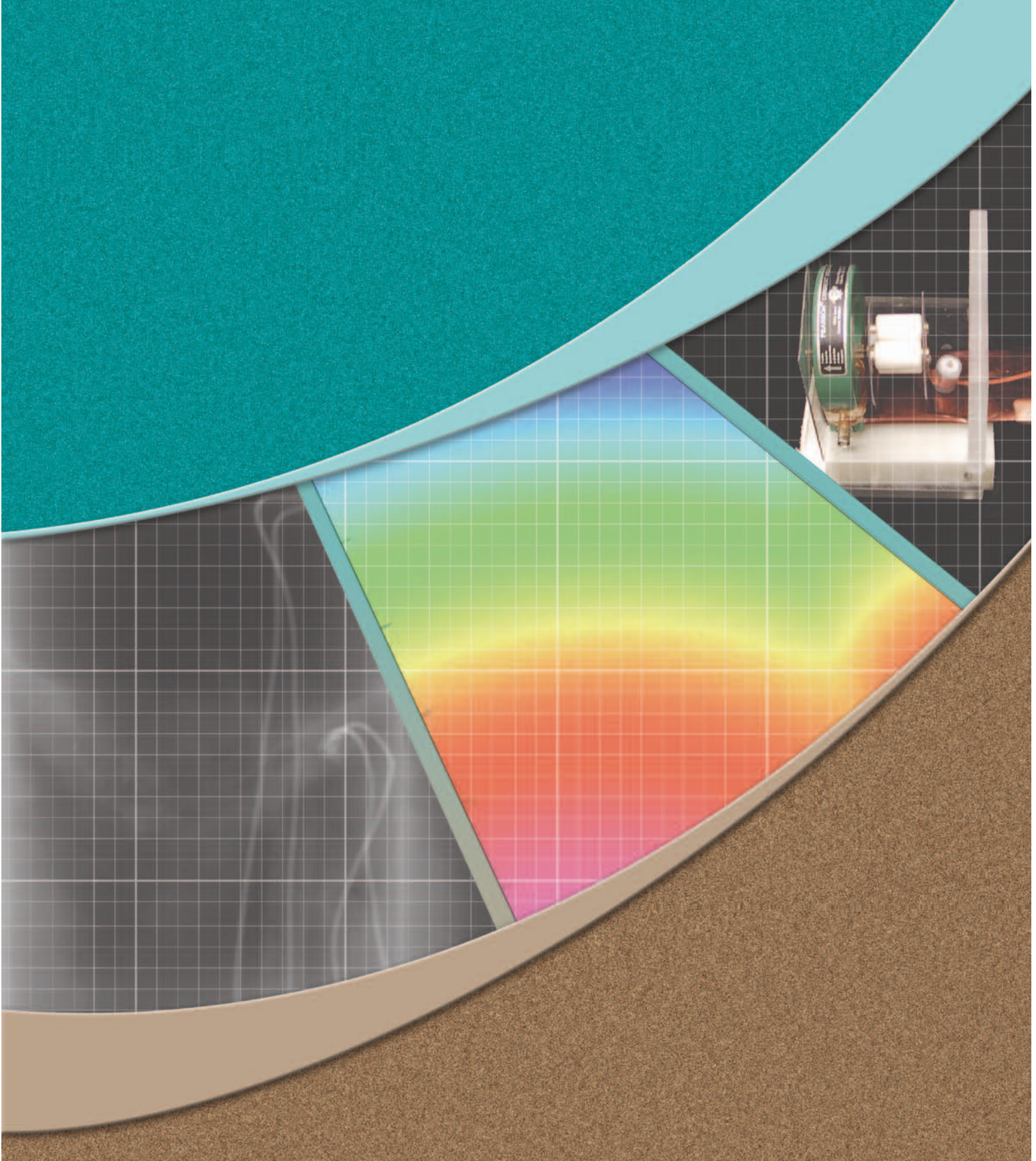
Persistent Monitoring Platforms

In this project, we plan to build and test the power plant for a stratospheric aircraft powered by thermal energy from the sun. Such an aircraft could maintain station over a designated ground location almost indefinitely, since it would not need fuel. By creating the technology for a sun-tracking solar-heat collector, a thermal storage reservoir, and a direct-drive high-efficiency heat engine, we are moving toward an efficiency nearly an order of magnitude better than the state of the art (Helios). We will also develop physics models for thermal transport, materials interactions, loss mechanisms, and engine performance in the stratospheric environment.

Project Goals

In preparation for constructing a prototype scale-model aircraft to demonstrate station-keeping capability at sea level, we will develop and validate the physics models to prove the principles involved in a solar thermal-powered aircraft. Successful demonstration of this technology would set the stage for construction of a stratospheric-altitude prototype capable of circumnavigating the globe.

Relevance to LLNL Mission

Persistent surveillance, having essentially unlimited dwell time over a region of interest, would enable the acquisition of a qualitatively new type of intelligence information for various national security applications, such as countering the proliferation of weapons of mass destruction. Furthermore, inexpensive persistent surveillance has direct application in border monitoring for homeland security missions.

Attenuation radiograph (Ln I_0/I)

Y slice CT image – 4 frame (ry480 – ry483) average
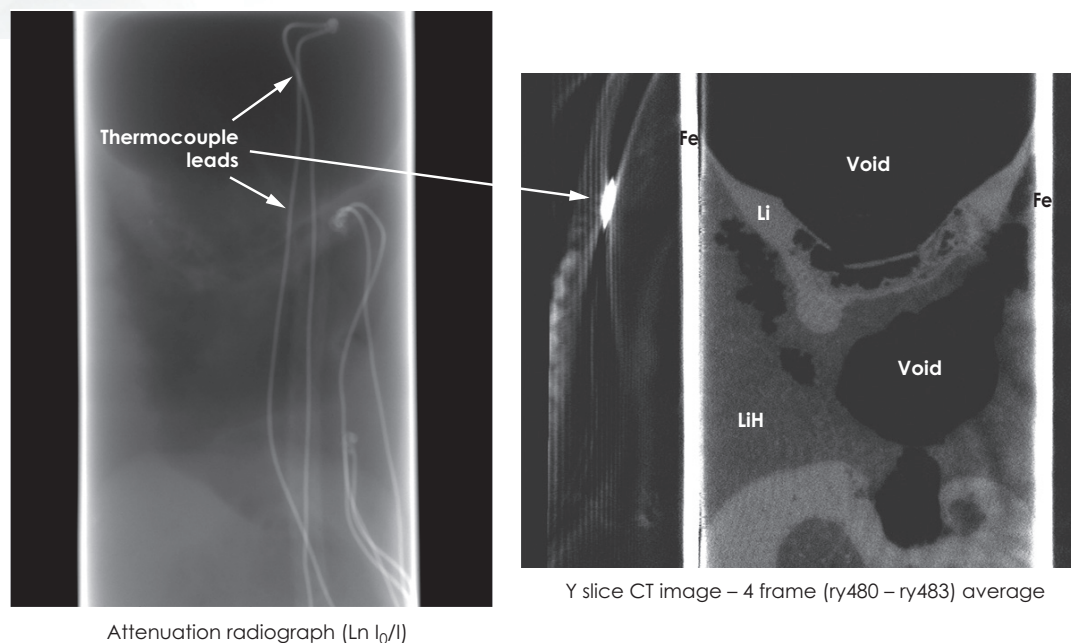
Figure 1. "Spongy LiH," allowing intimate coupling to Li for heat flow.

For more information contact
Charles Bennett
(925) 423-6131
bennett2@llnl.gov

FY2005 Accomplishments and Results

In FY2005, we demonstrated, with a prototype, that a LiH-Li thermal "battery" (Fig. 1) can deliver a specific thermal power of 7500 W/kg, and store a specific thermal energy of 1300 W-h/kg. These performance levels are well in excess of the minimum required to sustain a solar-powered aircraft in overnight flight. In addition, we invented a new type of heat engine that we believe may achieve, in practice, a higher efficiency for conversion of heat to power than the well-known Stirling engine.

Figure 2 shows the results for a prototype collector/receiver as we reached our initial goal of 1000 K.

FY2006 Proposed Work

In FY2006 we will focus on the R&D involved in the new heat engine concept, and on a ground-based quantification of the engine efficiency when coupled to a high-temperature thermal energy storage reservoir. Once the engine characteristics, especially the potentially hazardous features, are sufficiently well understood, we will use first an innocuous thermal energy storage medium such as hot sand, then the LiH-Li thermal battery developed in the earlier phases of this project. Our goal is to transition to outside sponsorship for the development of operationally useful systems, both from DARPA for the solar thermal aircraft itself, and from either state or federal sponsorship for the terrestrial solar energy applications.

(a)

(b)

Figure 2. (a) and (b): Prototype collector/receiver called "First Light." Orange glow at top in (a) indicates the attainment of the initial goal of 1000 K.

Multipoint Arc Initiation

This project examines the use of an array of arcs, rather than exploding bridge wire or exploding foil initiators, to detonate high explosives (HE). The array of arcs creates extreme temperatures and pressures to ignite HE using lower energy than conventional means.

Last year, we demonstrated the feasibility of this concept by creating a multipoint system with an arc-to-arc jitter less than 2 ns. This year we used an array of arcs to directly detonate Pentaerythritol Tetranitrate (PETN).
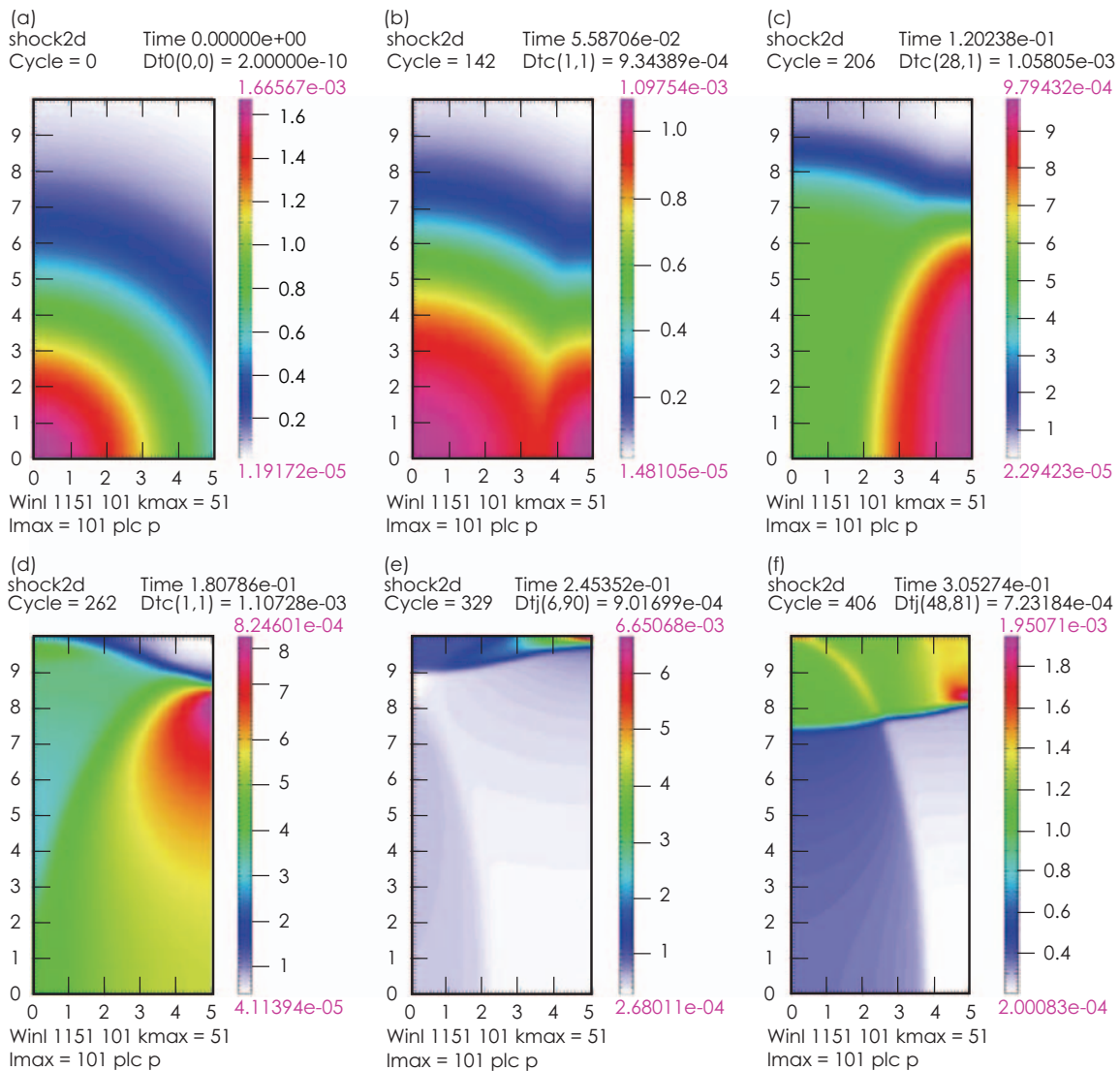
Figure 1. Pressure profiles: (a) shows the pressure at time zero, when pressure from only one point can be seen. In the subsequent figures (b) through (d) the pressure pulse develops until it contacts the surface in (e). The pressure reflection off the surface at Y = 10 is seen in (f). The pressure profile colors in each time snapshot are normalized to the maximum at that moment.

For more information contact
Christopher L. Robbins
(925) 422-2274
robbins12@llnl.gov

Project Goals

This project endeavors to demonstrate multi-arc HE initiation, to estimate the minimum energy required, and to examine the energy and safety advantages over conventional HE initiation.

Relevance to LLNL Mission

The results of these experiments show the energy required using multi-arc initiation is lower than conventional means and may make direct initiation of less sensitive HEs possible. The feasibility of an improved efficiency HE initiation, and its implications for enhanced safety, is of significant interest for DoD and DOE projects in which LLNL participates. In addition, this technology may prove beneficial for commercial explosives applications such as down-hole oil well initiators.

FY2005 Accomplishments and Results

CALE Simulations. A C-based Arbitrary Lagrangian-Eulerian (CALE) model was used in the planning of the experiments. The original intent was to study the effect of the array spacing on the uniformity of the pressure pulse developed against the surface, but it was also noticed that the peak pressure has an optimum with respect to the distance of the array from the surface. If too close, the pressure cannot form a sharp, shock-like structure; if too far, the pulse degrades via divergence. The initial set of runs considered an ideal gas with a cylindrical array of regions given instantaneous heating with a Gaussian profile, offset from a solid surface. Additional runs are needed to find the optimal location.

Figure 1 shows pressure profiles from a 2-D cross-section of an infinite array of arcs positioned on the x-axis at $X = \{\ldots,-10, 0, 10, \ldots\}$. A solid surface exist at $Y = 10$ and $Y = -10$. Due to symmetry, only $X = \{0 \ldots 5\}$ and $Y = \{0 \ldots 10\}$ are shown.

Experiments. A fireset (Figs. 2 and 3) was built for the laboratory testing of multipoint initiators. The fireset was used to fire two RISI RP1 Detonators. This fireset initiated the detonators with total circuit energy of only 86.3 mJ. Losses in the system have been calculated to consume approximately 20% of this energy, resulting in initiation of each detonator at only 35.0 mJ. This experiment demonstrated multipoint arc initiation of PETN at energies lower than those used by conventional means. The results are significant in that arc initiation requires very small amounts of energy, making it an appealing alternative to other initiation techniques when energy efficiency is important.

FY2006 Proposed Work

Work is needed to increase the number of simultaneous arcs. Further tests would also converge on the minimum energy required for initiation of various other HEs. Additional simulation studies will help to find optimal arc spacing and HE-stand-off distances. Using these results, and further experimentation, direct initiation of even less sensitive explosives may be possible.
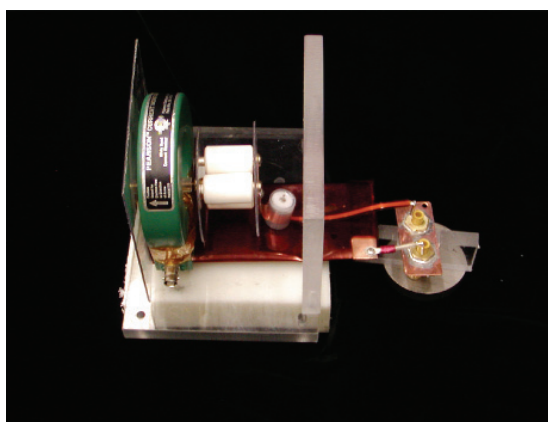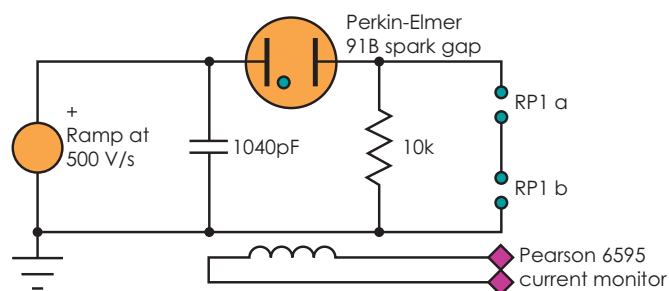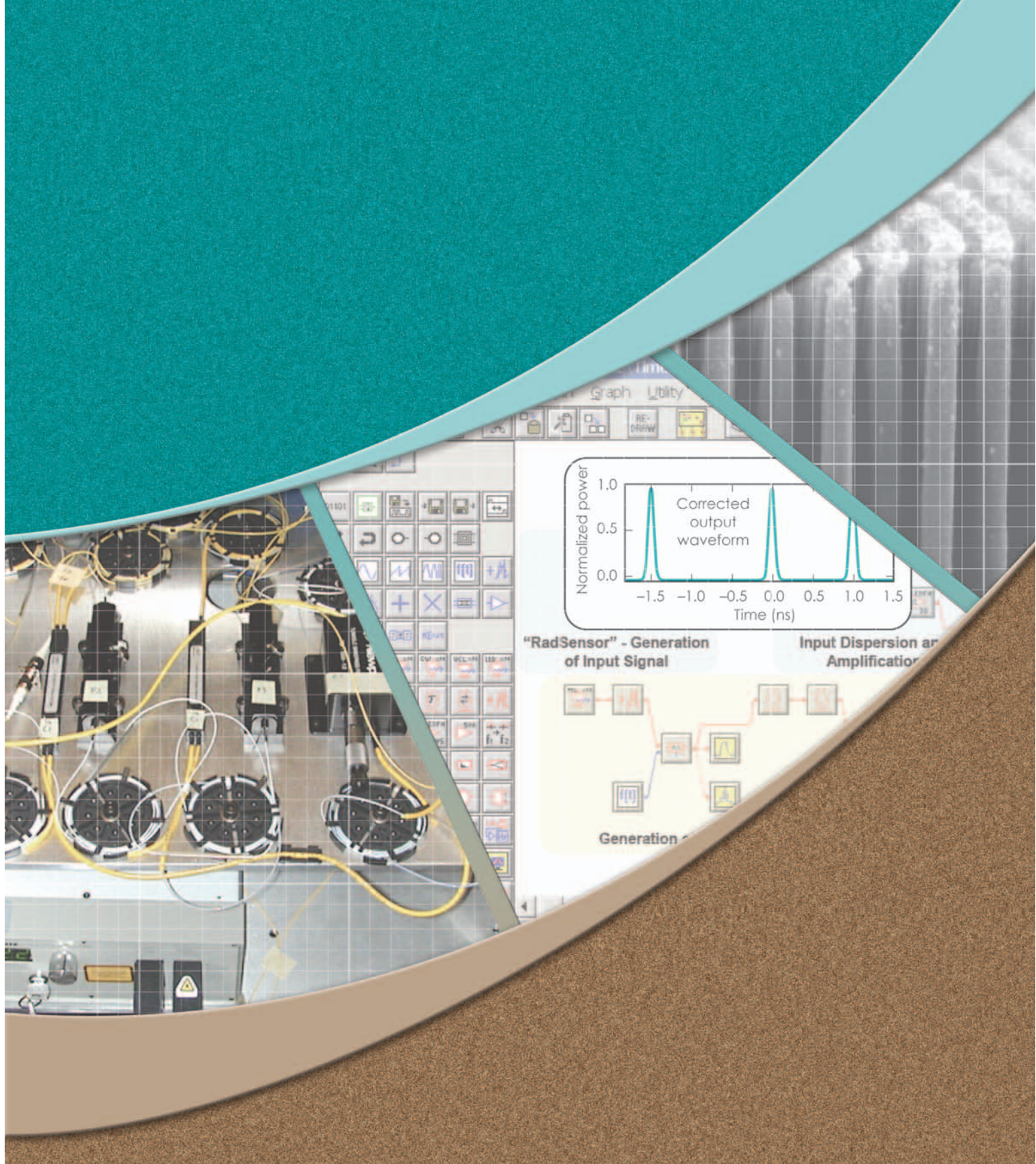

Figure 2. Fireset and load.

Figure 3. Electrical configuration of fireset.

Ultrafast Technologies

"RadSensor" - Generation
of Input Signal

Input Dispersion and
Amplification

Generation

Ultrafast Transient Recording Enhancements for Optical Streak Cameras

Several experiments at LLNL will require hard x-ray and neutron diagnostics with temporal resolution of ~ 1 ps and a high dynamic range, particularly those experiments involving ignition. The Linac Coherent Light Source (LCLS) at the Stanford Linear Accelerator Center (SLAC) will need to measure timing and pulse shapes of its 100-fs fwhm x-ray pulse. These measurement requirements are far beyond existing capabilities.

This project will develop a "time-microscope" front end for optical streak cameras. It will magnify (temporally stretch) signals having ultrafast optical detail so they can be recorded with slower-speed streak cameras with a much higher fidelity. The system will be compatible with a new class of ultrafast radiation detectors that produce a modulated optical carrier in response to ionizing radiation.

Project Goals

Temporal imaging is based on a space-time duality between how a beam of light spreads due to diffraction as it propagates in space, and how pulses of light spread as they propagate through dispersive media, such as grating systems or optical fiber (Fig. 1). We have chosen to implement a "time lens" through sum-frequency generation of a broadband-chirped optical pump with the input signal in a nonlinear crystal, because of the improved resolution it produces.

We are developing a temporal imaging system using fiber optic technologies. The system will accept an optical signal at a 1550-nm wavelength that has ~ 600-ps duration and subpicosecond detail. It will have a temporal resolution < 300 fs, and will produce an output with 100 x temporal magnification, simultaneously shifting the signal to a 775-nm-center wavelength. The 300-fs input details, magnified to 30 ps at the output, will then be recorded with high fidelity on an optical streak camera.
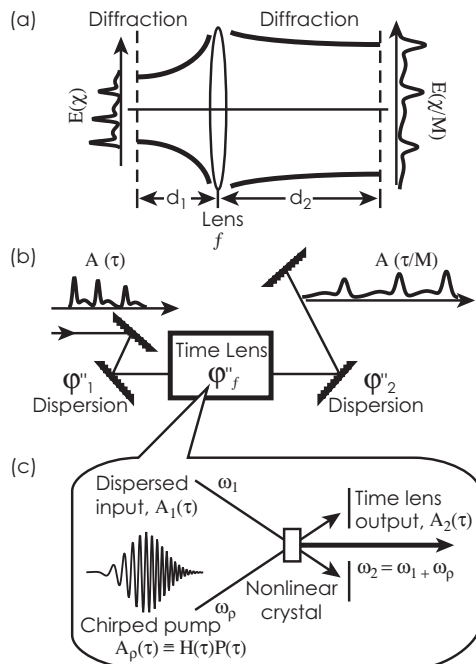
Relevance to LLNL Mission

The success of NIF is critical to LLNL's stockpile stewardship mission. Our goal is to ensure delivery of the next-generation ultrafast diagnostics needed for critical experiments at NIF and other facilities, such as LCLS.

FY2005 Accomplishments and Results

Our laser's mode-locker driver and phase-locked-loop electronics were rebuilt to make the system compatible with NIF. The system now operates at the standard OC-12 rate (~ 622 MHz), the fourth harmonic of the OC-3 clock used by NIF. This guarantees that there would always be a time-lens pump pulse at any possible NIF trigger time. We have achieved the desired time-lens characteristics, including a 12-nm bandwidth, 53 ps/nm effective focal dispersion, 625-ps pulse width, and hundreds of nanojoule pump energy.

Significant ringing in the system's impulse response was predicted due to higher-order spectral phase aberrations in the input dispersion system. We have designed a correction for this distortion by combining multiple types of fiber with opposite aberration effects, canceling the net effect. The

Figure 1. Comparison of (a) spatial and (b) temporal imaging systems. A time lens (c) is produced by mixing the input signal with a chirped optical pump pulse.

For more information contact
Corey V. Bennett
(925) 422-9394
bennett27@llnl.gov

modeling of the initial design along with predicted results for the improved input dispersion design are presented in Fig. 2.

We have designed and implemented a time-lens mixing system that uses noncolinear sum-frequency mixing in 1 mm of periodically polled lithium niobate (PPLN). The pump and dispersed input signals are delivered via fibers, but the frequency mixing set-up is a bulk optic design in a fixed period PPLN crystal. An improved design using chirped-period PPLN waveguides is also being pursued.

Related References

1. Bennett, C. V., and B. H. Kolner, "Upconversion Time Microscope Demonstrating 103x Magnification of Femtosecond Waveforms," *Optics Letters*, **24**, 11, pp. 783-785, June 1, 1999.
2. Bennett, C. V., and B. H. Kolner, "Principles of Parametric Temporal Imaging-Part I: System Configurations," *IEEE J. Quantum Electronics*, **36**, 4, pp. 430-437, April 2000.
3. Bennett, C. V., and B. H. Kolner, "Principles of Parametric Temporal Imaging-Part II: System Performance," *IEEE J. Quantum Electronics*, **36**, 6, pp. 649-655, June 2000.
4. Bennett, C. V., and B. H. Kolner, "Aberrations in Temporal Imaging," *IEEE J. Quantum Electronics*, **37**, 1, pp. 20-32, January 2001.

FY2006 Proposed Work

We plan to optimize the current bulk-optic-based time-lens mixing crystal design and work on a chirped-PPLN waveguide design with much higher efficiency. We will add the output dispersion to the system, completing the temporal-imaging system. Output dispersion technologies will be investigated, but the leading candidate is chirped-fiber Bragg gratings. We will optimize and fully characterize the performance of the system.
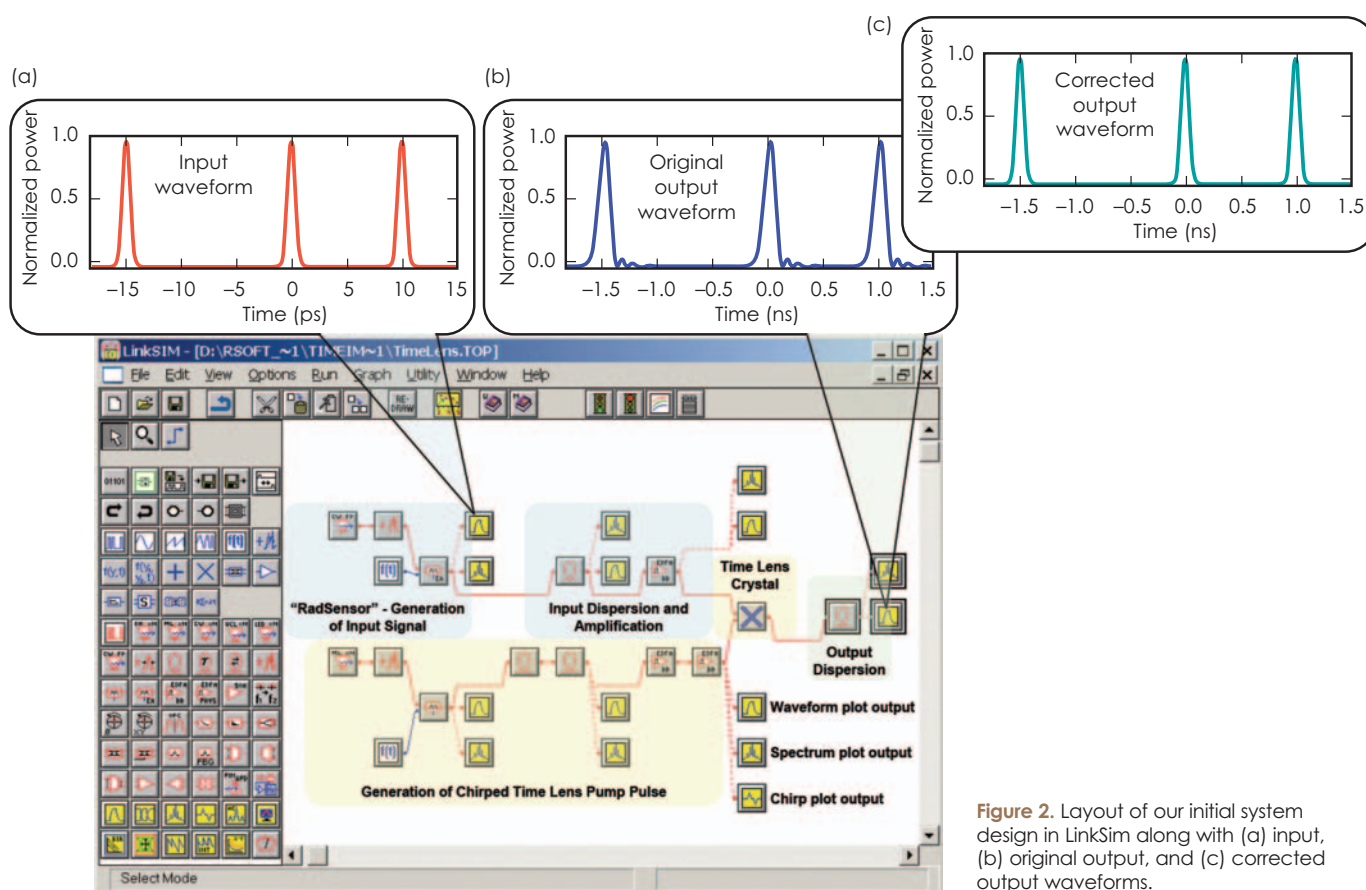
Figure 2. Layout of our initial system design in LinkSim along with (a) input, (b) original output, and (c) corrected output waveforms.

Terahertz Spectroscopic Imaging for Standoff Detection of High Explosives

The THz EM region, sandwiched between the microwave and IR regions of the spectrum is rich with information about the rotational and vibration characteristics of large molecules. In particular, preliminary studies have suggested that certain compounds used for high-explosive (HE) applications might exhibit characteristic signatures in the THz regime. Our research project focuses on standoff detection of HE; however, the techniques developed here could be used for other WMD detection applications, since many WMD could contain molecules that exhibit unique THz signatures.

As an initial step, we are assessing the feasibility of using THz radiation to remotely detect and identify HE materials in the 1- to 10-m range, but possibly as high as 100 m. *Detection* is meant to convey an answer to the question, "is there an item in our image that might possibly be HE?" by virtue of its shape, size, reflectivity, or other parameters. Such crude screening would be useful to identify regions to be subjected to HE spectroscopy and ultimately, identification. Here, *identification* is meant to imply the association of a specific identifier, like a chemical name, with each suspicious target.

Project Goals

If the initial step indicates feasibility, we propose to develop a new portal and standoff detection tool for WMD, with specific application to the important problem of HE detection. Until recently the THz region of the EM spectrum has been largely inaccessible, due to the lack of adequate sources, detectors, spectroscopic elements, and imagers. The present contribution seeks to leverage these emerging technological developments, while integrating key elements into a useful system.

Relevance to LLNL Mission

Robust detection of WMD, specifically HE, is a key national security mission at LLNL. This project will lead to a new capability in a fresh

DETECTION?

For more information contact
Farid U. Dowla
(925) 423-7579
dowla1@llnl.gov

and largely untapped region of the EM spectrum, and to new science and technology. Furthermore, the region of investigation is replete with multidisciplinary problems. The solution will require fundamental physics, chemistry, signal processing, and systems integration.

FY2005 Accomplishments and Results

We are conducting experiments to understand whether measurements made in the reflection mode at THz frequencies can provide adequate spectral information to enable characterization and ultimately, identification. Complicating issues such as material composition, surface roughness, target size, and physical orientation relative to the interrogating THz wave are being addressed. High-level analysis of a likely candidate system is being carried out to assess whether the goals are in the realm of possibility and to identify gaps in our scientific or technology base.

A full experimental campaign has been established that will use the University of California, Santa Barbara, THz facility, in particular their Fourier Transform and Infrared Spectrometer (FTIR) and Free Electron Laser (FEL) sources. Full spectra are currently being generated in their FTIR, and limited experimentation has been carried out using the FEL. The test materials have been "mock" HE and reduced-concentration HEs that qualify as harmless training aids.

Related References

1. Shen, Y. C., "Detection and Identification of Explosives Using Terahertz Pulsed Spectroscopy Imaging," *Applied Physics Letters*, **86**, August 2005.
2. "Existing and Potential Standoff Explosives Techniques," National Research Council of the National Academies, National Academy of Sciences, 2005.
3. *Proceedings of the DOE-NSF-NIH Workshop on Opportunities in THz Science*, Arlington, Virginia, February 12-14, 2004.

FY2006 Proposed Work

The combination of imaging and spectroscopy has been demonstrated as a very powerful technology in other regions of the spectrum. The fundamental reason for this is the ability of imaging to spatially localize EM signals. If spectroscopy is then performed on a pixel-by-pixel basis, the spectral signatures of threat species can be spatially isolated. This not only improves the signal quality of the spectroscopy (by reducing background noise), but also enables a contextual interpretation of the threat: "where is the bad stuff in relation to the rest of the viewed scene?" Thus, our standoff detection program will focus on hyperspectral sensing (imaging and spectroscopy) in the THz region of the EM spectrum. Our program for FY2006 is an application-driven (HE detection) systems approach.

IDENTIFICATION

Photonic Integrated Circuits: From Inverters to Sensors

Compound semiconductors are the building blocks of photonic integrated circuits due to their ability to both guide and emit light. The ability to etch structures with vertical and ultra-smooth surfaces and sidewalls (Fig. 1) is both a requirement for device fabrication and a challenge in these material systems. A core technology at LLNL is etching semiconductor materials (including GaAs, InP, and Si) along with dielectric materials with these requirements. We have achieved excellent results of single devices (etched facet lasers, ridge waveguides, and gratings). The next critical hurdle is to increase the integration level of these devices to fabricate photonic integrated circuits and advanced pixel arrays.

(a)

Sidewall scan

Surface scan

5kV, x 20k   1 μm
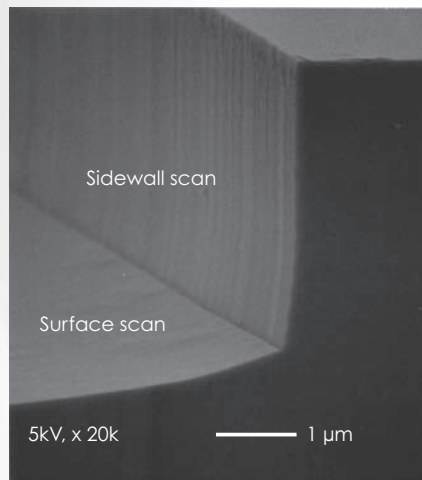
Figure 1. (a) Cross-sectional SEM photograph of etched GaAs, showing areas of scanning for atomic force microscopy analysis. The AFM data is summarized in the table (b) for both InP and GaAs materials.

(b)

AFM roughness data

	InP	GaAs
Sidewall	37 Å	33 Å
Surface	10 Å	13 Å

Project Goals

The fabrication processes in this project will satisfy specific ongoing efforts as well as increase our technology toolbox. Pixilated structures will be built with geometry of 100 x 100 pixels, with a fill factor of 50 %. For data routing we will build turning mirrors, splitters, and combiners (Fig. 2).

Relevance to LLNL Mission

We are supporting LLNL projects that require advanced InP- and GaAs-based processing technology. There are many different devices having broad applications that share the same fabrication hurdles. Having this technology will allow deployable microfabricated systems for several applications that are at the core of LLNL's national security mission, such as high-speed radiation-diagnostic devices for NIF; single-transient recording technologies; and devices for encryption applications and radiation detection.

FY2005 Accomplishments and Results

We have installed, set up, and configured an *in-situ* etch-point detection tool and temperature probe on the ECR plasma etch system. Figure 3 shows representative results. This allows the ability to etch materials with increased precision, which is a requirement of the 3-D integration in photonic integrated circuits. We have also produced a mask set for the fabrication of turning mirrors, which is our first element towards a higher level of integration. In the area of pixel arrays we have created recipes for pixels with a diameter from 250 nm to

For more information contact
Rebecca Welty Nikolić
(925) 423-7389
nikolic1@llnl.gov

2 μm with an aspect ratio as large as ~10. With the low-aspect-ratio pixels (similar to Fig. 3a) we have also optimized recipes for arrays 100 x 100 with a fill factor from 25 to 75 %.

Related References

1. Welty, R. J., C. E. Reinhardt, I. Y. Han, Y. Du, and S. J. Yoo, "Chlorine-Hydrogen ECR Etching of InGaAsP/InP," *International Semiconductor Device Research Symposium*, Washington DC, December 2003.

2. Thomas, S., III, K. K. Ko, and S. W. Pang, "Monitoring InP and GaAs Etched in Cl_2/Ar Using Optical Emission Spectroscopy and Mass Spectrometry," *American Vacuum Society*, **13**, 3, pp. 894-899, 1995.

3. Welty, R. J., T. C. Bond, E. Behymer, M. Pocha, G. Loomis, J. Wolfe, and S. Vernon, "Integrated Laser with Low-Loss High Index-Contrast Waveguides for OEICs," *SPIE - International Symposium on Integrated Optoelectronic Devices*, January 2005.

4. Pocha, M., T. Bond, R. Welty, S. Vernon, J. Kallman, and E. Behymer, "Gain lever Characterization in Monolithically Integrated Diode Lasers," S*PIE - International Symposium on Integrated Optoelectronic Devices*, January 2005.

5. Rangelow, I. W., "Critical Tasks in High Aspect Ratio Silicon Dry Etching for Microelectromechanical Systems," *Journal of Vacuum Science Technology A*, **21**, pp. 1550-1562, 2003.

FY2006 Proposed Work

We have an ECR plasma etch system for III-V-based compounds and an STS etcher for silicon-based materials. Using these tools we will etch the stated materials and evaluate the recipe that is used with scanning electron microscopy for the surface quality and surface profilometry for etch depth and rate determination. Using these known engineering techniques, our proposed work in the area of pixel arrays is to increase our aspect ratio from 10 to 25 for 2-μm pixels. These high-aspect-ratio pixels with an etch depth of 50 μm will require more robust masking materials. In the area of photonic integrated circuits our proposed work is to integrate individual laser elements with signal routing elements, such as turning mirrors, splitters, and combiners for higher device functionality.
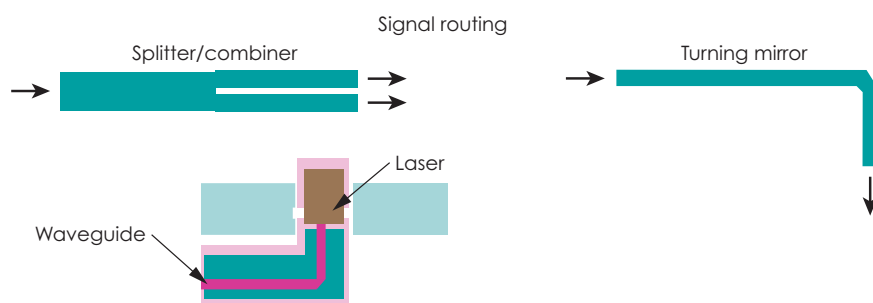
Figure 2. Schematics of splitters, combiners, and turning mirrors and their integration with laser and waveguide devices.
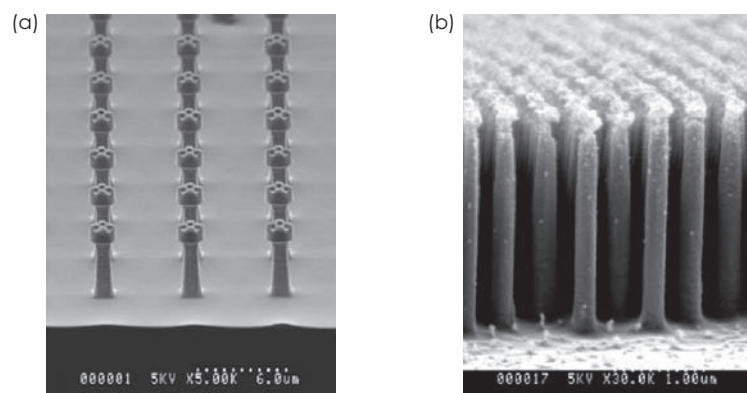
Figure 3. Representative SEM cross-sections of pixels etched with deep RIE with (a) pixel diameter of 2 μm, separation of 4 μm and an etch depth of 3.9 μm; and (b) nano-pillars of ~ 200 nm (with near equivalent separation) and an etch depth of 2.3 μm.

Transient Sampling Data Recorder

Many transient physical phenomena studied at LLNL exhibit complex dynamics that require picosecond or subpicosecond temporal resolution, which is faster than can be achieved with commercial storage oscilloscopes.
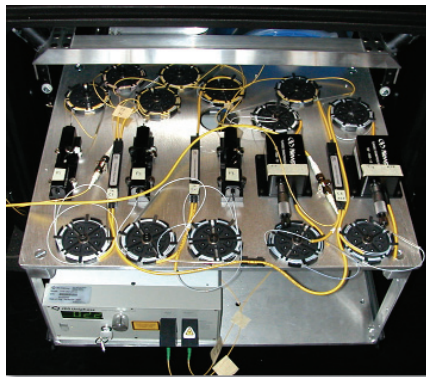
Figure 1. Transient recorder fiber-optic package.

One way to achieve better temporal resolution is to use the optical portion of the electromagnetic spectrum, which has several orders of magnitude greater bandwidth than the microwave portion used by fast electronics.

The transient sampling data recorder (Figs. 1 and 2) works by converting an electrical signal into an optical signal, which is injected into a recirculating fiber-optic loop. Each time the signal circulates in the loop, some of the signal is picked off and recorded with a sampling oscilloscope. After being sampled, the signal is regenerated using an erbium-doped fiber amplifier, and injected back into the loop. The process is repeated until a composite record of the original signal has been recorded on the sampling oscilloscope. The repeated sampling of the signal stored in the recirculating loop increases the temporal resolution.
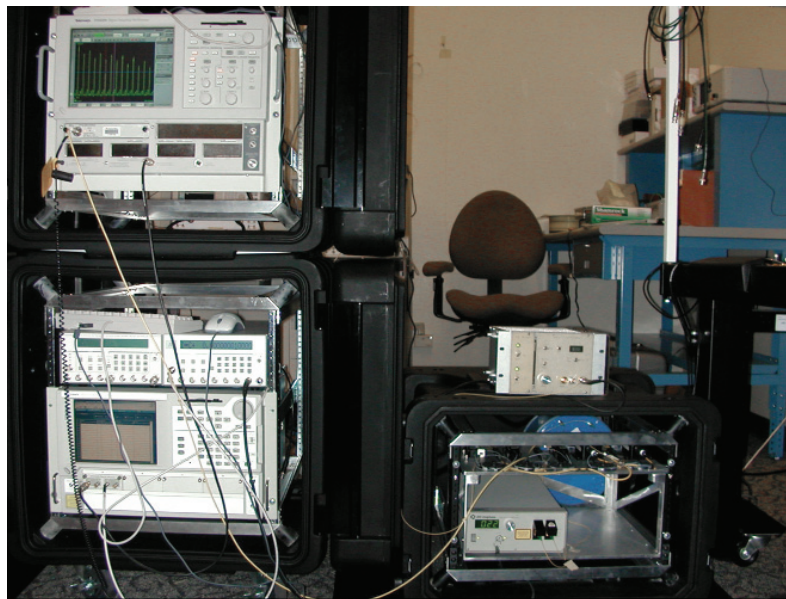
Figure 2. Transient recorder prepared for use on a gas-gun shot.

For more information contact
Craig S. Halvorson
(925) 422-6580
halvorson1@llnl.gov

Project Goals

The goal is to build a precision ultrafast data recorder that can be used in advanced diagnostics for shock physics, high-energy physics, and weapons testing.

Relevance to LLNL Mission

Ultrafast data recorders could reveal previously unresolved structure in the reaction history of exploding nuclear weapons, if testing should resume. Advanced diagnostics for high-energy physics at NIF require picosecond resolution to follow the evolution of complex processes driven by nanosecond and picosecond laser pulses. The next generation of shock-physics experiments will require a temporal resolution that cannot be provided by commercial storage oscilloscopes. A practical ultrafast transient data recorder could significantly advance weapons technology, high-energy-physics diagnostics, and shock-physics diagnostics.

FY2005 Accomplishments and Results

The basic technology was completed in FY2004. In FY2005, our emphasis was on determining the limits of the technology and producing a unit that could be used in the field.

The prototype was found to be sensitive to vibration. Vibration changes the conformation of the single mode optical fiber, changing the state of polarization so that it no longer matches as the signal recirculates around the loop. A series of experiments revealed that simple vibration isolation (placing 2 in. of foam under the fiber-optics unit) resulted in large improvements in the signal-to-noise ratio.

Trigger reliability was 90%; the cause for the lost triggers was the startup of the sampling oscilloscope DSP controllers. An alternative configuration using sampling modules was created. Eliminating the DSPs should also eliminate lost triggers. Sampling modules have an additional significant advantage in that they can be used in parallel, dramatically increasing the overall sampling rate.

Ultimately, the prototype data recorder was found to be capable of 50 GS/s, which is about 20% faster than the fastest commercially available storage oscilloscope. The transient that was recorded (Fig. 3) measured a 48-ps risetime on a test pulse that had an average risetime of 42 ps.

With the use of 10 sampling modules in parallel, the sample rate could be extended to 500 GS/s, which opens new possibilities for ultrafast diagnostics.

Related References

1. Sun, Y., J. L. Zyskind, and A. K. Srivastava, "Average Inversion Level, Modeling, and Physics of Erbium-Doped Fiber Amplifiers," *IEEE Journal of Selected Topics in Quantum Electronics,* **3**, p. 991, 1997.
2. Giles, C. R., J. M. Khan, S. K. Korotky, J. J. Veselka, C. A. Burrus, J. Perino, and H. M. Presby, "Polarization Effects on Ultralong Distance Signal Transmission in Amplified Optical-Fiber Loops," *IEEE Photonics Technology Letters,* **3**, p. 948, 1991.
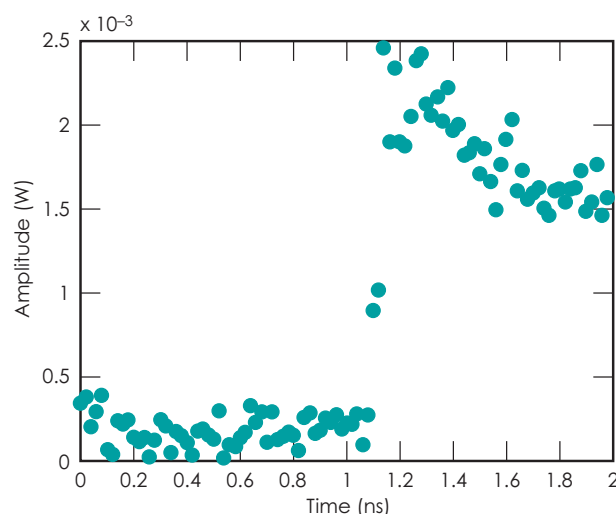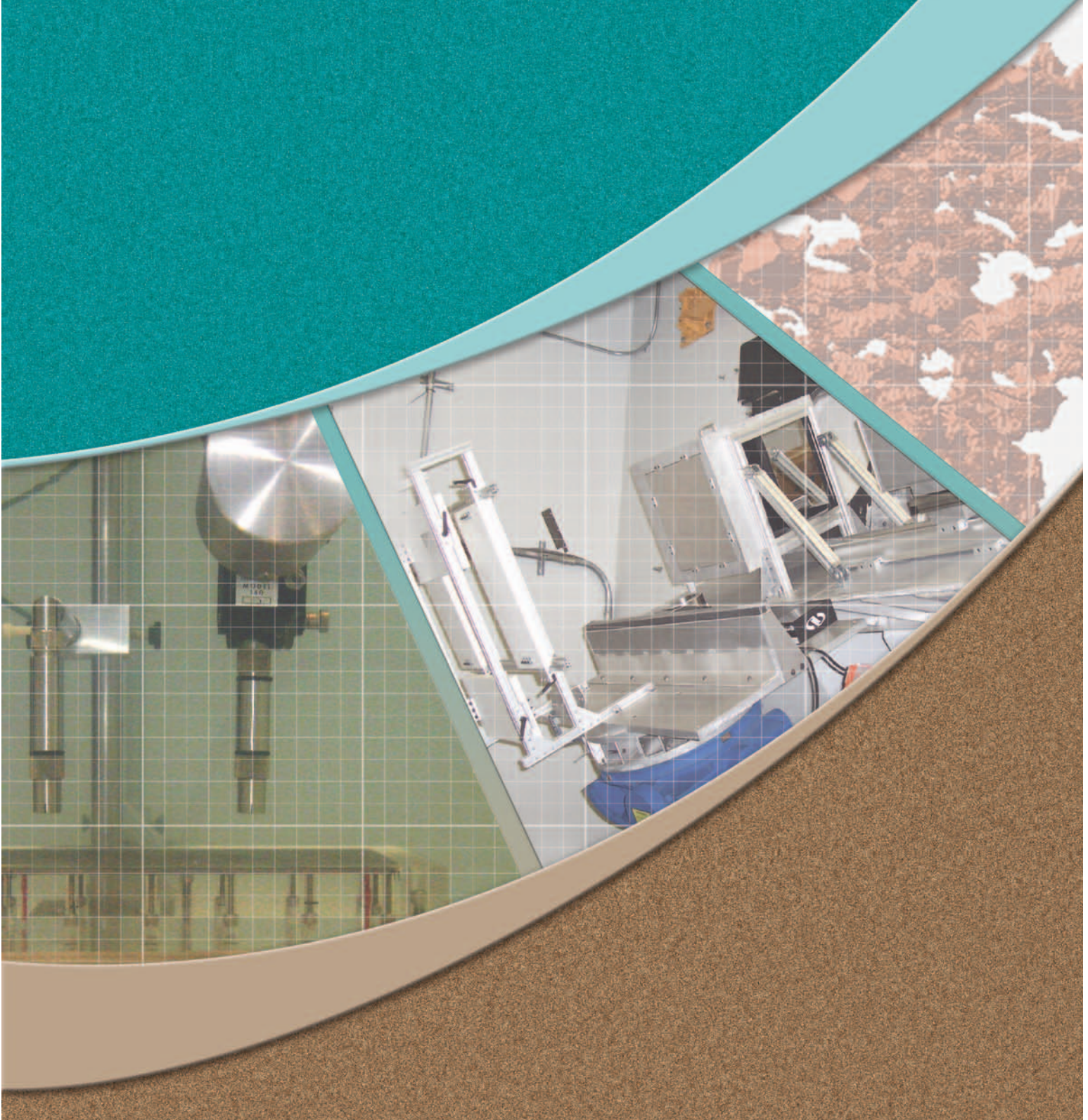

Figure 3. Transient record at 50 GS/s. The pulse risetime was 42 ps; the transient sampler recorded a 48-ps risetime.

Nondestructive Characterization

Acoustic Characterization of Mesoscale Objects

Mesoscience is an emerging area of science and engineering that focuses on the study of materials with dimensions, features, and structures that range from a few millimeters down to a few micrometers. Mesoscale nondestructive characterization technologies are required that can 1) penetrate into or through a few millimeters of diverse materials, and 2) provide spatial resolution of about a micrometer.

In addition to the spatial resolution requirements, many mesoscale objects require a noncontact technique to avoid damaging fragile surfaces. An acoustic technique is attractive because it offers high sensitivity to features such as thickness and interface quality that are important to mesoscale objects.

Project Goals

This research will achieve micrometer resolution characterization by extending the range of laser-acoustic testing (Fig. 1) to GHz frequencies. Materials and the geometry of components used in most LLNL mesoscale objects necessitate the use of a noncontact technique at frequencies from 100 MHz to 10 GHz. This frequency range is required to acoustically characterize features from 5 to 0.5 μm in size. For LLNL applications, mesoscale structures are on the order of 25 to 200 μm thick.

Figure 1. Schematic of laser-acoustic technology. Laser-acoustic testing uses a pulsed laser as a source to generate acoustic waves and a laser interferometer to detect acoustic waves. The source and receiver can be on opposite sides (as shown) or on the same side of the object. The acoustic wave travels through the object before it is detected. Use of a short-pulse laser gives temporal resolution to the detected signal.
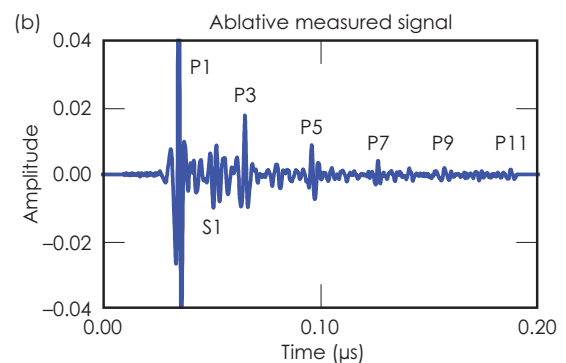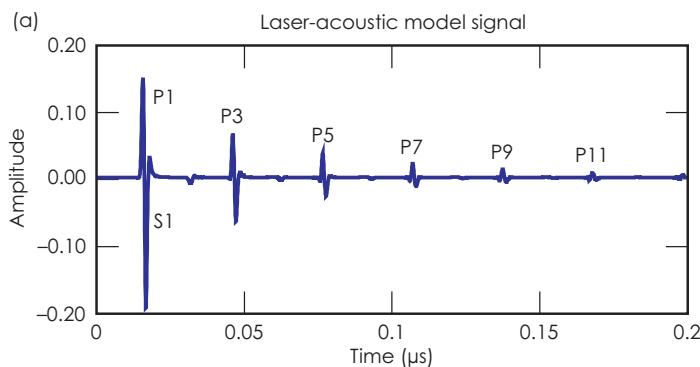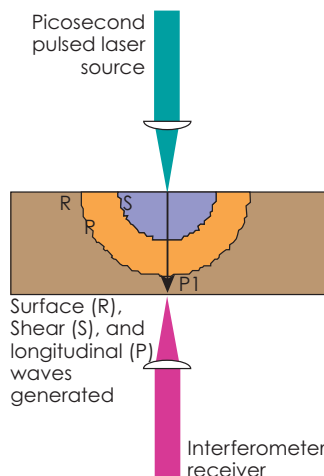
Figure 2. Results from experiments using the configuration in Fig. 1. Temporal signals from (a) modeled and (b) measured signals for a 100-μm-thick aluminum film show good correlation. Each peak in the signal represents an arrival of an acoustic wave at the epicentral location. The model in (a) combines a 2-D analytical laser-interaction solution with the LLNL E3D finite-difference acoustic wave propagation code. The modeled signal shows only longitudinal components (P) and does not capture shear (S) modes adequately. The measured signal in (b) shows higher shear components (S1) and has measurement noise.

For more information contact
Diane Chinn
(925) 423-5134
chinn3@llnl.gov

Relevance to LLNL Mission

This work directly addresses metrology and characterization gaps of interest for LLNL's mesoscale manufacturing R&D. As a characterization technique, the work also contributes to our Sensors-to-Knowledge toolbox. Of the different mesoscale characterization challenges at LLNL, the most relevant are the targets prepared for OMEGA and NIF. This proposal impacts the DNT, NIF, Engineering, and Chemistry and Materials Science Directorates through laser target fabrication and characterization.

FY2005 Accomplishments and Results

Major accomplishments to date are:
1. the determination of ultrasonic velocity and attenuation in several materials important to LLNL, at frequencies ranging from 500 MHz to 1 GHz, for thermoelastic and ablative wave generation;
2. the validation of acoustic and laser-acoustic models with experimental data (Fig. 2); and
3. the assembly of a prototype GHz laser ultrasound (UT) system (Fig. 3). The prototype system was assembled at Boston University and was transferred to LLNL in FY2005. This work is described in Reference 3.

Related References

1. Chambers, D., D. Chinn, and R. Huber, "Optical Mapping of the Acoustic Output of a Focused Transducer," *Proceedings of the 147th Acoustical Society of America Meeting, 2004.*

2. Hebert, H., F. Vidal, F. Martin, J.-C. Kieffer, A. Nadeau, and T. W. Johnston, "Ultrasound Generated by a Femtosecond and a Picosecond Laser Pulse Near the Ablation Threshold," *J. Appl. Physics,* **98**, 2005.

3. Huber, R. H., D. J. Chinn, O. O. Balogun, and T. W. Murray, "High Frequency Laser-Based Ultrasound," *Review of Progress in Quantitative Nondestructive Evaluation,* August 2005.

4. Martz, Jr., H. E., and G. F. Albrecht, "Nondestructive Characterization Technologies for Metrology of Micro/Mesoscale Assemblies," *Proceedings of Machines and Processes for Microscale and Mesoscale Fabrication, Metrology, and Assembly,* ASPE Winter Topical Meeting, Gainesville, Florida, pp. 131-141, January 22-23, 2003.

5. Scruby, C., Laser Ultrasonics: Techniques and Applications, Adam Hilger, New York, 1990.

FY2006 Proposed Work

Our work to date has enabled new research on acoustic wave generation, scattering mechanisms, and interface characterization in the GHz regime. Research in FY2006 will cover these specific areas:
1. Identifying the thermoelastic-ablative threshold for materials through modeling is important to applications requiring "sub-ablative" wave generation. GHz laser-acoustic wave generation will be studied with advanced laser-interaction models.
2. Interfaces such as repeating structures and gaps sized on the order of micrometers are two areas where performance of GHz waves is unknown. Capabilities of GHz characterization of interfaces will be studied using models and experiment.

Figure 3. The tabletop GHz laser-acoustic system uses a picosecond Nd:Yag laser to generate the acoustic wave and a frequency-doubled Nd:Yag laser in continuous-wave mode for interferometric detection of the acoustic wave. The source laser has a 4-μm spot, a 1.1-ns pulse length, and operates at approximately 0.15 mJ in ablative mode. The detection laser has a 600-nm spot.

Phase Effects on Mesoscale Object X-Ray Attenuation Radiographs

We are investigating the nondestructive characterization (NDC) of mesoscale objects—objects that have mm extent with μm features. Here we confine our discussions to x-ray digital radiography and computed tomography methods.

Project Goals

The goal is object recovery algorithms including phase, to enable emerging high-spatial resolution x-ray radiographic methods to "see" inside or image mesoscale-size materials and objects. To be successful, our characterization effort must be able to recover the object function to 1 μm or better spatial resolution over a few mm field-of-view, with very high contrast.

Relevance to LLNL Mission

Specific LLNL programs that would benefit from this new capability include the study of explosive samples for DoD and DOE; high-energy-density physics for DNT; novel sensors for NAI; and inertial confinement fusion experiments for NIF.

FY2005 Accomplishments and Results

Our approach includes the research, development and validation of algorithms to model phase-contrast effects observed in x-ray radiographic systems, and to use these algorithms for quantitative object recovery. This requires three tasks. First, we are modifying HADES to model x-ray phase contrast and are investigating whether multi-slice techniques within the object are needed to fully capture the physics seen in x-ray data. Second, we are developing object recovery approaches. Third, we are validating these simulations and object recovery

(a) (b)
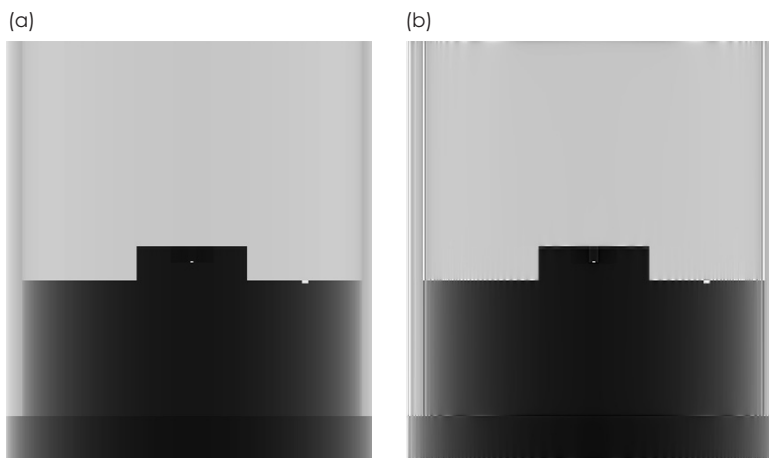
Figure 1. HADES simulated radiographs of cylindrical reference standard: (a) without and (b) with x-ray phase. Note x-ray phase effects create the well-known bright and dark edges.

Figure 2. Transmission profiles of the (a) single and (b) double C fiber projections. The measured data (dots) were collected by a Cu-anode source and a direct detection CCD camera. The simulated straight ray (green curve) and the multi-slice (dark blue curve) profiless have been convolved with a single Gaussian line-spread function with a Gaussian sigma value of 3.6 and 4.0 for the single and double fiber data, respectively. Note the very good agreement between both simulated results and the empirical data.
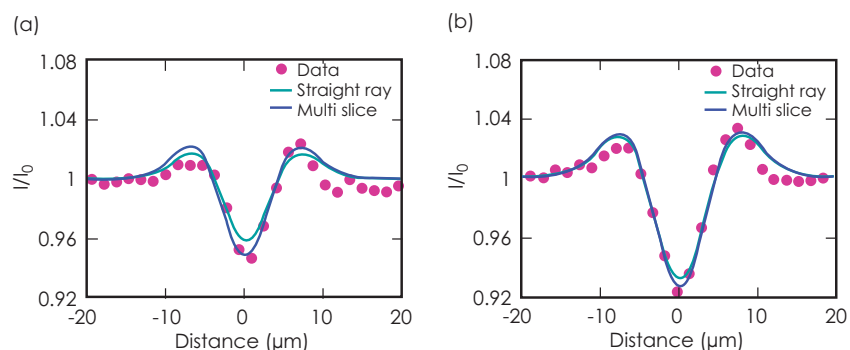
For more information contact
Harry E. Martz, Jr.
(925) 423-4269
martz2@llnl.gov

approaches against x-ray systems using well-known objects.

At the end of this R&D, we will have a set of validated x-ray forward modeling codes including the effects of phase, and an understanding of the current object recovery methods, applications, and limitations.

In the past year, we have fully integrated the Fresnel-Kirchoff diffraction theory into HADES modeling (Fig. 1). We have also merged into HADES the LBNL photoelectric absorption and phase cross-sections with the LLNL Evaluated Photon Data Library cross-sections for Compton and Rayleigh scattering, as well as pair production.

We have reached the point in x-ray imaging where the spatial resolution and object dimensions could theoretically result in the wave diffraction effects within the object becoming significant. We studied this possibility numerically using four simulation codes that incorporate x-ray phase effects. We refer to them as 1) the paraxial approximation multi-slice

simulation code; 2) a Kirchoff propagation simulation code; 3) a Mie-type analytical simulation code; and 4) HADES.

We used the paraxial approximation code with and without a multi-slice method and the Kirchoff propagation code at worst-case x-ray energies of ~8 keV and compared these results to empirical data. The conclusion, based on the results of the validated simulation codes, is that diffraction effects within the object are insignificant for $\geq$ 8 keV x-ray data with ~1-μm spatial resolution, and for objects up to 10 mm (Fig. 2).

We have applied multi-grid techniques to both synchrotron and non-synchrotron data (Fig. 3). Comparisons with simulated data have shown the range of these techniques to be limited to cases of 90% transmission or better for simple geometric objects. Most of our data are on the order of 20% transmission for objects with complex geometry; thus, this object recovery method is not very useful for most of our data.

The "multi-slice" phantom is fabricated to contain either 5-μm diameter carbon fibers or 4-μm outer-diameter tungsten wires in various pre-selected configurations. The fibers or wires are attached to a base and slide that are adjustable in separation length from 2 to 10.2 mm. Three 5-μm carbon fibers are inserted into the multi-slice phantom and the phantom is oriented such that the fibers are vertical in the digital radiographs (Fig. 3a) and rotation can be used to align the two carbon fibers that are separated by 10.2 mm.

Related References

1. Aufderheide, M. B., D. M. Slone, and A. E. Schach von Wittenau, "HADES, A Radiographic Simulation Code," *Review of Progress in Quantitative Nondestructive Evaluation,* **20A**, AIP Conference Proceedings 557, pp. 507-513, 2000.

2. Aufderheide, M.B., A. Barty, and H. E. Martz, Jr., "Simulation of Phase Effects in Imaging for Mesoscale NDE," *Review of Progress in Quantitative Nondestructive,* **24A**, AIP Proceedings 760, pp. 663-670, 2004.

3. Hau-Riege, S. P., "Extending the Size-Parameter Range for Plane-Wave Light Scattering from Infinite Homogeneous Circular Cylinders," *Appl. Opt.,* 2005.

4. Martz, Jr., H. E., and G. F. Albrecht, "Nondestructive Characterization Technologies for Metrology of Micro/Mesoscale Assemblies," *Proceedings of Machines and Processes for Microscale and Mesoscale Fabrication, Metrology, and Assembly,* ASPE Winter Topical Meeting, Gainesville, Florida, January 22-23, pp. 131-141, 2003.

(a)
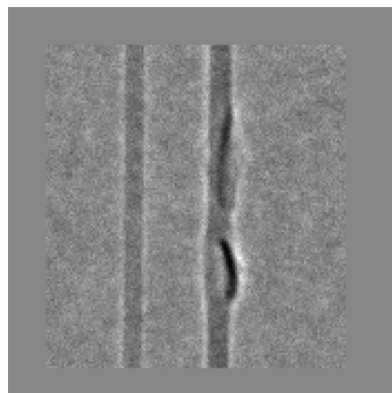
(b)
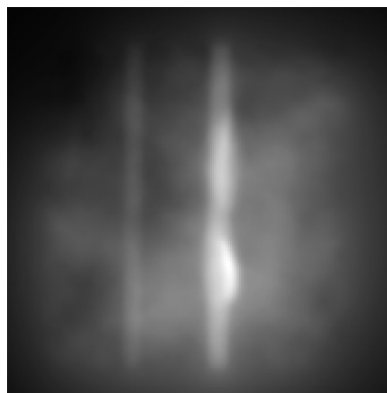
Figure 3. (a) digital radiograph of the two non-aligned C fibers acquired at 99 kV and 41 µA and pixel size of 0.6 µm at the object center; (b) electron density (related to x-ray phase) results from application of the weak absorption and uniform irradiance method on the digital radiograph shown in (a).

The Structure and Properties of Nanoporous Materials

The aim of the proposed research is to determine how the structure of highly porous metal and metal oxide foams changes with temperature, pressure, and surface environment. The research will also seek to understand how changes in the nanostructure of these foams alter their mechanical behavior. How these porous materials deform with thermal stresses and surface tension will be examined with a combination of Small Angle X-ray Scattering (SAXS) and high-resolution Synchrotron Radiation Computed Tomography (SRCT). Theoretical treatments of foam strength are based on the local stresses exceeding the yield strength in ductile metallic foams, or the flexural strength in brittle foams. However, these theories have never been tested at the densities and nanometer-length scales of the foams we propose to study.

Project Goals

Our goals are as follows:

1. High-spatial-resolution SAXS and SRCT measurements of the pore structure in metal oxide aerogels to determine the density, pore size, pore distribution, and aspect ratios of the cell backbone.
2. Extremely high-resolution diffraction imaging to determine the structure of the lattice of a select, low-density metal oxide foam and provide a basis for interpreting the SAXS data.
3. Finite-element modeling, using the structures determined in the first goal to study the effects of mechanical loading on the cell structures, and to map out relationships among processing, density, and strength. Thermal gradients, thermal stresses, and wetting will be explored.

Figure 1. Image showing the scattering intensity as a function of the wave vector, Q. Shape factors and the slope of the Porod region are characteristic of a rod-like structure with rough surfaces.
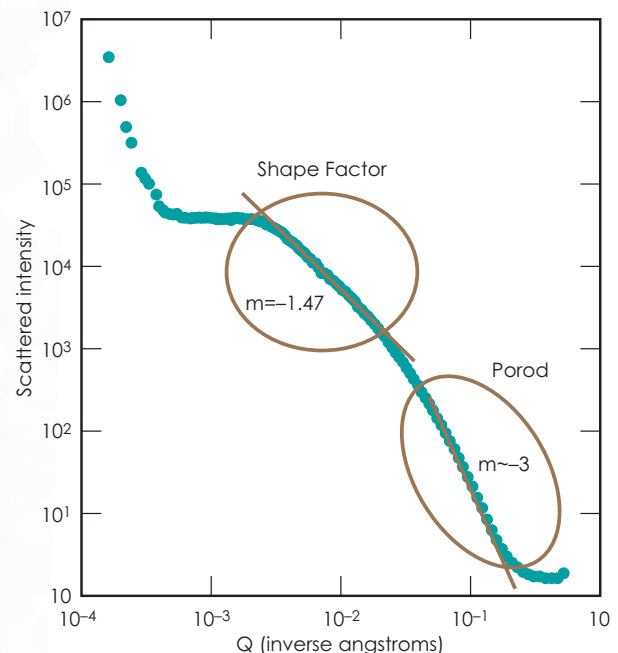
For more information contact
Anthony Van Buuren
(925) 423-5639
vanbuuren1@llnl.gov

4. Determining the extent of any anisotropy in lattice architecture, and improving spatial resolution to characterize graded-density structures.

Relevance to LLNL Mission

This program develops critical experimental technologies for many LLNL applications. A key deliverable will be the ability to predict the mechanical properties of nanoporous materials and characterize gradient-density foam microstructures for future laser targets.

FY2005 Accomplishments and Results

Ultra-small-angle x-ray scattering (USAXS) was performed at the Advanced Photon Source on a 100-mg/cc tantalum oxide (Ta_2O_5) foam. The scattering as a function of wave vector, Q, is indicative of scattering from a collection of rod-like structures with a rough surface (Fig. 1).

To get a complete understanding of the 3-D structure of the foam, a series of images were obtained using a lensless diffraction technique. The cell structure was determined from this image (Fig. 2).

The lensless images have enabled us to understand the meaning of the length scales determined from the USAXS experiments. We are confident that the USAXS data is providing us details about the cell size in these foams from 10 to 1000 nm.

We used a finite-element simulation to estimate the apparent elastic modulus of the foam structures using NIKE3D periodic boundary conditions. An apparent Young's modulus (E_s/E_b, where E_s is the modulus of the structure and E_b is the modulus of full-density Ta_2O_5) of 1.2×10^{-4} was determined. This is less than the value of 7.5×10^{-3} predicted from theory. However, theoretical models assume that all the mass is distributed within beams of uniform

shape. An attempt was made to distinguish between mass associated with nodes and mass associated only with the beams. We established that, for the 100 mg/cc Ta_2O_5 foam, approximately 85% of the mass was confined to the nodes. Correcting the scaling laws for the reduced apparent mass lowered the theoretical estimate to 1.7×10^{-4}, in excellent agreement with the simulations.

FY2006 Proposed Work

We plan to continue the characterization of pore structure as a function of preparation condition for Ta_2O_5 and other metal oxide foams, and determine how the pore structure is affected by mechanical deformation. Also we will start the high-resolution density measurements on the graded-density materials.
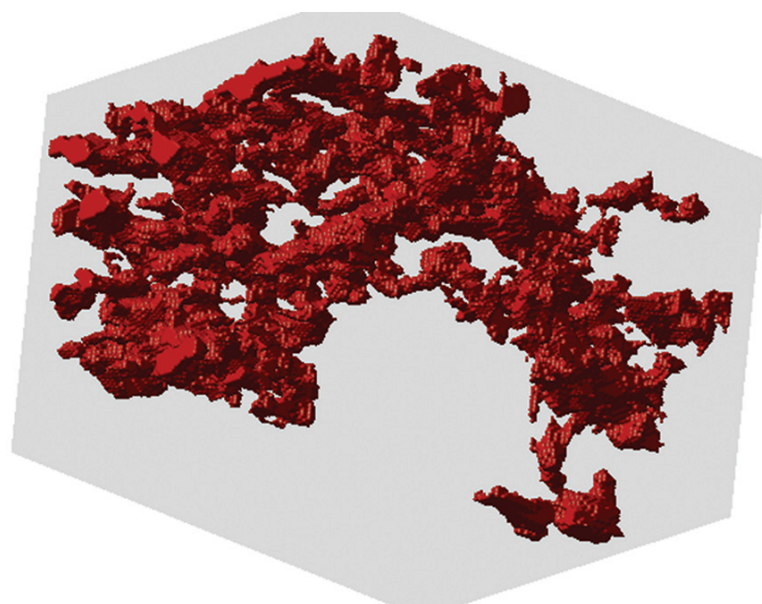
Figure 2. High-resolution reconstruction of a 500-nm cube from the interior of the foam (resolution 13 nm).

As-Built Modeling Translation Tool

A specific need exists within the "as-built" modeling effort at LLNL to facilitate the transfer of as-built geometries into certain data/image-processing tools, mesh-generation tools, and analysis codes. This project addresses that need.

Project Goals

The objective of this project was to create a simple tool to aid in formatting and converting data between multiple mesh-based geometry formats. The tool links a number of useful finite-element mesh-generation and image-processing tools with analysis codes within LLNL.

Relevance to LLNL Mission

This project directly supports LLNL's as-built modeling effort by enabling the transfer of data between software tools. The basic idea and goal of as-built computational modeling is to incorporate the most representative geometry and material information for a fabricated object into engineering and physics simulations, using nondestructive characterization and metrology techniques to provide the as-built feature information. As-built features might include geometry deviations (such as asymmetries and dents) or material anisotropies and flaws (such as inclusions, voids, cracks, delamination, and ablation regions). The features might originate from the manufacturing process or from the object's being exposed to a certain physical environment during service conditions. By incorporating more representative geometry and material features as initial conditions, the uncertainty in the finite-element simulation results could potentially be reduced, providing a new understanding of the event and object being modeled.

FY2005 Accomplishments and Results

A simple GUI-based Perl translation tool (see figure) was created. The tool eliminates the need to create a special translation script each time a transfer of data between certain software tools is required. This saves the analyst time and effort, and has already proven useful for analysts at LLNL and for outside contractors. Although a limited set of formats and utilities have been currently linked, the utility is easily expandable to include additional formats.

Some of the format conversion paths include:
1. Cubit (Exodus II) format → ALE3D, DYNA3D, NIKE3D, and Visualization Toolkit (VTK);
2. VTK (polydata triangle element) format → Cubit (facet surface mesh) and TrueGrid (ViewPoint surface mesh);
3. VTK (polydata line element) format → Cubit (line journal commands) and TrueGrid (3-D curves);
4. LLNL Dyna3D format → Cubit (Exodus II) format;
5. Abaqus format → ALE3D and VTK formats; and
6. LS-Dyna3D format → ALE3D and VTK formats.

As an example, we have completed the link: VTK mesh- or line-based surface → Cubit or TrueGrid format.

For more information contact
Edwin J. Kokko
(925) 422-4246
kokko1@llnl.gov

This conversion path is useful, since several utilities (Visit, ParaView) exist that can manipulate mesh- and image-based geometry for export to the VTK format. For example, an as-built surface or profile of interest could be isolated within these utilities using commands such as filtering, thresholding, slicing, decimation, and smoothing. The final isolated surface or profile could then be exported from the tool in the VTK format and converted with the translation utility into a useful Cubit or TrueGrid format. Once imported, surface and line data is useful for creating as-built finite-element meshes for subsequent analyses.

Schematic of input and output to the translation utility.

Super-Resolution Algorithms for Ultrasonic NDE Imaging

One of the most desired results from an NDE test of a mechanical part is a segmented image or image cube, showing the locations and physical characteristics of cracks, inclusions, voids, delaminations, ablations, and other flaws. A key NDE goal is to obtain images having the best possible spatio-temporal resolution. Unfortunately, the resolution of all ultrasonic measurements is severely limited by the inherent band-limited spectral transfer function of ultrasonic transducers, the uncertainty principle, and the diffraction limit. In the time domain, the transducer causes severe ringing that greatly limits resolution.

An earlier project prototyped and tested an algorithm that produced an optimal least-squares Wiener estimate of the impulse response of the material under test. The Wiener-based algorithm helped reduce the ringing. Studies have shown that this ringing can be reduced further through the use of advanced super-resolution algorithms.

Project Goals

The goals of this project are to implement and reduce to practice the Bandlimited Spectrum Extrapolation algorithm in combination with the Wiener algorithm, in an accessible form to provide an important new software tool for NDE applications. The goal for the current effort was to implement the super-resolution algorithm for processing 1-D waveforms, and report the results of tests using simulated data and limited existing programmatic data.

Relevance to LLNL Mission

Resolution enhancement will directly benefit all LLNL programs that require ultrasonic imaging tests.

FY2005 Accomplishments and Results

Extensive work was done on a code structure that would allow for a phased implementation effort. The phases to be considered were: the implementation of the super-resolution algorithm; the addition of the Wiener

Figure 1. Schematic of the ultrasonic image-formation process. A single pulse-echo A-scan is acquired at a fixed position of the transducer. The ideal reflection signal is a sequence of impulses, as shown on the right. The range resolution of the A-scan is limited by the ringing distortion introduced by the band-limited frequency response of the transducer.
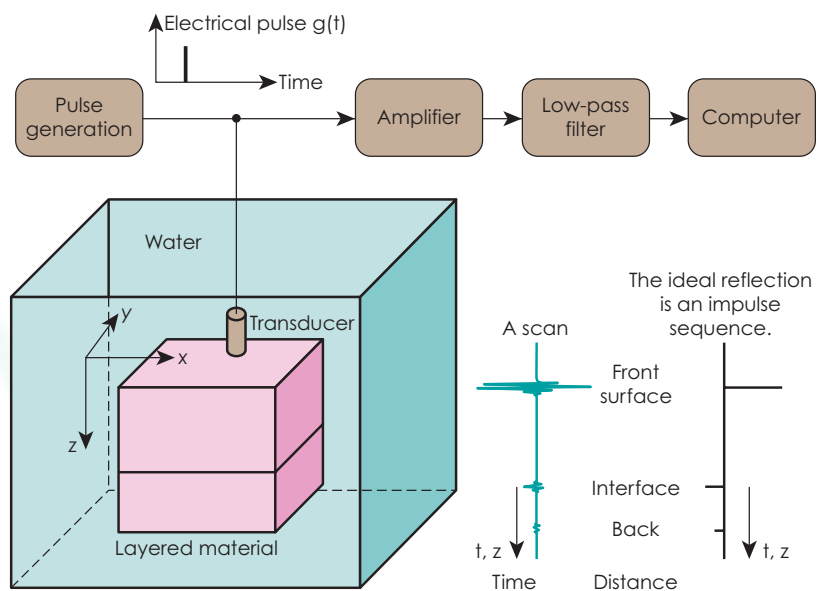
For more information contact
Grace A. Clark
(925) 423-9759
clark9@llnl.gov

algorithm; extension to 2-D and 3-D data processing; and the addition of a GUI.

The algorithms need to have a number of parameters defined by the user. We have included a user-defined parameter file to control and record the processing on each signal.

The Bandlimited Spectrum Extrapolation (BSE) code was implemented and tested with simulated test signals. The Wiener processing was added, and the entire
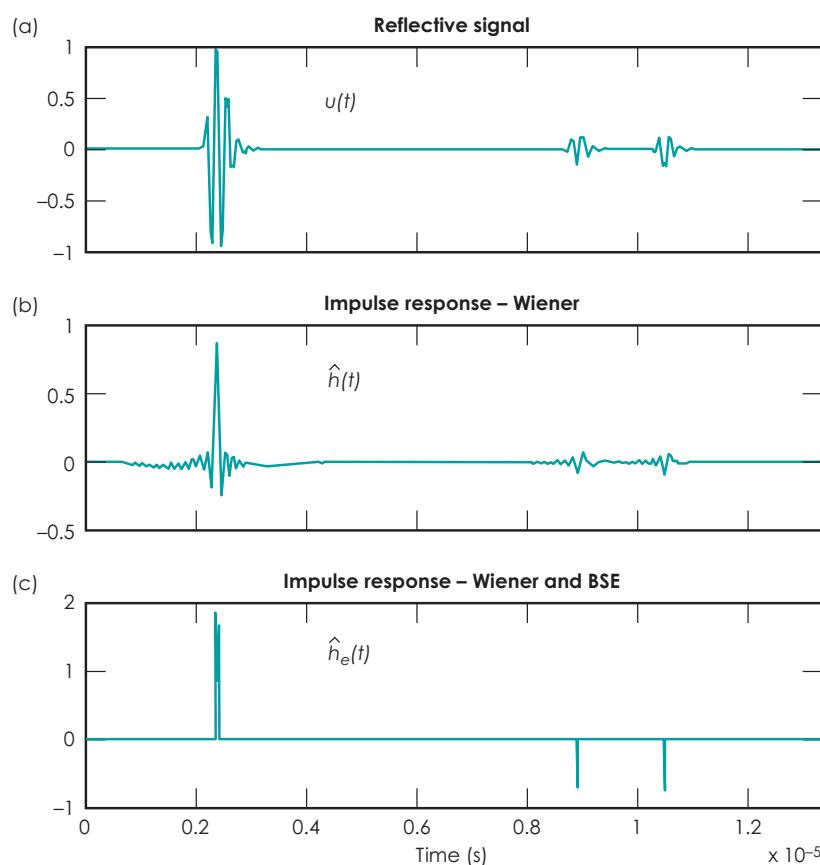
system was tested on signals from controlled experiments using a known "phantom" part. Figure 1 shows a schematic of the ultrasonic image-formation process.

Figure 2 shows the result of processing a signal acquired from a test phantom containing flat bottom holes. The original measured signal shows a reflection from the front surface of the phantom, followed by reflections from the top and bottom of the hole. The original signal contains

ringing at each interface. The impulse response estimated by the Wiener algorithm reduces the ringing, and the Bandlimited Spectrum Extrapolation algorithm nearly eliminates the ringing.

Related References

1. Clark, G. A., D. M. Tilly, and W. D. Cook, "Ultrasonic Signal/Image Restoration for Quantitative NDE," *NDT International*, **19**, 3, June 1986.

2. Candy, J. V., G. A. Clark, and D. M. Goodman, "Transient Electromagnetic Signal Processing: An Overview of Techniques," Time Domain Measurements in Electromagnetics, E. K. Miller, Ed., Van Nostrand Reinhold Co., New York, pp. 416-455, 1986.

3. Clark, G. A., and F. L. Barnes, "Ultrasonic Signal Resolution Enhancement for Adhesive Thickness Measurements," *Review of Progress in Quantitative NDE*, Williamsburg, Virginia, June 21-28, 1987.

4. Papoulis, A., and C. Chamzas, "Improvement of Range Resolution by Spectral Extrapolation," *Ultrasonic Imaging 1*, pp 121-135, 1979.

5. Youla, D. C., "Generalized Image Restoration by the Method of Alternating Orthogonal Projections," *IEEE Trans. Circuits and Systems*, *CAS-25*, **9**, September 1978.

FY2006 Proposed Work

The work for next year will involve the implementation of a user-friendly GUI for the system, and extending the software to include 2-D- and 3-D processing, so we can process volumetric data. Then the algorithms will be extensively tested and validated using existing programmatic data sets.

Figure 2. Results of processing a signal acquired from a test phantom, an aluminum block with nine known drilled, flat-bottom holes. (a) A single reflected signal (A-scan) u(t). (b) The estimated impulse response h(t) of the aluminum block. (c) The extrapolated impulse response h_e(t) of the block, obtained by extrapolating the spectrum of the impulse response estimate. The ringing in the signal is greatly reduced, improving the resolution of thickness measurements and flaw characterizations.

Prototype Ultrasonic Inspection System for Structural Damage

This project is constructing ultrasonic hardware that will generate images of damage to the surface of structures, such as optics with a set of multiple sensors applied to the outside surface and normal to the surface being inspected. The system will also be portable, enabling field-testing of optics or other structures such as weapons. A prototype will be built and demonstrated on glass optics with programmed defects and actual laser damage to assess detection and sizing capabilities.

Project Goals

Our goal is to detect and size actual laser damage on an optic with defects ranging in size from 100 μm to 10 mm or larger, by generating images of a laser-damaged optic that are easily interpreted by those less familiar with ultrasonics.

Relevance to LLNL Mission

This project will demonstrate a prototype system that could be subsequently deployed to inspect NIF optics on the target chamber or in the beamline. The technology is also applicable to generating 3-D images of weapons components or systems without scanning.

FY2005 Accomplishments and Results

We are investigating the application of two ultrasonic techniques, low-frequency longitudinal waves and high-frequency shear waves, to imaging surface damage in optics. To evaluate the techniques, we are using fused silica samples with programmed machined damage as well as a sample with actual laser-induced damage.

We performed experiments on an optic with programmed hemispherical defects machined into the surface. Defect sizes ranged in diameter from 0.5 mm to 5 mm. An array of 10-MHz shear wave sensors was placed on adjacent sides to collect high-frequency shear wave data. The data sets were merged by taking the product, to form an amplitude map of the reflection. The shear wave technique was able to accurately image and size all the machined defects.

The image in Fig. 1 shows the boundary of the defect. Accurate sizing is a significant advance, since previous acoustic methods failed to accurately size defects.
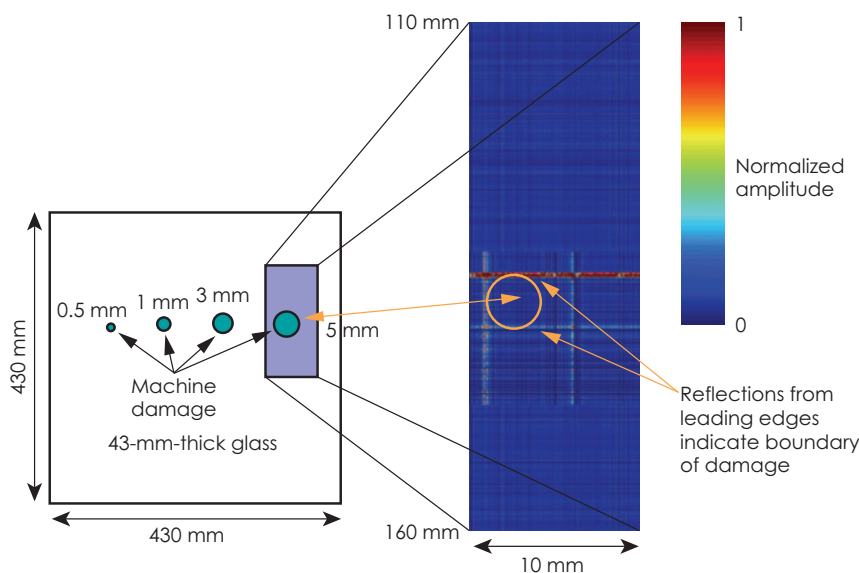
Figure 1. Image of a 50-mm-x-10-mm region showing a hemispherical machine damage site.

For more information contact
Michael J. Quarry
(925) 422-2427
quarry1@llnl.gov

Low-frequency longitudinal data was also taken using a 1-MHz array with omni-directional sensors. Tomographic techniques are currently being applied to the longitudinal data to generate images as well.

Initial experiments were also performed on an optic with laser damage induced under no vacuum loading conditions. A single 10-MHz shear-wave element was able to detect laser damage of sizes 0.5 mm to 8 mm in diameter (Figs. 2 and 3). A higher signal-to-noise ratio with virtually no effects of mode conversion or multiple echoes from the bottom surface was observed compared to previous 5-MHz longitudinal acoustic data.

Related Reference

Martin, P., D. Chambers, and G. Thomas, "Experimetal and Simulated Ultrasonic Characterization of Complex Damage in Fused Silica," *IEEE Transactions on Ultrasonics, Ferroelectrics, and Frequency Control*, **49**, 2, pp. 255-265, 2002.

FY2006 Proposed Work

In FY2006 algorithms and data collection will be optimized. Experiments will be performed on an optic with actual laser damage created while under a vacuum. Images of actual laser damage will be generated with the optimized techniques. Postprocessing techniques will also be done to make improvements. The final imaging capabilities of the low-frequency longitudinal tomography and high-frequency shear techniques will be compared.
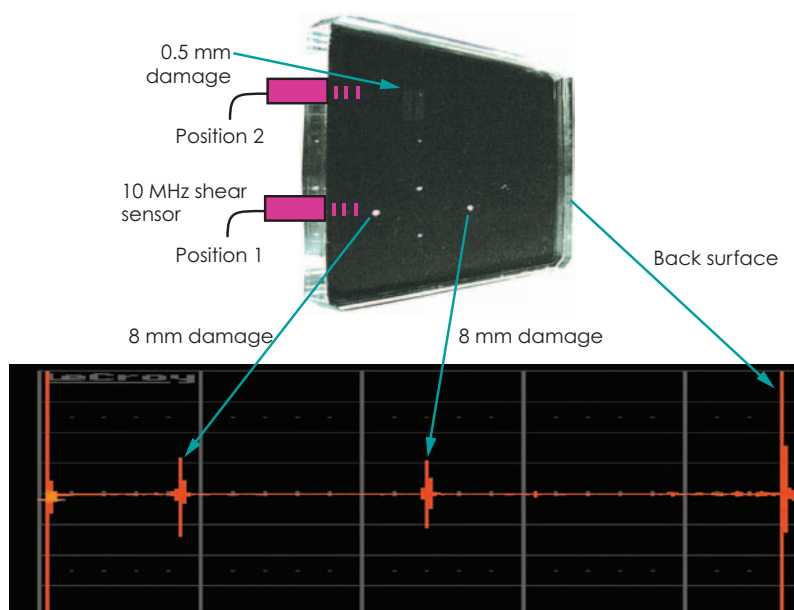
Figure 2. Sample experimental results. A 10-MHz shear wave sensor placed at Position 1 detects the echoes from two 8-mm laser damage sites on the surface of a 430-mm-x-430-mm-x-43-mm optic.

Figure 3. Sample experimental results. A 10-MHz shear-wave sensor placed at Position 2 on Fig. 2 detects the echoes from a 0.5-mm laser damage site.

Application of Seismic Unix to Nondestructive Imaging

We have applied existing seismic imaging codes and algorithms to characterize high-contrast multilayered planar structures at ultrasonic frequencies. These newly obtained competencies provide unique tools and leverage a wealth of prior knowledge from the seismic-geophysical scientific community. Realizing this technology has significantly enhanced LLNL's imaging and characterization capabilities, typically encountered with stockpile and recertification programs.

Project Goals

Our project goal was to assess the utility and applicability of state-of-the-art seismic imaging software to typical programmatic ultrasonic NDE problems. To evaluate the utility of these algorithms, we produced a simple planar test part containing multiple elastic layers with large acoustic impedance mismatches. With this simple test case we generated several numerical and experimental sets of data that were then used as input to the seismic reconstruction codes.

Relevance to LLNL Mission

The motivation for this project was to directly support long-range plans to enhance LLNL's core technologies relating to imaging and characterization. In doing so, we have generated a knowledge base, applicable to a variety of multilayered high-contrast elastic structures. These new competencies are directly applicable to numerous LLNL programs such as ADAPT, and the stockpile recertification initiatives.

Water	Tantalum	Acrylic	Sylastic
C_L = 1.5 mm/µs	C_L = 4.1 mm/µs	C_L = 2.5 mm/µs	C_L = 1.21 mm/µs
C_t = 1.5 mm/µs	C_t = 1.1 mm/µs	C_t = 1.3 mm/µs	C_t = 0.9 mm/µs
ρ = 1.0 gm/cm^3	ρ = 16.6 gm/cm^3	ρ = 1.1 gm/cm^3	ρ = 0.9 gm/cm^3
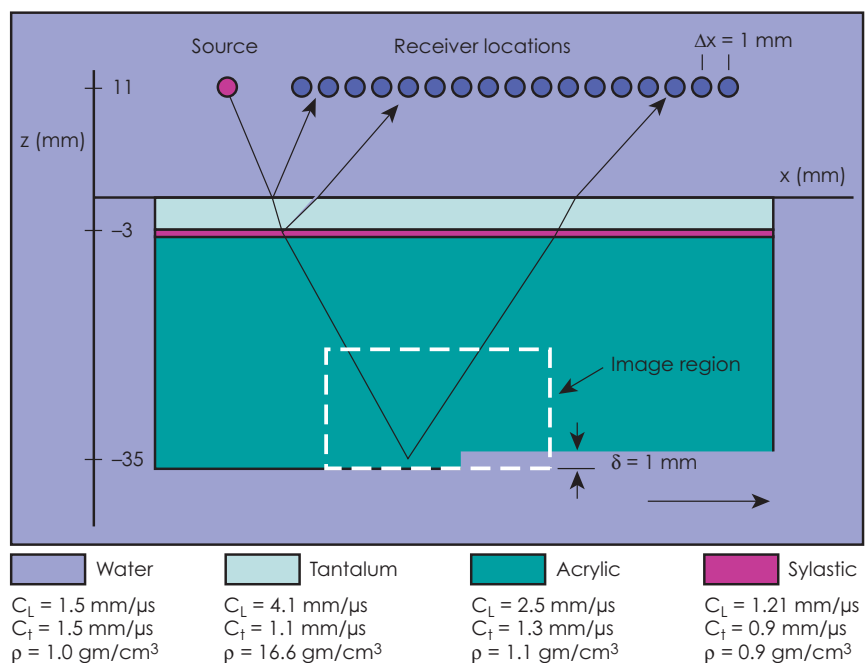
Figure 1. Geometry for the 2-D planar multilayered part. The lower acrylic boundary has a uniform step change of 1.0 mm. For each material, the longitudinal and shear wave speeds are listed along with the density. The dashed square is the imaging region shown in Figs. 3 and 4.

For more information contact
Karl A. Fisher
(925) 423-0132
fisher34@llnl.gov

FY2005 Accomplishments and Results

A planar test case was used to generate numerical and experimental data sets for the Stanford University Seismic Unix reconstruction package. The computational geometry and the corresponding source receiver locations relative to a multilayered planar elastic structure are shown in Fig. 1. The materials of the structure were specifically chosen to have large acoustic impedance mismatches between layers. This requirement was driven by the need to maintain relevant similarities to programmatic components and to test the robustness of the seismic migration algorithms.

We performed a series of numerical experiments on the multilayered planar part to simulate an ultrasonic scan. Elastic wave propagation was modeled using E3D, a finite-difference time-domain code. Numerical data sets were then created in a full multistatic process whereby multiple sources sequentially ensonified the part with a broadband pulse centered at 2.25 MHz. The corresponding scattered field was then recorded at each receiver location. The resulting numerical data was then input into the Seismic Unix application for image generation.

Figure 2 depicts how the experimental data were collected. A single linear scan along the upper surface of the part is generated by holding the source fixed while the receiver is moved relative to the source. The reflected acoustic signals are recorded at each receiver location as a function of time; this generates what is known in the seismic community as a "normal move out."

Numerical and experimental data were then input into the Seismic Unix processing environment.

Reconstructions of the numerical data for the multilayered planar part are shown in Fig. 3. The step feature is clearly visible with adequate localization of acoustic energy. Further effort could be expended to reduce the ripples and multiple echoes, but for a proof-of-concept analysis, this is sufficient.

Experimental results are illustrated in Fig. 4. Here the goal was to accurately locate the lower boundary of the acrylic layer using these seismic techniques.

In this study we have successfully shown that seismic approaches can be applied to ultrasonic NDE problems.

Related Reference

Fisher K. A., S. K. Lehman, and D. H. Chambers, "Development of a Multi-View Time Domain Imaging Algorithm with a Fermat Correction," *J. Acoust. Soc. Am.*, **118**, 5, pp. 1115-1136, 2005.
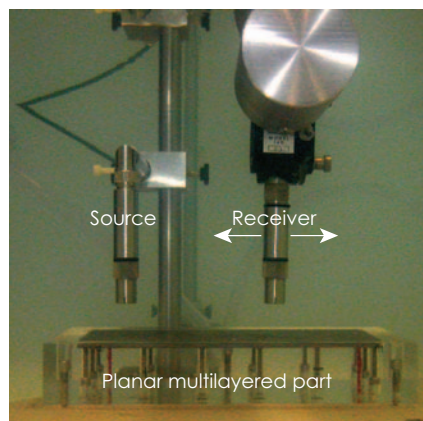
Figure 2. Photograph of the experimental scan geometry in the immersion tank. The source, a 2.25-MHz transducer, is held fixed relative to the upper surface of the planar multilayered part. The receiver is another 2.25-MHz transducer that is mechanically scanned along the axis of the part. The planar test part was constructed using the dimensions and materials properties shown in Fig. 1.
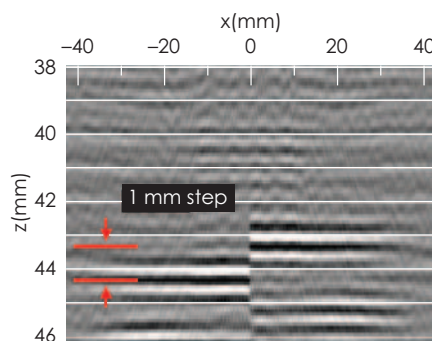
Figure 3. Numerical reconstruction of the lower acrylic boundary in the region near the planar step (dashed white box in Fig. 1). Several convolution filters in conjunction with the basic migration operation have clearly outlined the 1-mm step feature in the correct location. The boundaries are well defined with a minimum of pulse-induced artifacts.
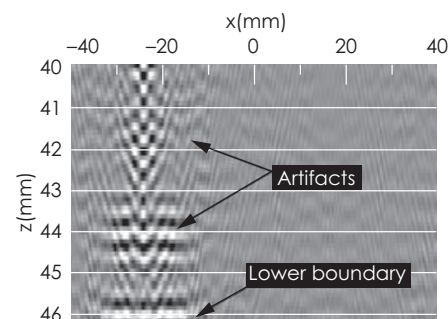
Figure 4. Experimental reconstruction of the lower acrylic boundary. The reduced quality of this reconstruction is a result of having only one source location. This limited data set introduces several artifacts in the image, resulting in a series of "phantoms" above the lower boundary. Multiple views would eliminate these artifacts. Reflection energy from the lower boundary is concentrated and accurately located.

Neutron DR/CT Upgrade at McLellan Nuclear Reactor Center

This is the second year of a two-year project in which LLNL and McLellan Nuclear Reactor Facility (MNRC, at the University of California, Davis) are collaborating on the upgrade of a neutron imaging DR/CT system.

Neutron imaging is a particularly useful nondestructive imaging technique for specimens containing trace amounts of hydrogen. Neutron-based inspections are recommended for evaluating fluid flow in soil and rocks, and in the inspection of high explosives (HE).

Project Goals

The overall goal of this collaborative work is the construction of DR/CT capabilities at MNRC enabling inspections with spatial resolution in the 50 to 100 μm range. The current properties of the scanner are 3 lp/mm (0.2 mm spatial resolution), and 4 % contrast for objects that fit in the field of view.

A number of specific tasks were undertaken:

1. collaborate with UC Davis staff on the fielding of hardware and the use of CT data;
2. perform studies of candidate scintillators;
3. perform DR/CT of soil and selected rock samples;
4. investigate DR/CT of HE samples; and
5. perform comparisons of data from LLNL x-ray systems and MNRC neutron scans.

Relevance to LLNL Mission

Scientists in energetic materials, environmental restoration, and earth sciences have applications for neutron-based inspections. Successful completion of this collaboration provides LLNL robust access to a world-class neutron-based inspection facility.

FY2005 Accomplishments and Results

Neutron DR/CT. The camera-scintillator-based scanner is fully operational at MNRC. A number of studies have been performed and numerous modifications applied to fielded hardware (Fig. 1). Several reference objects and geologic specimens have been scanned. Figure 2 contains slices from the CT scan of a rock sample scanned with a 9-in. field of view.

Figure 1. Neutron DR/CT scanner at MNRC.
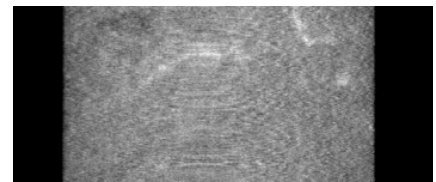
Figure 2. Vertical CT slice of geology sample showing traces of water residue (white voxels).

For more information contact
Daniel J. Schneberk
(925) 423-3531
schneberk1@llnl.gov

Scintillator evaluation studies. We obtained a number of Li-6 and GdSO$_4$ scintillators for evaluation of brightness. Figure 3 is an image from a candidate scintillator. Results showed the Li-6 scintillators provided the best brightness and were able to measure the available resolution for typical object placements. Figure 4 shows an acquired modulation transfer function (MTF) for the best scintillator.

Scans of geologic and aerospace samples. The bulk of the scanning performed at MNRC has focused on geologic samples. We have performed a variety of rock-sample and plant-hydrogen-uptake studies. Two LLNL samples and several commercial objects have also recently been scanned and the results are currently being processed. Figure 5 contains DR and CT images from a Boeing three-position valve, showing the clear way in which the neutron beam images hydrocarbon O-rings in an aluminum matrix.

Inspections. Current inspection work at LLNL for NASA has focused on the inspection of a cartridge explosive bolt, part of the release mechanism that separates the main shuttle rocket engine from the later stage items. We are recommending neutron radiography to determine the presence or absence of the explosive bolt, and CT for inspecting the integrity of the O-ring in the bolt.

Figure 3. Image from sample scintillator.
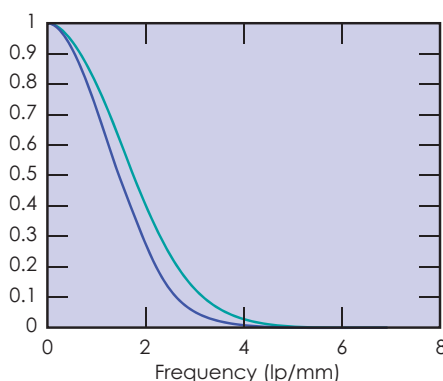
Figure 4. MTFs from the best of the scintillators studied.

(a)

(b)
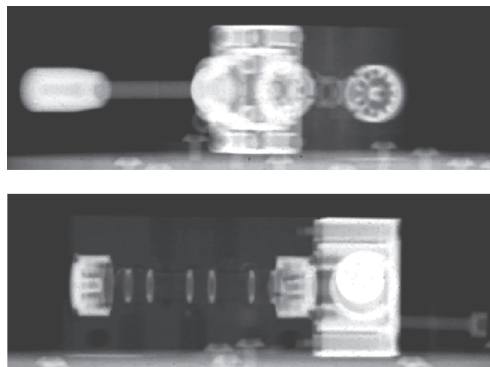
Neutron digital radiographs
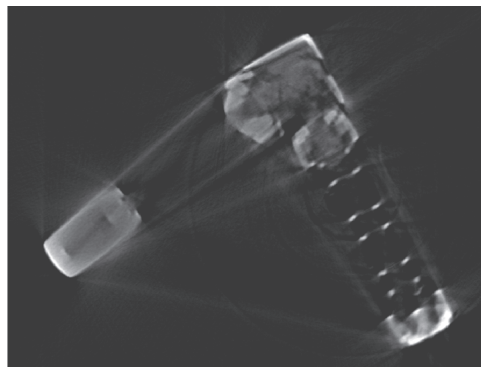
CT slice

Figure 5. Neutron (a) DR and (b) CT images of Boeing three-position valve.

Comparison of Methods of Registration for MRI Brain Images

We used a fully automated application for the registration of magnetic resonance images (MRI) for Alzheimer patients who were given the drug, *Aricept*®. Two different methods for image registration were implemented and compared: affine (rigid-body transformation) and nonlinear registration.

The affine registration algorithm is linear and is generated by means of an amplitude-modulated phase-only filter (AMPOF). The AMPOF is an extension of the classical match-filter (CMF) and is used as the correlation filter for the affine registration method.

The nonlinear registration method uses an elastic transformation based on a displacement vector field generated by means of Navier-Stokes continuum-mechanics fluid flow models. In contrast to other nonlinear warping methods using elastic transformations, we implemented the AMPOF shift coefficients as a translation to aid in the detection of feature boundaries, which are segmented by means of statistical feature extraction methods.

With our new validation method, we can quantitatively compare the performance of the affine and nonlinear registration algorithms using root-mean-squared (rms) error, where the output registered MRI is subtracted from the template MRI. The resulting pixel intensity difference is used to calculate the rms error of the image registration. Additionally, the registration validation is taken a step further by implementing 3-D spatial transform models and volume rendering to visually verify registration results for the Alzheimer MRIs.

Project Goals

The goal is to evaluate affine and nonlinear algorithms for image registration that may be used to detect anatomical variations resulting from pathology in the brain. Such variations could be used in the diagnosis of Alzheimer's and other central nervous system diseases, and to detect group-specific patterns of anatomic or functional alterations.

Relevance to LLNL Mission

Affine and nonlinear registration algorithms have distinct applications in the areas of interest to LLNL programs, such as medical technology, homeland security, and nondestructive evaluation. These algorithms can be used to extract features relevant to detecting aberrances within armory, such as finding cracks or defects in nuclear weapons.

FY2005 Accomplishments and Results

Affine Registration. AMPOFs used for pattern recognition have demonstrated better discrimination capabilities than CMFs. The flowchart in Fig. 1
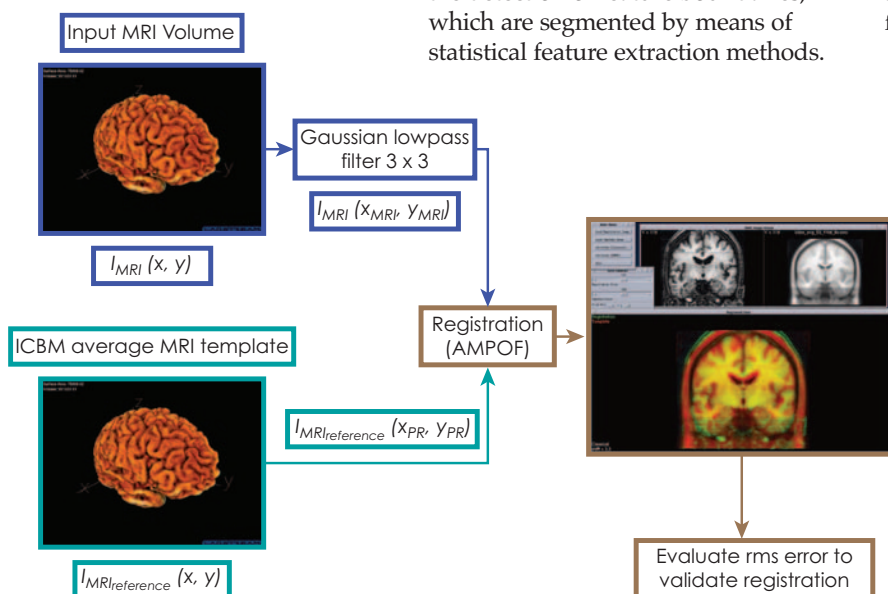
Figure 1. Affine registration using AMPOF.

Input MRI Volume

$I_{MRI}(x, y)$

Gaussian lowpass filter 3 x 3

$I_{MRI}(x_{MRI}, y_{MRI})$

ICBM average MRI template

$I_{MRI\,reference}(x, y)$

$I_{MRI\,reference}(x_{PR}, y_{PR})$

Registration (AMPOF)

Evaluate rms error to validate registration

For more information contact
Wilbert McClay
(925) 423-4153
mcclay2@llnl.gov

illustrates the affine registration method. The quality of the registration is quantified as an rms error calculated from the pixel intensity differences between the registered output MRI and the template MRI.

Nonlinear Registration using Continuum-Mechanics Warping. For nonlinear registration, the MRI volume from each patient is morphed to areas on the template image volume using a continuum-mechanics flow model. The flow model uses a field of normal vectors (perpendicular to surfaces of image intensity features in the 3-D volume) to steer shapes of intensity data from the patient into corresponding shapes in the International Consortium of Brain Mapping (ICBM) template. The steering is achieved through an iterative solving of a modified Navier-Stokes fluid flow for elastic media.

The resulting newly morphed patient image may be explored via interactive volume rendering visualization, which has been incorporated into this project's MRI registration software. The visualization also enables the user to superimpose the new image with the ICBM template, showing exactly how the intensities match between the two. An overall metric of rms error of the differences in intensities between the two volumes is also computed. The metric is recorded for each set of MRI images. Figure 2 shows a snapshot of the volume rendering of patient data during the morphing process, and the Automated Continuum-Mechanics flowchart.

Our conclusion is that, for MRIs, the nonlinear registration using continuum-mechanics warping models is approximately 31% more efficient than the affine (linear) registration method.

Related References

1. Thompson, P. M., and A. W. Toga, "Alzheimer's Disease: MRI Imaging of Progressive Brain Change," Encyclopedia of Neuroscience, G. Adelman and B. H. Smith, Eds., November 2003.

2. Thompson, P. M., K. M. Hayashi, G. de Zubicaray, A. L. Janke, E. R. Sowell, S. E. Rose, J. Semple, D. Herman, M. S. Hong, S. Dittmer, D. M. Doddrell, and A. W. Toga, "Dynamic Mapping of Alzheimer's Disease," *Proceeding of the 19th Collogque Medecine et Recherche*, IPSEN Foundation, Paris, France, March 2003.

3. Thompson, P. M., J. N. Giedd, R. P. Woods, D. MacDonald, A. C. Evans, and A. W. Toga, "Growth Patterns in the Developing Human Brain Detected by Using Continuum-Mechanical Tensor Maps," *Nature*, **404**, 6774, March 9, 2000.

4. McClay, W. A., III, A. A. S. Awwal, S. Burkhart, and J. V. Candy, "Optimization and Improvement of FOA Corner Cube Algorithm," *Photonic Devices and Algorithms for Computing VI*, *SPIE*, Denver, Colorado, August 2004.

5. Candy, J. V., W. McClay, A. A. S. Awwal, and W. Ferguson, "Optimal Position Estimation for the Automatic Alignment of a High Energy Laser," *Journal of the Optical Society of America*, **22**, 7, pp. 1348-1356, July 2005.

FY2006 Proposed Work

We will continue to create new models to solve registration problems of interest to LLNL programs.
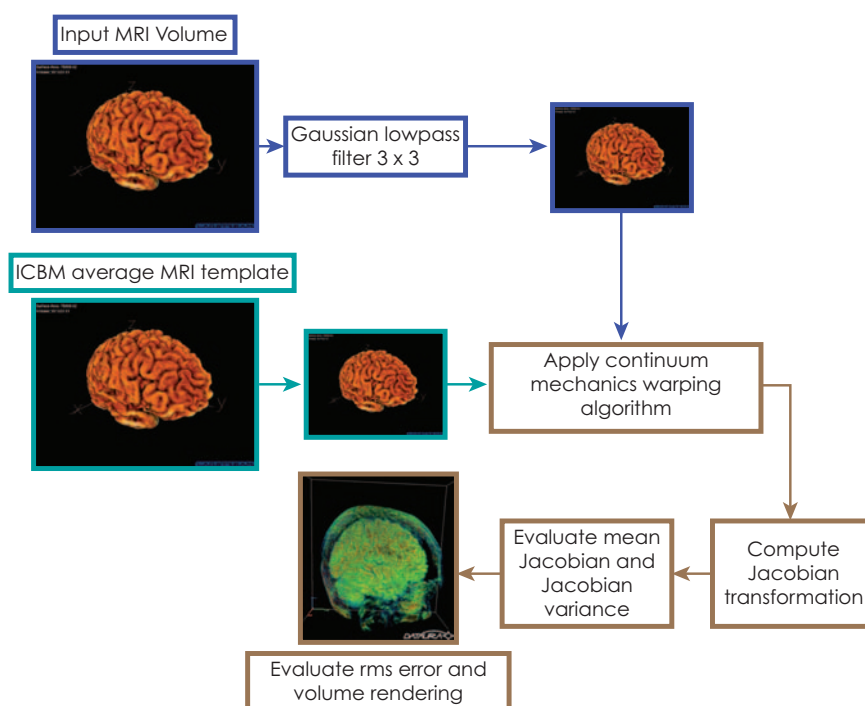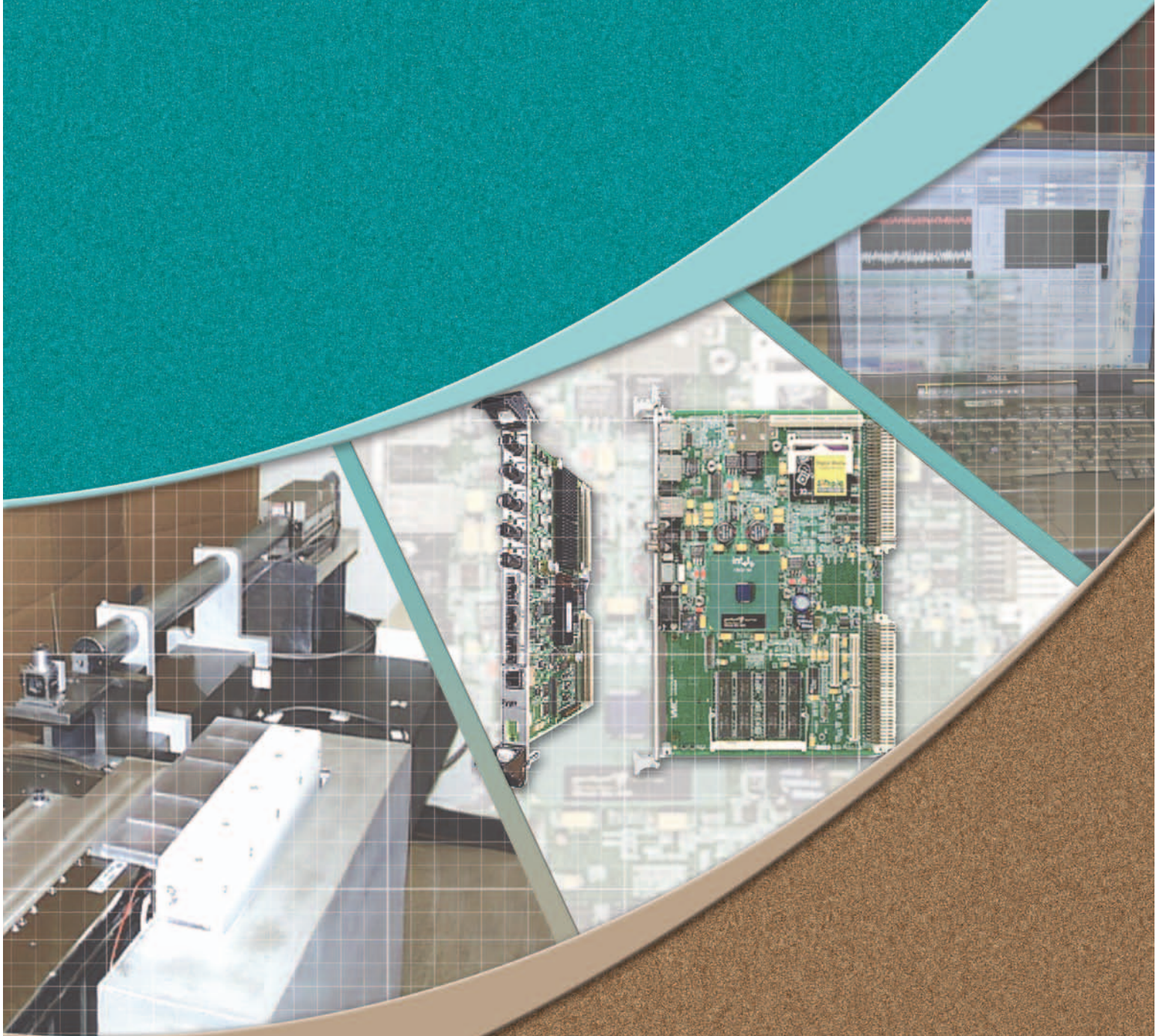

Figure 2. Automated Continuum-Mechanics flowchart and MRI volume rendering to validate nonlinear warping.

Precision Engineering

Interferometer Filter System for Precision Machine Tools

Displacement interferometers are used on many precision machine tools to measure and control machine motion. The interferometer electronics (IE) provide a digital feedback displacement signal directly to the machine-tool controller. Because the interferometer is a high-bandwidth system and the machine-tool controller has a relatively low sample rate, an alias signal can be downshifted into the control bandwidth of the motion controller and cause false machine motion.

As precision machines are approaching nanometer levels of displacement control, the alias of a high-frequency signal, such as a mirror-mount resonance, must be considered. There can be no mechanical resonance or noise measured by the interferometer that is greater than one half of the machine-tool controller sample rate. The interferometer electronics output signal is in digital form, and filtering at the controller sample rate can not remove the alias signal. The only way to properly handle the problem is to over-sample the interferometer output signal, and then process this signal with a digital filter to bandwidth limit it to less than half the controller sample rate.

Project Goals

The goal of this project is to use off-the-shelf IE and couple these electronics with a dedicated computer running a real-time operating system that will over-sample the IE and digitally filter the data. The results will then be presented to the machine controller in the proper data format and at the machine-controller sample rate (Fig. 1).

Our final products are the hardware and software needed to reach this goal.
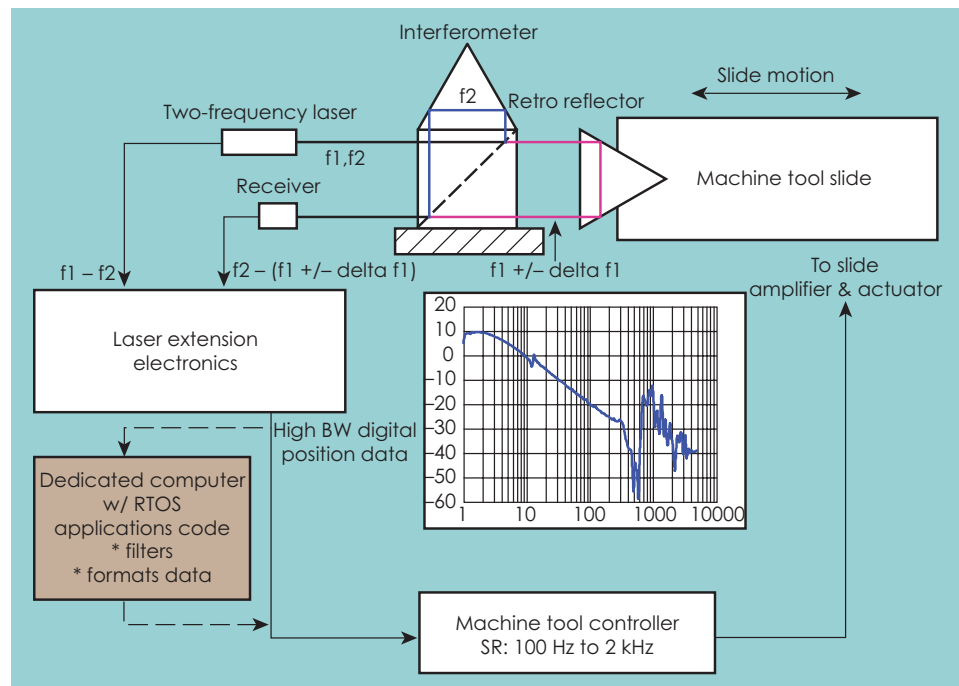
Figure 1. Concept diagram of the project. The laser extension electronics is the VME-based four-channel IE. The pink box represents the CPU that over-samples the IE and then filters and formats the data for the machine-tool controller.

For more information contact
David J. Hopkins
(925) 423-6134
hopkins3@llnl.gov

Relevance to LLNL Mission

This project supports the LLNL precision manufacturing infrastructure. It will be used for new machine tools and allows a path to retrofit old machines.

FY2005 Accomplishments and Results

Displacement interferometry measurement is typically done by electronically interpolating the wavelength of a red laser light (633 nm). The highest resolution interpolation electronics (0.15 nm for a plane mirror interferometer) is commercially available only as a card

based on the Versa Module Eurocard (VME) bus form factor (Fig. 2). In this project, a VME-bus-based embedded computer system was assembled to process the signal from an IE card. A real-time operating system is the software foundation of this system, since the measured and processed data must be delivered in a time-critical fashion to the machine controller.

Besides the assembly of the system, application code has been written in C++ to set up the hardware, read the interferometer card, create second-order bi-quad filters, and process the raw interferometer data through these filters. The function of the filters has been confirmed with simulated data. The number of second-order filters is selectable, as is the five-filter coefficients per filter.

A laser head and interferometer have been set up on a test machine

(Fig. 3) so the interferometer can be moved to provide a signal for the VME interferometer card. The testing algorithm is to excite the moving slide through a range of frequencies and record the frequency spectrum before and after the filters of the system are activated. Figure 4 shows an example of expected results.

During software coding, a problem was found with hardware system interrupts. The interrupt is used to sync this system with the machine controller. Future work will address the interrupt problem and allow for final testing.

Related References

1. Lam, H., Analog and Digital Filters Design and Realization, Prentice Hall, New Jersey, 1979.
2. Peterson, W., The VMEbus Handbook, VMEbus International Trade Association, 1989.

Figure 2. VME-bus-based cards, four-channel interferometer extension electronics, and CPU card.
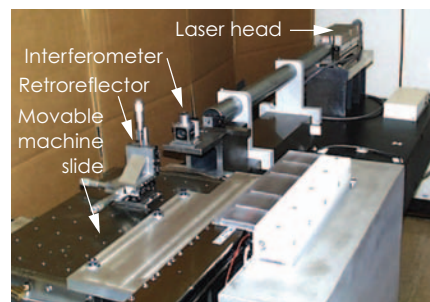
Figure 3. Interferometer test set-up.
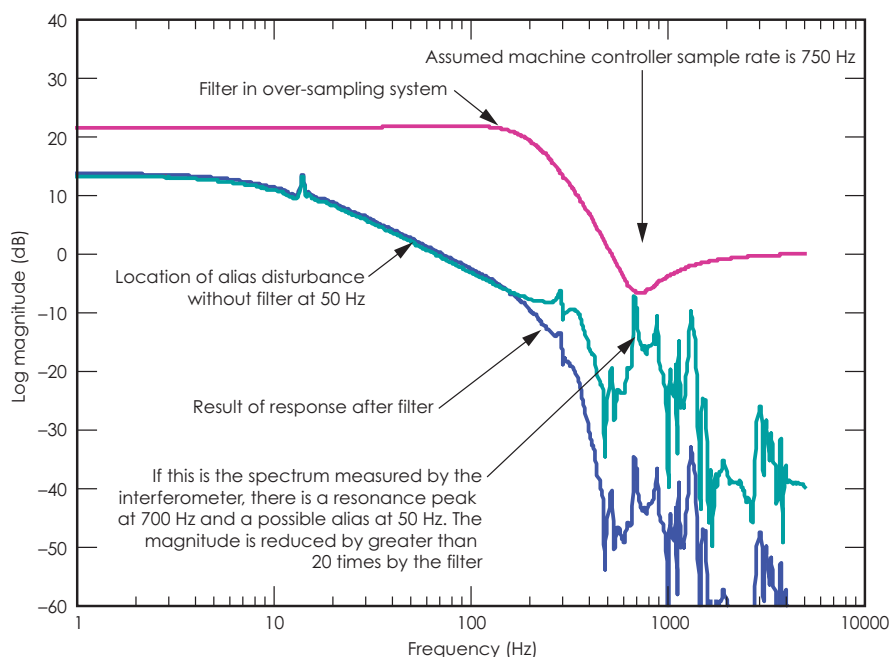
Figure 4. Example transfer function showing the possible alias issue with the project solution.

Digital Tachometer for Precision Machine Tools

Several LLNL high-resolution and precision diamond turning machines (DTM) rely on high-sensitivity analog tachometers for velocity-loop feedback to provide smooth machine motion at diamond-turning feed-rates. The analog velocity loop provides mass damping and smooth machine motion during the digital position loop update. Analog compensation is inflexible and costly to implement, but it provides the required dynamic range and resolution to cover machine speeds from rapid travel to diamond-turning feed-rates. This dynamic range can be greater than one million. For example, for a

capstan driven DTM, rapid travel may be one revolution of the motor per minute versus less than one revolution of the motor per year at diamond turning federates.

This project is a part of an overall goal to replace aging and obsolete machine-tool controllers on several LLNL precision machines. A modern controller will reduce machine maintenance costs and allow greater machine capability. Replacing the analog velocity loop with a digital loop simplifies the cost of a machine retrofit.

Our approach is to digitize the analog tachometer with sufficient

resolution for direct input to the new controller. The conversion must be able to handle a dynamic range of 20 bits or greater for the controller to properly provide digital compensation of a velocity loop. In addition, the converter must be monotonic as it is used in a servo loop. A delta-sigma A/D converter has sufficient number of bits and monotonic behavior.

Project Goals

The goal is to digitize the analog tachometer signal and provide the synchronization and data formatting for the machine-tool controller (Fig. 1). Additionally, it is desirable to connect
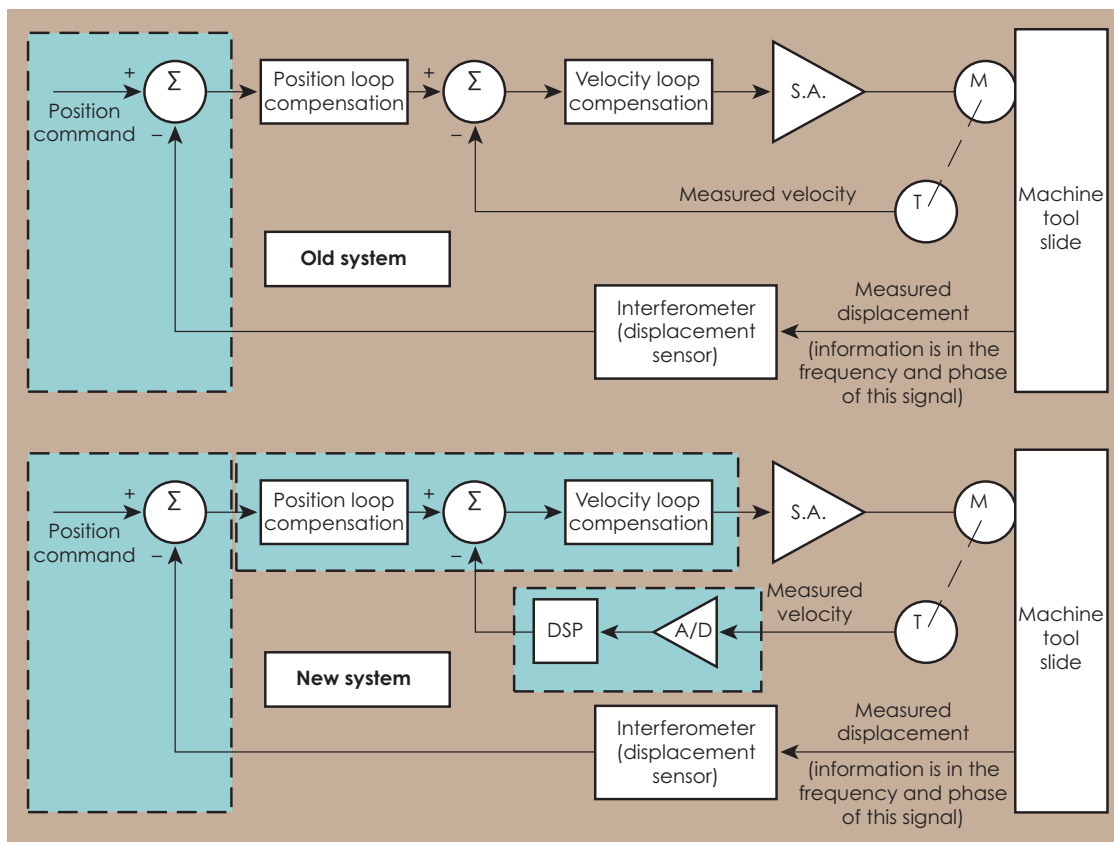
Figure 1. Block diagram comparison between the old and new systems. The green highlighted background indicates the digital implementation.

For more information contact
David J. Hopkins
(925) 423-6134
hopkins3@llnl.gov

the system to a precision machine and show smooth machine-tool motion at diamond-turning feed-rates. The project is to produce a set of documentation and software algorithms for implementing this approach on any tachometer-based machine tool.

Relevance to LLNL Mission

The project will add to the tools available to upgrade precision machine tools and help the learning curve for using a new machine-tool controller. This project also indirectly supports target fabrication, NIF optic fixtures, and NAI.

FY2005 Accomplishments and Results

An off-the-shelf PC-based digital signal processing (DSP) board was selected for the test-bed hardware. The converters on this board can run at effective sample rates of up to 192 kHz. The processed converter signal is sent to a 24 bit I/O port of the DSP board and then connected to the digital input port of the machine-tool controller.

The software environment is TI Code Composer Studio. C++ code was written to configure the converters and I/O port, and to set up the machine-tool controller. The code is a multi-threaded application and allows changes in sample rate and enabled channels during testing. Also included in the code, is the ability to activate multiple second-order bi-quad filters to filter the sampled A/D data.

The ideal results of this project would be to obtain several kHz of frequency response from the system. This would minimize phase delay in the velocity loop and allow this system to approach the bandwidth limitations of the machine controller. Unfortunately, the measured transfer

function (machine controller output vs. tachometer input) is only a few hundred Hertz (Fig. 2). The bandwidth limitation is due to the inherent delay in the delta-sigma converter and the delay caused by DSP board architecture. The system is usable for low-bandwidth machines but is limiting for some higher performing machines.

This project has proven the approach works, but increasing the bandwidth by using a different processing architecture would be desirable.

Related References

1. Bowling, S., "Understanding A/D Converter Performance Specifications," *Application Note AN693, Microchip Technology, Inc.,* 2000.
2. "PCM1804 Full Differential Analog Input 24-Bit, 192-KHz Stereo A/D converter," *Texas Instruments Data Sheet,* Burr-Brown Products from Texas Instruments, Texas Instruments Inc., 2001-2005.
3. Technical Staff, "Delfin User's Manual," Innovative Integration, 2003.
4. "Code Composer Studio, Getting Started Guide," *Texas Instruments SPRU509C,* 2004.
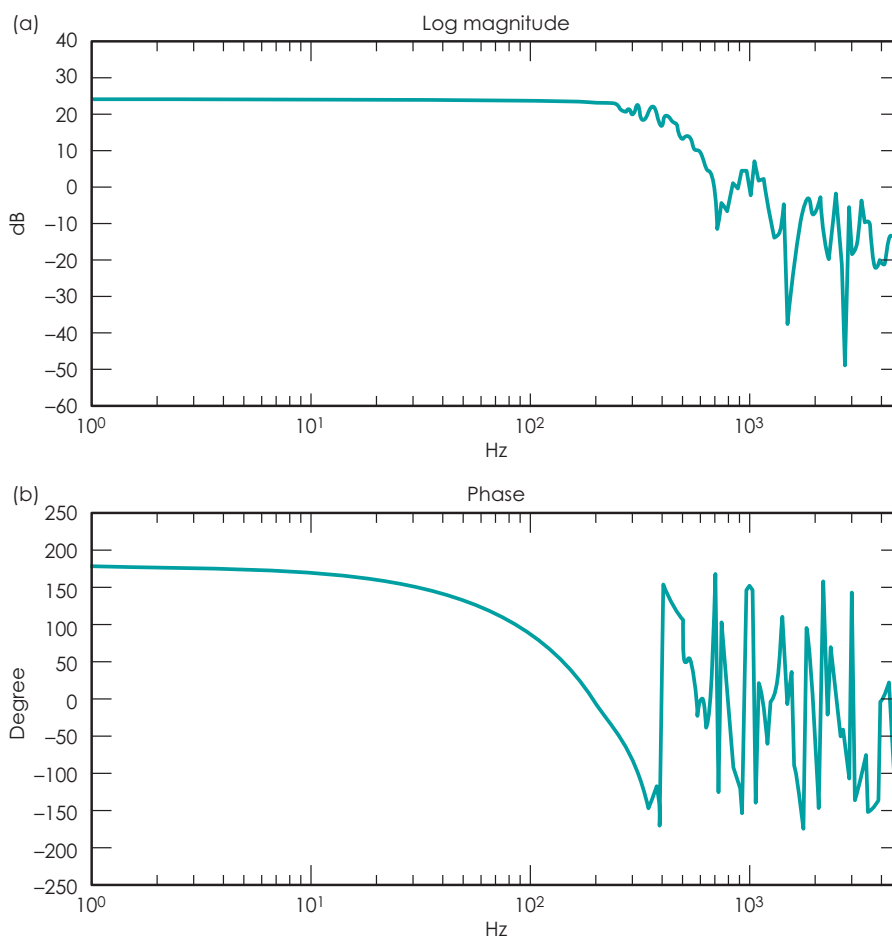
Figure 2. Measured transfer function: (a) gain, and (b) phase.

Hydraulic Power Unit for Hydrostatic Bearings

This project is focused on two hydraulic power units (HPU) for hydrostatic (oil) bearings. The first unit powers the hydrostatic bearings of a precision machine tool axis; the second powers those of a precision machine tool spindle. In this project, a precision machine tool is defined as a machine capable of nanometer position control with 50 nm accuracy throughout the work volume of the machine. The two hydraulic units cover a range of thermal heat loads and bearing flow rates to maintain a high degree of stable pressure and temperature control.

Key factors addressed are computer models that aid in the construction of hydrostatic fluid pressure and temperature control systems; a system controller that provides PID and logic functions, with an integrated interface to a machine tool controller; and an operator interface to provide data trending and error notification.

Figure 1 shows a block diagram of the pressure and temperature control system for an oil hydraulic power unit for hydrostatic bearings.

Project Goals

The goals in the second year of this project are to complete the assembly and testing of the two HPU systems. Changes were made this year in the system controller hardware to minimize programming efforts. Modernized temperature signal conditioning electronics are to be completed. Tests of the system are to be conducted to verify the system computer models.

Relevance to LLNL Mission

LLNL has a long history of contributions to the field of precision engineering and precision machine tool design. Some of our machines support fabrication of NIF KDP final optics, weapons compoonents and metrology equipment for a number of programs. This project supports the ability to build new precision machines and to modernize older ones, for to achieve nanometer level of machine performance, it is essential to control the pressure and temperature of the bearing fluid for hydrostatic bearings.

Legend:
- Fluid system
- Chilled water system
- Electronic control system
- Fault system
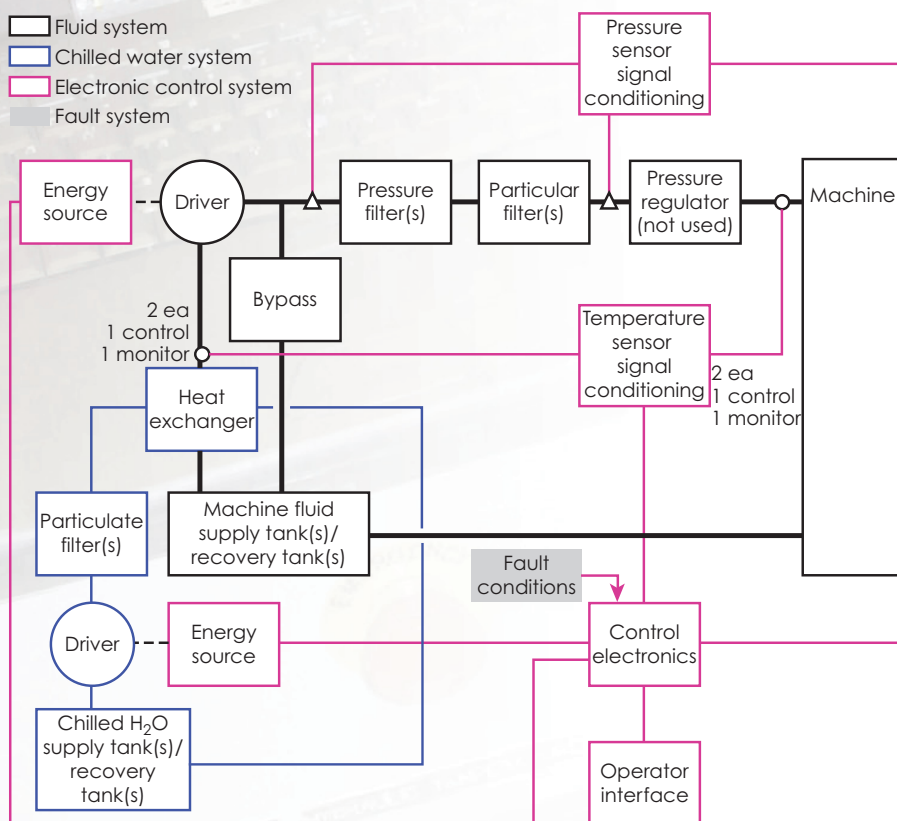
Figure 1. Block diagram of the pressure and temperature control system of the HPU.

For more information contact
David J. Hopkins
(925) 423-6134
hopkins3@llnl.gov

FY2005 Accomplishments and Results

In this second year we completed the mechanical assembly of the two HPUs and two mechanical low-pass filters. We also completed the electronic control system enclosures. The project's electronic control system must provide an operator interface for status and data trending of pressure and temperature. In addition, it must support cascaded or dual-PID control loops. The inner control loop is the faster responding loop and is sensed at the controlling source. The outer loop is slower responding and is sensed at the delivery point of the machine. To create these capabilities and to minimize programming time, new controller hardware was chosen this year that provides the required bandwidth and allows the complete system to be programmed in one language, LabView (Fig. 2).

Last year we worked on modernized AC-bridge signal-conditioning electronics for temperature sensing at millidegree levels (20 mV / m°C). In this second year, we completed the assembly of two four-channel thermistor signal-conditioning boards (Fig. 3).

Testing done this year confirms our ability to maintain a desired set-point in pressure, with a pressure fluctuation of under 0.1% directly out of the pump. This value is primarily at the fundamental of pump gear meshing frequency. It is further attenuated through the mechanical low-pass filter.

The frequency spectrum of the pressure transducer directly out of the pump is shown in Fig. 4.

Related References

1. Skaistis, S., Noise Control of Hydraulic Machinery, Marcel Dekker, Inc., New York, 1988.
2. Viersma, T., Analysis, Synthesis, and Design of Hydraulic Servosystems and Pipelines, Elsevier Publishing Co., New York, 1980.
3. Stansfield, F., Hydrostatic Bearings for Machine Tools, Machinery Publishing Co., Ltd, London, 1970.

Figure 3. High-sensitivity four-channel thermistor signal-conditioning board for temperature control.

Figure 2. Front panel of HPU and a network-interfaced laptop with LabView set-point and data trending display.

−20 = 12.5 PSI change

−40 = 1.25 PSI change

−60 = 0.125 PSI change

−80 = 0.0125 PSI change
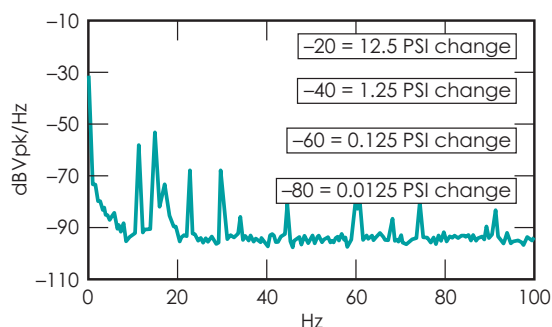
Figure 4. Pressure noise spectrum directly measured at the pump output at 320 psi operating pressure. The first accumulator was charged to 250 psi.

Materials Engineering
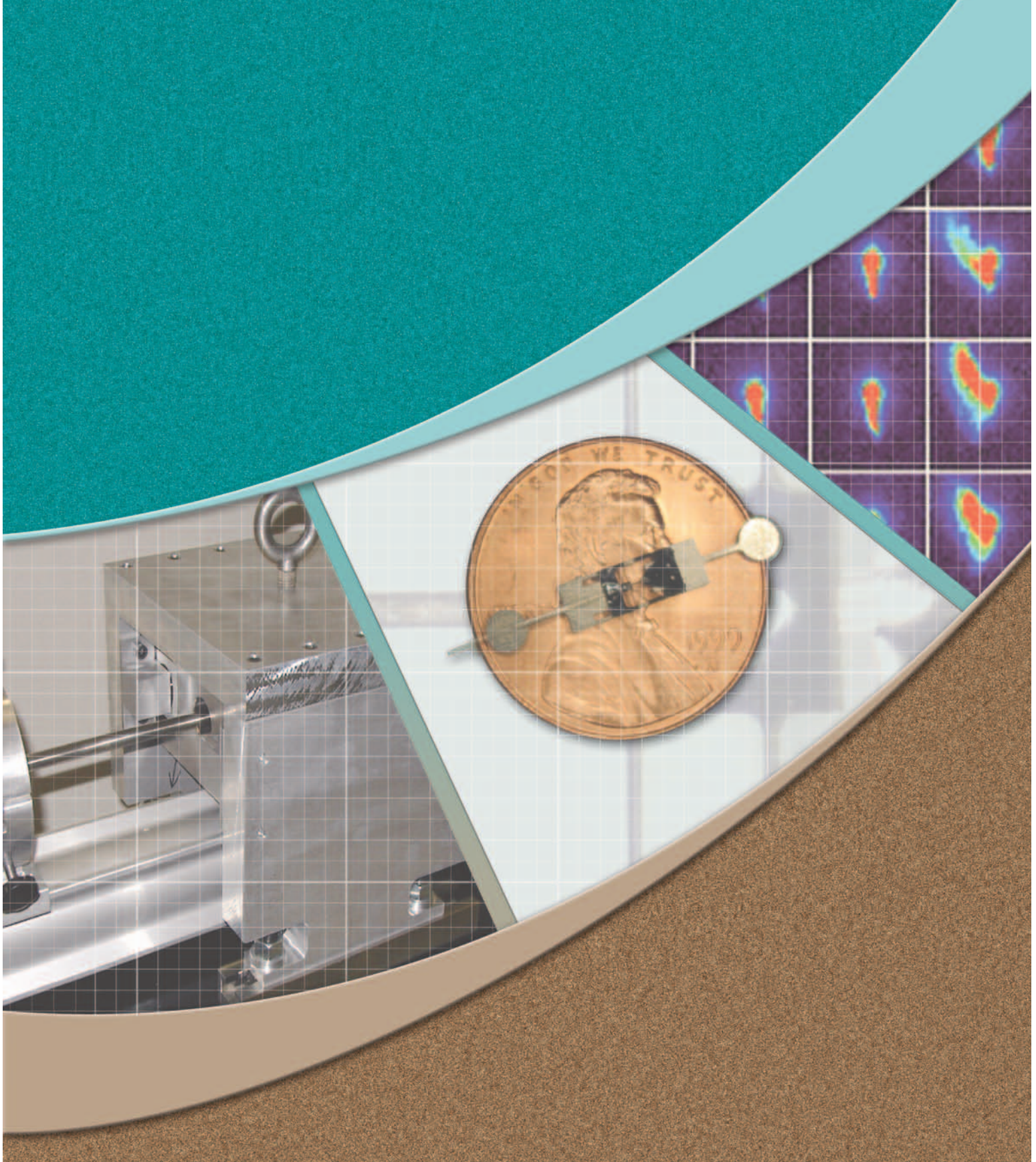
Multiscale Characterization of bcc Crystals Deformed to Large Extents of Strain

Experimental data is crucial in the process of constructing and validating the multiscale crystal plasticity models used in computer code simulations of materials deformed under extreme conditions, such as high strain rate, high pressure, and large extents of strain. The "6 Degrees of Freedom" (6DOF) experiment was designed specifically for this task and has provided data on the behavior of bcc crystals that may revolutionize the field.

Until now, the experimental data and simulation efforts have focused on relatively small extents of plastic deformation (0.5%). Both experiments and modeling must now be extended to large strain deformations on the order of tens of percent. At these larger extents of strain, the use of multiscale characterization tools can be improved to better understand the fundamental behavior.

Project Goals

Our goal is to develop large strain experiments that will provide the essential data to enhance LLNL's multiscale modeling capability through the validation of dislocation dynamics (DD) simulations and the construction of continuum strength models.

Relevance to LLNL Mission

Understanding and simulating the plastic, or non-reversible, deformation of body-centered cubic (bcc) metals, is a major component of LLNL's Stockpile Stewardship Program and will be used to simulate future NIF experiments.

FY2005 Accomplishments and Results

Experimental technique and large strain data. Using the accomplishments from FY2004, a full-field 3-D image correlation strain measurement system that compares sequential photos to determine the local movement of spots has been incorporated into the 6DOF experiment. Unlike traditional testing techniques, ours allows essentially unconstrained deformation of the crystal. Figure 1 shows results from an experiment on a zinc single crystal, performed to verify the accuracy of the 6DOF experiment and highlight the use of the image correlation method.

A major challenge in conducting experiments to large strains is that due to the anisotropic nature of the deformation, or slip, of a single crystal, a severe shape change can develop, which can lead to errors in the analysis and development of the models. To

Figure 1. Zinc experiment validating the 6DOF experiment. (a) Image correlation strain map superimposed onto the sample. (b) Translation of the bottom of the sample, which matches exactly with theoretical predictions.
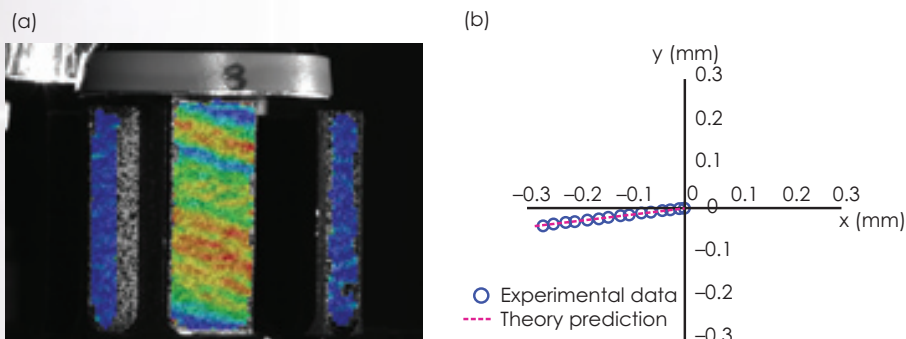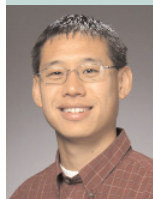
For more information contact
Jeffrey Florando
(925) 422-0698
florando1@llnl.gov

combat this issue, samples can be remachined to maintain a nominally uniform shape. A molybdenum (Mo) sample (bcc structure), which was previously deformed to 2.5% strain, has been remachined and deformed an additional 2.5%, for a total of 5% strain. The corresponding stress-strain curve and translation of the sample (Fig. 2) show that the underlying deformation mechanisms are similar before and after remachining, and are still significantly different from predictions of conventional theories.

Characterization of the deformed material. One method of

characterizing the deformed material is using the x-ray microdiffraction beamline at the Advanced Light Source at Lawrence Berkeley National Laboratory. The high-energy synchrotron light source allows the analysis of subsurface dislocation structure. This technique can detect features over an area larger than that using transmission electron microscopy (TEM). Results on deformed Mo samples show streaking of the x-ray spots (Fig. 3), indicating considerable deformation on the anomalous plane and confirming the 6DOF compression results.

Connection between experiments and simulations. In a coordinated effort with the dislocation dynamics (DD) simulation development team, the underlying physics of high-temperature deformation of bcc metals is being investigated. Large strain experiments on symmetrically oriented samples, [001] and [110], at 500 K have been performed. Both the experimental and the DD results show a large difference in the strain hardening rate between the [001] and [110] samples. This orientation dependence can be explained with four-node junctions, which is an effect first seen in the DD code and verified experimentally.

Related References

1. Lassila, D.H., M. M. LeBlanc, and G. J. Kay, "Uniaxial Stress Deformation Experiments for Validation of 3-D Dislocation Dynamics Simulations," *J. Eng. Mat. Tech.*, **124**, p. 290, 2002.
2. Bulatov, V. V., and W. Cai, "Nodal Effects in Dislocation Mobility," *Phys. Review Letters*, **89**, p. 115501-1, 2000.
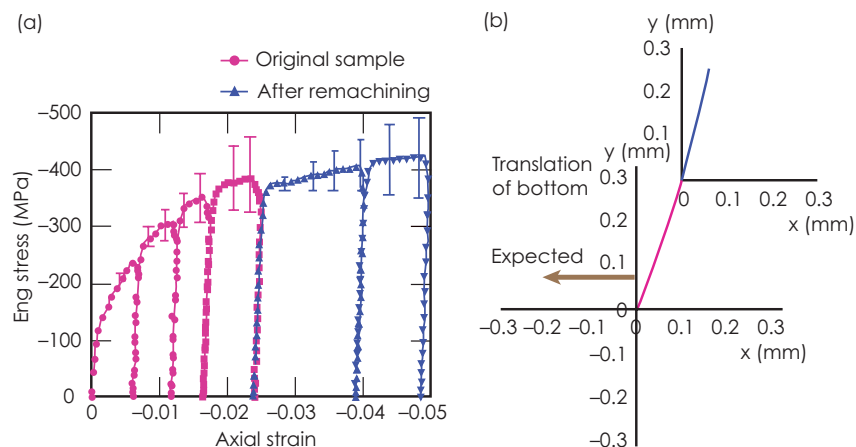
Figure 2. Experimental results on Mo sample before and after remachining. (a) Stress-strain curve showing behavior out to 5% strain. (b) Translation of the bottom of the sample, inconsistent with theoretical predictions.

FY2006 Proposed Work
Asymmetric-oriented Mo samples will continue to be remachined to achieve strain values out to 15%. The deformed samples will be characterized using x-ray microdiffraction and TEM to study the evolution of the dislocation structure. New theories that might explain the experimentally observed anomalous behavior will be implemented into the DD code. Experiments on Mo single crystals of different orientations will be conducted for comparison with the new theories.

Figure 3. X-ray microdiffraction results on deformed Mo sample (011) plane. Each spot represents a 2-μm area; the spacing between spots is 3 μm. (a) Undeformed sample showing round spots. (b) Deformed sample showing extensive streaking.

IR Diagnostics for Dynamic Failure of Materials

This project explores the thermodynamics of dynamic deformation and failure of materials using high-speed spatially-resolved IR measurements of temperature. During deformation, mechanical work is converted to different forms of energy depending on the deformation processes. For example, it can be dissipated as heat in purely plastic deformation, stored as strain energy in dislocations in metals and in oriented polymeric molecular structures, and expended during the generation of new surfaces during damage and fracture.

How this work is converted into these various forms is not well understood. In fact, there exists a controversy for the relatively simple case regarding the amount of work dissipated as heat during uniform plastic deformation. In this project we developed dynamic IR temperature measurement techniques, and then applied them to gain a better understanding of the dynamic failure processes in both metals and polymeric composite materials. The experimental results were compared against predictions of existing constitutive models and guide the development of higher fidelity models if needed.

Project Goals

The first goal of this project was devoted to characterizing the fractional conversion of mechanical work to heat, also known as the Taylor-Quinney coefficient, β, in uniform plastic deformation experiments. A controversy existed between those expecting values of $\beta = 1$, *i.e.*, all of the mechanical work dissipated as heat, and others expecting $\beta < 1$.

LS-DYNA modeling was used to identify the circumstances required to achieve nearly adiabatic conditions for the different materials tested at different stain rates. An IR imaging system based on a 16-element linear high-speed detector array were used in the uniform plastic deformation experiments.

Anvil contact surface (conduction)

Symmetry surfaces (adiabatic)

Cylindrical surface (convection, radiation)

Fringe levels
46.98
45.90
44.82
43.74
42.66
41.58

Figure 1. LS-DYNA modeling results, showing that adiabatic conditions prevail away from specimen ends during intermediate rate deformation.
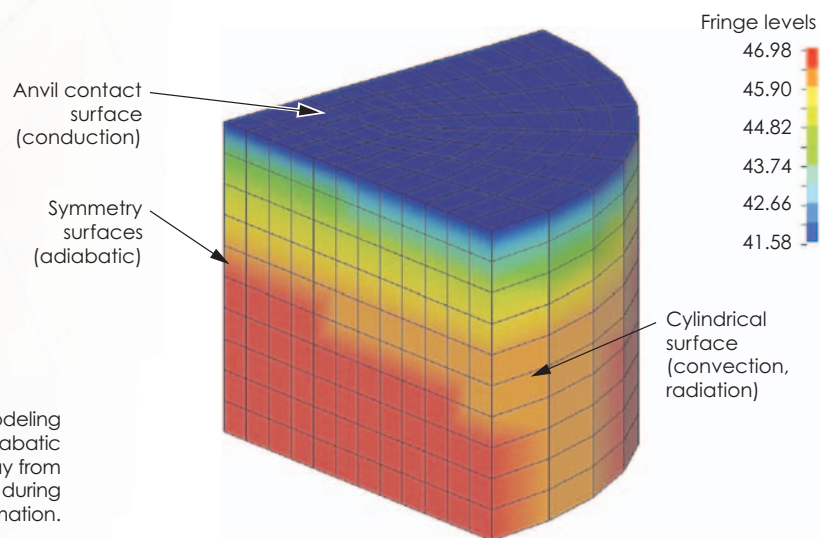
For more information contact
Michael McElfresh
(925) 422-8686
mcelfresh1@llnl.gov

The next goal will be to study the more complicated problem of fracture of metals and high-explosive simulants. This will require a higher resolution 2-D IR detector with a 64-element 8-x-8 array. Shear banding and other forms of deformation are known to precede crack propagation in ductile materials, and our ability to temporally and spatial resolve temperature gradients due to these incipient failure mechanisms ahead of a crack tip will provide valuable insight into the failure process.

Relevance to LLNL Mission

This project will develop a more complete understanding of the mechanisms of material failure, and produce advanced capabilities to acquire IR thermographic data for materials undergoing dynamic deformation and for other dynamic events leading to temperature gradients. Potential LLNL applications of the IR temperature measurement technology include machining and safety aspects of explosives; precision machining (such as modeling temperature factors at the diamond/piece interface); laser optics *in situ* inspection; hydrodynamics; temperature effects associated with rapidly moving wavefronts; NIF target modeling; and plasma deposition processes.

FY2005 Accomplishments and Results

LS-DYNA modeling results (Fig. 1) show that adiabatic conditions prevail away from specimen ends during intermediate strain-rate deformation, suggesting that results of IR measurements can be directly compared with thermocouple measurements. Initial experiments to discern whether or not $\beta = 1$ under uniform strain were undertaken using thermocouples welded to the samples.

As shown in Fig. 2, these results on aluminum show that β can be significantly less than 1 under uniform loading conditions, and that β is strain-dependent. Other experiments with thermocouples on tantalum samples showed evidence of shear banding. In the development of the IR imaging system, it was determined that the Newtonian optical system was not suitable for these types of experiments.

The optical system was redesigned to incorporate Cassegrain optics. A linear IR imaging system based on the Fermionics 16-element high-speed array was constructed. Studies indicated that the emissivity showed changes after deformation. Studies of appropriate surface finishes were made to ameliorate this issue. Also, insignificant differences were observed when IR measurements were done in a vacuum rather than in the atmosphere.
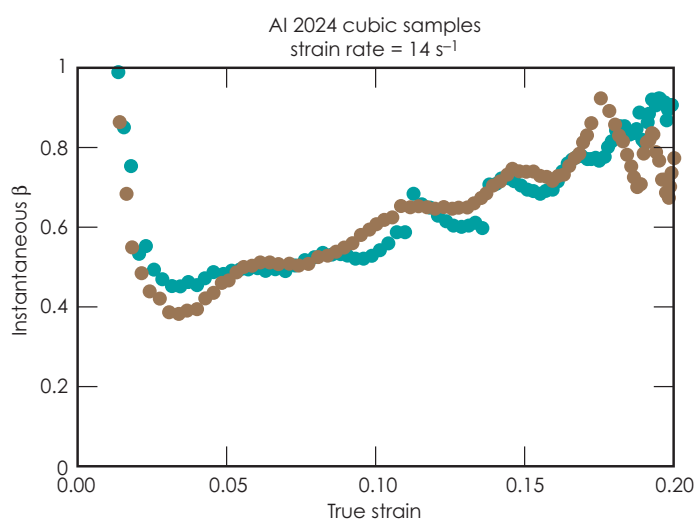
Figure 2. Fractional conversion of mechanical work to heat. The Taylor-Quinney coefficient, β, is shown to be dependent on the strain in aluminum samples subjected to uniform strain.

Nanobarometers: An *In-Situ* Diagnostic for High-Pressure Experiments

The mechanistic understanding of high-pressure phenomena requires the capability to probe the local material response at high spatial resolution using experiments with complex loading history. Such experiments rely heavily on computational simulations for the interpretation of local conditions such as temperature and pressure history. The development of an *in-situ* nanoscale pressure sensor provides a means to assess the quality of these simulations through the direct measurement of local peak pressure and comparison with simulation.

The diagnostic developed under this project consists of nanoscale sensors that are imbedded within, or in contact with, the medium to be measured. The local peak pressure is recorded and may be read out following the experiment using a variety of microspectroscopy techniques. The small size of the nanosensors, combined with low-volume fractions, limits the influence of the sensors on the high-pressure phenomena being studied, while allowing for high spatial resolution of the local peak pressure.

Preliminary work indicates that the fabrication, deployment, and read-out of the nanoscale pressure sensors are possible. We are executing a comprehensive plan to explore the scale dependence, concentration limits, and pressure sensitivity of nanoscale pressure sensors. The final product will be an *in-situ* nanoscale pressure sensing capability that has been calibrated over a wide range of pressures and a broad range of deformation conditions. The development of an *in-situ*, nanometer-scale pressure sensor will provide a valuable tool for many existing high-pressure applications and will be an enabling technology for new uses and novel experiments. A natural extension would be to design new materials to extend the useful pressure range of the proposed sensors to both lower and higher pressures.

Project Goals

Our goal is to develop an *in-situ* diagnostic for high-pressure experiments, capable of providing local peak-pressure information at high resolution (<1 μm) and over a broad range of pressure (30 to 300 kbar). Key issues to be addressed include calibration and sensitivity analysis of the nanosensors to both quasistatic and shock-loading conditions. Major goals of the proposed research are to quantify the extent of pressure-induced changes in the sensor material, determine their
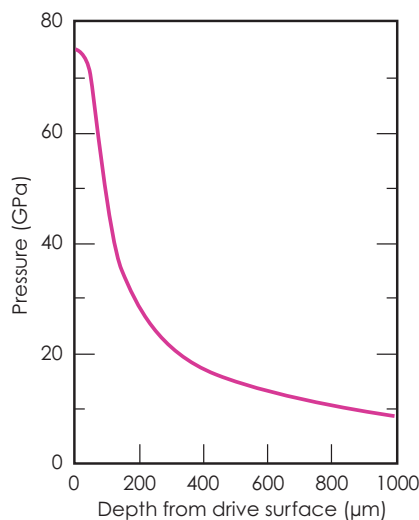
Figure 1. Computed peak-pressure profile due to a laser-driven shock.

For more information contact
James S. Stölken
(925) 423-2234
stolken1@llnl.gov

dependence on sensor size, and establish the sensitivity of pressure-induced structural changes to static loading.

Relevance to LLNL Mission

The study of high-pressure phenomena is at the core of many DNT- and NIF-related programs, with many important applications, such as fragmentation and spall, in the range of a few hundred kilobars. Such experiments rely heavily on computational simulations for the interpretation of local conditions such as temperature and pressure history. The development of an *in-situ* nanoscale pressure sensor provides a means to assess the quality of these simulations through the direct measurement of local peak pressure and comparison with simulation. Such a capability is especially useful in laser-driven experiments with complex wave profiles and nonsteady loading (Fig. 1). The proposed nanosensors complement many existing LLNL

programs in multiscale modeling, material failure and fracture, and laser-driven experiments. Potential application to three classes of experiments is envisioned: quasistatic experiments in bulk materials, unsteady shocks in bulk materials, and high explosives. There is a need for an accurate, local measure of material peak pressure for a variety of gas-gun and laser-driven experiments and test shots.

FY2005 Accomplishments and Results

A key question regarding the existence and nature of the densification mechanism in silica nanoparticles has been explored. The issue was whether or not the densification phenomena observed in bulk silica occurred in nanoparticles. Since the success of the entire project is predicated upon this, it was crucial to experimentally verify this assertion.

The results of our initial series of Raman spectroscopy and diamond

anvil experiments on silica nanoparticles are shown in Figs. 2 and 3. The permanent shift in the Raman spectra in clearly visible in Fig. 2, consistent with the published results in bulk silica glass. To our knowledge, this is the first such measurement in nanoparticles as a function of particle size. Not unexpected is the dependence of the Raman shift upon the particle size, a key research question to be addressed by this project. Note that each experimental point represents an entire sequence of spectra taken upon loading and unloading of each sample. The spectra shown in Fig. 2 correspond to the highest-pressure data points for the 1.2-μm particles shown in Fig. 3, which summarizes the results of 105 individual spectral measurements.

Related Reference

Stölken, J., "Pressure Sensors at High Pressures and Temperatures," *Study of Matter at Extreme Conditions (SMEC)*, Miami, Florida, April 17-21, 2005.
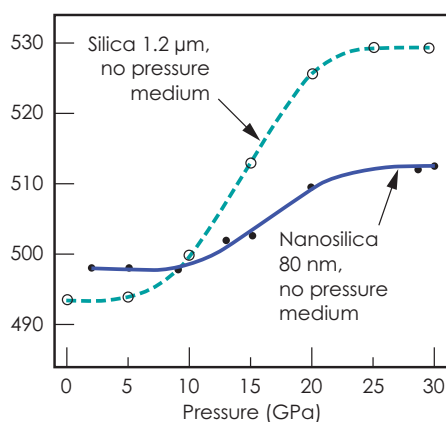
Figure 2. Permanent shift in Raman spectra as a function of particle size and peak pressure.
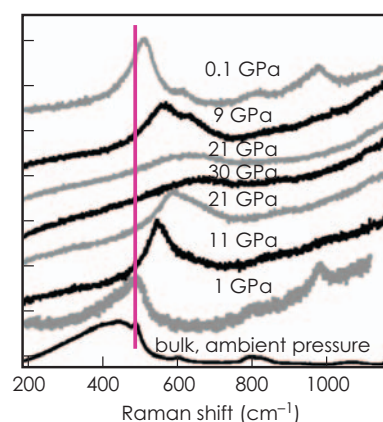
Figure 3. Raman spectra as a function of pressure for 1.2-μm silica particle.

Temperature Capability for *In-Situ* TEM Nanostage

Nanomaterials are roughly defined as solids with characteristic dimensions that are 200 nm or less. The engineering properties of nanomaterials are frequently different from typical engineering properties. For example, some newly invented composite materials that incorporate nanomaterials in their structure have very high yield strength and excellent fracture toughness. In essence, it is the very small dimensions and concurrent surface-area-to-volume ratio of the nanomaterials that give rise to these properties and make them inherently different from traditional engineering materials. In addition, it is important to be able to characterize the mechanical behavior of these materials under different temperature regimes, especially as nanomaterials and structures become used in sensors and other programmatic applications.

Project Goals

The goal of this project is to establish a new capability to experimentally measure the mechanical response of nanomaterials and structures in the Transmission Electron Microscope (TEM), over a range of temperature from 100 to 500 K. To accomplish this goal, a loading stage must be built that is compatible with the TEM, and a loading cartridge, which holds the nano-sized sample, must be fabricated to fit on the end of the stage and transfer the load onto the sample, while measuring the strain. The scope of the project is to establish and test the new capability, and provide documentation on the utility for future studies.

Relevance to LLNL Mission

This project will add to the ever-increasing capabilities LLNL engineering will need to characterize and use nanomaterials and structures. Because of their small size and unique engineering properties, nanomaterials have the potential to play a key role in the production of sensors for programmatic applications.

The first use of this capability will be to quantify the dislocation velocity as a function of applied stress in single
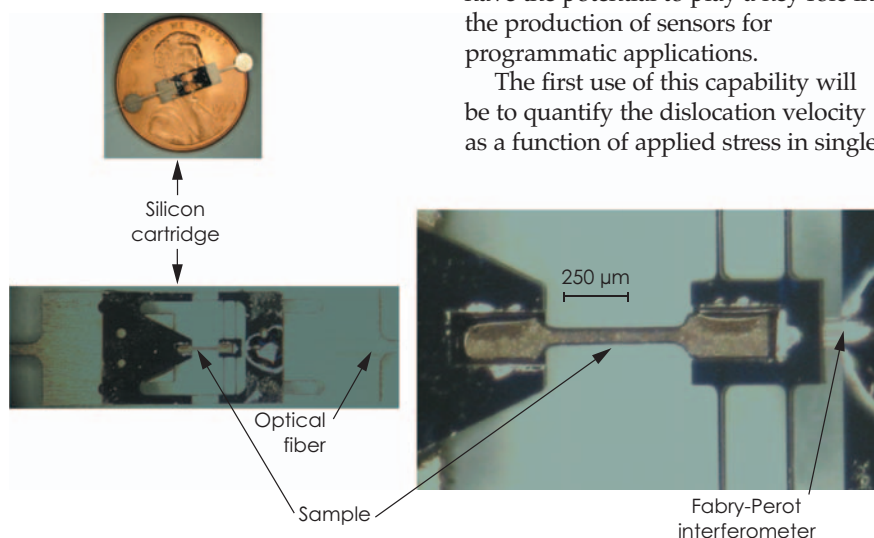
Figure 1. Photographs of the loading cartridge. Counterclockwise: the cartridge in relation to a penny; the complete cartridge; and a blow-up near the sample region.

For more information contact
Mary M. LeBlanc
(925) 422-8954
leblanc2@llnl.gov

crystals. These dislocation mobility values have never been accurately measured, and are essential input for LLNL's multiscale modeling program.

FY2005 Accomplishments and Results

Loading cartridge. The room-temperature loading cartridge is shown in Fig. 1. A method has been devised to calibrate the cartridge. The results of the calibration (Fig. 2) show that this technique has a displacement resolution on the order of a few nanometers, and a load resolution of about 10 mN. Extending this technique to a range of temperatures requires a modification to the loading cartridge, and that modification has been completed.

Loading stage. The loading stage, which applies load to the sample *in situ*, has been configured to fit inside the Philips 300 TEM. The fabrication of the stage (Fig. 3) has been completed. This stage requires only a slight modification to the tip to extend the capability to the range of temperatures of interest. A series of temperature calculations have been completed to guide the configuration of the tip. Based on those results, the tip design is in progress and the appropriate materials have been selected.

FY2006 Proposed Work

In FY2006, the temperature tip for the stage and the temperature cartridge will be fabricated. In addition, the hardware to control the temperature in the TEM, which includes a cold finger and heater, will be fabricated. Finally, the completed system will be assembled and tested.
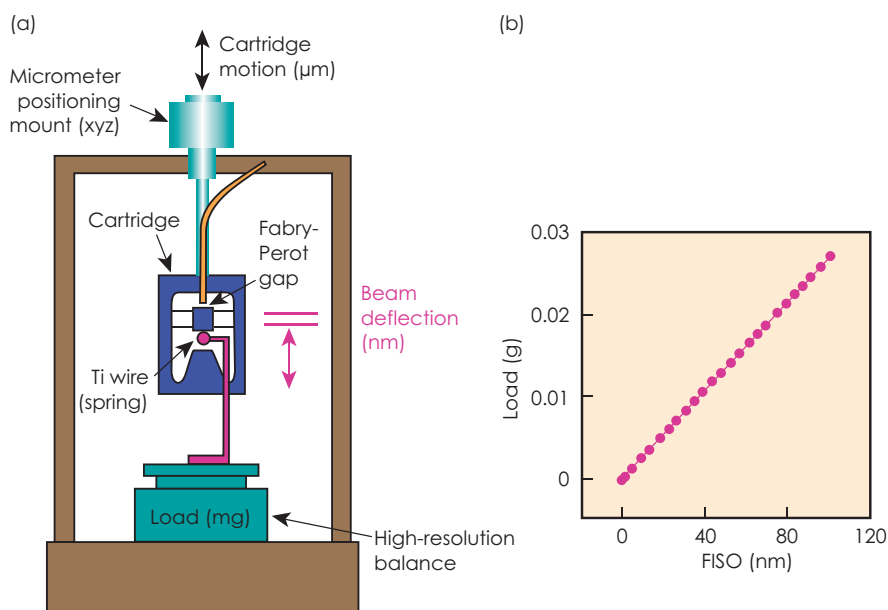
Figure 2. (a) Schematic of the calibration apparatus. The cartridge moves up and down via the micrometer, and the Ti wire applies a force to the beams in the cartridge. The load is measured with a high-resolution balance, and the displacement of the beams is measured by the Fabry-Perot interferometer. (b) The corresponding calibration curve, showing the expected linear response and verifying the high load and displacement resolution of the technique.
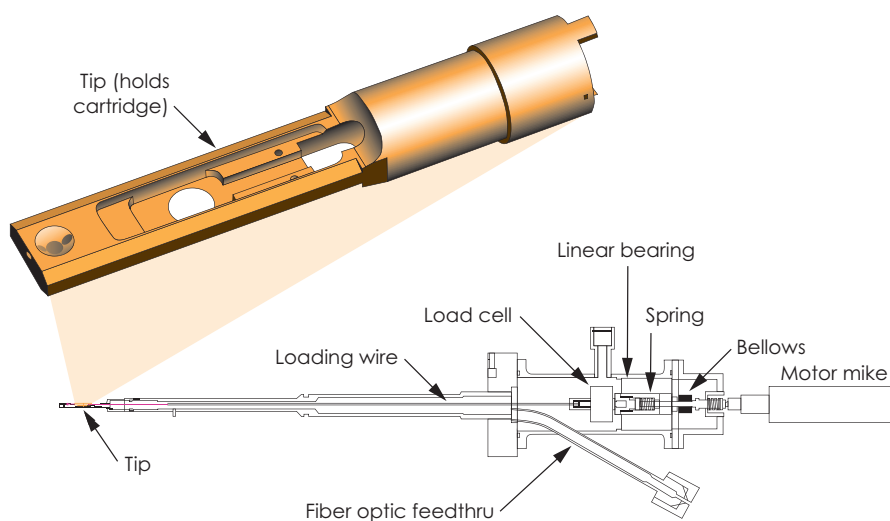
Figure 3. Schematic of the loading stage.

Dynamic Impact Test Capability

This one-year project was to build a new dual-use dynamic impact system that can be used as a small gas gun for study of dynamic deformation and failure behavior of materials of interest to LLNL. It would also be used as a new projectile-driving system for the existing and a new Kolsky/Hopkinson Pressure Bar (KHPB) apparatus. The new gas gun will have the capability to impact our target materials with projectiles of up to 2.5 kg at a velocity in the range of 30 to 120 m/s. This velocity range has been used to study the formation/initiation and growth/propagation of deformation shear bands, and fracture cracks in the dynamic deformation and fracture of metals, ceramics, and other materials.

We also proposed to build a unique KHPB apparatus for characterizing the dynamic compression properties of low-strength materials such as polymers and foams, and for characterizing the response of new miniature shock sensors and accelerometers under controlled high-"g" loading. The KHPB apparatus will be activated by a projectile driven by the new gas gun.

Project Goals

Our goal is to provide the basic test and characterization needs of materials under dynamic loading conditions.

Relevance to LLNL Mission

Existing gas guns at LLNL can generate projectile velocities from a few hundred m/s to several km/s, and are used in shock physics studies. However, these gas guns are incapable of generating impact velocities of 30 m/s to 120 m/s reliably, and these velocities are needed for studies of dynamic deformation and of material failure of interest to LLNL.

FY2005 Accomplishments and Results

A schematic of the system is shown in Fig. 1; the actual system as built is shown in Figs. 2 and 3.

The basic system consists of the gas gun and the KHPB systems placed on a 30-ft-long I-beam raised 3 ft from the floor by six equally spaced legs. The gas gun is composed of the air-pressure vessel, pressure valve, air hose, barrel adapter and barrel. The barrel's length is about 10 ft long, if the gas gun is used as a projectile-driving

Figure 1. Schematics of the proposed small gas gun-KHPB system.
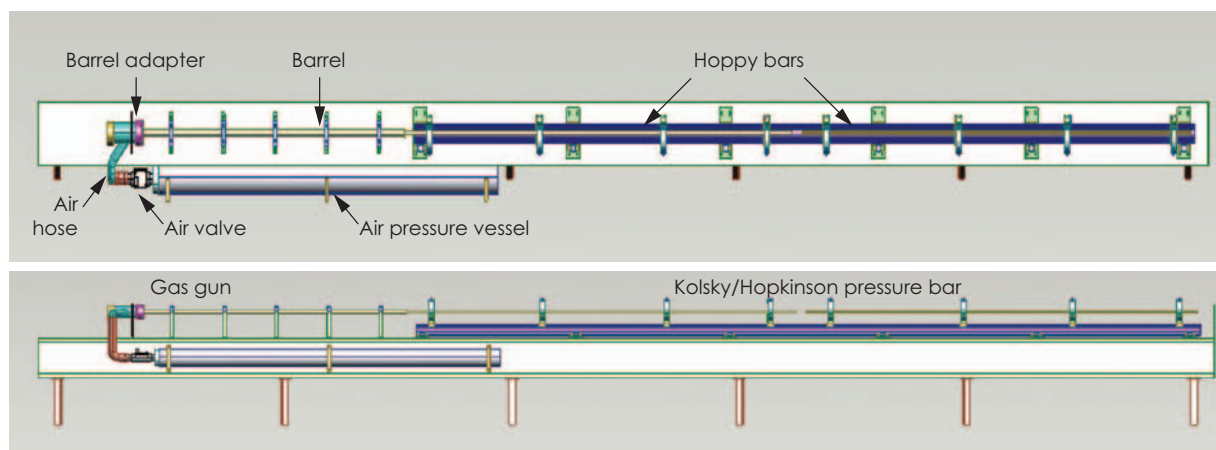
For more information contact
Chol K. Syn
(925) 423-8226
syn1@llnl.gov

mechanism for the KHPB set-up. The barrel length can be extended to 20 ft if the gas gun needs to generate the upper range of projectile speed. When the system is to be used only as a gas gun, the KHPB set-up will be dismantled, and a dynamic fracture/impact test specimen set-up will be installed.

The gas gun will be able to launch inert metal projectiles up to a maximum of 120 m/s. The gun will operate using stored energy from compressed air, and will be actuated using a commercially available solenoid valve with a fire-control circuit. The fire-control circuit contains safety interlocks and uses light beams to provide projectile velocity data. Once the gun is fired, the compressed gas accelerates the projectile. The momentum of the projectile is transferred to the KHPB apparatus for dynamic deformation of a specimen inserted between the bars, or to a dynamic fracture test specimen with pre-existing flaws.

FY2006 Proposed Work

We have prepared documentation for review. The next steps will be integration and testing of the system.

(a)

(b)
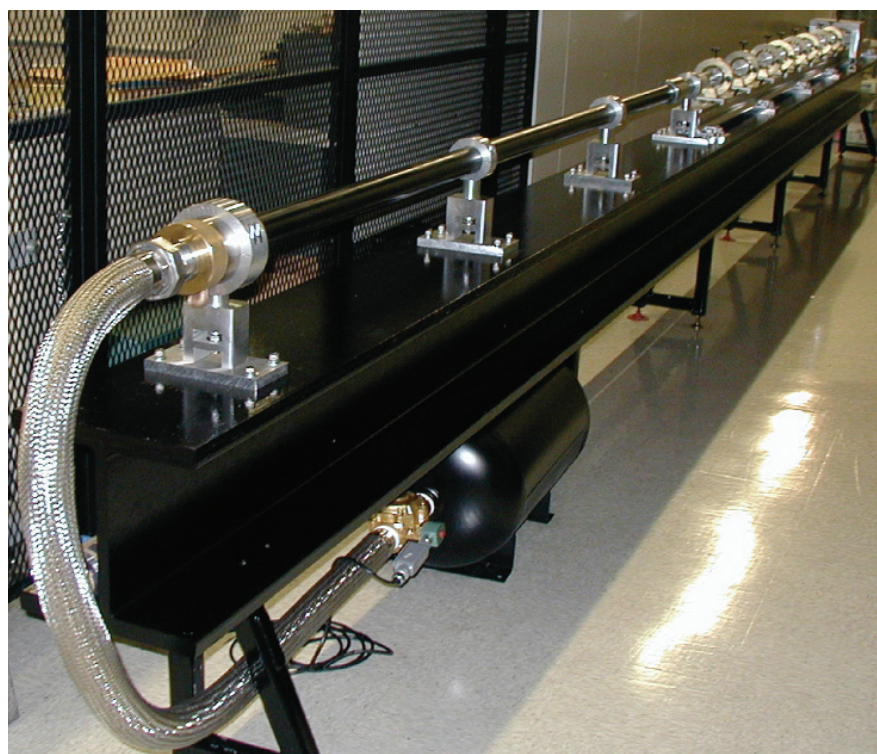
Figure 2. Photograph showing the gas gun-KHPB system assembled. The air pressure vessel, air valve, air hose, barrel adapter, and barrel of the gas gun side shown in Fig. 1 are visible in the foreground.
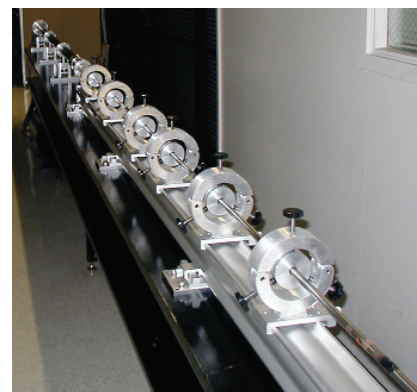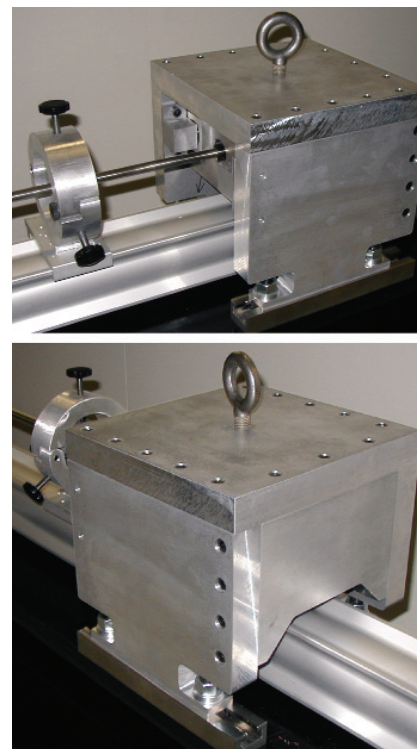
Figure 3. (a) Photograph of the gas gun-KHPB system assembled. The assembly shown in Fig. 1 is visible in the foreground. (b) Two images of the damper assembly mounted at the end of the KHPB system.

Author Index

AUTHOR INDEX

ENGINEERING

Lawrence Livermore National Laboratory
University of California
P.O. Box 808, L-151
Livermore, California 94551
http://www-eng.llnl.gov/